NUREG/CR-6804
ANL-02/28

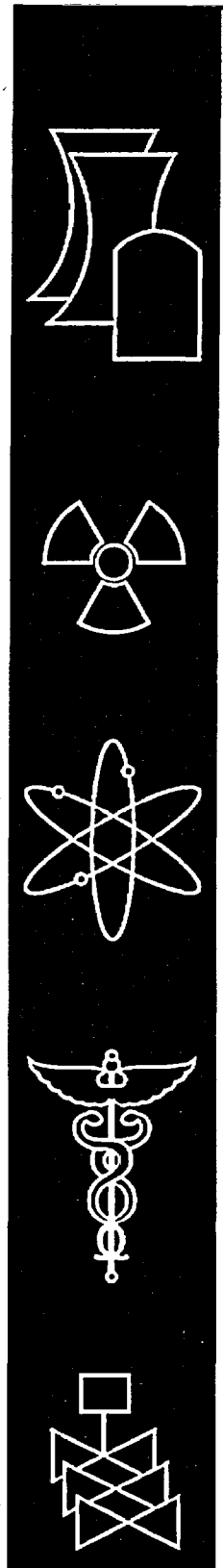

Second U.S. Nuclear Regulatory Commission International Steam Generator Tube Integrity Research Program

Final Project Summary Report

Argonne National Laboratory

U.S. Nuclear Regulatory Commission
Office of Nuclear Regulatory Research
Washington, DC 20555-0001

AVAILABILITY OF REFERENCE MATERIALS IN NRC PUBLICATIONS

NRC Reference Material

As of November 1999, you may electronically access NUREG-series publications and other NRC records at NRC's Public Electronic Reading Room at http://www.nrc.gov/reading-rm.html. Publicly released records include, to name a few, NUREG-series publications; *Federal Register* notices; applicant, licensee, and vendor documents and correspondence; NRC correspondence and internal memoranda; bulletins and information notices; inspection and investigative reports; licensee event reports; and Commission papers and their attachments.

NRC publications in the NUREG series, NRC regulations, and *Title 10, Energy*, in the Code of *Federal Regulations* may also be purchased from one of these two sources.

1. The Superintendent of Documents
   U.S. Government Printing Office
   Mail Stop SSOP
   Washington, DC 20402–0001
   Internet: bookstore.gpo.gov
   Telephone: 202-512-1800
   Fax: 202-512-2250
2. The National Technical Information Service
   Springfield, VA 22161–0002
   www.ntis.gov
   1–800–553–6847 or, locally, 703–605–6000

A single copy of each NRC draft report for comment is available free, to the extent of supply, upon written request as follows:

Address: Office of the Chief Information Officer,
Reproduction and Distribution
Services Section
U.S. Nuclear Regulatory Commission
Washington, DC 20555-0001
E-mail: DISTRIBUTION@nrc.gov
Facsimile: 301–415–2289

Some publications in the NUREG series that are posted at NRC's Web site address http://www.nrc.gov/reading-rm/doc-collections/nuregs are updated periodically and may differ from the last printed version. Although references to material found on a Web site bear the date the material was accessed, the material available on the date cited may subsequently be removed from the site.

Non-NRC Reference Material

Documents available from public and special technical libraries include all open literature items, such as books, journal articles, and transactions, *Federal Register* notices, Federal and State legislation, and congressional reports. Such documents as theses, dissertations, foreign reports and translations, and non-NRC conference proceedings may be purchased from their sponsoring organization.

Copies of industry codes and standards used in a substantive manner in the NRC regulatory process are maintained at—

The NRC Technical Library
Two White Flint North
11545 Rockville Pike
Rockville, MD 20852–2738

These standards are available in the library for reference use by the public. Codes and standards are usually copyrighted and may be purchased from the originating organization or, if they are American National Standards, from—

American National Standards Institute
11 West 42nd Street
New York, NY 10036–8002
www.ansi.org
212–642–4900

Legally binding regulatory requirements are stated only in laws; NRC regulations; licenses, including technical specifications; or orders, not in NUREG-series publications. The views expressed in contractor-prepared publications in this series are not necessarily those of the NRC.

The NUREG series comprises (1) technical and administrative reports and books prepared by the staff (NUREG–XXXX) or agency contractors (NUREG/CR–XXXX), (2) proceedings of conferences (NUREG/CP–XXXX), (3) reports resulting from international agreements (NUREG/IA–XXXX), (4) brochures (NUREG/BR–XXXX), and (5) compilations of legal decisions and orders of the Commission and Atomic and Safety Licensing Boards and of Directors' decisions under Section 2.206 of NRC's regulations (NUREG–0750).

NUREG/CR-6804
ANL-02/28

Second U.S. Nuclear Regulatory Commission International Steam Generator Tube Integrity Research Program

Final Project Summary Report

Manuscript Completed: August 2002
Date Published: September 2003

Prepared by
S. Bakhtiari, K. E. Kasza, D. S. Kupperman,
S. Majumdar, J. Y. Park, W. J. Shack,
D. R. Diercks

Argonne National Laboratory
9700 South Cass Avenue
Argonne, IL 60439

J. Muscara, NRC Project Manager

Prepared for
Division of Engineering
Office of Nuclear Regulatory Research
U.S. Nuclear Regulatory Commission
Washington, DC 20555-0001
NRC Job Code W6487

NUREG/CR-6804, has been reproduced from the best available copy.

Abstract

This report summarizes work performed under the USNRC Steam Generator Integrity Program at Argonne National Laboratory. The areas addressed by the program include assessment of procedures and equipment used for in-service (ISI) inspection of steam generator (SG) tubes; recommendations for criteria and requirements to improve the reliability and accuracy of ISI; validation and improvement of correlations and models that are used to evaluate integrity and leakage of degraded SG tubes; and validation and improvement of correlations and models that predict the generation and progression of degradation in SG tubes as a function of aging.

Contents

Figures

Tables

Executive Summary

Assessment of Inspection Reliability

The development and implementation of two key concepts, condition monitoring and operational assessment, is a major outcome of regulatory activity over the past ten years. That effort was intended to develop guidance for tube integrity assessments. Condition monitoring involves an assessment of the current state of the steam generator (SG) relative to the performance criteria for structural integrity. An operational assessment is an attempt to assess the state of the generator relative to the structural integrity performance criteria at the end of the next inspection cycle. Predictions of the operational assessment from the previous cycle can be compared with the results of the condition monitoring assessment to verify the adequacy of the methods and data used to perform the operational assessment.

The reliability of nondestructive evaluation (NDE) techniques used to determine the flaw distribution in terms of detection and characterization of flaws and the capability to assess their impacts on the structural integrity (i.e., structural and leakage integrity) of SG tubes is a key factor in establishing the reliability of operational assessments and condition monitoring. An NDE round-robin exercise has been used to independently assess SG inspection reliability. The NDE round-robin exerecise was conducted using a steam generator mock-up at Argonne National Laboratory (ANL).

The steam generator mock-up consists of 400 Alloy 600 tubes made up of nine test sections, each 0.3 m (1 ft) long. The test sections are arranged in nine levels, each having 400 tube sections. The lowest level simulates the tube sheet, while three other levels simulate tube support plate (TSP) intersections. The remaining five levels are free-span regions. Tubes rolled into ferritic steel collars simulate the tube sheet geometry. Thus, both the roll transition geometry and the effect of the ferritic tube sheet are simulated. In the TSP crevice, the presence of magnetite was simulated by filling the crevice with magnetic tape or a ferromagnetic fluid. A mixture of magnetite and copper powder in an epoxy binder simulated sludge deposits.

The mock-up contains hundreds of cracks and simulations of artifacts, such as corrosion deposits, support structures, and tube geometry variations that generally make the detection and characterization of cracks more difficult. An expert NDE Task Group from ISI vendors, utilities, ANL, the Electric Power Research Institute (EPRI), and the U.S. Nuclear Regulatory Commission (NRC) has reviewed the eddy current signals from laboratory-grown cracks used in the mock-up to ensure that they provide a realistic simulation of cracks obtained in the field. The number of tubes inspected and the number of teams participating in the round-were selected to provide better statistical data on the probability of detection (POD) and characterization accuracy than is currently available from industry performance demonstration programs.

The reference state for each flaw in the mock-up, i.e., crack geometry and size, was established by using an ANL-developed algorithm for multiparameter eddy current (EC) data analysis. Both pre- and post-assembly inspection results were used for this purpose. Throughout the development stage of the algorithm, the NDE predictions were compared with results obtained by destructive analyses for dozens of flaws. A final validation was performed

by comparing the NDE results to destructive analyses in a blind test on a set of 23 flawed specimens. The results from this comparison were used to estimate the uncertainties associated with the depth estimates from the multiparameter algorithm. Further validation was carried out by destructive examination of selected tubes removed from the mock-up and tubes removed from steam generators from McGuire Unit One.

Eleven teams participated in the analysis round-robin. Each team provided nine reports: a primary, a secondary, and a resolution analysts' report for each of the three optical data disks containing the inspection results [bobbin coil (BC) data for all tubes, rotating pancake coil (RPC) data for all tube-sheet test sections, and RPC data for a set of selected test sections]. Results were analyzed for all teams. Team–to–team variation in the POD presented, along with the population average. The detection results for the 11 teams were used to develop POD curves as a function of maximum depth and the parameter m_p, which can be interpreted as a stress multiplier that relates the stress in the ligament ahead of the crack to the stress in an unflawed tube under the same loading. Because m_p incorporates the effect of both crack depth and length, it better characterizes the effect of a flaw on the strength (i.e., structural and leakage integrity) of a tube than do traditional indicators such as maximum depth. The effect of both statistical uncertainties inherent in sampling from distributions and the uncertainties due to errors in the estimates of maximum depth and m_p were estimated. The 95% one-sided confidence limits, which include errors in maximum depth estimates, are presented along with the POD curves.

Deplugged tubes and tube sheet sections removed from retired steam generators at McGuire Unit One were inspected before removal using +Point, "3-coil" pancake, and bobbin coil probes. The results were compared with results from previous inspections of the tubes. In all cases the BC voltages increased over time. The most likely cause of the voltage change is a change in the character of the corrosion deposits on the cracks, but other factors that could result in voltage increases include crack growth and a change in crack width.

Several flawed tubes from McGuire have been reexamined at Argonne in a glovebox facility that can handle contaminated tubes. In general, the voltages measured at Argonne are slightly lower than those measured before removal, with the phase essentially unchanged, except for one flaw with a particularly large voltage. The observed differences could be the result of variations in the mix and changes in conduction paths across the crack faces resulting from the tube pulling procedure (i.e., crack faces now touching).

Research on Inservice Inspection Technology

Research on improved ISI technology of steam generator tubes focused on four areas: evaluation of analytical methods for the prediction of EC responses as a function of probe design, flaw characteristics, and material properties; assessment of effective signal analysis procedures; assessment of flaw imaging and display methods for simple and accurate flaw characterization; and evaluation of improved probe designs that use directional arrays so that axial and circumferential defects can be examined simultaneously. The reliability and effectiveness of improved inspection techniques were evaluated through laboratory testing of SG tubes that contain various flaws and the SG tube bundle mock-up. Some validation efforts utilized the in–service-degraded SG tubing from McGuire.

Several analytical and computational approaches to electromagnetic modeling for simulating EC probe response in the NDE of SG tubing have been examined. Most of the efforts focused on the applications of a general-purpose 3-D FEM-based code for steady-state and transient-field calculations.

In conventional EC data analysis of SG tubing, human analysts are trained to differentiate flaw-induced signals from artifacts by analysis of the behavior of signals, typically extracted from their impedance plane trajectory and signal amplitude, through application of a series of rules. For example, clockwise (CW) and counter-clockwise (CCW) rotation of the impedance plane signal trajectory is commonly used to determine the flaw origin. When the phase angles at all frequencies from a TW flaw are set to a fixed value, flaw indications of OD origin exhibit CCW rotations, and those of ID origin have smaller CW rotations.

Manual analysis of multiple-frequency EC data is a tedious and challenging process. No qualified technique, manual or automated, currently exists that could provide reliable estimation of flaw size over a wide range of SG tubing damage. Conventional data analysis methods become rather subjective when dealing with complex forms of degradation such as SCC. Signal distortion by interference from internal/external artifacts in the vicinity of a flaw further complicates discrimination of flaw signals from noise. Analogous to the manual analysis of EC inspection data, computer-aided data analysis algorithms can be developed from analysis of the characteristic behavior of EC signals as a function of frequency. Because all available information can be examined rather than a selected subset in the case of a manual analysis, such algorithms allow more effective identification of subtle forms of degradation. Computer-based algorithms that imitate some form of human decision making are generally labeled as expert systems.

Multiparameter algorithms for the computer-aided analysis of EC NDE data have been developed and implemented in a set of data analysis and signal processing algorithms that have been written using the PC-based software MATLAB, a high-level scripting language that provides an efficient environment for data manipulation and computation, together with convenient graphical user interfaces (GUIs) and graphical displays of the results. Phase angle information from multiple channels is used to construct a model that correlates the NDE results to flaw size and origin. The flaw size and origin are assumed to be related to the phase angle information at the different frequencies. Eddy current measurements on a calibration standard tube are used to determine the regression coefficients in the relation. The effectiveness of the multiparameter algorithms for the computer-aided analysis of EC NDE data has been evaluated in studies on electrodischarge machined (EDM) notches, laboratory-grown flaws, and in-service flaws.

Research on Degradation Modes and Integrity

Because degraded tubing from operating or retired SGs is difficult and expensive to obtain and the availability of such tubing is limited, it was necessary to produce prototypical degradation in tubes as a part of the program. The degraded tubes were used in the SG mock-up and for pressure and leak-rate testing. Techniques have been developed to produce SCC degradation of various sizes, depths, and orientations that are prototypical of field-degraded SG tubes. During the course of the program, a total of about nine-hundred 22.2-mm ($^7/_8$-in.)-diameter Alloy 600 tubes were processed to produce axial and circumferential outer-diameter stress corrosion cracking (ODSCC), axial and circumferential

inner-diameter stress corrosion cracking (IDSCC), and SCC in skewed orientations. Some of the specimens were produced with multiple cracks or combination of multiple cracks of different orientations. Most of the specimens were straight tubes, but some were roll–expanded, dented, or ovalized.

One of the phenomena considered in NUREG–1570 was the potential for the propagation of tube failures during severe accidents. In the event of a tube failure, the escaping jet of superheated steam could entrain particles from the core debris and impinge on a neighboring tube. The particle-laden jet could then erode through the neighboring tube, leading to another escaping jet and the possibility of a cascading failure event in the steam generator. Some analyses were reported in NUREG–1570 to estimate the time required for a jet from a failed tube to induce failure in an adjacent tube. It was noted that the analyses were at best scoping estimates. An investigation was carried out in the present program to analyze the potential for such a failure in more detail. The effort included high-temperature erosion tests conducted at the University of Cincinnati, a computational fluid dynamics analysis of the escaping jet, and development of a model for calculating the crack opening area as a function of time. The results showed that, even after some conservative assumptions are made, failure of an adjacent tube would take >10 h. Thus, jet impingement is very unlikely to play any significant role in the failures.

Under design-basis conditions, two basic erosion damage mechanisms, droplet impact and cavitation, are believed possible from fluid jets associated with flawed SG tubes. In the case of jets consisting of water droplets, the impact of the droplet gives rise to fluctuating stresses in the target, which produce fatigue damage. In the case of cavitation, bubbles form in the liquid stream and then collapse on impact, again producing fluctuating stresses and fatigue in the target.

Tests has been conduced to determine the susceptibility of steam generator tubes to erosive damage from impacting jets of superheated water or steam leaking from adjacent tubes. The tests show that the impact erosion depth varies with water temperature, and the erosion rate is substantially reduced with decreasing and increasing subcooling on either side of the peak damage temperature range. The peak erosion rates occur for degrees of subcooling typical of the cold leg, though cracking is much less likely to occur here. Erosion rates are much lower for conditions more typical of the hot leg. Even in the case of the cold leg, where the erosion rates are higher, the likelihood of failure propagation by jet erosion appears to be very low.

Analysis and testing have been performed to develop models for predicting failure pressures and leak rates in steam generator tubes with axial and circumferential cracks under normal operation and design-basis and severe accident conditions. The models can account for effects of the constraint exerted by support structures such as the tube support plates. In addition to models for the unstable failure (burst) of the tube, extensive tests on rectangular as well as trapezoidal and triangular part-throughwall flaws were conducted to derive a correlation for predicting the failure of radial ligaments in tubes with axial notches, either shallow or deep.

A procedure has been developed for defining an equivalent rectangular crack for an arbitrarily shaped notch or crack. Structural and leak rate analyses of the flaws and comparison with experimental data have shown that the radial ligament failure pressure in

nonrectangular notches or SCCs can be predicted reasonably well by using a flow stress model that is strictly applicable to rectangular part-throughwall cracks and replacing the actual crack profile by an equivalent rectangular crack. An empirical approach for calculating crack growth by stable ligament rupture has been developed by an extension of the equivalent rectangular crack method. The approach has been used to calculate the incremental ligament rupture of non-rectangular notches as well as stress corrosion cracks.

Interaction effects between two or more throughwall notches as influenced by ligaments separating the notches are analyzed by finite element analyses. Interaction effects (with respect to radial ligament rupture) between two or more part-throughwall notches can be estimated by the equivalent rectangular crack approach.

The calculated crack opening displacements (areas) for rectangular and trapezoidal throughwall notches were in reasonable agreement with measured values. Leak rates for tests on specimens with EDM notches or open cracks can be predicted reasonably well by using the well-known formula for single-phase flow through smooth circular orifices and by replacing the orifice area by the crack opening area. In tests conducted to date, the equations can predict the ligament rupture pressures and leak rates for rectangular and trapezoidal EDM notches at both room temperature and 282°C if the appropriate densities of water are used. The correlation will break down at lower levels of leak rates for very tight stress corrosion cracks, particularly at elevated temperatures where flashing may occur inside the cracks; but such a limit has not yet been established.

A creep rupture-based criterion was developed for predicting radial ligament rupture during severe accident conditions. The ligament rupture criteria for part-throughwall cracks were validated with SG tubes having rectangular EDM notches in tests conducted at room temperature, 282°C, and >600°C.

The behavior of flawed tubes with Electrosleeve™ repairs during severe accidents was examined. Although the nanocrystalline Electrosleeve™ has superior mechanical properties compared to Alloy 600 at reactor operating temperatures, it loses strength at high temperatures because of grain growth. A flow-stress based ligament rupture criterion was developed for predicting failure of Electrosleeved tubes with 80–100% deep throughwall cracks in the parent tubes and was validated with high-temperature tests on EDM-notched Electrosleeved tubes supplied by Framatome Technologies, Inc.

Integrated Model for Steam Generator Integrity Assessments

The models for predicting radial ligament rupture, unstable burst, and leak rate of flawed Alloy 600 tubes developed in the program have been incorporated into the integrity assessment code for SG tubes, CANTIA, which was originally developed by Dominion Engineering for the Canadian Nuclear Safety Commission. Several other modifications were also made in ANL/CANTIA. The source language of the code was updated to Visual BASIC 6. The treatment of the basic flaw was changed from one- to two-dimensional, and the calculation routines for crack growth were made more rigorous. Two well-known SCC growth models from the literature were included as options, and a simple residual stress model was added. ANL/CANTIA can handle either axial or circumferential cracks, but not both simultaneously.

Preliminary trial runs demonstrated that it is very difficult to grow stress corrosion cracks in SG tubes by pressure stress alone. Several trial runs with residual stress were conducted to demonstrate the importance of POD and initiation of new cracks on rupture and leak rate probabilities.

Acknowledgments

The authors thank C. Vulyak and L. Knoblich for their contributions to the experimental effort and P. Heasler and R. Kurtz for discussions related to the statistical analysis. The authors also thank the NDE Task Group Members, G. Henry and J. Benson (EPRI), T. Richards and R. Miranda (Framatome Technology), D. Adamonis and R. Maurer (Westinghouse), D. Mayes (Duke Engineering and Services), S. Redner (Northern States Power), and B. Vollmer and N. Farenbaugh (Zetec, Inc.). They also thank H. Houserman and H. Smith for their input in this effort. The authors acknowledge the contributions of C. Gortemiller, C. Smith, S. Taylor, and the staff from Zetec Inc. to the data acquisition and analysis effort. The authors also thank proctors S. Gopalsami, K. Uherka, and M. Petri, as well as ABB-CE, Anatec, DE&S, FTI, KAITEC, Ontario Power Generation, Westinghouse, and Zetec for providing round-robin analysis teams. This work is sponsored by the Office of Nuclear Regulatory Research of the U.S. Nuclear Regulatory Commission under Job Code W6487. The Program Manager is Dr. J. Muscara, who provided helpful guidance in the performance of this work.

Acronyms and Abbreviations

ABB-CE	ASEA Brown-Boveri-Combustion Engineering
AECL	Atomic Energy of Canada, Ltd.
ANL	Argonne National Laboratory
APC	alternative plugging criterion
ARC	alternative repair criterion
ASME	American Society of Mechanical Engineers
BC	bobbin coil
CCW	counter clockwise
CIDSCC	circumferential inner-diameter stress corrosion crack/cracking
CODSCC	circumferential outer-diameter stress corrosion crack/cracking
COD	crack opening displacement
CW	closckwise
DE&S	Duke Engineering and Services
EC	eddy current
ECT	eddy current testing
EDM	electrodischarge machining
EFPY	equivalent full power years
EM	electromagnetic
EPRI	Electric Power Research Institute
FEA	fintie element analysis
FEM	finite element method
FIR	finite-impulse response
FS	freespan
FTI	Framatome Technology
ID	inner diameter
IGA	intergranular attack
INEEL	Idaho National Engineering and Environmental Laboratory
ISI	inservice inspection
LIDSCC	longitudinal inner-diameter stress corrosion crack/cracking
LODSCC	longitudinal outer-diameter stress corrosion crack/cracking
LS	least squares
MLR	multiple linear regression
MRPC	motorized rotating pancake coil
MSLB	main steam line break
NDE	nondestructive evaluation
NDD	nondetectable degradation
NRC	U.S. Nuclear Regulatory Commission
OD	outer diameter
OPG	Ontario Power Generation
OSL	One-sided 95% confidence limits
PCR	principal component regression
PLS	partial least squares
PNNL	Pacific Northwest National Laboratory
POD	probability of detection
PSI	Paul Scherrer Institute
PWR	pressurized water reactor

PWSCC	primary-water stress corrosion crack/cracking
RPC	rotating pancake coil
RR	round-robin
RTZ	roll transition zone
SCC	stress corrosion crack/cracking
SG	steam generator
S/N	signal to noise ratio
SS	stainless steel
SVD	singular value decomposition
TS	tube sheet
TSP	tube support plate
TTS	top of tube sheet
TW	throughwall
UT	ultrasonic testing
V_{pp}	peak-to-peak voltage
W	Westinghouse

1 Introduction

The objective of this program is to provide the experimental data and predictive correlations and models needed to permit the U.S. Nuclear Regulatory Commission (NRC) to independently evaluate the integrity of steam generator (SG) tubes as plants age and degradation proceeds, new forms of degradation appear, and new defect-specific management schemes are implemented. The areas addressed by the program include assessment of procedures and equipment used for inservice inspection (ISI) of SG tubes; and recommendations for criteria and requirements to improve the reliability and accuracy of ISI; validation and improvement of correlations and models that are used to evaluate integrity and leakage of degraded SG tubes; and validation and improvement of correlations and models that predict the generation and progression of degradation in SG tubes as a function of aging.

This program is divided into four technical tasks and one management task: Assessment of Inspection Reliability; Research on ISI Technology; Research on Degradation Modes and Integrity; Integration of Results, Methodology, and Technical Assessments for Current and Emerging Regulatory Issues; and Program Management.

This report summarizes the results and accomplishments over the duration of this program from its inception in August 1995 through its conclusion in December 2001.

2. Assessment of Inspection Reliability (D. S. Kupperman and S. Bakhtiari)

2.1 Steam Generator Mock-Up Round Robin

2.1.1 Introduction

One major outcome of regulatory activity over the past 10 years intended to develop guidance for tube integrity assessments is the development and implementation of two key concepts: condition monitoring and operational assessment. Condition monitoring involves an assessment of the current state of the SG relative to the performance criteria of structural integrity. An operational assessment is an attempt to assess what the SG state will be relative to the structural integrity performance criteria at the end of the next inspection cycle. The predictions of the operational assessment from the previous cycle can be compared with the results of the condition monitoring assessment to verify the adequacy of the methods and data used to perform the operational assessment. The reliability of the in-service inspection (ISI) is critical to the effectiveness of the assessment processes. Quantitative information on probability of detection (POD) and sizing accuracy of current-day flaws for techniques used for SG tubes is needed to determine if tube-integrity performance criteria were met during the last operating cycle, and if performance criteria for SG tube integrity will continue to be met until the next scheduled ISI. Information on inspection reliability will permit estimation of the true state of SG tubes after an ISI by including the flaws that were missed because of imperfect POD. Similarly, knowledge of sizing accuracy will permit corrections to be made to flaw sizes obtained from ISI.

Eddy-current (EC) inspection techniques are the primary means of ISI for assessing the condition of SG tubes in current use. Detection of flaws by EC depends on detecting the changes in impedance produced by the flaw. Although the impedance changes are small ($\approx 10^{-6}$), they are readily detected by modern electronic instrumentation. However, many other variables, including tube material properties, tube geometry, and degradation morphology, can produce impedance changes, and the accuracy of distinguishing between the changes produced by such artifacts and those produced by flaws is strongly influenced by EC data analysis and acquisition practices (including human factors). Similarly, although it can be shown that the depth of a defect into the tube wall is related to the EC signal phase response, in practice, those factors that affect detection also affect sizing capability.

The most desirable approach to establishing the reliability of current ISI methods is to carry out round-robin (RR) exercises in the field on either operating SGs or those removed from service. However, access to such facilities and validation of the results would difficult. Such work would also be prohibitively expensive. In addition, obtaining data on all morphologies of interest would require tubes from many different plants.

The approach chosen for this program was to develop an SG tube bundle mock-up that simulates the key features of an operating SG so that the inspection results from the mock-up would be representative of those for operating SGs. Considerable effort was expended in preparing realistic flaws and verifying that their EC signals and morphologies are representative of those from operating SGs. The mock-up includes stress corrosion cracks of different orientations and morphologies at various locations in the mock-up and simulates the

artifacts and support structures that may affect the EC signals. Factors that influence detection of flaws include probe wear, eddy current signal noise, signal-to-noise ratio, analyst fatigue, and the subjective nature of interpreting complex eddy current signals. In this exercise, all analysts examine the same data provided on optical disks that contain copies of the data to be analyzed. The team-to-team variation in detection capability is the result of analyst variability in interpretation of eddy current signals. The mock-up will also be used as a test bed for evaluating emerging technologies for the ISI of SG tubes.

2.1.2 Steam Generator Mock-Up Facility

The mock-up tube bundle consists of four-hundred Alloy 600 tubes (22.2-mm [0.875-in.]-diameter) consisting of 9 test sections, each 0.3 m (1 ft) long. Test sections are arranged in nine levels, with 400 test sections at any elevation. The centers of the tubes are separated by 3.25 cm (1.28 in.). Tie rods hold the test sections together. The ends of each test section are pressed into 19-mm (0.75-in.)-thick high-density polyethylene plates that hold the test sections in alignment. One end of each tube is spring-loaded. The lowest level (A) has a roll transition zone (RTZ) and simulates the tube sheet, while the 4^{th}, 7^{th}, and 9^{th} levels simulate drilled hole tube support plate (TSP) intersections. The other five levels are freespan regions. Above the 9th level is a 0.91-m (3-ft)-long probe run-out section (see Fig. 2.1 for the tube bundle diagram and Fig. 2.2 for photograph of the mock-up).

Most of the degraded test sections were produced at ANL, although some were produced by Pacific Northwest National Laboratory (PNNL); Westinghouse; Equipos Nucleares, SA (ENSA); and the Program for the Inspection of Steel Components (PISC).

Alloy 600 test sections at ANL were cracked by using a 1 M aqueous solution of sodium tetrathionate at room temperature and atmospheric pressure. Localized environmental exposure, low applied load, and electrochemical potential were utilized to produce various crack geometries. Masking by coating areas of the tubes with lacquer was used to limit or localize the cracking area. The tubes were internally pressurized to generate hoop stresses to produce axial cracks and axially loaded to produce circumferential cracks. Various OD and ID crack geometries were produced: axial, circumferential, skewed, or combinations of these. Many of the specimens contained multiple cracks separated by short axial or circumferential ligaments. Prior to exposure to the sodium tetrathionate solution, specimens were sensitized by heat-treating at 600°C (1112°F) for 48 h to produce a microstructure that is susceptible to cracking. The mock-up was seeded with sensitized flaw-free test sections with and without artifacts so that the possibility of distinguishing sensitized from unsensitized test sections would not be an indicator that a flaw was present in that test section. In addition, many cracks from Westinghouse were grown without sensitizing the test sections.

Dye-penetrant examination (see Fig. 2.3 for example), as well as destructive metallography, were performed on many samples to provide documentation of the mock-up crack morphology. Figure 2.4 shows examples of LODSCC. Cracks in the mock-up provided by PNNL (about 50) were produced by Westinghouse using a proprietary doped steam method. Axial and circumferential cracks, both ID and OD, were produced for the freespan, TSP, and roll transitions. Several IGA specimens, as well as fatigue and wastage samples, were also provided by PNNL.

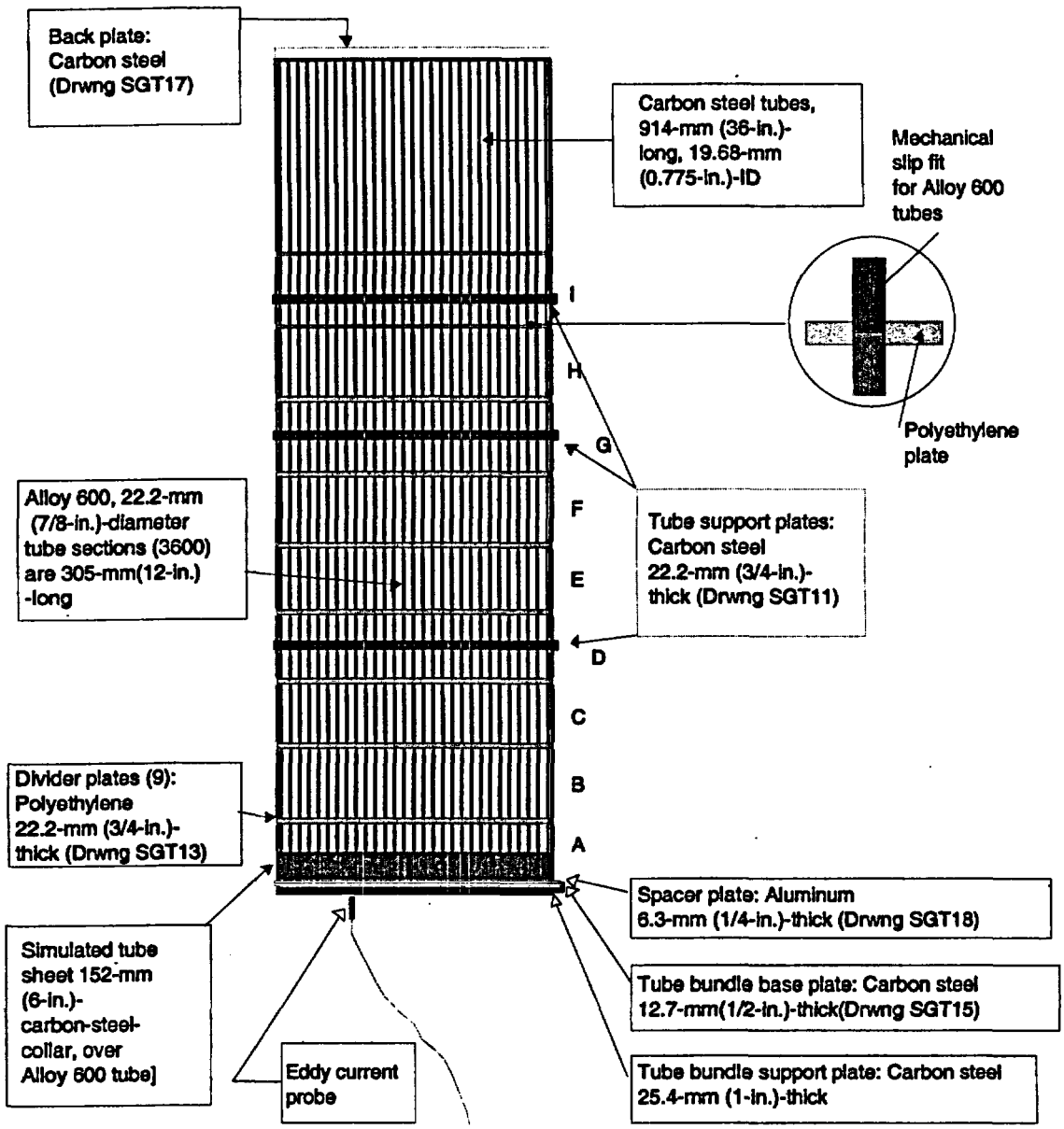

Figure 2.1. Schematic representation of tube bundle in steam generator mock-up.

Table 2.1 shows the distribution of flaw types in the mock-up. The flaw depths are distributed into three ranges, 0-40% TW, 41%-80% TW, and 81-100% TW. The distribution is skewed toward deeper cracks. This skewing is necessary to obtain high confidence in the high POD for the deeper cracks. Draft Regulatory Guide 1074 ("Steam Generator Tube Integrity") describes criteria for performance demonstrations to quantify defect detection performance (POD for a given defect). While the distribution of flaw sizes for the round-robin is not as uniform as required in Draft Regulatory Guide 1074, other requirements involving extraneous signals, signals from fabricated defects, and detection and false calls have, for the most part, been met.

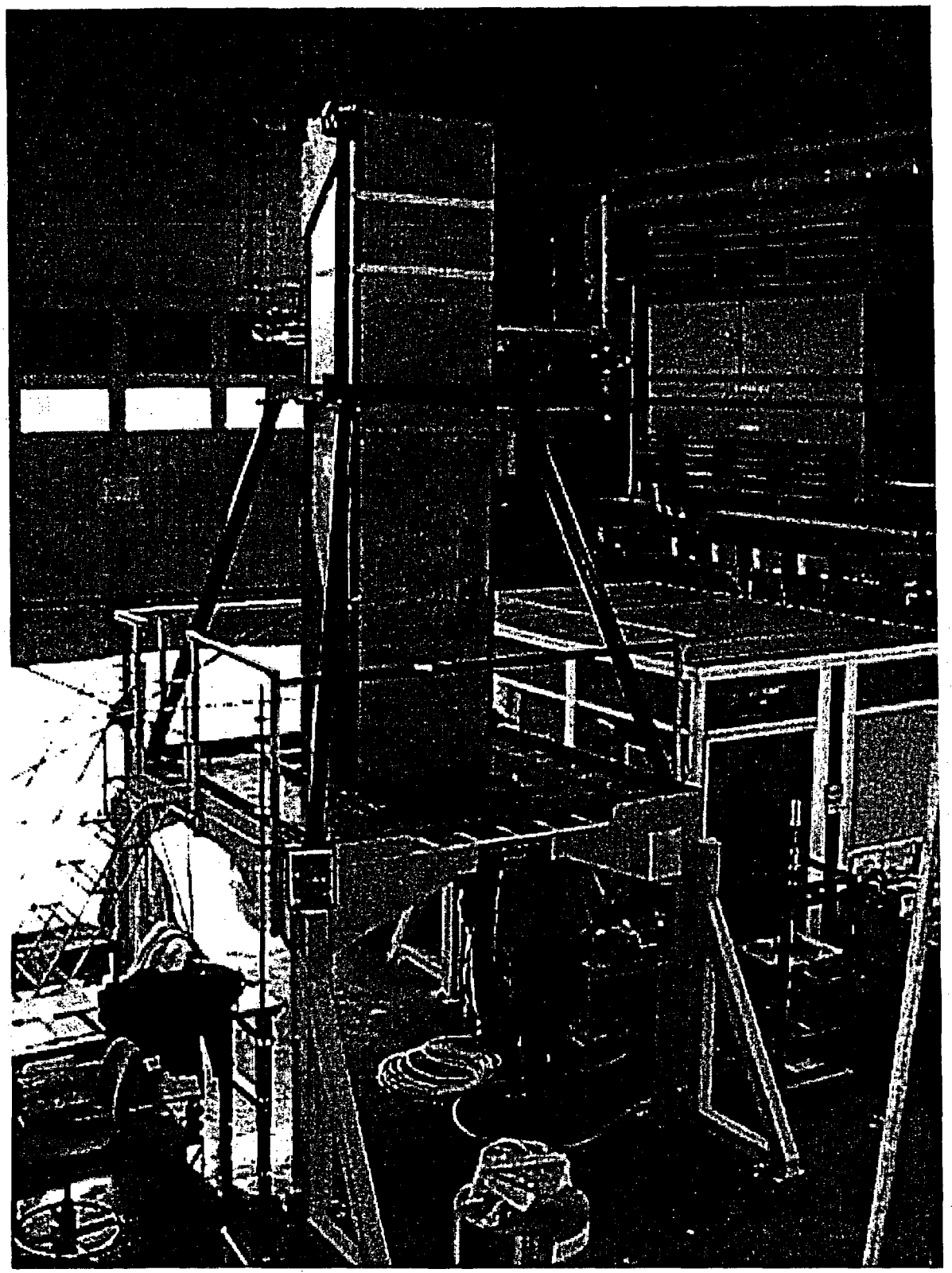

Figure 2.2. Photograph of mock-up during acquisition of eddy current data.

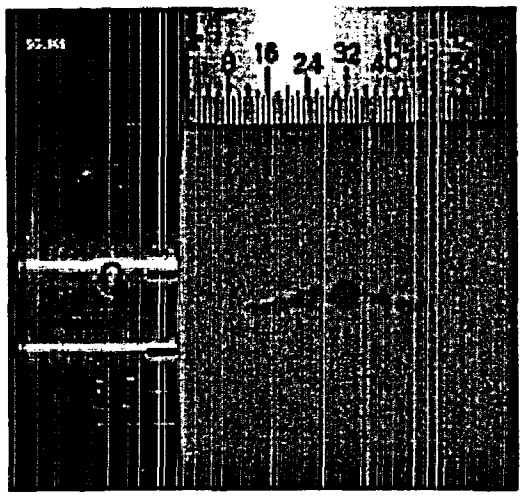

Figure 2.3.
Dye-penetrant examination of tube specimen SGL865 showing an LODSCC.

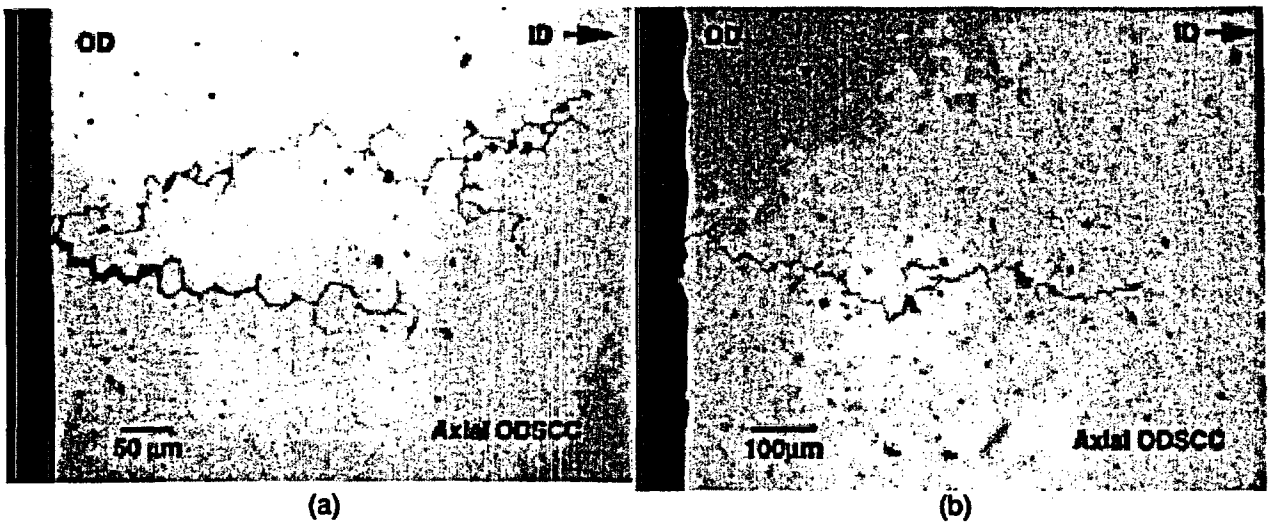

Figure 2.4 Cross-sectional optical metallography: (a) branched LODSCC and (b) LODSCC.

In the tube support plate (TSP) regions, filling the crevice with magnetic tape or a ferromagnetic fluid simulated magnetite in the crevices. A mixture of magnetite and copper bonded with epoxy was used to simulate sludge deposits. Simulated sludge was placed above the RTZ and at some TSP intersections. Many test sections had sludge or magnetite but no flaws. LODSCC and LIDSCC, both planar and segmented, and are present at TSP locations with and without denting. Some flaw-free test sections were dented. Cracks in the freespan are primarily LODSCC, both planar and segmented. Axial and circumferential ID and OD cracks are found in the RTZ. A small number of other flaw types such as IGA and wear were placed in the tube bundle. The mock-up also contains test sections with electric-discharge-machined (EDM) notches and laser-cut slots. Table 2.2 summarizes the degradation types and their locations in the mock-up.

Table 2.1. Distribution of flaw types

Max. Depth Range	EDM & Laser-Cut Slots	IGA	ODSCC TS	ODSCC TSP	ODSCC Free-span	PWSCC TS	PWSCC TSP	PWSCC Free-span	Wear/ Wast-age	Fatigue
0-40% TW	7	2	3	14	15	4	8	1	6	0
41-80% TW	13	9	2	14	26	8	16	0	6	0
81-100% TW	1	2	16	41	49	35	7	3	0	3

Table 2.2. Flaw types and quantity

Location	EDM & Laser-Cut Slots	IGA	ODSCC	PWSCC	Wear/ Wastage	Fatigue
Top of Tube Sheet	-		21	47	-	-
Freespan	14	8	90	4	3	-
TSPs	7	5	69	31	9	3

Magnetite-filled epoxy markers placed at the ends of all test sections provide a reference for the angular location of flaws when collecting data with a rotating or array probe. The analysts were instructed to ignore the region 25 mm (1 in.) from each test section end.

Prior to assembly, flawed test sections in the tube bundle were examined with both bobbin coil (BC) and a three-coil rotating probe that incorporates a +Point coil, a 2.9-mm (0.115-in.)-diameter pancake coil, and a 2-mm (0.080-in.)-diameter shielded pancake coil. In addition to a full EC examination, many cracked test sections were examined by dye-penetrant before being incorporated into the mock-up tube bundle. If EC data, dye penetrant results, or crack growth parameters indicated that a crack must be present, the test section was included in the mock-up. Because primary interest is with deep flaws, the majority of cracks selected for the mock-up had a +Point phase angle consistent with deep (> 60% TW) cracks. Because of the large fraction of deep flaws, high voltage signals are more common in the mock-up than in an actual steam generator.

The flaw types selected for the mock-up are those currently found in operating steam generators. Since about 1980, SG tube degradation has been dominated by SCC, which can occur on either the primary or secondary side, unlike the wastage and denting that occur exclusively on the secondary side (OD) of the tubes. Primary water stress corrosion cracking (PWSCC) is most likely to occur at regions of high residual stress, such as at the tube expansion transition and immediately above the tube sheet, at U-bends (particularly the small-radius U-bends), and in tube regions deformed by secondary-side denting. As a result, the mock-up consists primarily of ID and OD SCC at the TSP (with and without dents), at and above the roll transitions, as well as in the freespan. Outer-diameter intergranular attack (IGA) commonly occurs in crevices or under corrosion product scales. Such locations include the TSP crevice, the region near the top of the tube sheet, freespan areas under corrosion products or deposits, and regions under sludge buildup. As a result, some outer-diameter IGA is

present in the mock-up. In addition, there are some fatigue cracks, some test sections with wastage, and some with wear.

The distribution of voltages in the BC data from the mock-up was analyzed. The histograms show a reasonable distribution of BC voltages (up to 20 V) for cracks and conditions, and cracks alone. The voltages and phases for mock-up cracks are similar to those observed in field data such as from the McGuire Nuclear Plant.

To provide additional validation of the similarity of the mock up specimens to cracks in operating SGs, pulled tubes from a retired McGuire steam generator have been inspected at Argonne in a large glovebox modified for NDE studies. The NDE glovebox allows for the EC inspection of radioactive test sections, including samples with loose radioactive contamination. Figure 2.5 shows the BC Lissajous figure for an LODSCC from a dented TSP region of the McGuire steam generator. Two standards (one an ASME standard, the other an 18 EDM notch standard) were in line with the McGuire test section during the inspection. The BC data from the standards are seen in the linear traces on the left side of Fig. 2.5. Figure 2.6 shows a comparable BC Lissajous figure from an LODSCC in the mock-up. The similarity of the BC signals for the two LODSCC provides evidence of the ability to grow, under laboratory conditions, SCC that mimics the EC signals of field flaws.

As part of the development of the multiparameter algorithm, results have been compared to fractographic results on a wide variety of SCC cracks and EDM and laser-cut notches. To provide an objective benchmark, however, an additional set of 29 SCC cracks was produced and used in a blind test of the predictions of the algorithm against fractographic measurements of the crack geometry. Six of the benchmark samples have not yet been destructively analyzed because they will also be used for leak and ligament rupture tests that have not yet been performed.

The stress corrosion cracks for the blind test were produced by the same technique in 1 M aqueous solutions of sodium tetrathionate as described above. A variety of OD and ID crack geometries was produced: axial, circumferential, skewed, and combinations of these. Many of the specimens contained multiple cracks separated by short axial or circumferential ligaments. Cracked tubes were examined by dye-penetrant techniques, conventional eddy current NDE, the multiparameter algorithm, and destructive methods.

Data collection procedures for multifrequency inspection of the mock-up tubes are described in Ref. 3. These guidelines define the instrumentation setup (coil excitation frequencies, gain setting, cable length, sampling rate, probe speed, etc.) and calibration procedures for a given probe (e.g., bobbin, rotating, and array probes). Although the quality of data affects both detection and sizing, this issue is of particular concern when quantitative estimates of flaw size are to be determined. The multiparameter algorithm used to obtain flaw size estimates for the mock-up requires data at three frequencies and the minimum sampling rate recommended in the Examination Technique Specification Sheet (ETSS) for MRPC probes [3]. The multiple-frequency EC data were acquired with a standard three-coil rotating probe that incorporates a 2.92-mm (0.115-in.)-diameter mid-range primary pancake coil, a mid-range +Point™, and 2.03-mm (0.080-in.)-diameter high-frequency pancake coil. Initial amplitude profiles are obtained from the +Point coil at a single channel. The final estimated depth profiles are obtained by using multichannel information from the mid-range primary pancake coil for

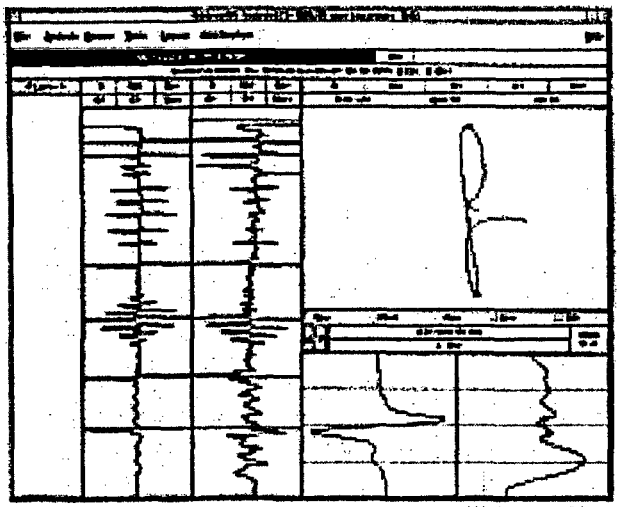

Figure 2.5.
Differential bobbin coil Lissajous figure at 400 kHz from crack in McGuire SG (LODSCC7243). EC data were taken from a McGuire pulled tube using Argonne's NDE glove-box facility.

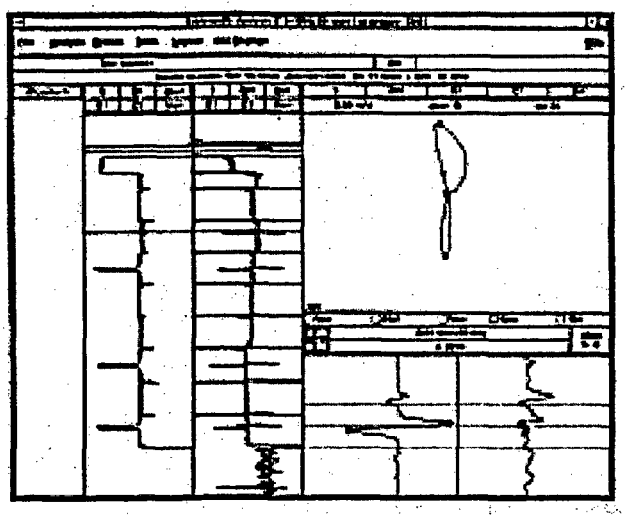

Figure 2.6.
Differential bobbin coil Lissajous figure at 400 kHz from Argonne-grown mock-up crack (LODSCC300). The BC signal shape, amplitude, and phase of the McGuire and Argonne SCC are similar.

multiparameter data analysis. The algorithm and the data quality issue are discussed in detail in Ref. 2, which also describes the conversion of Eddynet formatted data to a standard format for off-line analysis.

For the destructive examination, the samples were heat-tinted before fracture to permit differentiation of the SCC and fracture opening surfaces. The specimens were then chilled in liquid nitrogen, and cracks were opened by fracture. The fracture surfaces were examined macroscopically and with optical and scanning electron microscopy. The fractography and NDE data were digitized to obtain tabular and graphical comparisons of the depths as a function of axial or circumferential position. Well-defined markers on the test sections provided a means to accurately overlap the profiles. The fractured surfaces were recorded by digital photography at magnifications of 0.2–10X (Fig. 2.7).

Figure 2.7. Fractography of tube specimen SGL-413.

Crack profiles were obtained from digitized photographs of the fracture surfaces. The sampling distance depends on the complexity of the crack geometry. Short sampling distances were used for complicated geometries over a small scale, while longer distances were used for simpler geometries, e.g., straightline or smooth contours. Fractography and NDE results were plotted in a same figure for comparison (e.g., Fig. 2.8). Drawing lines through the EC data points generates the NDE profiles (nominally 12 points per centimeter [30 per inch] around the circumference and 12 points per centimeter [30 per inch] axially). The NDE and fractography profiles were then compared at many axial and circumferential positions, and the differences were used to establish the NDE uncertainty as a function of depth. The NDE uncertainties were then used to generate the lower 95% confidence limits for the POD curves presented in this report.

In the development of the multiparameter algorithm, the results from the algorithm have been compared to fractographic results on a wide variety of SCCs and EDM and laser-cut notches. To provide an objective benchmark, however, additional SCCs were produced and used for a blind test of the predictions of the algorithm against fractographic measurements of the crack geometry. Crack profiles from the destructive analyses are compared with those obtained from the multiparameter algorithm in Refs. 1-3. Figure 2.9 the maximum depths as determined by both fractography and by the multiparameter algorithm. A linear regression fit and 95% confidence bounds for the observed data as a function of the multiparameter estimates are shown in the figure. The overall root-mean-square error (RMSE) in the predicted maximum depths is 13.7%. If the comparison is limited to deeper cracks, the RMSE is smaller, namely 9.7% for depths 30–100% TW and 8.2% for ODSCC of depths 50–100% TW. The data are too few, however, to determine whether the apparent variation of the RMSE with depth is statistically significant.

Because the field of view of the rotating pancake probe is limited, the depth measurements at points ≥5 mm (≥0.2 in.) apart along the crack profile are essentially independent, and additional comparisons of the estimated depths with those determined by fractography were made at various points along the crack profile. To avoid observer bias in the selection of the data for comparison, the intersections of the crack profiles with the major

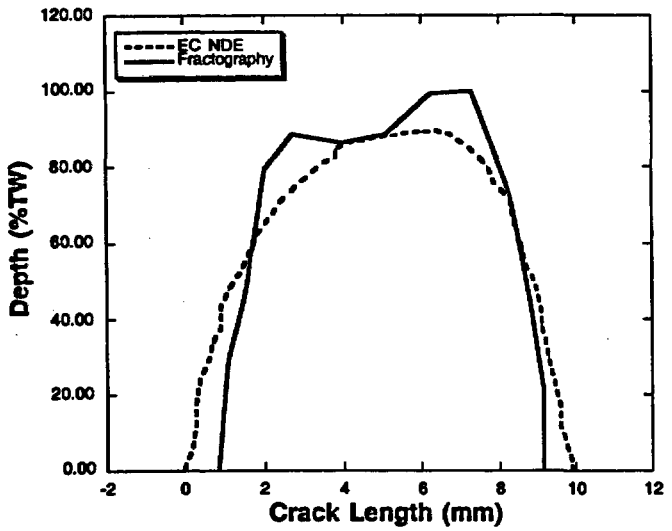

Figure 2.8.
Sizes and shapes of LODSCCs in tube specimen AGL-536 determined by EC NDE using the multiparameter algorithm (dotted curve) and fractography (smooth curve).

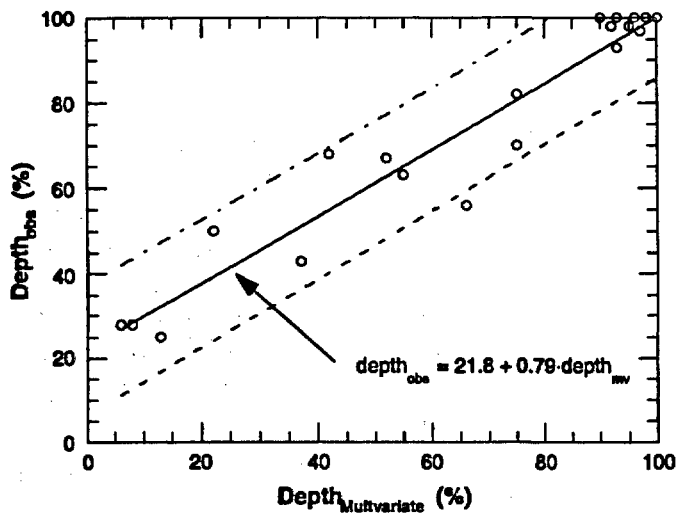

Figure 2.9.
Comparison of maximum depth determined by the multiparameter algorithm with that determined by fractography.

gridlines in the graphs of the superimposed profiles were chosen as the points for comparison. This corresponds, in most cases, to a spacing of 5-10 mm (0.2-0.4 in.) between points. Figures 2.10 and 2.11 show the results for 89 points from 20 different cracks, axial and circumferential, ID and OD. A linear regression curve and 95% confidence bounds for the observed data as a function of the multiparameter estimates are shown. The intercept in Fig. 2.10 is 13.8, somewhat less than that generated from the maximum depth data (Fig. 2.9), but the slope of 0.78 is almost identical to the linear regression line slope for the maximum depth data.

2.1.2.1 Accuracy of Maximum Depth for Mock-Up Cracks

Accuracy in estimating the maximum depth of cracks in the mock-up was determined by a comparison between crack profiles generated by ANL's multiparameter algorithm and profiles determined from fractography. The overall RMSE for all cracks of all depths is 15.1%, but the RMSE varies significantly with depth. The RMSE value is significantly better for 80–100% TW cracks than for cracks with other depths.

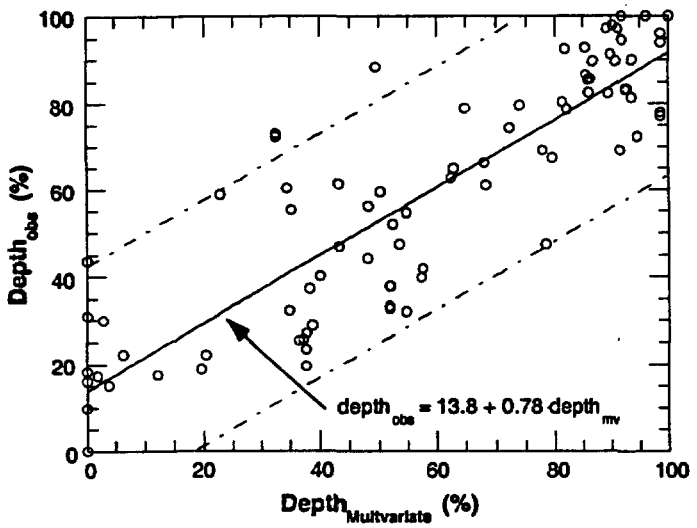

Figure 2.10.
Comparison of depths (% TW) determined by the multiparameter algorithm with those by fractography and regression fit as a function of the multiparameter depth estimate. Estimated 95% bounds for the observed depth are also given.

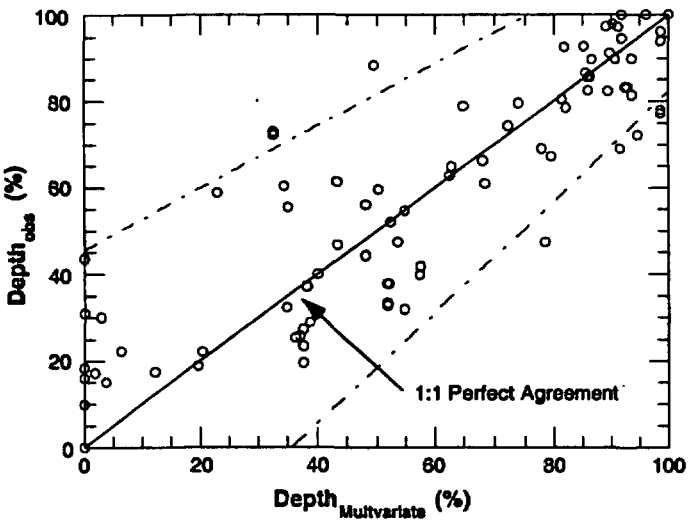

Figure 2.11.
Comparison of depths (% TW) determined by the multiparameter algorithm with those by fractography. In this case, the observed and predicted results are shown in terms of the "perfect agreement" 1:1 line and estimated 95% bounds that account for the variation in the uncertainty with depth.

Two sets of RMSE values are given. One set is based on the values obtained directly from the multiparameter algorithm, and the other on "corrected" values obtained from the regression fit shown in Fig. 2.10. For the shallowest cracks, the "corrected" values give a significantly lower RMSE value, but when all the data are considered, the differences in the RMSE for corrected and uncorrected predictions are small. This finding indicates little systematic bias in the predictions of the multiparameter algorithm, i.e., the errors are random.

These sizing-accuracy results can be used to estimate the uncertainty in POD curves if the multiparameter algorithm is used to determine the "true" state of the mock-up for the NDE round-robin. Instead of characterizing the error in the depths in terms of the overall average for all depths (≈15%), the error was taken as a function of depth. The values of RMSE given in Fig. 2.12 are assumed to apply at the midpoint of the depth range for each bin. The error at other depths is then estimated by linear interpolation of these values.

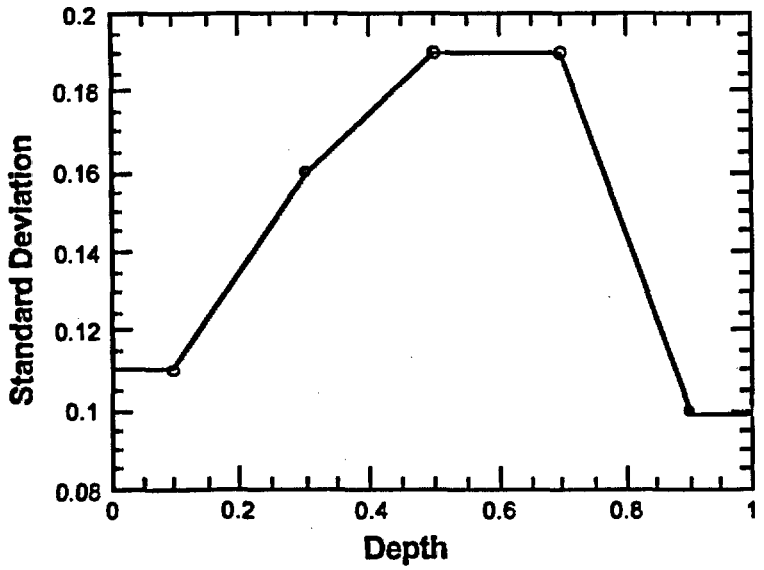

Figure 2.12.
Standard deviation in percent throughwall as a function of maximum depth.

A set of 20 test sections analyzed with the multiparameter algorithm was destructively analyzed by PNNL in an exercise carried out before the 23 test-section set was evaluated. While these 20 test sections, which were prepared using doped-steam techniques, represented a small subset of the mock-up test sections, the NDE results from this set provided guidance for selecting the multiparameter approach. Many NDE techniques were evaluated before selecting the multiparameter algorithm for establishing the reference state of the mock-up flaws. The evaluated techniques include phase analysis of EC +Point data, multivariate regression analysis of EC data, multiparameter analysis of EC data with neural networks, high-frequency ultrasonics (UT) from the OD, Lamb waves, acoustic microscopy, and a combination of UT and EC data (from the ID). The multiparameter algorithm provided the best accuracy for sizing the cracks.

Following the completion of the analysis round robin, several test sections in the mock-up were removed and destructively analyzed to further help validate the multiparameter algorithm for profiling and providing maximum depth. The agreement between the results of the destructive analysis and the multiparameter algorithm was good.

Although the probability of detection is normally expressed in terms of the maximum depth of the crack, it is also useful to express POD in terms of a parameter that better characterizes the structural integrity (i.e., ligament rupture) of the tube. A useful parameter for this purpose is m_p, which is defined as

$$m_p = \frac{p_b}{p_{sc}}, \qquad (1)$$

where p_b is the burst pressure of an unflawed tube, and p_{sc} is the ligament failure pressure of a part-throughwall crack. The parameter m_p can be interpreted as a stress multiplier that relates the stress in the ligament ahead of the crack to the stress in an unflawed tube under the same loading. Because this parameter incorporates the effect of both crack depth and

length, it better characterizes the effect of a flaw on the integrity of a tube than does maximum depth. For short cracks, the ligament may not correspond to tube bursting pressure. The crack may just "pop" through without increasing in length.

In Fig. 2.12, the standard deviation in depth (expressed as % TW) is plotted against the maximum depth. The largest uncertainty is in the 50-70% TW range. While the deviation is small for the shallow cracks, it represents a relatively large error. For example, the standard deviation for 20% TW is 12% TW.

The overall RMSE for all cracks of all depths is 15.1%, but it is somewhat misleading to look at this overall value because there is a significant variation in the RMSE with depth. The RMSE value is significantly better for the 80–100% TW bin than for the other depth bins.

The reference-state table for the mock-up provides all the relevant information for analyzing the round-robin analysts' results. Reference 3 provides the primary information for a flaw in the table. The flaw type, BC volts, BC phase, whether ID or OD, three-letter code for the flaw, maximum depth as determined by multiparameter algorithm, flaw length, average depth, and m_p are all included in the flaw table.

2.1.3 Design and Organization of Round-Robin

As noted previously, an expert Task Group was formed to provide input to help ensure that the RR simulated an ISI inspection. The Task Group included members from utilities, vendors, EPRI, NRC, and ANL. The industry members are G. Henry and J. Benson (EPRI), T. Richards and R. Miranda (FTI), D. Adamonis and R. Maurer (Westinghouse), D. Mayes (Duke), S. Redner (Northern States Power), and B. Vollmer and N. Farenbaugh (Zetec).

The Task Group provided input related to the make-up of the mock-up, the quality of the data collected for the RR, the nature of the flaws, procedures for analyzing data, and documentation. The Task Group provided input on the analysis guidelines, data acquisition, degradation assessment, the training manual, and examination technique specification sheets (ETSSs). The RR began only after the Task Group approved the documentation used for the RR and concluded that the flaws in the mock-up had EC signals similar to those observed under field conditions.

Consistent with current practice, the analysis teams had five members, including a primary, a secondary, and two equally qualified resolution analysts to analyze the EC data. The fifth member, the independent qualified data analyst (QDA), came from a utility. The primary and secondary analysts reported their observations independently. The resolution analysts reviewed calls when the primary and secondary analysts' calls differed. The independent QDA monitored the effort, looking for possible excess overcalls and sampled 40 test sections to ascertain if flaws might have been missed.

The mock-up was treated as a steam generator owned by a utility. The role of the utility in this case was taken by ANL. The ISI followed the process and procedures used by industry. ANL was responsible for preparing documentation, monitoring data collection, monitoring data analysis, and carrying out statistical analysis.

Four documents were prepared for the mock-up testing and for the RR data analysis. They are ANL001 Rev. 2 "Argonne Analysis Guideline," ANL002 Rev. 3 "Multifrequency EC Examination of Tubing within the ANL SG Mock-up," ANL003 Rev. 3 "SG Mock-up Tubing Degradation Assessment and Technique Qualification," and ANL004 Rev. 3 "Training Manual." These documents are discussed in some detail in Ref. 3.

The "SG Mock-up Tubing Degradation Assessment and Technique Qualification" (ANL003 Rev. 3) was prepared per the requirements specified in NEI-97-06 [5] and Revision 5 of the EPRI PWR Steam Generator Examination Guidelines. In accordance with Rev. 5 of the EPRI PWR Steam Generator Examination Guidelines [6], EPRI-qualified techniques were reviewed to ensure that application of these techniques was pertinent to site-specific conditions of the mock-up.

The document "Multifrequency EC Examination of Tubing within the ANL SG Mock-up" (ANL002 Rev. 3) provides all information necessary to collect the RR data. The procedures mimic those of an actual ISI. The basis of the data acquisition is the ETSS. The document defines the frequencies, axial and rotational speeds, and calibration procedures. The two ETSSs developed for the ANL mock-up were based on reviews of EPRI ETSSs for the various degradation mechanisms in the mock-up and combining them into the two used.

The "ANL Analysis Guideline" (ANL001 Rev. 3) provided the technical direction for the performance of EC examinations of the ANL SG mock-up. This procedure was applicable to all examination personnel and generally mimics industry ISI guidelines.

A "Training Manual" (ANL004 Rev. 3) was developed for review by all analysts before the RR exercise was begun. The manual provided information on the mock-up design, including a schematic diagram, information on type of artifacts present, a discussion regarding the presence of the circumferential markers, discussion of how the data for the RR were acquired, and a table showing the format for entering data.

Before development of the mock-up ETSS, the essential variables for all EPRI-qualified techniques were reviewed. This ensured that the applications of the EPRI techniques are pertinent to the site-specific mock-up steam generator conditions.

During June and August of 1999, a qualified three-man team from Zetec collected data from the mock-up. The data acquisition team included a QDA Level IIa and a QDA Level IIIa. Data were acquired with a 10-D pusher-puller, MIZ30 with 36-pin cables, and Eddynet software. BC data from a mag-biased probe were collected from all 3600 test sections of the mock-up. The BC data were calibrated before and after the 4-h interval required to collect the data. No change in voltage from the standard was detectable during this time period. A mag-biased rotating three-coil probe that includes a +Point, 2.9-mm (0.115-in.)-diameter pancake, and high-frequency shielded coil was used to collect data from all 400 tube sheet test sections and all special-interest (spin call) test sections. A comparison of magnetically biased and unbiased coils showed that biasing eliminates the voltage shift and noise in the +Point EC signal resulting from tube sensitization.

The BC data were taken at 0.53 m/s (21 in./s), maintaining a digitization rate of 37 samples per inch. Bobbin coil data were taken at 400, 200, 100, and 20 kHz (differential and absolute). MRPC data were taken from all degraded test sections in addition to hundreds

of clean test sections and test sections with artifacts. An ASME standard and a standard with 18 ID and OD axial and circumferential EDM notches (20, 40, 60, 80, and 100% TW) were used for calibration. MRPC data were taken at 900 rpm and an axial speed of 12.7 mm/s (0.5 in./s) to maintain a digitization rate of 12 samples/cm (30 samples per in.) in the circumferential direction and 12 samples/cm (30 samples per in.) in the axial direction. Data were taken at 600, 400, 300, 200, and 100 kHz. Nine +Point probes were used during this exercise because of probe wear. MRPC probes were replaced when one of the channels could not be nulled. This condition appears on the computer screen as an alert "flag."

The mock-up data collected by Zetec were analyzed at ANL (by ANL personnel) with Eddynet98 software. The locations of the flaw signals were checked against the location data of the flaw map.

Companies participating in the RR provided a list of analysts who would be available to participate. For those companies who supplied more names than would be needed, ANL randomly selected the team members from the list provided. The team members were expected to be available during the entire exercise, generally seven to eight working days. Analysts were generally QDA Level IIa or III. The resolution analysts and independent QDAs were Level III or IIIa. During the RR exercise, the primary and secondary analysts did not communicate with each other or the resolution analysts. Upon submitting their reports, the primary and secondary analysts could discuss their reports with the resolution analysts, but their reports were not changed as a result. The resolution analysts provided the final report used for establishing POD.

Before the RR exercise was started, a training manual, supplemental schematics, and final reports for the training data were sent to the teams for review. The training optical disk was either sent for review before the exercise was started or was provided by the proctor upon arrival. The ANL proctor arrived at the analysts' site with exams, documentation (analysts' guidelines, etc.), and optical disks containing all the data to be analyzed. The proctor provided nondisclosure agreements signed by all analysts participating in the RR and collected all analyst certifications. After the analysts finished studying the training manual, analyst guidelines, the training disk, and supplemental schematics, the ANL proctor gave and graded the written and practical site-specific exams. The passing grade for the written exam was 80%. For the BC practical exam, the analysts had to correctly call all "I" codes without excessive overcalling. For the MRPC data, the analysts had to correctly indicate the presence of all cracks and their orientations (circumferential vs. axial). About 10% of the analysts had to take the second practical exam, which they passed. The ANL proctor retrieved the exam disk after testing was completed. The process of evaluating the analysts closely followed standard industry practice.

After the analysts completed the site-specific exam, the proctor provided a third disk containing all BC data. The primary and secondary analysts analyzed the BC data, and their reports were recorded on the disk. The resolution analysts resolved the primary/secondary discrepancies. A resolution analyst's report was provided along with primary and secondary analyst reports. The Argonne BC disk contained primary, secondary, and resolution analysts' reports for BC data at the conclusion of the BC analysis. The proctor collected hard copies of these reports and the data disk.

The ANL proctor then provided a fourth disk containing MRPC special-interest data. The primary and secondary analysts analyzed the MRPC data, and their reports were recorded on the disk except for tube sheet data, which were analyzed later. Analysts reported the depth at maximum amplitude and location information, following the instructions in the training manual. The resolution analysts resolved the primary/secondary discrepancies and provided a report. Upon completion of the special-interest data, the special interest disk contained primary, secondary, and resolution analysts' reports for MRPC data at other than the tube sheet level. The proctor collected hard copies of these reports and the data disk.

The ANL proctor then provided a fifth disk containing only tube sheet (Level A) MRPC data from all 400 tubes. The primary and secondary analysts analyzed the data for the tube sheet level and provided their report. The resolution analysts resolved any discrepancies and provided their report. The completed tube sheet disk contains primary, secondary, and resolution analysts' reports for the tube sheet. The report was printed, and the hard copy given to the ANL proctor, who also collected the data disk.

After testing, the proctor returned to ANL with all the optical disks containing the analysis reports for the team.

2.1.4 Comparison of Round-Robin Data Acquisition and Analysis to Field ISI

The RR exercise was intended to closely mimic a field ISI. The procedures, equipment used, and documentation are based on industry practices for the inspection of steam generators. Similar to field inspections, a Zetec MIZ30 instrument, along with a 10-D pusher-puller and Eddynet 98 software, was used to collect the data. A standard mag-biased bobbin coil and an MRPC with 2.9-mm (0.115-in.)-diameter pancake, +Point, and 2.0-mm (0.080-in.)-diameter shielded high-frequency pancake coils were used. Round-robin teams used Eddynet98 software to analyze the data. While flaws and flaw responses have been shown to be representative of field flaws, the mock-up is mechanically different from a steam generator. The mock-up had no U-bends. Test sections are in contact with each other, resulting in strong EC signals similar to a 360° 100% TW circumferential crack at the test section ends. The analysts, through training and practice, easily adjusted to these signals, and there is no indication that the PODs reported are compromised by this mechanical arrangement. Another physical difference is the presence of a circumferential marker at the bottom of each test section. Again, through review of training examples, the analysts quickly became adjusted to the marker signals, and their presence appears to have had no effect on the POD results.

Noise levels in the mock-up are generally lower than those in field data. Although many of the test sections had sludge and magnetite on the OD, many test sections with flaws did not. Noise as severe as that in the U-bends of plants such as Indian Point 2 was not present in the mock-up freespan and TSP levels. A review of BC field data from seven plants provided a general idea of the noise from a BC field inspection. Baseline noise in the BC voltage trace of field data was generally ≈0.7 V (excluding U-bends and tube sheet). The mock-up BC baseline noise level was less, about 0.3 to 0.4 V. This low noise suggests that the results from the mock-up are an upper limit on POD for the TSP and freespan levels for flaws with low-voltage BC signals. While it is possible to have a deep crack with a low BC voltage, the difference in baseline noise levels between the field and the mock-up would affect the POD only somewhat for shallow cracks and is not expected to have a significant effect on the logistic fit. Noise in the mock-up tube sheet level, however, was significant and did play a role in the ability of

analysts to detect and correctly characterize the flaws in and around the roll transition zone (RTZ). The tube sheet noise is present in the mechanically expanded portion and in the roll transition. Variations in the geometry of the RTZ contribute to the difficulty of analyzing data from the tube sheet.

As in field inspections, the analyst involved with the RR decides whether the quality of the data is sufficient to analyze for flaws. In one example from the field (Callaway), the bobbin coil is replaced when the peak-to-peak voltage (V_{pp}) exceeds twice the initial control level (from a reference tube). In the RR, the quality of the bobbin coil data did not vary during the time BC data were collected. At Callaway, for example, the signals from notches in the standard must be clearly discernible from background noise when MRPC data are collected; otherwise, the probe is replaced. A similar protocol was followed for the RR, except that if the MPRC probe could not be nulled, it was replaced. This procedure led to high-quality MRPC data from the mock-up test sections.

EC examination parameters are typical of current ISI practice. The 100, 200, 300, and 400 kHz frequencies used for the BC allow use of the conventional 100-400 kHz mix to suppress the TSP indication. The range of frequencies used for the MPRC data covers the requirements of the EPRI ETSSs for flaws present in the mock-up. The mock-up may have a greater variety of flaws than might be present in any given steam generator. Nevertheless, the analysts were familiar with the EC responses to all types of flaws in the mock-up, as demonstrated by their passing the EPRI personnel qualification exams. The variety of flaws in the mock-up should not impact the POD results.

The reporting requirements are slightly different than for a field ISI. In the analyst reports for the mock-up, an extra column shows whether the flaw indication is OD or ID. In addition, the location of an indication is given by data point, not number of inches from a physical reference. Another variation from conventional reporting is the requirement to report no more than four flaws (two axial and two circumferential) at any given axial location. These variations were necessary to provide an exercise that could be completed in a reasonable time (7-8 days) and provide as much information as possible while not negatively affecting the work of the analysts. These variations from standard practice are carefully described in the training manual and analyst guidelines. The analysts made the adjustment to the mock-up reporting requirements quickly.

A primary objective of the RR is to establish the POD for deep flaws. While some deep flaws may result in relatively low EC signal amplitude, the deep flaws generally have high signal amplitudes. As a result, although the voltage histogram for the mock-up flaws looks reasonable, there are more high-voltage signals than expected from a field inspection. A review of field data, such as from the McGuire Nuclear Plant (a better than average plant), shows that while BC signals from TTS can be many volts in amplitude (>10 V), the signals from the TSP regions are primarily less than 3 V, with most less than 1 V in the 100-400 kHz mix channel. Stronger TSP flaw signals can be found in the mock-up because of the emphasis on deep flaws.

2.1.5 Strategy for Evaluation of Results

POD has been determined for the flaws in the mock-up as a function of flaw type and flaw location (i.e., freespan, TSP, and tube sheet). The PODs have been plotted against maximum depth, m_p, average depth, and, for the case of circumferential cracking, area. Logistic fits have

been calculated and include errors in depth sizing and false call rates. Upper and lower 95% confidence limits are included in the logistic fit curves. An analyst is given credit for detecting a flaw if the call is an "I" code (e.g., NQI, DNI, DTI for BC calls, MAI, SAI, SCI, MCI, and MMI for MRPC calls) and the location is within 25 mm (1 in.) of the ends of the flaw.

The location error allowed for calls made from bobbin coil data is 25 mm (1 in.) from either end of the flaw along the tube axis. This allowed error converts to 30 data points for bobbin coil data. For MRPC data, the error allowed in the axial direction is also 25 mm (1 in.) from the ends of the flaw along the tube axis. This allowed error converts to 3000 data points for the MRPC data.

Analysts' reports were used to determine the false call rate. The rate was determined from a review of randomly selected flaw-free test sections in the mock-up and the number of "I" codes called in those test sections. An "I" code call (NQI, DTI, DNI) signifies a flaw indication in the section even though no flaw was actually present. A total of 522 test sections was analyzed. No known stress corrosion cracks were in any of the test sections. With 11 teams, there were 5742 chances to make a false call. The result was a 6% false call rate for the tube sheet level using MRPC data, 1.7% for the TSP with BC data, and 0.1% for the freespan with BC data. These rates are low enough to avoid any consideration of penalizing the analysts for false calls. The false call rates for the TSP and freespan are lower than in field inspections because of the lower noise levels in the mock-up. The false call rate for the tube sheet is of the same order found in the field. Since higher false call rates would lead to higher POD curves, the results presented in this report could be considered conservative. However, even doubling the false call rate would have no discernible effect on the POD curves presented in this report.

Data from the eleven teams participating in the RR exercise were first handled by using the EPRI "Shell" software. The optical disks used by the analysts contained the analysts' reports and were read by the "Shell" software. The "Shell" program sorts the data. Calls from primary, secondary, and resolution analysts can be compared to the results of expert opinion. Note that the result of the comparison to expert opinion is not the result sought because expert opinion does not always provide the true state of the flaws. The reference state of the flaws was provided by the ANL flaw characterization algorithm, which uses a multiparameter approach to analyze the EC data taken at multiple frequencies. Three reports are analyzed for each team for each of the three parts of the RR: the BC data, the MRPC tube sheet data, and the MRPC special-interest (spin call) data. The "Shell" program sorts the data by degradation and, for LODSCC at the tube support plate, by voltage. One team was not able to complete the special-interest MRPC disk.

The Eddynet software provides a series of files that contain the reports of results from each analyst who participated in the RR. These data are saved under an Eddynet environment and are identified by extensions that refer to primary, secondary, and resolution analysts' reports. These files are then read by a text editor and converted into a format usable for off-line manipulation. The text files were then imported into Excel. Excel macros were written to sort the results and carry out the grading.

2.1.6 Statistical Analysis

The probability of detection as a function of depth was assumed to be expressed as a linear logistic function of x:

$$p(x) = \frac{1}{1+e^{a+bx}}, \tag{2.2}$$

or

$$p(x) = \text{logistic}(a + bx), \tag{2.3}$$

where a and b are parameters that are determined by comparison with the observed results. Other forms for the POD curve can be chosen, but the linear logistic curve has been widely used for this purpose and is widely used in other fields to describe binomial responses (detected or not detected) [7].

The Method of Maximum Likelihood [8] is widely used to estimate statistical parameters such as a and b. For quantities that are normally distributed, it can be shown to be equivalent to the familiar method of least squares [8,9]. It is more generally applicable, however, and can be applied to events such as detection of cracks that are not normally distributed. If p(x) is the probability that a crack of depth x will be detected by an inspection team, the probability that the crack will not be detected is 1–p(x). The probability that n out of N teams of inspectors will detect a crack of depth x is

$$\binom{N}{n} p^n (1-p)^{N-n}, \tag{2.4}$$

where $\binom{N}{n} = \frac{N!}{n!(N-n)!}$ is the combinatorial symbol. Equation (2.4) assumes that the teams are equally capable and are independent of each other.

The probability L that a collection of K cracks of depth $x_1, x_2, \ldots, x_K$ will be detected successfully $n_1, n_2, \ldots, n_K$ times is just the product of the probabilities for the individual cracks:

$$L = \prod_{k=1}^{K} \binom{N_k}{n_k} p_k^{n_k} (1-p_k)^{N_k - n_k}, \tag{2.5}$$

where $p_k = p(a, b, x_k)$ and a and b are the parameters of the logistic fit. The Method of Maximum Likelihood seeks to determine a, b such that the probability of the observed outcome, L, is maximized. It is more convenient to deal with the log of Eq. (2.5):

$$\ln(L) = \sum_{k=1}^{K} \ln\left(\binom{N_k}{n_k}\right) + \sum_{k=1}^{K} [n_k \ln(p_k) + (N_k - n_k)\ln(1-p_k)]. \tag{2.6a}$$

$$D = \sum_{k=1}^{K} [n_k \ln(p_k) + (N_k - n_k)\ln(1-p_k)]. \tag{2.6b}$$

The first summation in Eq. (2.6a) is a constant that is independent of the choice of a and b. Defining D as the second summation in Eq. (2.6a), we can determine the choice of a and b that maximizes D or L by solving

$$\frac{\partial D}{\partial a} = 0$$
$$\frac{\partial D}{\partial b} = 0$$

or

$$\sum_{k=1}^{K} \frac{n_k - N_k p_k}{p_k(1-p_k)} \frac{\partial p_k}{\partial a} = 0$$
$$\sum_{k=1}^{K} \frac{n_k - N_k p_k}{p_k(1-p_k)} \frac{\partial p_k}{\partial b} = 0 \qquad (2.7)$$

Differentiating Eq. (2.7), we find that

$$\frac{\partial p_k}{\partial a} = -p_k(1-p_k)$$
$$\frac{\partial p_k}{\partial b} = -p_k(1-p_k)x_k \qquad (2.8)$$

Using Eqs. (2.5) and (2.6), Eqs. (2.7) and (2.8) reduce to

$$\sum_{k=1}^{K} (n_k - N_k p_k) = 0$$
$$\sum_{k=1}^{K} (n_k - N_k p_k)x_k = 0 \qquad (2.9)$$

Equations (2.8) and (2.9) are a pair of simultaneous nonlinear equations for a and b. For computation, it is generally more convenient to determine a and b by algorithms that directly maximize D rather than to attempt to solve these equations. Excel spreadsheets were developed for this purpose and benchmarked against the commercial statistical software package STATA.

Equations (2.9) can be solved for a and b. These values depend on the round robin results, i.e, on n_1, n_2, etc. If the round robin was repeated with a different set of teams or a different set of cracks, different values would be obtained for a and b, i.e., there will be a distribution of values for a and b. Similarly, the depths of the cracks, x_k, are not known exactly; instead we have a measured value $\hat{x}_k = x_k + \varepsilon_k$, where ε_k is the error in the measured value of x_k. The errors will be random variables. The distributions for a and b can be characterized by mean values and variances. The mean values can be found by solving Eq. (2.9), although it is generally easier to obtain a and b by direct maximization of D [Eq (2.6b)]. However, Eq. (2.9) involve the unknown quantities x_k, where, in reality, only the measured values, $\hat{x}_k$, are known. The impact of the uncertainties in x_k can be estimated. The details are given in Ref. 3.

In comparing POD results, one must be sure that differences are statistically significant. There are several ways to test whether two POD curves are the same. The test described below

is the easiest to carry out, because it requires only the logistic regression results. A logistic regression is run on two sets of data. Each regression fit has as a result a set of parameter estimates u = (a,b) and an associated covariance matrix C. The two data sets are designated by Greek letters α and β, and the two regression fits are described by

$$p_{\alpha,i} = \text{logistic}(a_{\alpha,1} + b_{\alpha,2}\, x_{\alpha,i}) \tag{2.10}$$

$$p_{\beta,i} = \text{logistic}(a_{\beta,1} + b_{\beta,2}\, x_{\beta,i}). \tag{2.11}$$

The regression fits produce the estimates u_a and u_b, along with covariance matrices C_a and C_b. To test whether $u_a = u_b$, one forms a chi-squared statistic:

$$\chi^2 = (u_\alpha - u_\beta)^T [C_\alpha + C_\beta]^{-1} (u_\alpha - u_\beta), \tag{2.12}$$

and compares χ^2 to a critical value obtained from a chi-squared table. The degree of freedom associated with the critical value equals the number of model parameters, in this case, two. The two sets of parameters are equal when χ^2 is less than the critical value. For example, to conduct the test at a 10% level of significance, the critical value would be 4.61.

A chi-squared table can also be used to assign a p-value to the statistic χ^2. When performing this test, a less stringent level of significance than typical can be used, such as 10% or 20% instead of the typical 5%. This approach has been used to determine if POD curves by different teams using the same data are different by chance or if the difference is significant.

2.1.7 Results of the Analysis Round-Robin

2.1.7.1 Bobbin Coil Results

Figure 2.13 shows the maximum likelihood logistic fit for the POD with LODSCC and LIDSCC at the TSP as a function of maximum depth (as determined from the multiparameter algorithm). The NDE uncertainty in depth is included in the one-sided 95% lower confidence limit (OSL). In general, the curves are consistent with the behavior typically expected for POD curves. The POD for ID cracks is higher than for OD cracks (99% with 98% OSL at 60% TW vs. 75% with 65% OSL at 60% TW). Figure 2.14 shows raw data and the logistic fit curve for the BC POD for one of the RR teams. As can be seen, the probability of a hit is very high for the deepest flaws, which are dominant in this set of cracks.

Figure 2.15 compares the POD results (with OSL) for the TSP cracks with the results for freespan cracks. While as expected the POD for freespan LODSCC (95% at 60% TW) is higher than the POD for TSP LODSCC (75% at 60% TW), it is lower than the POD for TSP LIDSCC (99% at 60% TW).

In addition to examining the RR data as a function of flaw depth, the POD has also been evaluated as a function of BC voltage for TSP SCC. The results are shown in Fig. 2.16. A pattern similar to that found for POD versus depth is observed for the POD vs. TSP bobbin coil voltage. In this figure, the percentage of correctly calling a flaw is plotted against binned data as indicated in the graph. Figure 2.17 shows the logistic fits to the POD vs. voltage data for LODSCC and LIDSCC, along with the 95% one-sided confidence limits. In contrast to the case

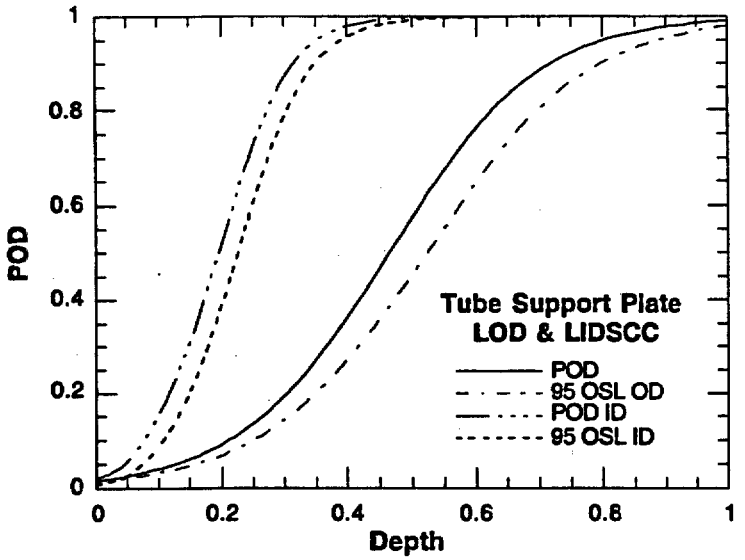

Figure 2.13.
BC POD for TSP data as a function of maximum depth (as fraction throughwall) for LODSCC and LIDSCC using maximum likelihood fit with one-sided 95% confidence limit (OSL). Maximum depth uncertainty is included in the OSL. Depths are determined with the multiparameter algorithm.

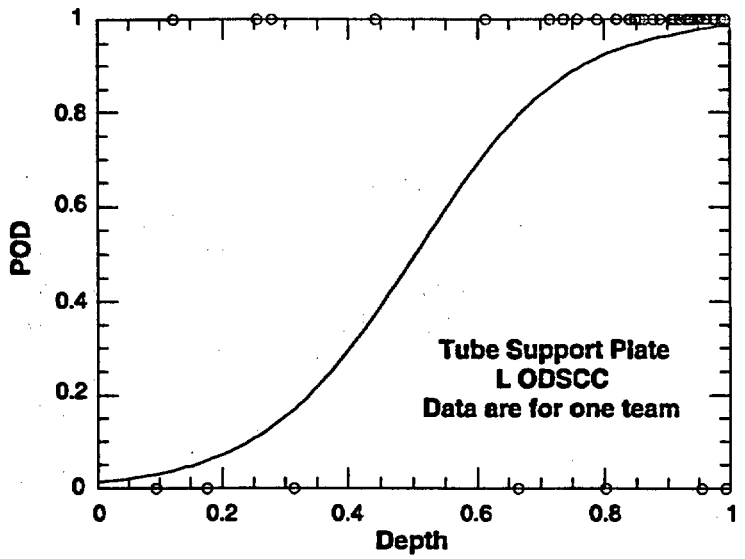

Figure 2.14.
BC POD for TSP data as a function of maximum depth (as fraction throughwall) for LODSCC using maximum likelihood fit (solid line). The logistic fit is to data from one team only. The circles show the raw data from which the curve is generated. Depths are determined with the multiparameter algorithm.

of POD as a function of depth, the POD as a function of voltage for LIDSCC at the TSP is lower than that for LODSCC. The lower POD vs. voltage curve for LIDSCC is possibly the result of missing shallow cracks that are in dents with high voltages.

Because BC voltages are directly used to characterize tube integrity for plants operating under Generic Letter 95-05 [10], the BC voltages reported for LODSCC at tube support plates have been analyzed to determine the team-to-team variability in the reported voltages. For each LODSCC, an average BC voltage and a corresponding standard deviation were computed. The cumulative distribution of the normalized standard deviations (i.e., the standard deviation divided by the corresponding value of the average voltage) can be fit well by a Weibull distribution (the RMS difference between the observed distribution and the Weibull fit is <0.03). The fitted distribution is shown in Fig. 2.18. For almost 90% of the indications, the normalized

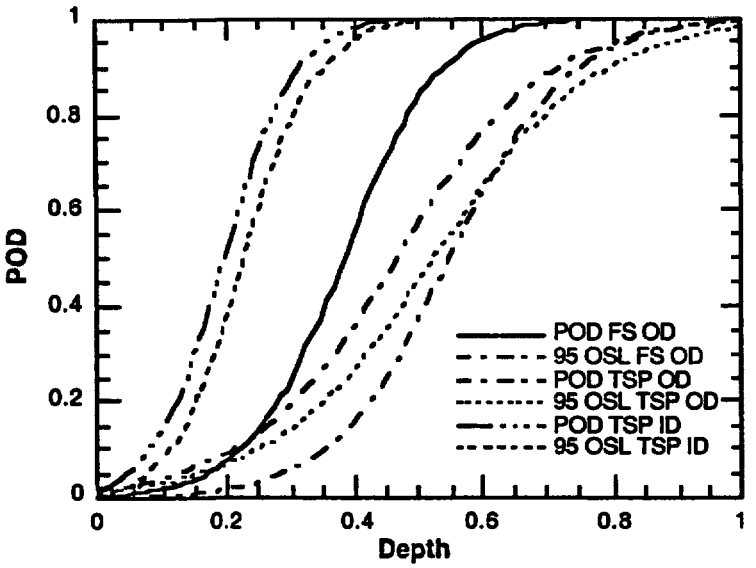

Figure 2.15.
BC POD for freespan and TSP data as a function of maximum depth (as fraction throughwall) for LODSCC and LIDSCC by using maximum likelihood fit with the one-sided 95% confidence limit. Maximum depth uncertainty is included. Depths are determined with the multiparameter algorithm.

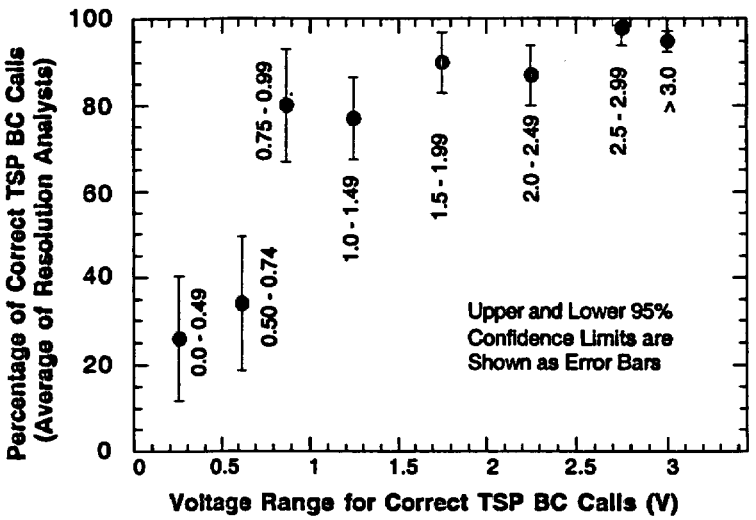

Figure 2.16.
Round-robin TSP bobbin coil resolution analysts' results as a function of BC voltage. The BC POD was evaluated for LODSCC at the TSP. Depths are determined with the multiparameter algorithm.

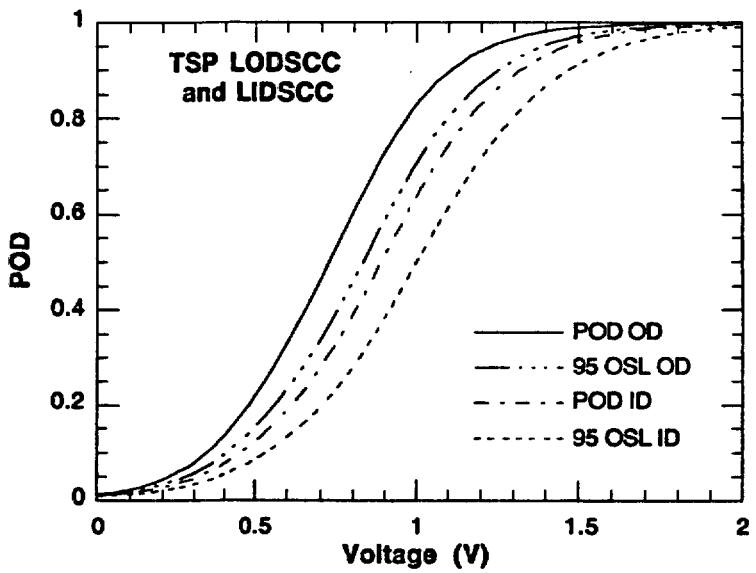

Figure 2.17.
Logistic fit curves for TSP BC POD as a function of voltage for LODSCC and LIDSCC.

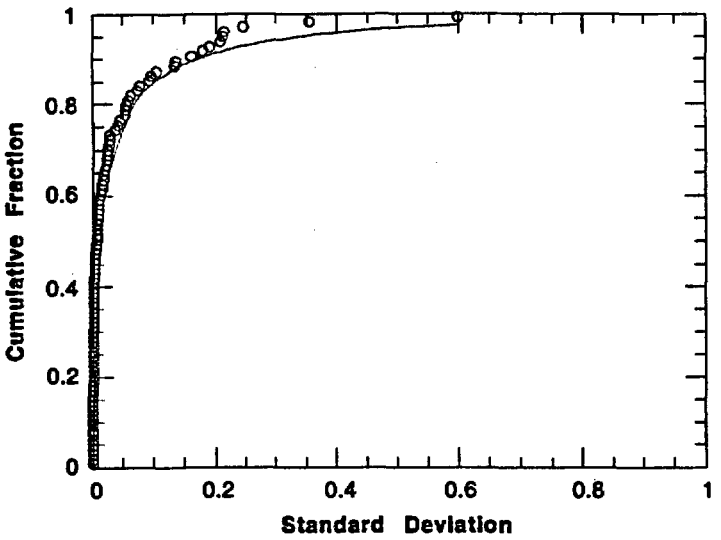

Figure 2.18.
Cumulative distribution of normalized standard deviations for BC voltages for LODSCC at tube support plates.

standard deviation in the reported voltages is <0.15. This result is consistent with Generic letter 95-05 [10], which assumes a 15% cutoff for the voltage-response variability distribution is acceptable. The indications with larger variations are not associated with particularly high or low voltages (i.e., approximately half the signals with standard deviations >0.1 have voltages of >2 V), but rather with the complexity of the signal and the difficulty in identifying the peak voltage.

The results were analyzed by the teams to determine whether there were strong team–to–team variations in the POD. For this exercise, all teams were given optical disks containing the same data sets to analyze. All analysts were given the same instructions and documents related to analyzing the data. Team-to-team variations thus result from variations in analyst interpretation of the same signals. The results as a function of team for freespan and TSP LODSCC combined are shown in Fig. 2.19. The performance of most of the teams cluster rather tightly, although significant variation exists between best and worst. Figure 2.20 shows team-by-team variation for the freespan LODSCC alone. Figure 2.21 shows team-by-team variation for the TSP LIDSCC alone.

From these findings, the probability that team-to-team variations in logistic fits to data are due to chance can be estimated. For LIDSCC at the TSP, the variation from best to worst (Fig. 2.21) is very significant. The probability is <0.1% that the difference is due to chance (DTC). For FS OD, the variation from best to worst (Fig. 2.20) is probably significant (DTC is <20%). For TSP OD, the variation from best to worst DTC is >60% and is thus probably not significant.

Figure 2.22 shows the POD logistic fits for LODSCC at the TSP as a function of m_p. Figure 2.23 shows the corresponding results for LIDSCC at the TSP. Figure 2.24 shows the logistic fits for POD for axial SCC in freespan test sections as a function of m_p. The errors in calculating m_p by using the NDE characterization of the crack geometry compared to using fractography data have been determined with the 23-tube set. Because only one value of m_p

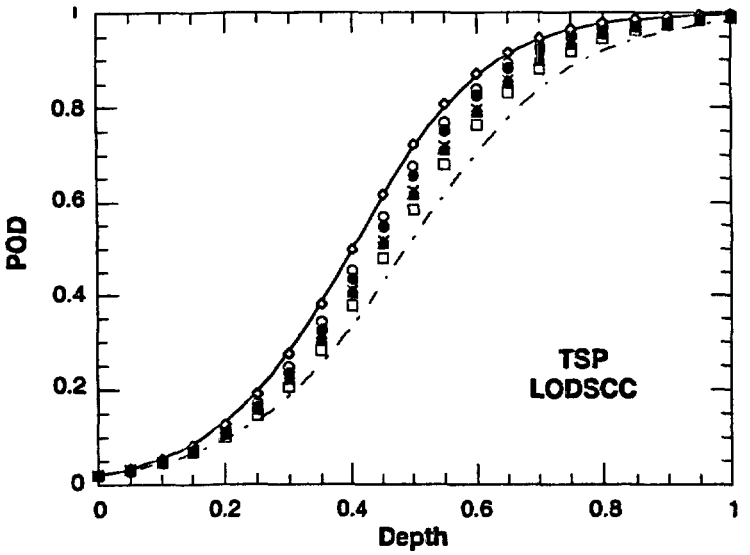

Figure 2.19.
BC POD by team for TSP LODSCC. The maximum crack depth (as fraction of wall) was determined by the multiparameter algorithm. The highest solid line represents the best team, the lowest dashed line represents the worst team, and the other symbols represent the remaining teams.

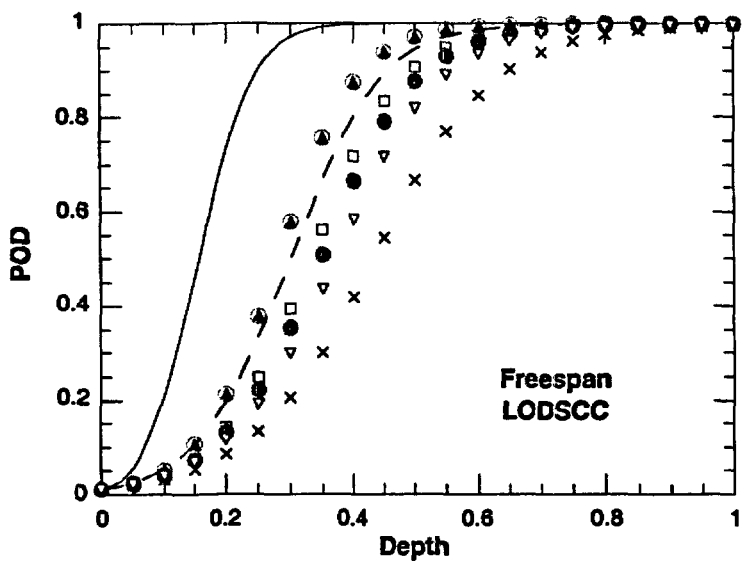

Figure 2.20.
BC POD by team for freespan LODSCC. The maximum crack depth (as fraction of wall) was determined by the multiparameter algorithm. The solid line represents the best team, while the symbols and dashed line represent the remaining teams.

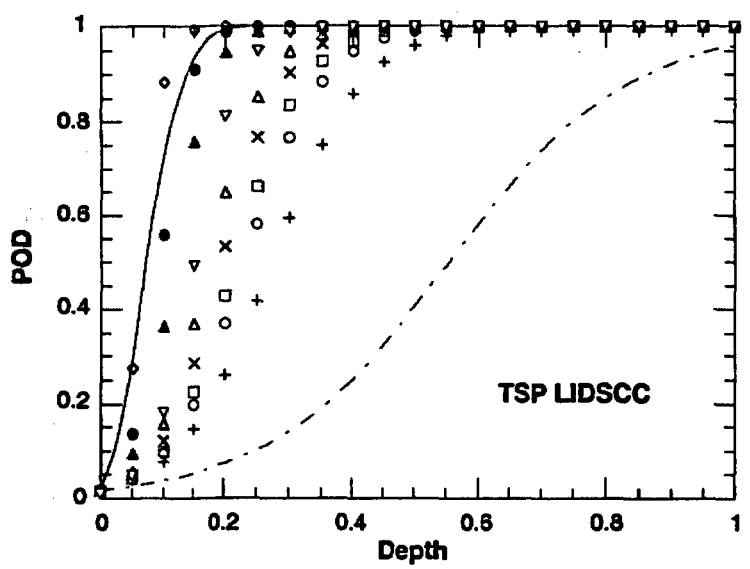

Figure 2.21.
BC POD by team for TSP LIDSCC. The maximum crack depth (as fraction of wall) was determined by the multiparameter algorithm. The solid line represents the best team, the dashed line represents the worst team, and the symbols represent the remaining teams.

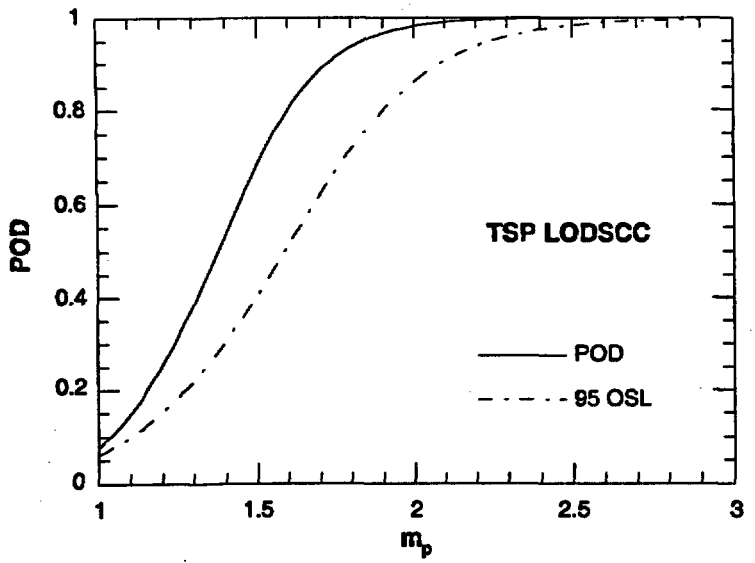

Figure 2.22.
BC POD for TSP LODSCC as a function of m_p by using maximum likelihood fit with an estimate of the one-sided 95% confidence limit. The values of m_p are derived by using depths from the multiparameter algorithm.

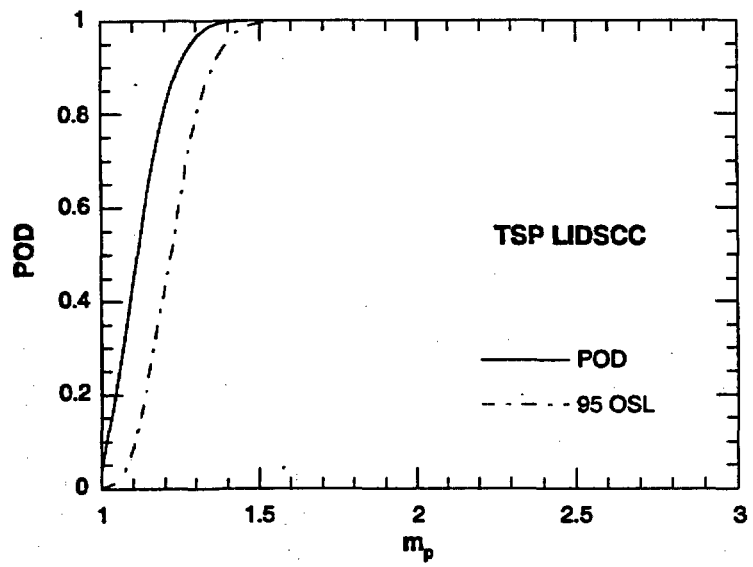

Figure 2.23.
BC POD for TSP LIDSCC as a function of m_p by using maximum likelihood fit with an estimate of the one-sided 95% confidence limit. The values of m_p are derived by using depths from the multiparameter algorithm.

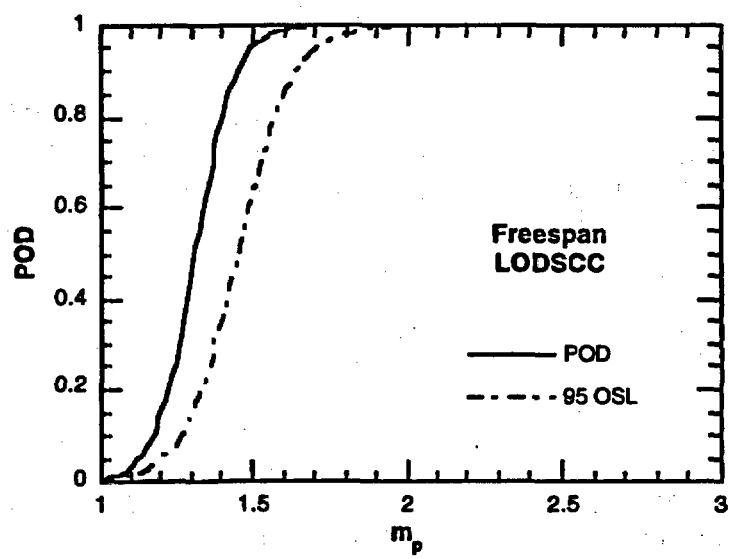

Figure 2.24.
BC POD for freespan data for LODSCC as a function of m_p by using maximum likelihood fit with an estimate of the one-sided 95% confidence limit. The values of m_p are derived by using depths from the multiparameter algorithm.

per crack is obtained, fewer data are available than in the case of depth (multiple points per crack); hence, estimates of m_p have greater uncertainty. In all three graphs, the 95% one-sided lower confidence limit includes the error due to the use of NDE data to calculate m_p, as well as the statistical uncertainties associated with finite samples. In the TSP and FS regions, the POD for cracks that would fail or leak under 3Δp internal pressure (corresponding to $m_p \approx 2.3$) is >95%, even when accounting for depth uncertainties.

The analysis presented in this section is based on the results of the resolution analysts' reports. In some cases, the bobbin coil signal was difficult to analyze, and significant disagreement occurred between the calls of the resolution analysts and the primary and secondary analysts. Three examples for the TSP are presented here. The first is for a 23% TW LIDSCC, the second is for a 67% TW LODSCC, and the third is for a very short 99% TW LODSCC. Table 2.3 shows that, while for some teams all analysts were in agreement with respect to making I-code calls with the bobbin coil data (13 out of 33), for other teams there was disagreement. In some cases (also 13 out of 33), the resolution analyst incorrectly dismissed a correct call by the primary and/or secondary analyst. In four cases, the resolution analysts made a correct call, while the primary and/or secondary analysts did not. These examples show that significant team-to-team variations exist for difficult-to-analyze signals, and that it might be more prudent to limit the impact that resolution analysts have in making the final call for these types of SCC.

2.1.7.2 MRPC Tube Sheet Results

Figure 2.25 shows the POD for SCC in the tube sheet region as a function of maximum depth for LIDSCC and CIDSCC combined and LODSCC and CODSCC combined. (Note that the false call rate for the tube sheet is fairly high, ≈6%). The POD for IDSCC is higher than for ODSCC, as expected. At 60% TW, the POD for IDSCC is ≈90% with an OSL of ≈75%. Figure 2.26 shows the POD as a function of maximum depth for axial and circumferential SCCs in the tube separated into a POD curve for LIDSCC only and for LIDSCC combined with CIDSCC. The highest POD curve is for LIDSCC, where the POD at 60% TW is 95%. Figure 2.27 shows MRPC POD by team as a function of maximum depth (as estimated by the multiparameter algorithm) for axial and circumferential IDSCC and ODSCC in the tube sheet. The POD at 60% TW ranges from 90% to 70%. Based on the discussion in Section 2.5.1, the probability that team-to-team variations in logistic fits to data are due to chance can be estimated.

Figures 2.28-2.30 compare the tube sheet BC POD and tube sheet MRPC POD. Figure 2.28 shows, for all SCC, a higher POD curve for the MRPC (80% vs. 40% at 60% TW). Figure 2.29 compares BC and MRPC PODs for tube sheet LIDSCC and CIDSCC, with the MRPC curve substantially higher. Figure 2.30 compares BC and MRPC POD for tube sheet LIDSCC only. The MRPC POD at 60% TW is 95%, while the BC POD is only 40%.

The MRPC results were reviewed for TSP LODSCC BC voltages between 2.0 and 5.6 V was carried out. Such calls are normally reviewed to confirm or dismiss the BC call. There were 17 TSP LODSCC flaws with BC voltages in the range 2.0 to 5.6 V, and maximum depths were estimated to be >70% TW (by the multiparameter algorithm). The average correct call using the MRPC data for this set of cracks was 98% (with a 96% lower 95% confidence limit). One other LODSCC in the TSP with BC voltage in the 2.0–5.6 V range had an estimated maximum depth of 28% TW. None of the teams correctly called this flaw with the MRPC data.

Table 2.3 Bobbin coil calls of primary, secondary and resolution analysts for SCC at the TSP. Note that the deep (99%TW) LODSCC is very short.

	LIDSCC (23% TW)	LODSCC (67% TW)	LODSCC (99% TW)
Number of teams where the resolution, primary, and secondary analysts all made a correct bobbin coil I-code call.	4	6	3
Number of teams where the resolution analysts made a correct bobbin coil I-code call, but the primary and/or secondary analyst did not.	1	3	0
Number of teams where the resolution analysts did not make a correct bobbin coil I-code call, but the primary and/or secondary analyst did.	5	2	6
Number of teams where the resolution, primary, and secondary analysts all failed to make a correct bobbin coil I-code call.	1	0	2

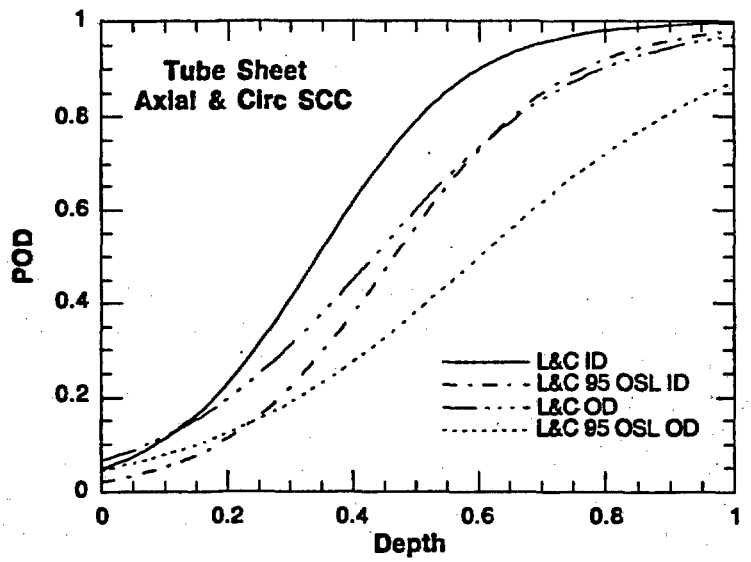

Figure 2.25.
MRPC POD as a function of maximum depth (as fraction of wall) for LIDSCC and CIDSCC combined and LODSCC and CODSCC combined at the tube sheet. Curves include maximum likelihood fit and an estimate of the one-sided 95% confidence limit that includes uncertainty in maximum depth. Depths are determined with the multiparameter algorithm.

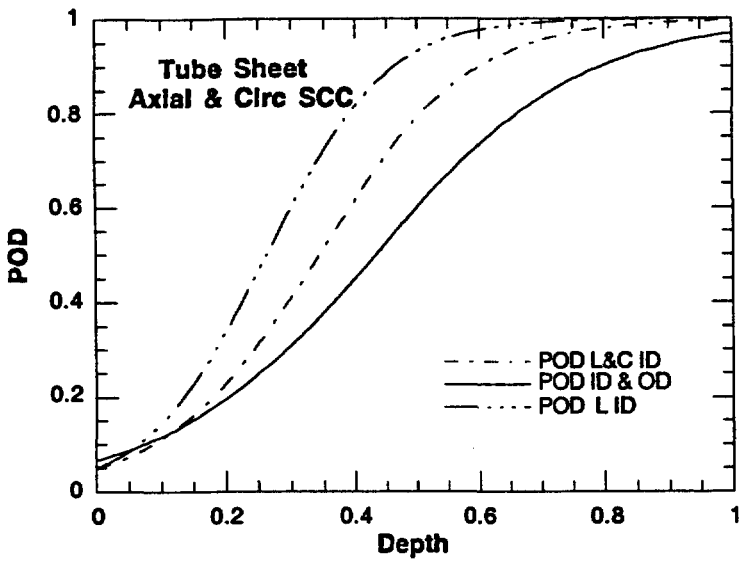

Figure 2.26.
MRPC POD as a function of maximum depth (as fraction of wall) for axial and circumferential IDSCC and ODSCC in the tube sheet. The upper dashed line is for all-LIDSCC only, the lower dashed line is for LIDSCC and CIDSCC. Depths are determined with the multiparameter algorithm. Combined ID and OD should not be used except for comparison of relative effectiveness of probes.

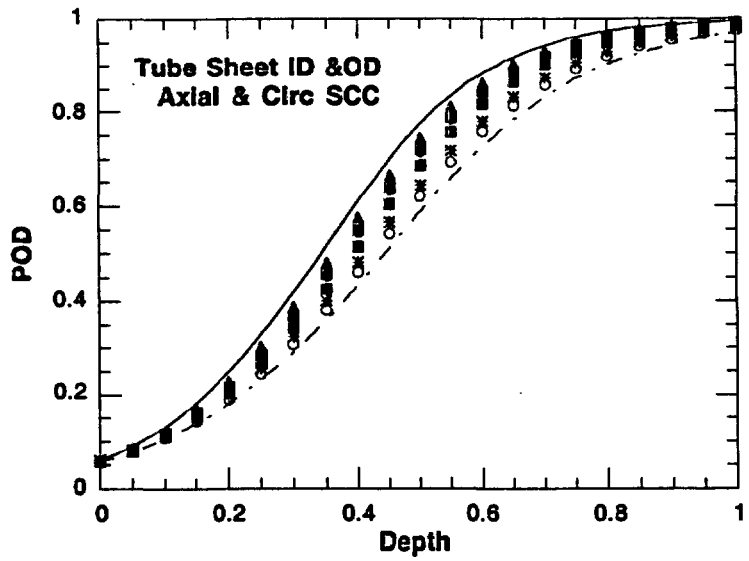

Figure 2.27.
MRPC POD by team as a function of maximum depth (as fraction of wall) in the tube sheet. The solid line represents the best team, the dashed line represents the worst team, and the symbols represent the remaining teams. ID and OD are combined for the purpose of comparing teams.

The possibility of a crack with a high BC voltage being missed by the subsequent MRPC data analysis could arise when a flaw is shallow and long, shallow and volumetric, or deep and short. An example is shown in Fig. 2.31. The crack profile in this case is generated from mock-up data with the multiparameter algorithm. This axial TSP LODSCC with maximum depth of 99% TW was missed by all teams analyzing MRPC data. In this case, the MRPC +Point voltage at 300 kHz was only ≈0.2 V. The largest part of the segmented crack has a length of about 10 mm. Figure 2.31b shows the crack along the test section axis. The m_p for this flaw is ≈4.5, indicating that the tube would leak at pressures well below 3Δp. The BC voltage for this crack can, depending on analyst, vary from 4.5 to 8 V. The dye penetrant image of the crack intersection with the tube OD is consistent with the isometric image generated by the multiparameter algorithm.

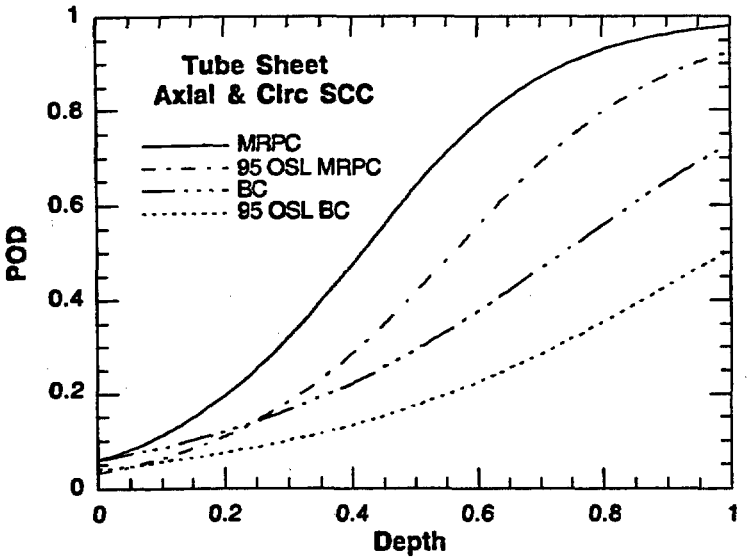

Figure 2.28.
BC and MRPC POD for axial and circumferential IDSCC and ODSCC at the tube sheet. The lower 95% one-sided confidence limits (OSL) are shown (includes uncertainties in depths). Combined ID and OD should not be used except for comparison of relative effectiveness of probes.

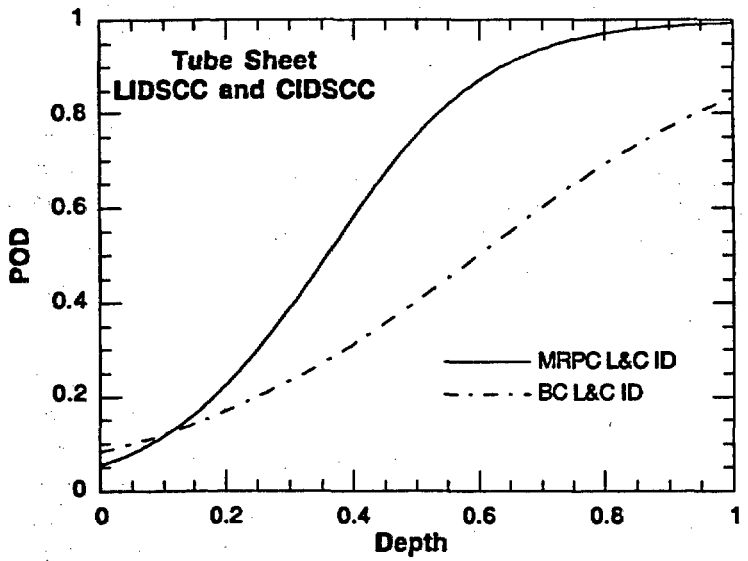

Figure 2.29.
BC and MRPC POD for CIDSCC and LIDSCC at the tube sheet. Depths are determined with the multiparameter algorithm.

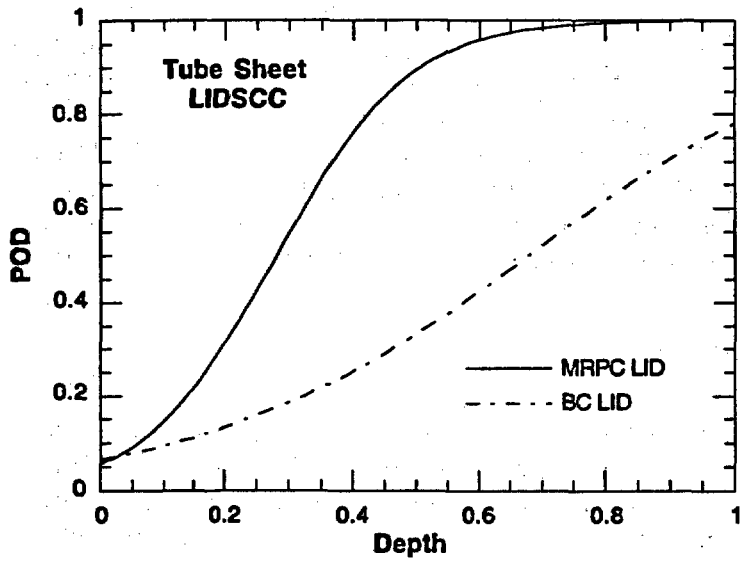

Figure 2.30.
BC and MRPC POD for LIDSCC at the tube sheet. Depths (as fraction of wall) are determined with the multiparameter algorithm.

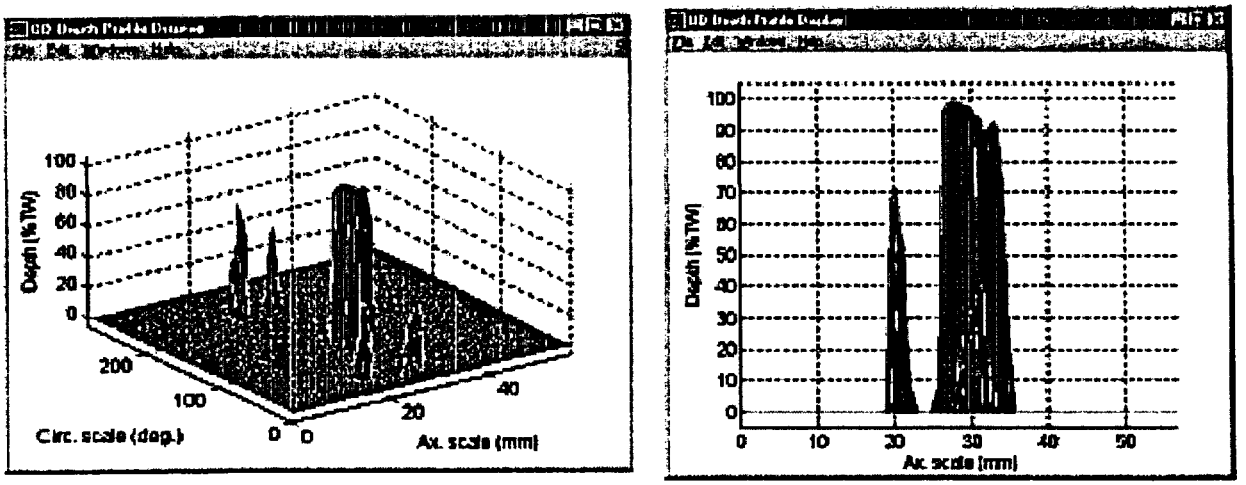

(a) (b)

Figure 2.31. (a) TSP LODSCC with maximum depth of 99% TW that was missed by teams analyzing MRPC data. The largest piece of the segmented crack has a length of about 10 mm (0.4 in.). (b) Projection of the crack along the test section axis.

These results suggest that flaws detected correctly by the bobbin coil could subsequently be dismissed upon further examination of MRPC data even when flaws are relatively deep. The MRPC probes are very effective in characterizing defects, compared to bobbin coils, but may be less effective than bobbin coils in recognizing that a crack is present.

2.1.8 Nature of Missed Flaws

The primary cause of missing a flaw is that the flaw signal is distorted by geometry or deposits and is no longer recognized. A tight crack that does not generate a significant EC signal is another cause for missing a flaw. Another possibility is that the signal from an EC coil does not conform to what is expected (i.e., the signal could be out of the flaw plane or could be generated by multiple cracks). Very long flaws may be missed because the analysts may concentrate on a small portion of the flaw, thereby missing the overall response. Confusion could also arise from conflicting behavior of two or more coils. For example, there could be a clear BC signal but nothing reportable from an MRPC. Analysts have a preconceived idea of what flaw responses at various locations should be like and might not pursue anomalous indications that are actually from a flaw. A few cracks in the mock-up have been called by the bobbin coil and dismissed following an MRPC analysis. Some cracks detectable with an MRPC are not detected by the bobbin coil. The reasons vary, as described above, but in the case of a crack and a BC indication, the crack is not called because the indication has a very high phase angle or is out of the flaw plane.

2.1.9 Nature of Overcalls

Overcalls are the result of signals from certain coils that tend to generate flaw-like signals from geometrical distortions and deposits. Overcalls could also be the result of confusion from conflicting behavior of two or more coils. In a round-robin exercise, participants tend to make calls that might not be made under field conditions because there is no penalty for overcalling

as long as the overcalling is not abused. In fact, the reports from resolution analysts show a reasonably low overcalling rate for the freespan (0.1%) and TSP (1.7%). The overcalling at the tube sheet level is significantly higher (6%). The complex nature of the roll transition is probably the root cause of the tube sheet overcalling, although further review and destructive analysis suggests that unintentional flaws may have been introduced to the tube sheet level during tube expansion, flaw fabrication, and assembly.

2.1.10 Implications of the Round-Robin Results

In summary, the detection capability of current ISI technology and procedures has been assessed by carrying out an eddy current RR exercise with a steam generator tube bundle mock-up. Inspection of the mock-up and analysis of the data mimicked industry ISI practices conducted on operating steam generators. All documentation for conducting the inspection was prepared with input from an industry-based NDE Task Group, and the realism of the mock-up was established. Data were acquired in June and August 1999, and these data were analyzed by 11 commercial teams in December 2000. Each team consisted of five qualified analysts. The exercise took seven to eight working days per team.

The conclusion from the analysis of round-robin results is that good POD can be achieved for deep flaws when commercial techniques are used in a similar manner to the RR exercise. The level of success in detection of SCC did vary with flaw location. The maximum depth from eddy current crack profiles and false call rates was estimated to establish POD as a function of depth and m_p. Logistic fits to the data were generated. The BC POD for TSP ID cracks is higher than for OD cracks (99% with 98% OSL at 60% TW vs. 75% with 65% OSL at 60% TW). The BC POD for freespan LODSCC is ≈95% at 60% TW. The POD for IDSCC is ≈90% with an OSL of ≈75%. The highest POD curve is for LIDSCC, where the POD at 60% TW is 95%. The MRPC results for BC voltage between 2.0 and 5.6 V were reviewed. Such calls are normally reviewed to confirm or dismiss the BC flaw call. The result for LODSCC >74% TW is an average correct call of 98%. All teams missed an LODSCC at the TSP with an estimated maximum depth of 28% TW. Another example illustrates the possibility that a deep crack with a weak MRPC signal might not be called a crack by analysts. The example presented had an estimated maximum depth of 99% TW with only a few tenths of a volt generated by the +Point coil at 300 kHz.

No useful correlation was found between signal amplitude or phase and the maximum depth of the mock-up flaws. When the PODs are considered as a function of m_p, in the TSP and FS regions, the POD for cracks that would fail or leak under $3\Delta p$ internal pressure (corresponding to $m_p \approx 2.3$) is >95% even when uncertainties are accounted for.

These analyses also established the adequacy of the multiparameter algorithm for obtaining profiles and maximum depth. The curves for POD as a function of depth or m_p were based on the profiles generated with the multiparameter algorithm.

2.2 Tube Removal from McGuire 1 Retired Steam Generator

2.2.1 Review of Duke ISI Data

Steam-generator EC data were obtained from the Duke Power Company's McGuire plant on a magneto-optical disk in the form of the raw inspection data. These data were analyzed

using Zetec Eddynet95 software in an effort to optimize the selection of tubes for the tube removal effort from two retired steam generators. Tubes with single and multiple axial and circumferential indications in the TS and the first TSP ,were the main priority, and several tubes were selected as candidates for removal. Areas where defects are somewhat clustered were also identified. These areas are of greatest interest because selecting tubes in a relatively small area minimizes the total cost of procuring tube samples.

2.2.2 Results of Field NDE of Deplugged McGuire Tubes

Twenty tubes from the McGuire 1 steam generator D (SGD) were selected for plug removal. Nineteen of these 20 tubes were successfully deplugged in June 1997. Eighteen of these 19 tubes were subsequently examined by NDE, and the results were used to select tubes for tube pulling.

Deplugged tubes and TS sections removed from the McGuire Station SGD were inspected before removal using +Point, "3-coil" pancake, and bobbin coil probes. This inspection and the subsequent analyses were carried out by staff from ANL, Duke, and the EPRI NDE Center. An ASME standard and a standard with 18 axial and circumferential OD and ID EDM notches were used in the data collection.

To determine any changes in EC voltages between current and previous inspections of deplugged tubes, the analysis team followed the procedure specified in the "Eddy Current Analysis Guidelines—McGuire Nuclear Station Unit 1." Unprocessed (raw) bobbin coil data taken in previous ISIs were used to reproduce, for the tubes selected, the amplitude and phase results reported in the Duke EOC10 (December 1995) and EOC9 (August 1994) summary sheets. The same procedure was applied to the data taken July 1997, using the same reference standards and normalizations employed in the previous ISI. The BC voltages are presented in Table 2.4; in all cases, the voltage increased after deplugging. Factors that could result in voltage increases include crack growth, widening of cracks, or a change in deposits. Note that for the one tube plugged in August 1994 (R7 C24), the voltage increase was the most dramatic.

In Table 2.5, results for a standard 2.92-mm (0.115-in.)-diameter pancake coil are compared. Reproducing the results in the Duke summary sheets from raw EC data of previous ISIs was more difficult for the RPC data than for the bobbin coil because the analysis is somewhat more subjective. After deplugging, the RPC voltages, except for R33 C33 and R5 C17, were about the same or increased with time. Again, for the tubes plugged in 1994 (R7 C24 and R39 C46), the voltage increase was most dramatic.

In addition, several new indications were identified from relatively weak EC signals. These resulted primarily from new signals from probes similar to those used before and from the availability of new +Point data (not taken during previous ISI). A review of some earlier EC data indicated that these new calls would not have been made with the data available during previous inspections because either (1) the EC signals initiated after the December 1995 ISI, or (2) the EC signals were too weak to be called flaw indications with probes used at that time but had since grown sufficiently to be detectable. An example is shown in Figs. 2.32 and 2.33. These figures present standard pancake data in the form of an isometric plot (c-scan) around

Table 2.4. Bobbin coil voltages before plugging and EC voltages after deplugging for selected tubes from hot-leg side of McGuire steam generator D.

Tube Position	Bobbin Coil Volts		Call/ Location[b]	Difference	
	Before Plugging[a]	After Deplugging[a]		Volts	Percent
R4 C43	0.56	1.56	MAI/1st TSP	1.00	179
R5 C17	0.32	0.70	MAI/2nd TSP	0.38	119
R5 C44	8.0	14.00	MCI/TTS	6.00	75
R5 C51	0.45	1.30	MAI/1st TSP	0.85	189
R7 C24	0.56	6.66	MAI/2nd TSP	6.10	1089
R11 C96	10.54	12.50	SCI/TTS[c]	1.96	19
R13 C89	3.88	5.22	SCI/TTS	1.34	35
R14 C55	0.35	0.91	MAI/2nd TSP	0.56	160
R17 C90	4.07	4.90	MAI-MCI/TTS	0.83	20
R19 C20	0.52	0.54	Vol/5th TSP+	0.02	4
R33 C33	6.61	10.00	MCI-MAI/TTS	3.39	51
R39 C57	1.14	1.80	SAI/1st TSP[c]	0.66	58
R45 C40	0.27	0.57	MAI/1st TSP[c]	0.30	111

[a]Tubes plugged 12/95, except R7 C24 plugged 8/94; all tubes deplugged 7/97.

[b]MAI = multiple axial indication, MCI = multiple circumferential indication, SAI = single axial indication, SCI = single circumferential indication, Vol = volumetric indication.

[c]Nearly throughwall indication from ISI before plugging.

Table 2.5. Rotating pancake coil voltages before plugging and EC voltages after deplugging for selected tubes from hot-leg side of McGuire steam generator D.

Tube Position	RPC Volts		Call/ Location[b]	Difference	
	Before Plugging[a]	After Deplugging[a]		Volts	Percent
R4 C43	0.47	1.20	MAI/1st TSP	0.73	155
R5 C17	0.48	0.37	MAI/2nd TSP	-0.11	-23
R5 C44	0.59	0.90	MCI/TTS	0.31	53
R5 C51	0.22	0.93	MAI/1st TSP	0.71	323
R7 C24	0.35	2.75	MAI/2nd TSP	2.40	686
R11 C96	7.64	-	SCI/TTS[c]	-	-
R13 C89	0.34	0.66	SCI/TTS	0.32	94
R14 C55	0.34	0.69	MAI/2nd TSP	0.35	103
R17 C90	0.52	2.40	MAI-MCI/TTS	1.88	362
R19 C20	0.93	1.04	Vol/5th TSP+	0.11	12
R33 C33	2.74	1.02	MCI-MAI/TTS	-1.72	-63
R39 C46	0.7	2.80	MAI-SCI/TTS	2.10	300
R39 C57	0.57	1.17	SAI/1st TSP[c]	0.60	105
R45 C40	0.27	0.39	MAI/1st TSP[c]	0.12	44

[a]Tubes plugged 12/95, except R7C24 plugged 8/94; all tubes deplugged 7/97.

[b]MAI = multiple axial indication, MCI = multiple circumferential indication, SAI = single axial indication, SCI = single circumferential indication, Vol = volumetric indication.

[c]Nearly throughwall indication from ISI before plugging.

the top of the tube sheet (TTS). In 1995, there was no clear evidence of a crack. In 1997, the EC signal pattern had changed, and multiple axial and circumferential crack calls were made. This example suggests growth of EC signals in plugged tubes.

2.2.3 EC Signal Growth

The growth of an EC signal attributed to an SCC can be seen in the c-scan plots of Figs. 2.34 and 2.35, which were generated using a 2.92-mm (0.115-in.)-diameter MRPC. In Fig. 2.36, the arrow points to an EC signal at the TTS in tube R39 C46. This indication was called an SCC in August 1994. Figure 2.35 shows the TTS in July 1997, after the tube was deplugged. The signal has grown considerably relative to the roll transition (Fig. 2.36) for one or more of the reasons suggested above.

Several SCCs from McGuire have been examined at Argonne using a modified glovebox, a 4D Pusher Puller, a MIZ30, and Eddynet 98 software. Table 2.6 compares the BC voltage and phase angle measured at McGuire before pulling and at Argonne after pulling. The Argonne data include results both with and without a ring over the crack to simulate the TSP. Measurements made at Argonne followed the same procedure as that used at McGuire. This procedure entailed use of an ASME standard, setting the 550-130 kHz mix channel for the four 20% TW holes to 2.75 V and the phase angle setting of the 100% TW hole to 40°. In general, the voltages measured at Argonne are slightly lower, with the phase essentially unchanged except for SCC noted as A in the table. The differences noted could be the result of variations in the mix and changes in conduction paths across the crack faces resulting from the tube pulling procedure (i.e., crack faces now touching). All test sections were pressurized at room temperature to a maximum pressure of 51.7 MPa (7500 psi). Tube B failed at 49.0 MPa (7100 psi) and leaked at a rate of 32.2 L/min (8.5 gal/min). Tube E failed at 35.2 MPa (5100 psi). The others did not fail at the maximum system pressure of 51.7 MPa (7500 psi).

2.3 Effect of Surface Oxide Films on Eddy Current Signals from SCC

The effect of corrosion products (thin oxide films) formed on crack faces on the EC signal from an SCC has been investigated. Alloy 600 tubes with axial ODSCC were exposed under PWR water chemistry conditions (300°C and 3-8 ppb oxygen) for about two months. The cracks were examined with both magnetically biased ("mag-biased") BCs and a +Point coil before and after corrosion products were formed. The voltages for the BCs increased significantly with the creation of the thin oxide film. However, the general shape of the Lissajous figures remained unchanged. In contrast, the results for the +Point coil were inconclusive. In two cases, the +Point voltage did not change, while in a third, the voltage dropped significantly after the oxide film formed. Figure 2.37 shows the BC Lissajous figure, along with voltage and phase information for one of the tubes. Table 2.7 summarizes the BC results for two tubes. While voltages increased significantly, the phase angle did not. The creation of corrosion products in the crack could lead to a reduction in the number of electrically conducting paths from contacting crack faces. In that case, the EC signal would be expected to increase, as observed, while the depth remains essentially the same.

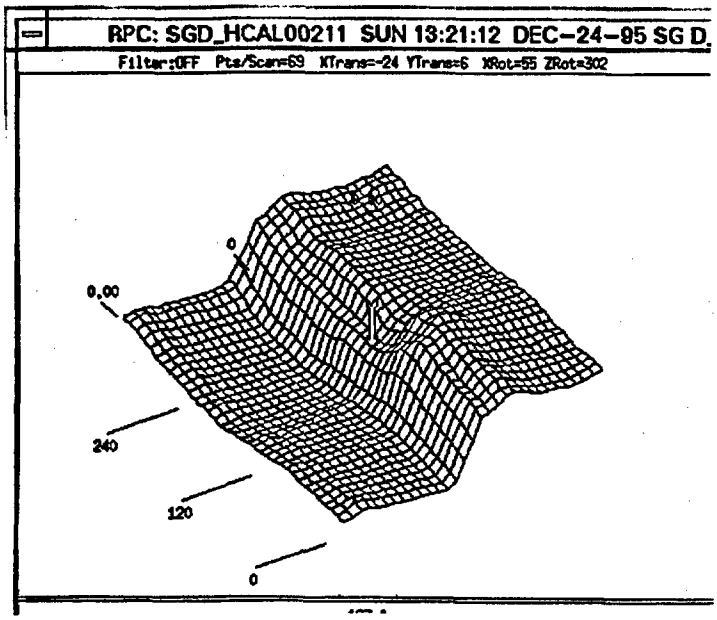

Figure 2.32.
C-scan plot of tube R45C40 using a 2.92-mm (0.115-in.)-diameter MRPC showing top of tube sheet in December 1995. No crack call was made at that time. The tube axis is from lower left to upper right, with full 360° shown. The roll transition in indicated by the arrow.

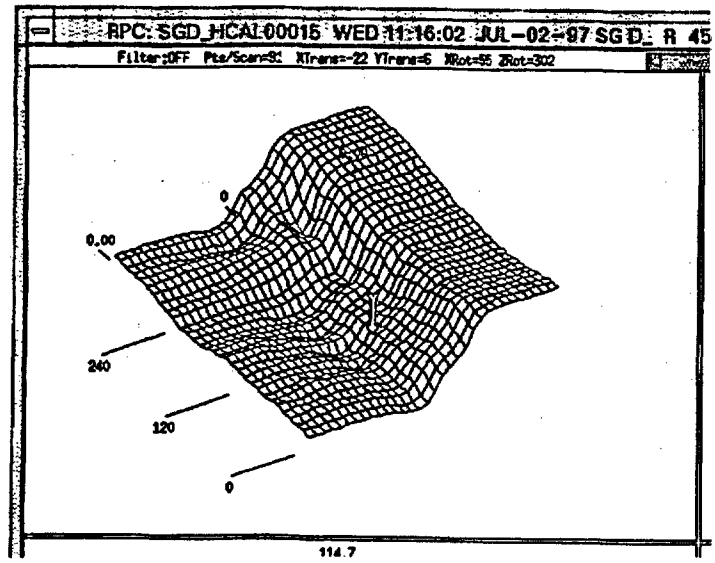

Figure 2.33.
C-scan plot of tube R45C40 using a 2.92-mm (0.115-in.)-diameter MRPC showing top of tube sheet in July 1997. Multiple axial and circumferential cracks were called at that time. The tube axis is from lower left to upper right, with full 360° shown. The roll transition is indicated by the arrow. The variation in EC signal from 1995 (Fig. 2.32) can easily be seen.

2.4 Crack Sizing

Mock-up data for several cracks were used to compare the profiling results from industry experts to the results obtained from application of the Argonne multiparameter algorithm. The objective of the exercise was to obtain information of the variation possible for maximum depth estimates when using the same EC data. Figure 2.38 shows the maximum depths for a variety of crack morphologies estimated by two recognized EC NDE experts using the same procedure with +Point data at 300 kHz and by Argonne using the multiparameter algorithm with input primarily from pancake phase and amplitude data. The deeper the crack, the better the comparison. For one TSP (No. 4), the variation was only about 10%. In another case (No. 3),

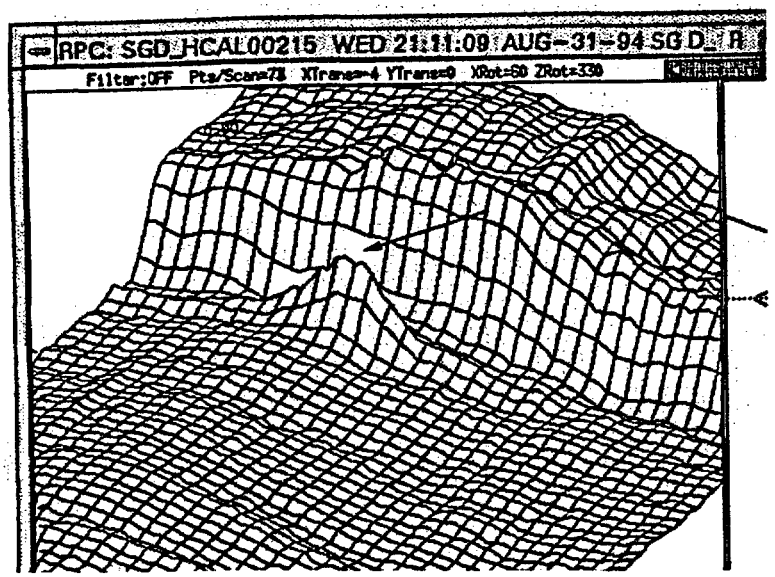

Figure 2.34.
C-scan plot from a 2.92-mm (0.115-in.)-diameter MRPC; arrow points to indication at top of tube sheet (TTS) in tube R39 C46. This indication was called an SCC in August 1994. Tube axis is from lower left to upper right, with 360° of tube shown.

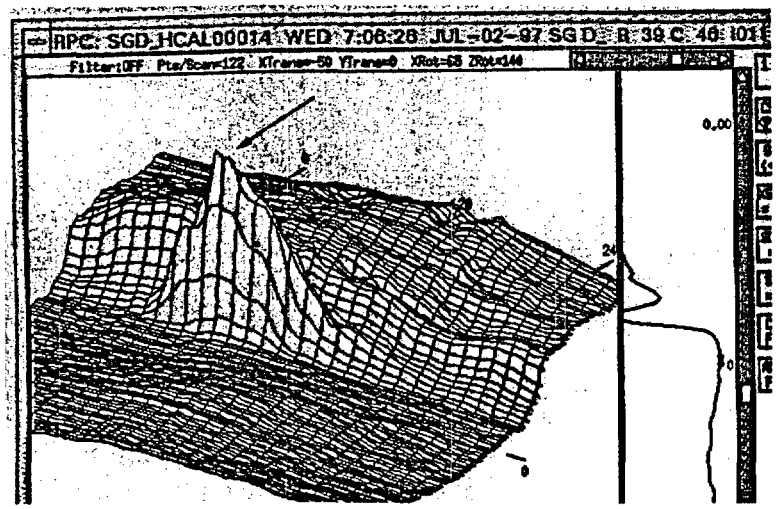

Figure 2.35.
C-scan plot of same region shown in Fig. 2.34 taken with a 2.92-mm (0.115-in.)-diameter MRPC in July 1997 after tube was deplugged. Signal (arrow) has grown considerably relative to roll transition. Tube axis is from lower left to upper right, with 360° of tube shown.

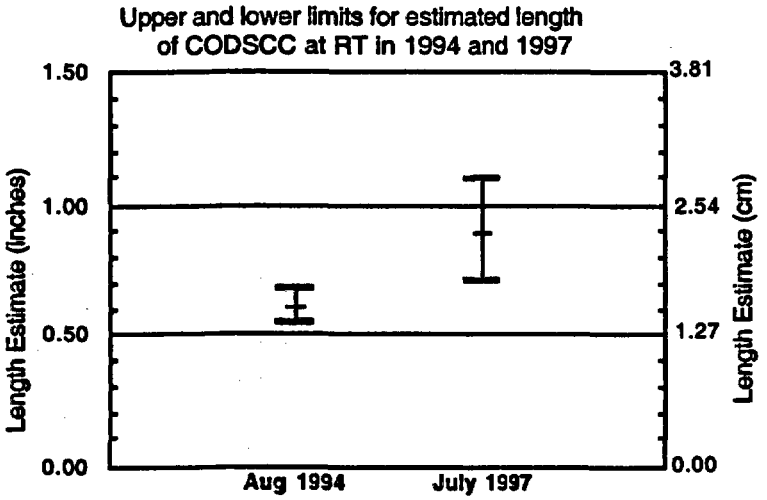

Figure 2.36.
Estimated length with range of uncertainty for CODSCC at top of tube sheet in Tube 39-46 of McGuire retired steam generator before (August 1994) and after (July 1997) plugging.

Table 2.6. Comparison of BC data before and after tube pull

Flaw Type and Location	BC Voltage and Phase Measured at McGuire (550-130 kHz Mix) before Tube was Pulled	BC Voltage and Phase Measured at Argonne (550-130 kHz Mix) with and without TSP Simulation
A. 1st TSP, LODSCC	1.3 V/83°	1.1 V/130° with TSP 1.2 V/123°, no TSP
B. 1st TSP, LODSCC	1.6 V/87°	1.3 V/ 87° with TSP 1.0 V/ 69°, no TSP
C. 2nd TSP, LODSCC	6.7 V/81°	3.9 V/ 79° with TSP 4.3 V/ 82°, no TSP
D. 2nd TSP, LODSCC	0.9 V/120°	0.8 V/133° with TSP 0.9 V/137°, no TSP
E. 1st TSP, LODSCC	1.8 V/46°	1.8 V/ 40° with TSP 1.8 V/ 40°, no TSP

the variation was over 50% (TS CIDSCC). One analyst (B) was not able to make a good estimate for that case. The variation was greatest for the TS SCC.

2.5 Array Probes

The X-Probe is a transmit-receive EC array consisting of pancake coils in a bracelet configuration. The transmit coil establishes the EC, while receive coils read flaw-created disruptions in currents, represented as phase and amplitude variations in the voltage plane. The advantages of the X-Probe are its sensitivity to flaw orientation and characterization of noise signals. The array can travel through tubing at speeds comparable to BCs and much faster than rotating coils, while still providing spatial and orientation information for both axial and circumferential cracks.

A group of NDE experts brought the X-probe to ANL to inspect the NRC steam generator mock-up. The purpose was to test the probe performance with the mock-up and finalize analyst guidelines for an X-Probe evaluation exercise. The data acquired were analyzed without previous knowledge of flaw location. The results are currently being reviewed by ANL personnel. Documentation, including training manuals and schedules, are currently being prepared.

Figures 3.39-3.42 compare X-Probe and +Point 3D signal amplitude plots with a 3D image generated by the Argonne multiparameter algorithm that uses amplitude and phase information to generate depth profiles. The +Point probe is the rotating probe of choice for ISIs involving the steam generator TS as well as special-interest locations. The multiparameter results are derived from phase and amplitude data from a standard rotating pancake coil. Note that the ANL multiparameter plot provides depth vs. position, while the X-Probe and +Point plots show signal amplitude and do not represent depth very well, if at all. These images illustrate the differences in spatial resolution and ability to suppress noise for one of the mock-up cracks in the TS simulation.

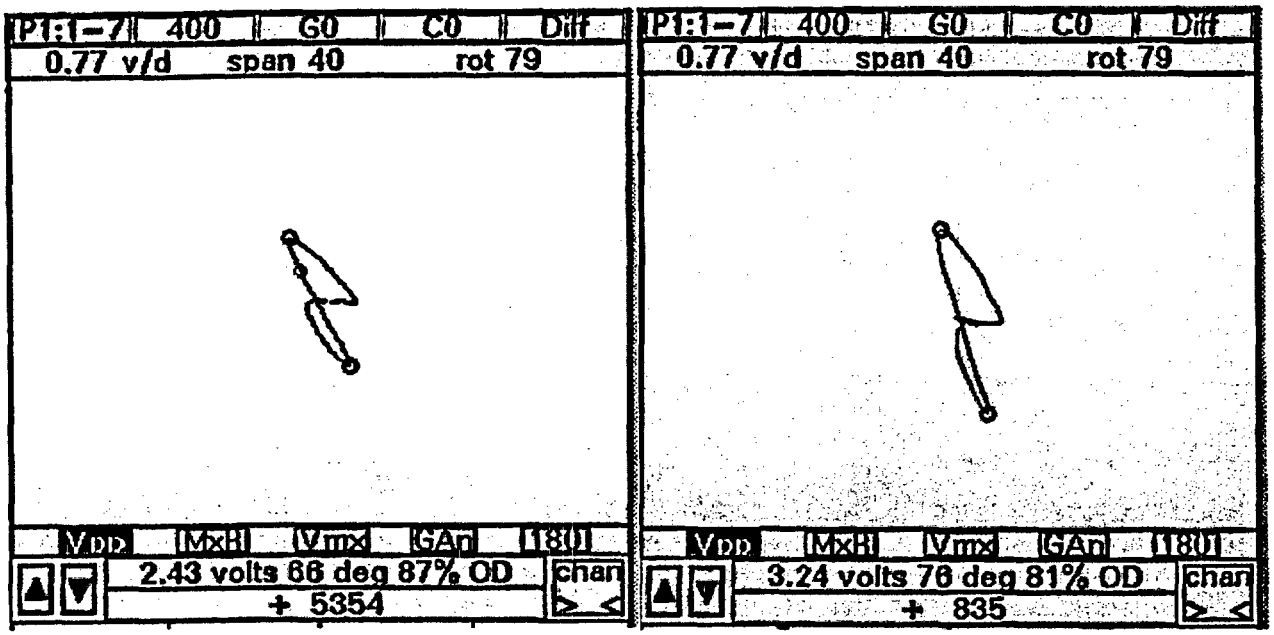

(a) (b)

Figure 2.37. Mag-biased BC Lissajous figures before (top) and after (bottom) corrosion products (thin oxide film) were formed in a tube with axial ODSCC by exposing the tube to PWR conditions for about two months. Voltage increased from 2.43 to 3.24 V, suggesting less contact at crack faces. Estimated depth changed from 87 to 81% TW.

Table 2.7. BC voltages and phase angles for two tubes before and after exposure to PWR water conditions, resulting in formation of corrosion products. Each tube has an axial ODSCC that is ≈15-mm (0.60-in.) long.

Tube No.	BC Voltage (V)	BC Phase Angle	BC % TW
SGL-197 (before)	2.43	66°	87
SGL-197 (after)	3.24	76°	81
SGL-149 (before)	3.27	87°	73
SGL-149 (after)	4.51	89°	72

The mock-up was also examined with an array probe developed by Mitsubishi Heavy Industries (MHI) of Japan. This probe combines the speed of the BC with the detectability of a rotating coil. The 24-channel design includes thin-film pick-up coils. Results of their study were presented at the 20th Annual EPRI Steam Generator NDE Workshop in Orlando, Florida, July 9-11, 2001.[11] For mock-up cracks, the quality of images from the MHI array are comparable to images generated by the X-Probe, though the MHI probe exhibited higher spatial resolution in some cases.

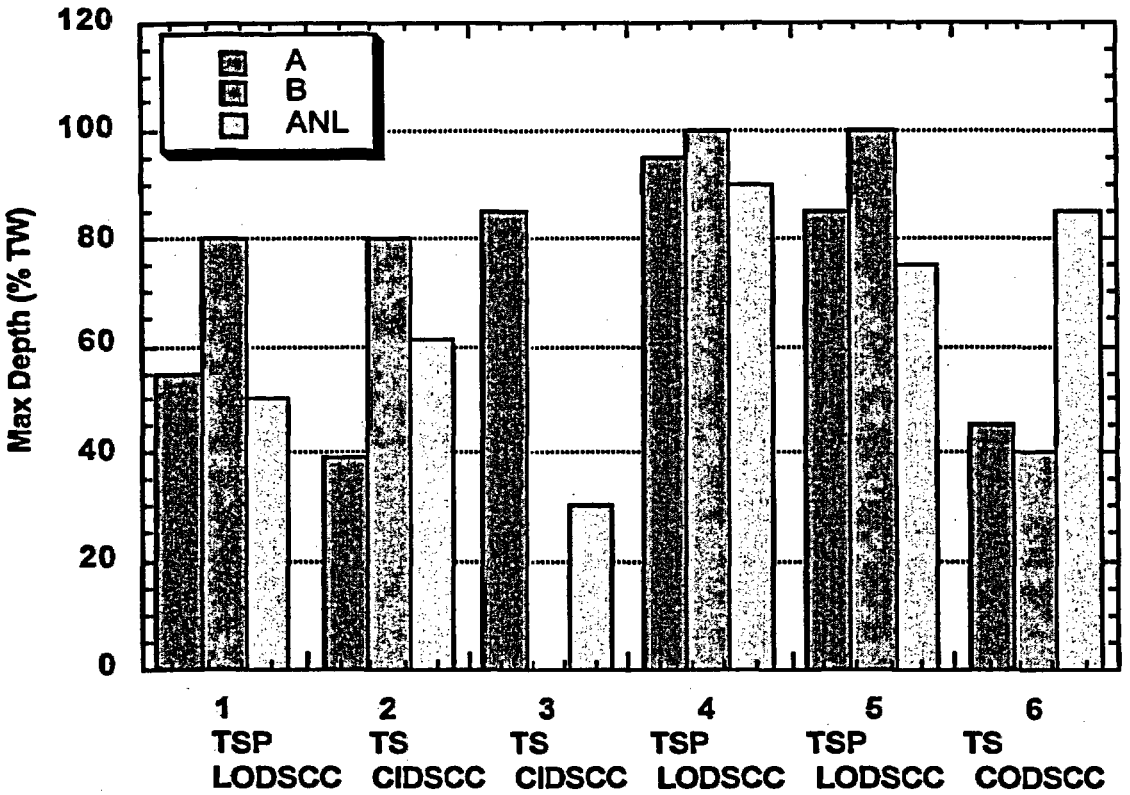

Figure 2.38. Maximum depths for a variety of crack morphologies estimated by two recognized EC NDE experts (A and B) using the same procedure with +Point data at 300 kHz and by Argonne using the multiparameter algorithm with input mainly from pancake phase and amplitude data.

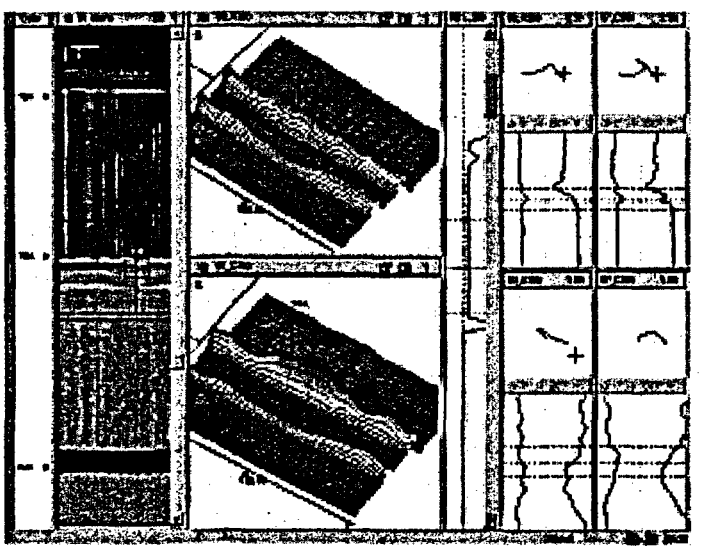

Figure 2.39.
X-Probe 3D image of EC signal amplitude as function of position around a test section in tube sheet simulation level of NRC steam generator mock-up. Tube axis is from lower left to upper right.

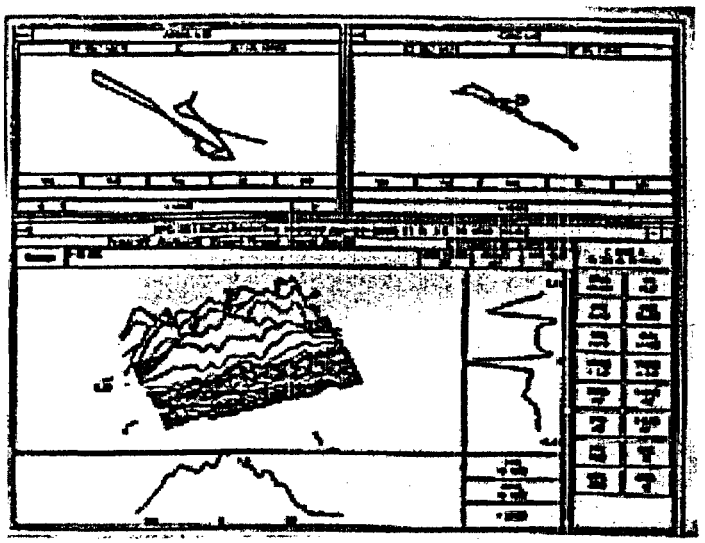

Figure 2.40.
+Point 3D image of EC signal amplitude as function of position around same mock-up test section as shown in Fig. 2.39. Tube axis is from lower right to upper left.

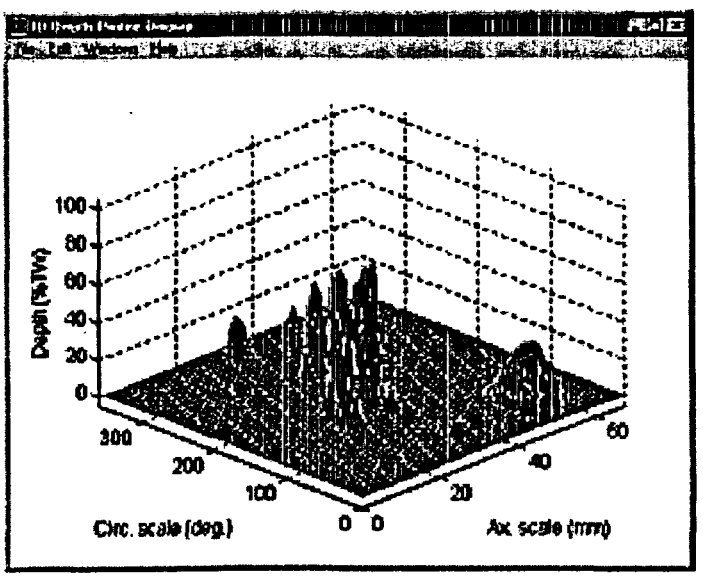

Figure 2.41.
3D plot of depth vs. position around same mock-up test section as shown in Figs. 2.39 and 2.40 generated by ANL multiparameter algorithm. Tube axis is from lower left to upper left. Improved spatial resolution is evident, along with crack depth information not available in X-Probe and +Point images. Phase and amplitude information are used to generate these images.

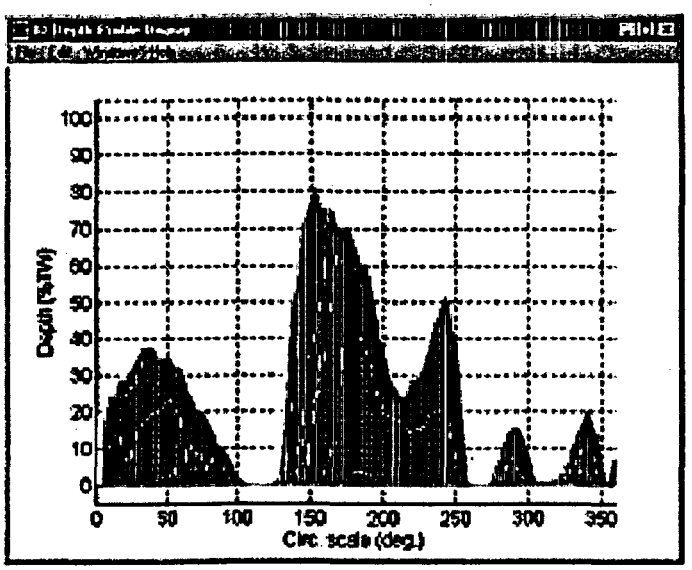

Figure 2.42.
Cross-section profile showing depth vs. circumferential position for same mock-up test section as shown in Figure 2.41 generated by ANL multiparameter algorithm. Improved spatial resolution is evident, along with crack depth information not available from X-Probe and +Point images. Phase and amplitude information are used to generate these images.

2.6 Use of Lamb Waves

The possibility of characterizing the mock-up tubes with UT waves to obtain depth estimates has been investigated. Lamb waves were explored as a possible method to help characterize defects in the steam generator mock-up tubes and to help identify attributes that may be useful for characterizing defects in field tubes. A specially fabricated Lamb wave probe with a 6-mm (0.24-in.) piezoelectric crystal on a wedge, operating in a pulse echo mode, was employed for the results described in this report. Lamb wave inspection was carried out from the inside of the tube with the tube filled with water and the contoured plastic wedge of the probe in contact with the tube ID surface. One significant advantage of Lamb waves is their insensitivity to the presence of roll transitions, making it easier to detect cracks at the transition of rolled tubes. In addition, Lamb waves are less sensitive to the presence of artifacts such as support plates and deposits and can be used to detect flaws at a distance.

Figure 2.43 shows the echo from a CODSCC in an Alloy 600 tube, 22.2-mm (0.875-in.)-diameter, with a laboratory-grown crack in the transition of a mechanically rolled tube. Ultrasonic diffraction and EC evaluation of the crack suggests a maximum depth of 80% TW. With the probe on the inside of the tube and 75 mm (3 in.) from the crack, the Lamb wave echo is clearly evident. The crack is about 140° in circumferential extent. With the probe on the opposite side from the crack, only a relatively weak signal from the roll transition is evident. The echo is visible with only moderate variation in signal amplitude as the probe is moved along the axis. Thus, by moving the probe a measured amount and noting the change in transit time of the echo, the Lamb wave velocity can be measured. For this tube, a value of 4800 m/s (15,750 ft/s) was measured at a UT frequency of 1.2 MHz. Rose et al.[12] reported, for an Alloy 600 tube, a measured velocity of 4790 m/s (15,720 ft/s) and a theoretically derived L(0,2) mode group velocity of 4670 m/s (15,320 ft/s) at 1.2 MHz and a wall thickness of 1.25 mm (0.047 in.). Consistent with the current evaluation, Rose et al. noted that the frequency of 1.2 MHz was especially effective for water-filled tubes. In general, Lamb waves have relatively low attenuation, and echoes from defects in the tube wall can, in principle, be obtained for long distances between probe and defect.

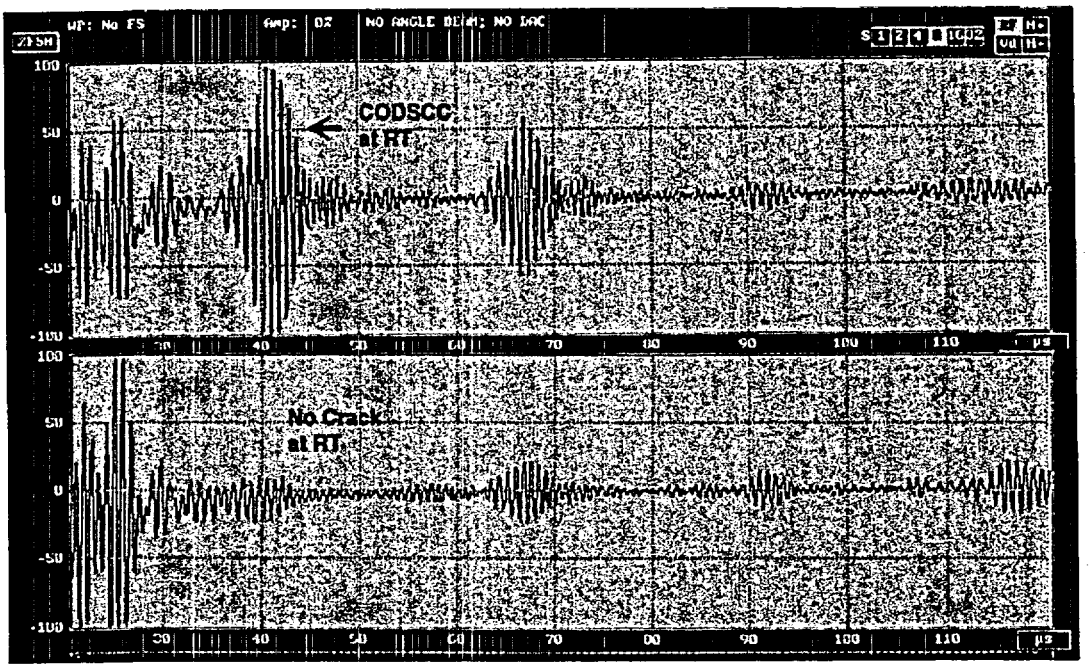

Figure 2.43. Ultrasonic Lamb wave echo (top half of figure) from a CODSCC in Alloy 600 tube with laboratory-grown crack in the roll transition. UT and EC evaluation of crack suggests a maximum depth of 80% TW.

3 Research on ISI Technology (S. Bakhtiari and D. S. Kupperman)

The objective of this task is to evaluate advanced NDE and signal analysis techniques for the reliable ISI of original and repaired SG tubes. Improved correlations between EC probe response and flaw morphology, leak rate, and failure pressure will be developed and validated. In addition, the reliability of the voltage parameter and other EC parameters and techniques will be evaluated with respect to their ranges of applicability.

The work in the task focuses on four primary areas: (a) analytical prediction of EC response as a function of probe design, flaw characteristics, and material properties; (b) development of effective signal analysis procedures; (c) development of flaw imaging and display methods for simple and accurate flaw characterization; and (d) evaluation of improved probe designs that may use directional arrays so that defects of arbitrary orientation can be examined simultaneously. The reliability and effectiveness of the proposed inspection techniques and the robustness of potential correlations were substantiated through laboratory testing on the SG tube bundle mock-up and on SG tubes that contain laboratory-grown flaws. Some additional validation was performed on service-degraded tubes.

3.1 Analytical Modeling of EC NDE

The interaction of induced fields and currents produced by an EC coil with flawed steam generator tubes is a complex phenomenon. One must distinguish between real defect signals and those due to background, such as probe response from tube support plates, probe wobble (liftoff), material inhomogeneities, and thickness variations, etc. Experiments do not always provide the level of detail and repeatability needed to understand the interactions. A-priori knowledge of the probe response is helpful in the interpretation of the measured data.

Several analytical and computational EM modeling approaches to the simulation of EC probe response for NDE of SG tubing have been examined. Most of the efforts focused on the application of a general-purpose 3-D FEM-based code for steady-state and transient-field calculations. In the FEM model, the governing EM field equations are expressed in terms of magnetic-vector and electric-scalar potentials in conducting media and in terms of reduced or total scalar potentials in nonconducting regions. The field equations are solved by finite-element discretization. The signal trajectory in the impedance plane due to probe motion is determined by calculating the response at discrete points along the tube axis. Various earlier reports [13-16] provide descriptions of the governing field equations, the lumped element equivalent circuit of the probe and test piece, and conversion formulas for comparison of numerical with NDE measurement parameters of interest. Results of representative test cases that simulate steady-state solutions with both differential and absolute bobbin coils are discussed here.

Test simulations were carried out to verify the accuracy of the FEM approach by comparing the solutions with detailed experimental measurements. The experimental EC data, supplied by C. V. Dodd, formerly of Oak Ridge National Laboratory, were obtained from tests on a large aluminum tube that contained throughwall holes and axial slits. Measurements were made at three frequencies with a Hewlett-Packard impedance analyzer and a specially constructed absolute bobbin coil (SN480A). The results were expressed in terms of both calculated impedance variations as a function of probe position inside the tube and

impedance-plane plots that simulate conventional EC instrument display. Excellent agreement was found between theory and experiment [13].

These studies also investigated the differences in EC probe response to volumetric (e.g., hole) and nonvolumetric (e.g., crack) flaw geometries. The calculations demonstrated that BC signal amplitude cannot be regarded as an absolute indication of the extent of defects when comparing different flaw geometries. A throughwall hole with a greater volume than an axial notch results in a smaller perturbation of the coil impedance, which is linearly proportional to the probe output voltage. Eddy currents always flow through the path of least resistance in a conducting medium. The discontinuity (infinite resistance) introduced by the thin but long axial notch forces the currents to take a contour around the defect, which, in turn, gives rise to a larger impedance mismatch for the probe.

The response of bobbin coil probes to simulated cracks in Alloy 600 tubing was studied. The effects of the length, width, and ligament size of axial cracks on the EC indications from conventional ISI bobbin probes were determined. To determine the effect of crack length on absolute-BC signal amplitude, the absolute-BC probe response to axial slits, 100% throughwall, on 22.2-mm (0.875-in.)-OD Alloy 600 tubing with a nominal wall thickness of 1.27-mm (0.05-in.) and a conductivity of 100 $\mu\Omega$-cm was calculated. The modeled probe was a conventional 18.3-mm (0.72-in.)-OD absolute bobbin coil. Simulations were carried out at frequencies of f = 100 and 400 kHz. The results were expressed both as current distribution along the tube and also in terms of change in the magnitude of the probe impedance, which is linearly proportional to its output voltage (i.e., related by a constant multiplier that is proportional to the coil current density). For the test cases considered, the width of the slit was chosen to be 0.127 mm (0.005 in.), and the length was varied from 0.25 to 50 mm (0.010 to 2 in.). The coil was initially positioned symmetrically in the middle of the slit and the coil's length and height were taken to be 1.27 and 1.525 mm (0.050 and 0.060 in.), respectively.

The calculations showed that the narrow crack forces circumferentially induced currents to take a flow contour around the defect. There is a nonlinear relationship between crack length and EC voltage amplitude that is frequency dependent. For defect lengths < 2 mm (0.08 in.), the perturbation of the EC absolute-BC signal is small. The slope of the curve decreases with an increase in defect length. For example, at 100 kHz, the relative variation in the signal amplitude for an increase in crack length from 5 to 25 mm (0.2 to 1 in.) is more than five times that due to a change in length from 25 to 50 mm (1 to 2 in.). This saturation occurs much faster for the differential than the absolute coil configuration. The effect of crack length on BC probe amplitude is much more significant for deep OD flaws approaching 100% TW. The effect of length increases with increasing depth of OD flaws. This suggests that a single-point voltage-based criterion for the determination of OD degradation extent could result in unreliable estimates for nonvolumetric flaws.

To examine the effect of crack width on absolute BC response, a series of computations for different defect widths were carried out with the coil located symmetrically under the discontinuity. The crack length was taken to be 25.0 mm (1 in.) and the width was varied from 0.015 mm (0.0006 in.) to 1.0 mm (0.04 in.). Although the results obtained at higher frequency show slightly larger variation of the signal amplitude, the variation of the EC voltage amplitude with defect width over the range of 0.015 to 1 mm (0.0006 to 0.04 in.) is relatively small at both frequencies (100 and 400 kHz). This finding is in agreement with the concept that conduction loss is proportional to the path length of EC flow, which is a frequency-dependent parameter.

Note that all simulations are based on a nonzero crack width and do not represent a tight crack with contact areas over the crack faces.

The computations show that the signal amplitude drops exponentially with defect depth. Also, the response to OD flaws is smaller at the higher frequency in all cases, and the relative difference in the response between OD and ID flaws increases as the flaw depth decreases. Due to higher conduction loss at higher frequencies, the drops in the signal amplitudes as the OD notch depth decreases are much larger at higher frequencies. Although the resistive and reactive signal components display different responses as a function of position, the maximum signal magnitude for all test cases occurs in the center of the defect.

The calculations demonstrate that the calibration of BC amplitude based on 20% TW drilled holes on an ASME standard tube does not imply detection of short axial cracks of comparable depth. For a 6.35-mm (0.25-in.)-long axial notch, the BC probe amplitude begins to approach that of four 20% TW drilled holes only for notch depths approaching 80% TW. Therefore, under realistic ISI conditions (i.e., in the presence of noise), short, shallow OD cracks (e.g., <40% TW) could go undetected during BC examinations because of their lower voltage response. It could be argued that, for nonvolumetric degradations, even the 40% TW OD depth may not be a conservative estimate for BC examinations because field-induced cracks are often much tighter than machined flaws, which could further degrade the signal-to-noise (S/N) ratio and, in turn, detection capability. The large differences in signal amplitude between holes and notches can be attributed to both the defect geometry and probe characteristics. The volume of the four 20% TW OD holes in the ASME calibration-standard tube is much larger than that of a notch of comparable length and depth, and this condition results in a much greater perturbation of the probe's impedance. The effect of the volume of a discontinuity on signal amplitude is especially significant for BC probes, where the coil output at each axial position along the tube represents an integrated reading around the circumference.

In practice, single isolated cracks are less likely to occur than a series of short cracks separated by short ligaments. Calculations were performed to examine the effect of such ligaments on bobbin coil response. The probes modeled were conventional 18.3-mm (0.72-in.)-OD differential and absolute bobbin coils, and the frequencies considered were 100 and 400 kHz, which are typical for multifrequency ISI of SG tubes. We considered two axial flaws, 100 and 75% TW, both of which were 12.7-mm (0.5-in.) long and separated by a ligament of varying length in Alloy 600 tubing the same dimensions and conductivity as before. Results were obtained in terms of current distribution along the tube and computed resistance and reactance values as a function of probe position.

We showed that even small ligaments (0.127 mm [0.005 in.]) create a conducting path for the circumferentially induced currents to flow across the discontinuity, which consequently results in a reduction of the probe signal due to the smaller impedance mismatch. This finding is more apparent in the impedance plane trajectory (Lissajous trace) than in the absolute signal amplitude, where, for example, a 2-mm (0.08-in.) ligament in a 100% TW axial notch could significantly reduce the signal amplitude.

3.2 Correlation of Failure Pressure with Bobbin Coil Signals

Conventional repair and plugging criteria for SG tube integrity have been based on estimated degradation depth. Tubes with EC indications that correspond to degradation greater than a specified limit (typically > 40% of nominal tube wall thickness) are either repaired (by sleeving) or taken out of service (e.g., plugged). For some types of degradation, e.g., those characterized by short deep crack segments separated by ligaments, depth measurements of an individual crack may not be the best measure of structural integrity. For ODSCC indications at TSP intersections, a voltage-based alternate plugging criterion (APC) has been developed. The criterion is based on a correlation between BC voltage amplitude, rather than estimated defect depth, and failure pressure and leak rate. NRC guidance for the application and development of such criteria are provided in Generic Letter 95-05 [17]. The correlations between voltage and failure pressure and leak rate were developed empirically from tests on service-degraded pulled-tube specimens and laboratory-grown cracks.

Multivariate regression analysis and neural networks were used to develop alternative empirical models to relate BC probe data with tube failure pressures. This effort was based on a reanalysis of the data on pulled and model boiler tube specimens that were originally used by the Westinghouse Owners Group to develop an APC for ODSCC indications at TSP locations in Westinghouse plants that use drilled-tube support plates. Both multiple linear regression (MLR) and neural-network models were successful in producing reasonable correlations for the individual data sets. Signal features, such as maximum and integrated amplitude, were considered as model parameters. The signal features ultimately selected were the integrated amplitudes at multiple original and mixed frequencies. Preliminary studies on pulled-tube data suggested that an optimal (i.e., minimum number of indications for an acceptable correlation) calibration/training set should include representative tubes that describe the range of variation in inspection data that is included from each SG unit. As expected, prediction confidence intervals were narrower for the model boiler test set. Subsequent attempts to develop correlation models with a combined set of pulled and model boiler specimens by using similar EC test parameters failed to produce acceptable prediction confidence intervals. Eventually, an independent normalization procedure was devised for this analysis. Note that the robustness of any correlations developed in this study might be limited by the range of crack morphologies and inspection artifacts included in the available database.

3.2.1 Multiple Linear Regression and Neural-Network Model; ARC Data Base

Current alternate plugging and repair criteria for ODSCC degradation at TSP intersections for 22.2-mm (0.875-in.)-diameter tubing are based on BC voltage amplitude (e.g., signal amplitude from 400/100 kHz mixed frequency channel). Multivariate regression analysis procedures were used to analyze the relationship between BC probe signals for ODSCC degradation in the TSP area and tube failure pressure. Forty-one indications from the alternate repair criterion (ARC) database were used in the analysis. The indications were from 22 model-boiler and 19 pulled tubes. All of the examined tubing was 22.2-mm (0.875-in.) in diameter, with a nominal wall thickness of 1.27-mm (0.05-in.). The pulled-tube indications were from the first three TSPs on the hot-leg side. The pulled-tube specimens are from three plants. Table 3.1 lists the number of specimens from each SG unit that were incorporated for analysis. Table 3.2 lists the crack depth, crack length, and failure pressure from the ARC model-boiler tube database.

Table 3.1. Pulled-tube specimens from ARC database incorporated for failure pressure analysis.

Plant	SG Unit	Indication no.
A	1	1 – 4
A	2	5 – 8
B	1	9 – 11
C	1	12 – 19

Table 3.2. Destructive examination and failure pressure measurements for pulled tubes from ARC model–boiler database that contained ODSCC degradation at TSP intersections.

Specimen No.	Destructive Examination[a] Maximum Depth (%)	Destructive Examination[a] Length[b] (in.)	Adjusted Pressure[c] (psi)
528–2	100	0.67 (0.5)	4,668
532–1	100	0.7 (0.52)	4,010
532–2	100	0.75 (0.58)	4,087
535–1	100	0.28 (0.11)	8,265
555–3	100	0.75 (0.42)	4,209
533–4	100	0.34 (0.14)	6,964
536–1	90	0.4	7,959
542–4	N/A	N/A[d]	> 4,867
543–1	N/A	N/A	> 2,633
543–2	N/A	N/A	> 3,153
543–4	98	0.52	5,459
547–1	N/A	N/A	5,561
576–2	100	0.3 (0.22)	6,628
576–4	100	0.6 (0.43)	5,602
557–1	90	0.18	> 7500
557–2	100	0.52 (0.44)	> 4,974
557–4	N/A	N/A	11,633
558–1	100	0.4 (0.32)	5,969
568–1	100	0.33 (0.25)	6390
568–2	N/A	N/A	> 4,635
571–1	100	0.44 (0.35)	> 4,950
574–4	100	0.39 (0.33)	5,506

[a]Measurements were carried out by Westinghouse Electric Corporation.
[b]Total crack network length, with throughwall degradation length given in parentheses.
[c]Normalized to 150 ksi flow stress (sum of yield and ultimate stress).
[d]N/A: Data not available.

Before a specimen was included in the analysis, the following information about it was required: an ASME calibration standard data file, a measured failure pressure, and data at a consistent set of EC inspection test frequencies (400, 200, 100 kHz absolute and differential channels). Although procedures to correlate EC readings at different test frequencies for similar probes have been proposed, such procedures were not used to avoid an additional source of uncertainty.

Figure 3.1 is a histogram of the distribution of measured failure pressure for pulled- and model-boiler-tube indications. As noted previously, the pulled- and model-boiler tube populations cluster at high and low failure pressures, respectively, with relatively few data points at intermediate pressures. Furthermore, the NDE measurements are affected by such factors as variations among calibration standards, probe wear, and dissimilarity of tube/artifact geometry (NDE carried out with or without TSPs in place, presence or absence of deposits, etc.) as well as actual differences in defect size and morphology.

To reduce the influence of such factors on NDE data, the EC readings were normalized and frequency mixed. The normalization procedure consisted of automatic phase-angle adjustment for each channel and amplitude scaling in reference to four 20% flat-bottom holes on an ASME calibration standard tube. For 400/100, 400/200, and 200/100 kHz, where the upper frequency was taken as the primary channel, linear two-frequency least-squares mixes were used to reduce/suppress the TSP signal. A 400/200/100 kHz mix was also examined and, based on the regression analysis results, provided a small improvement over the 400/100 kHz mix. The mixing algorithm was carried out for all data files regardless of whether or not the file contained a TSP indication. The resampled data points for the mixed signals were chosen to cover the entire support plate region.

A series of computer codes was written to perform all the manipulations of NDE data, such as searching each file for proper channel configuration, selecting data segments that contain indications at the TSP region, normalizing, resampling, and constructing mixed-frequency channels.

The integrated area under each TSP indication was determined by the equation

$$S_f^{A,D} = \sum_{n=-N/2}^{N/2} \left(|H_n + i * V_n| \right), \tag{3.1}$$

where S represents the integrated signal magnitude at frequency f for each absolute A and differential D channel, and H and V are the horizontal and vertical signal components at each frequency. The integrated region was bounded by $N/2$ points on either side of the TSP center ($n = 0$), with the sampling rate of each data segment being adjusted in accordance with the simulated TSP ring from the corresponding ASME tube standard.

Although the integrated TSP signal of Eq. 3.1 could be correlated reasonably well with the tube failure pressure when the model-boiler and pulled-tube data sets were considered separately, the correlation was poor when both types of specimens were included in a single database. Consequently, additional transformations of the signals were explored. The selected transformation involved mean-centering and energy-scaling of each data segment

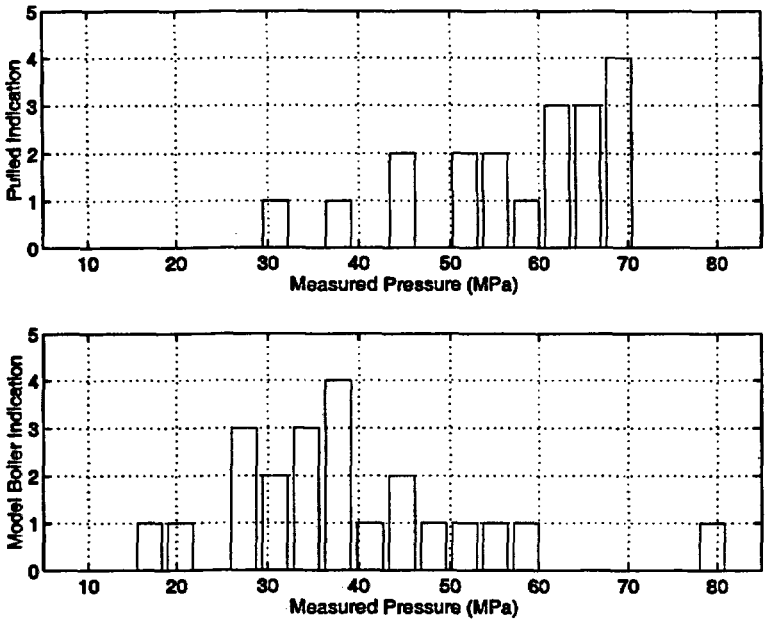

Figure 3.1.
Distribution of pulled–tube (top) and model–boiler (bottom) indications as a function of failure pressure used for multivariate analysis.

independently. Mean–centering is performed to reduce the effect of signal offsets; energy–scaling, to render equal weight for each data segment. As in the case of Eq. 3.1, the integrated area under the transformed signals was determined by

$$\hat{S}_f^{A,D} = \sum_{n=-N/2}^{N/2} \left(\hat{H}_n + t * \hat{V}_n \right), \tag{3.2}$$

where the transformed $\hat{H}$ and $\hat{V}$ components are defined as

$$\hat{X}_n = \left(X_n - \mu^X \right) / \xi^X, \tag{3.3}$$

where μ represents the mean and ξ is the signal energy. For an equal–length mean–centered signal component ξ^X is proportional to the standard deviation σ^X of each trace. Transformation in accordance with Eq. 3.3 will retain the shape of the original impedance plane trajectory (i.e., a Lissajous trace). Training and prediction schemes were subsequently employed to evaluate the ability of each correlation model to capture all of the useful trends in the data.

Figure 3.2 displays the multivariate regression and the neural–network fits when all samples are incorporated for the model–building stage. Also shown are the upper and lower bounds of the 95% confidence interval, calculated through a first–order least–squares fit to the measured–vs.–predicted pressure. As expected, the neural network (Fig. 3.2b) can better capture all the variations in the data. However, this test case does not represent the prediction capability of the model but rather the ability of the model to construct a fit to all of the data. Figure 3.3 displays the prediction results of the two models when ≈ 50% of the indications from each tube category are included in the training stage. For this test case, comparable confidence intervals were achieved by both methods. Finally, Fig. 3.4 displays the prediction

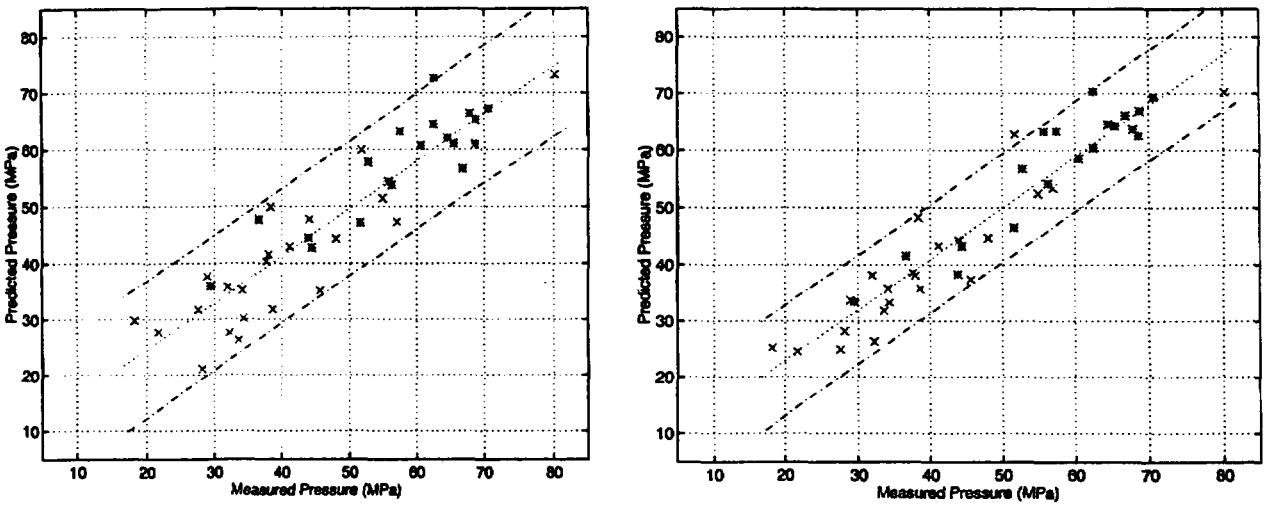

Figure 3.2. (a) Predicted vs. measured failure pressures for (a) regression and (b) neural–network fits when all model–boiler (x) and pulled–tube (•) indications are included for training. Also shown are the upper and lower bounds of the 95% confidence interval, based on a linear least–squares fit to the data.

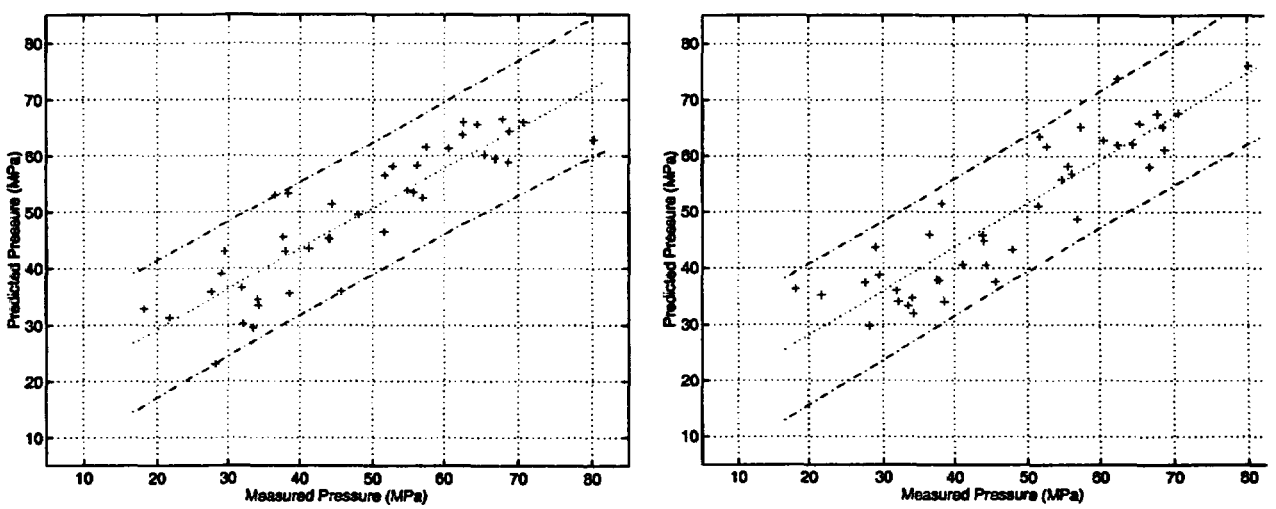

Figure 3.3. (a) Predicted vs. measured failure pressures for (a) regression and (b) neural–network fits when ≈ 50% of model–boiler and pulled–tube indications are randomly selected for training. Also shown are the upper and lower bounds of the 95% confidence interval, based on a linear least–squares fit to the data.

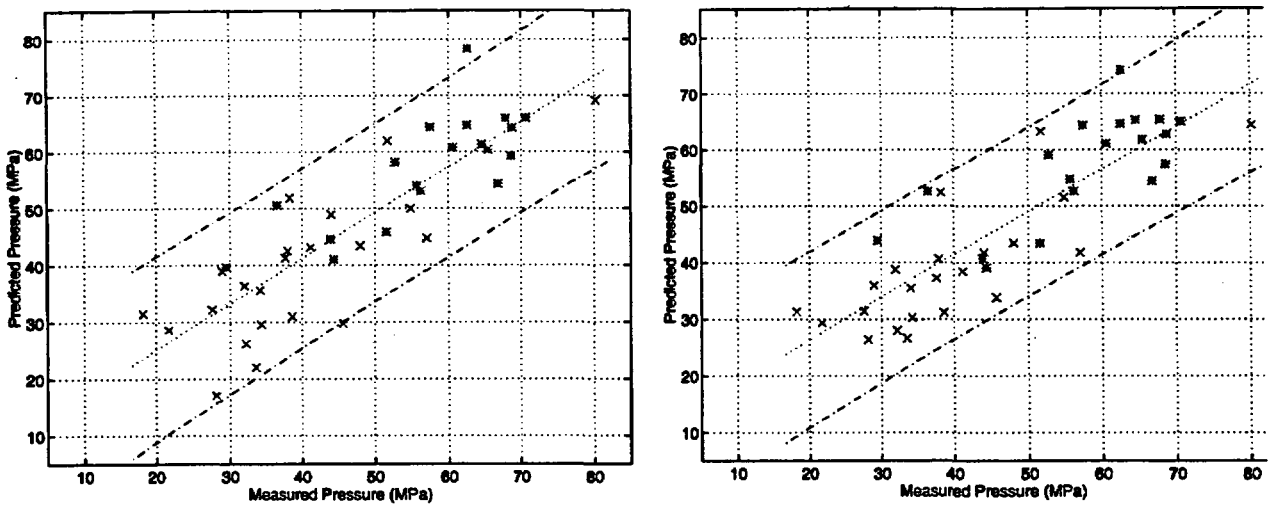

Figure 3.4. Predicted vs. measured failure pressures for (a) regression– and (b) neural–network fits for model–boiler (x) and pulled–tube (•) indications, with LOOT training and prediction method. Also shown are the upper and lower bounds of the 95% confidence interval based on a linear least–squares fit to the data.

results of the two models based on the leave-one-out training (LOOT) and prediction scheme. Once more, the confidence intervals for both methods of fitting show comparable prediction accuracy.

Figure 3.5 is a plot of residual vs. regression–predicted failure pressure when all model–boiler and pulled–tube specimens are included in the training. The distribution of residual pressures does not display any distinct pattern, a finding that is consistent with the assumption that a normal distribution of residual pressures is implicit in the calculation of the confidence interval. Figure 3.6 shows the changes in residual failure pressures when the LOOT training and prediction procedure is performed. For multivariate models, the variation of residual pressure obtained with the LOOT procedure is an indicator of model stability. For a stable model, the predictions should be relatively independent of individual data points in the training set, i.e., the residual pressures in Fig. 3.5 should be small when compared with the predicted failure pressures. In the present case, the change in the residuals is ≈ 10%. For this type of data, such a change is reasonably small.

Figure 3.6a shows the cumulative distribution of the residual pressure, assuming that it is normally distributed when the training set includes all of the available indications. Figure 3.6b shows similar results when a LOOT training/prediction procedure is implemented. The standard deviation of the distribution when the LOOT procedure is followed is ≈ 50% greater than when all of the data are used to fit the model. The LOOT training scheme may provide the most conservative estimate of the accuracy of the predictors.

A study was also carried out to indirectly assess the prediction accuracy of the multivariate regression model by comparing the results presented above with those obtained by a linear regression model. The data set used in this work was developed by renormalizing the EC inspection results that were used to develop the voltage–based APC model. The renormalization was performed by referencing all measurements to a single ASME tube

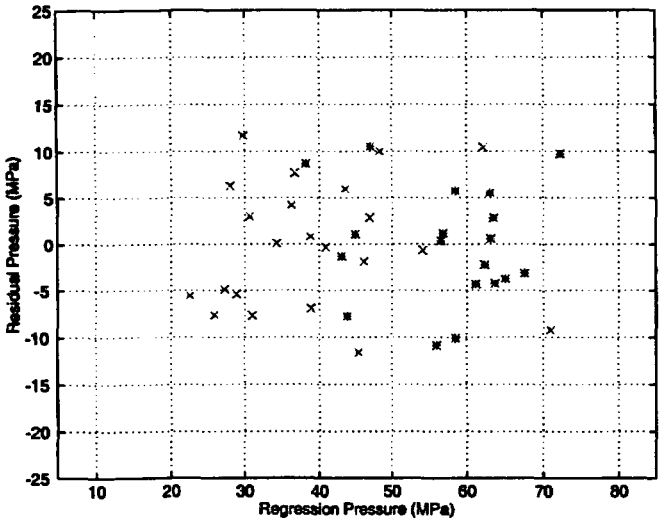

Figure 3.5.
Residual vs. regression–predicted failure pressures when all model–boiler (x) and pulled–tube (*) specimens are included for training.

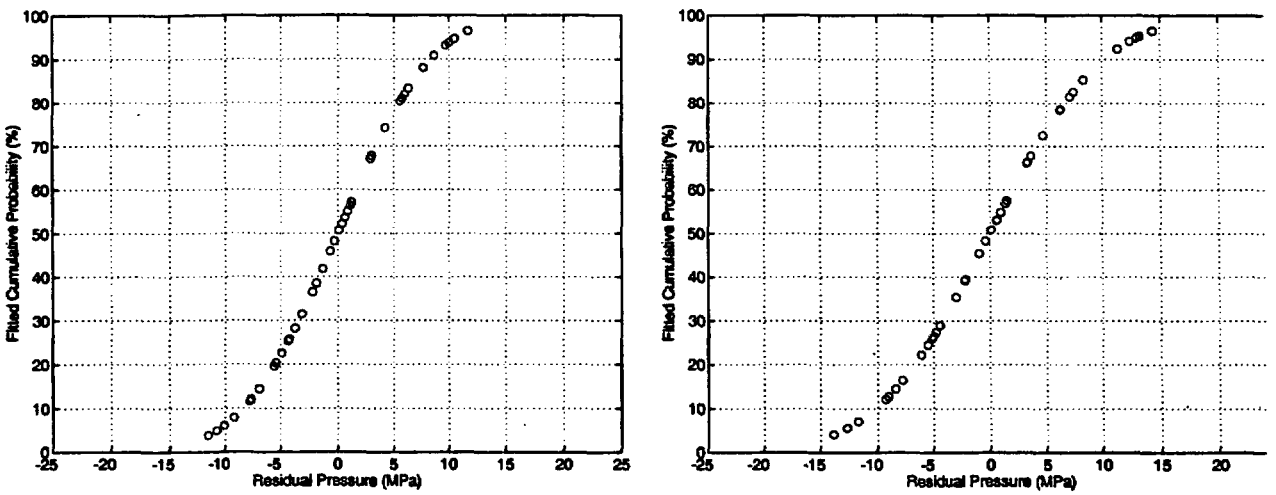

Figure 3.6. Cumulative distribution of residual failure pressure. Normal distribution function was assumed, with training and prediction based on (a) all indications and (b) LOOT.

standard. A linear least–squares fit to the logarithm ($\log_{10}$) of the measured voltage–vs.–failure pressure was implemented in accordance with the APC–recommended model. Although a direct analogy between the APC linear regression and multivariate models cannot readily be described, comparison of the predicted residual pressures suggests a tighter global prediction for the multivariate model.

The failure pressures predicted by the APC linear regression model vs. measured failure pressures are shown in Fig. 3.7. Also shown is the 95% confidence interval for the first order least–squares fit of the measured–vs.–predicted failure pressures. A linear correlation coefficient R of ≈ 0.88 was calculated for this fit. Figure 3.8 is a plot of the residual failure pressure vs. regression–predicted pressures. Once again, the distribution of the residual pressures does not display any distinct pattern. Assuming that the residual failure pressures are normally distributed, the cumulative distribution of the residual pressure is shown in Fig. 3.9.

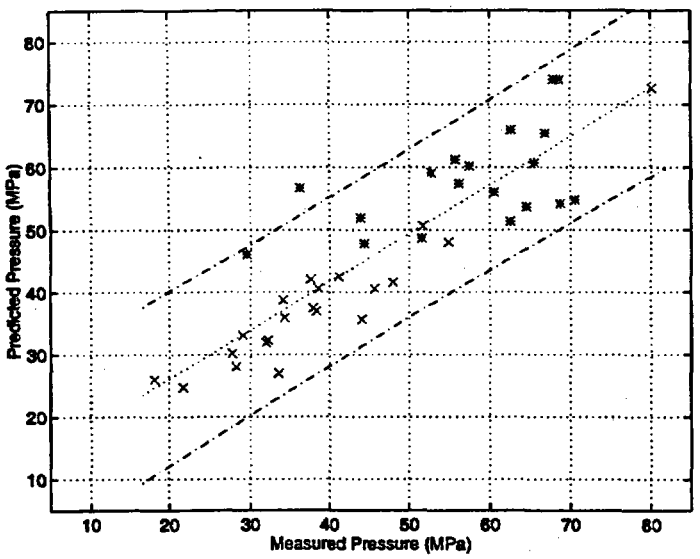

Figure 3.7.
Regression–predicted vs. measured failure pressures for all model–boiler (x) and pulled–tube (•) indications, using the APC model. Also shown are the upper and lower bounds of the 95% confidence interval based on a linear least–squares fit to the data.

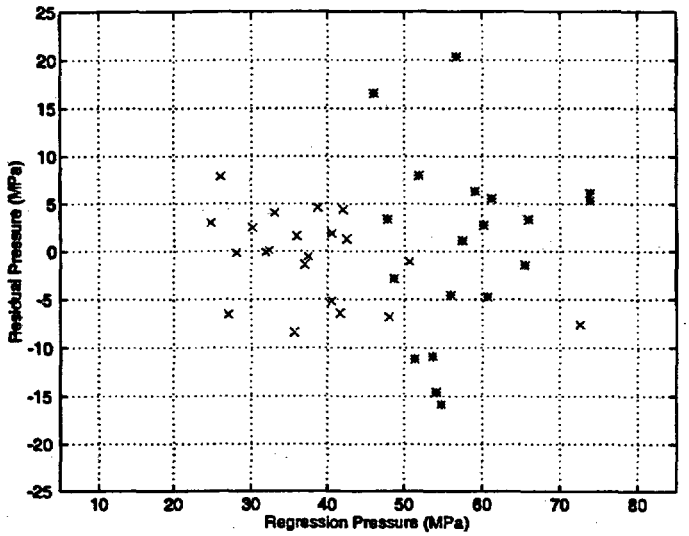

Figure 3.8.
Residual vs. regression–predicted failure pressures for all model–boiler (x) and pulled–tube (•) specimens, using the APC model.

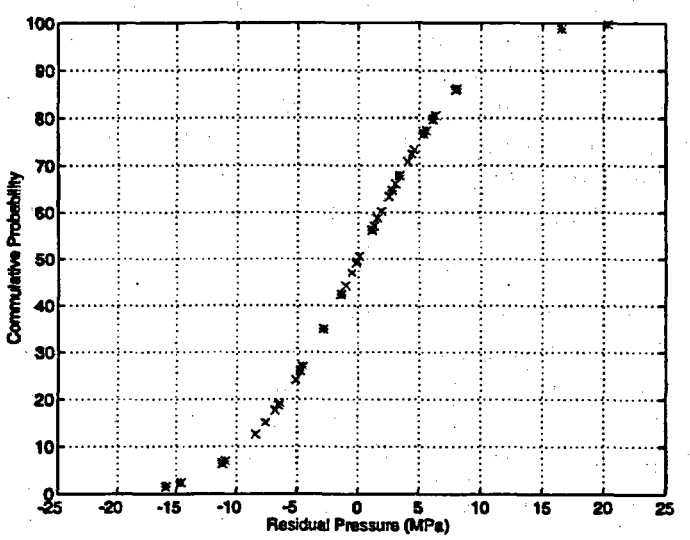

Figure 3.9.
Cumulative distribution of APC model residual failure pressures, based on an assumed normal distribution function.

3.3 Computer-aided Analysis of Eddy Current Inspection Data

Manual analysis of multiple-frequency EC data is a tedious and challenging process. At present, no qualified technique, manual or automated, exists that provides reliable estimation of flaw size over a wide range of SG tubing damage. Conventional data analysis methods become rather subjective when dealing with complex forms of degradation such as stress corrosion cracking. Signal distortion by interference from internal/external artifacts in the vicinity of a flaw further complicates discrimination of flaw signals from noise. In this context, noise refers to any random or coherent signal that is not induced by a flaw.

In comparison to high-speed BC inspections, high-resolution multicoil rotating and array probes generate enormous amounts of data over comparable scanning lengths. Rotating probe ISI of SG tubing is thus generally restricted to areas that are historically predisposed to known damage mechanisms and sections of particular interest that are flagged by the initial BC examinations. More extensive application of such probes for improving NDE reliability rests, in part, on automating various stages of the data screening process. Computer-aided data analysis is a viable means to overcome many of the challenges associated with reliable processing of data acquired with high-resolution probes.

A key objective of the work has been to characterize flaws in the ANL steam generator mock-up in order to minimize the need for destructive examinations and to further assist in parallel studies on prediction of tube structural integrity from NDE estimates of flaw profile. Application of the methods developed has been limited so far to analyses of data from rotating pancake coils; however, many of the fundamental processes described here are applicable to other probe geometries and coil configurations.

3.3.1 Data Processing Structure

Computer-aided data analysis here refers to software to carry out various stages of processing raw EC inspection data. Figure 3.10 depicts the basic structure of the algorithm developed to allow for off-line analysis of data acquired with a commercial EC testing instrument. Blocks associated with the processes mentioned in this report are numbered. The output of the acquisition block shown in Fig. 3.10 is the digitized output of a multiple-frequency inspection system. The EC testing instrumentation and software used at ANL are a Miz-30™ (Zetec, Inc.) remote data acquisition unit that is controlled under the HP-UX-based Eddynet™ (Zetec, Inc.) environment. The raw inspection data are converted to a standard file format. All data analysis and signal processing algorithms were written using the PC-based software MATLAB, which is a high-level scripting language that provides an efficient environment for data manipulation and computation, together with convenient graphical user interfaces (GUIs) and graphical displays of the results.

The block diagram shown in Fig. 3.10 can be divided into three basic components: data conversion, calibration, and analysis. Each block is described in the following sections. In the conversion stage (block 1) digitized recordings of inspection data that sequentially represent the in-phase and quadrature signal components are converted to a readable format for off-line manipulations. In the subsequent stage (block 2), multiple-frequency raw EC data are calibrated for all the recorded frequency channels. Finally, in the data analysis stage, (blocks 3-6), calibrated data are processed to produce depth estimates for the flaw indications in a selected test section of a tube.

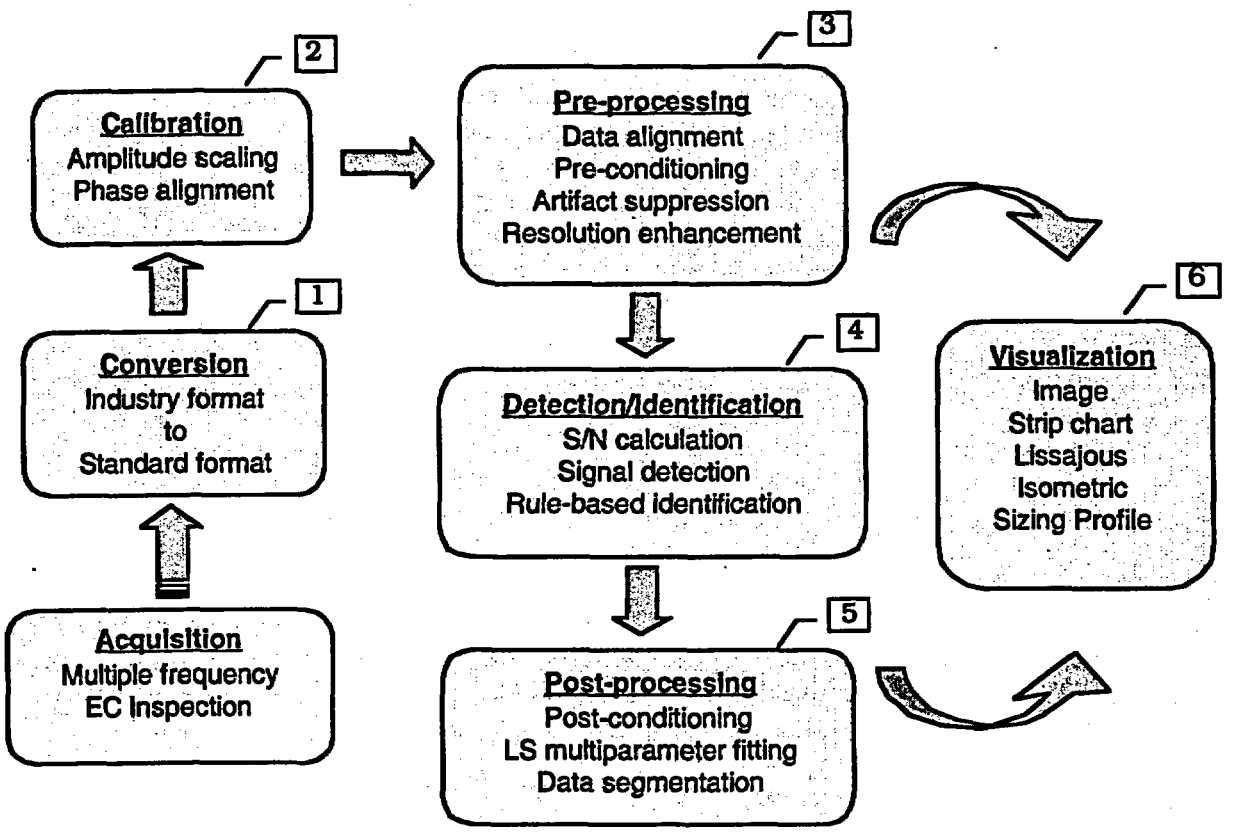

Figure 3.10. Schematic diagram showing basic structure of computer-aided data analysis algorithm. Blocks associated with operations described in this report are numbered.

3.3.2 Conversion and Calibration Routines

A series of algorithms has been implemented under the MATLAB environment to carry out the conversion, normalization, and reformatting of the raw EC data. An interactive MATLAB program, *ECTool*, calls the data retrieval and calibration routines through a single GUI control window. This software currently retrieves and processes inspection data acquired with either the Zetec MIZ-18 or MIZ-30 EC inspection instruments. With appropriate modifications, the software could also be used to convert inspection results from other standard commercial instruments.

The main control window contains virtual instrument controls such as pull-down menus, editable text, and push buttons that activate various functions for the manipulation of the NDE results. Data files in Eddynet format are initially read by these codes. The data conversion routine extracts the essential header information (currently assumed to be from MIZ-18 or MIZ-30 instruments), such as the number of channels and their associated frequencies, from the original Eddynet-formatted files. The decoded header information contains the frequency and channel configuration that is subsequently used to sort out raw EC readings. The reformatted data matrix, along with the header and coil configuration information, is then

stored in a user-defined data file. Normalization values of all the available channels are calculated by using the inspection results from a calibration standard tube. These values consist of amplitude scaling factors, phase angle rotations, and null values that are automatically calculated based on user-defined approximate locations of known indications on the tube. Although the necessary information for standard normalization procedures is defined as a set of default values in the program, the code also allows calculation of these values in an arbitrary fashion. Finally, the raw EC readings are calibrated by another code that is also activated from the main menu and applies the previously calculated normalization factors to each new raw data file. To avoid incorrect application of normalization factors, the codes initially check the header information for consistency between the original calibration standard tube and new data files that are subsequently loaded.

3.3.2.1 Data Conversion

Eddynet provides inspection data in MIZ-18 and MIZ-30 formats. The header sizes for MIZ-18 and MIZ-30 are currently preset to contain a fixed number of bytes. Following the header is a data stream that sequentially contains the horizontal and vertical signal components for all channels that are stored in 2-byte signed integer format. The necessary information can be extracted from the header to carry out the data conversion. This information reveals whether the data are in the MIZ-18 or MIZ-30 formats and the numbers of channels in the data file. Once these two pieces of information are determined, the conversion routine can retrieve and convert EC data files to a format suitable for any future manipulations.

3.3.2.2 Automated Data Calibration

Calibration of raw EC data plays an important role in any data analysis procedure. Conventional phase-angle calibration for normalizing EC data is carried out manually and routinely involves visual alignment of the impedance-plane signal trajectory (i.e., Lissajous trace) with respect to some reference indication. This implies that the extent of background fluctuations and S/N ratio, as well as analyst judgment, could affect the calibration process and consequently lead to varying estimates of a desired parameter. Because estimates of flaw depth from phase angle information of multifrequency inspection data depend heavily on initial calibrations, computer-aided data calibration routines play an essential role in uniform and accurate normalization of raw EC data.

Signals from machined flaws on a calibration standard tube are used to normalize the amplitude and phase of raw EC data. Amplitude scaling is performed with respect to peak signal voltage from a known indication on the calibration standard. Alignment of the phase angle at each frequency is typically made in reference to either a shallow ID or a throughwall flaw.

Figure 3.11 displays the user interfaces along with intermediate and final stages of calibration of raw EC readings collected with the 2.92-mm (0.115-in.)-diameter primary pancake coil of a three-coil rotating probe on a 18-notch standard. The code sequentially asks the user to interactively provide information on the approximate positions of lift-off, a sound portion of the tube, and an indication for amplitude scaling; it calculates the phase-angle rotation, null value, and scaling factors for uniform normalization of all the data files that belong to the same calibration group.

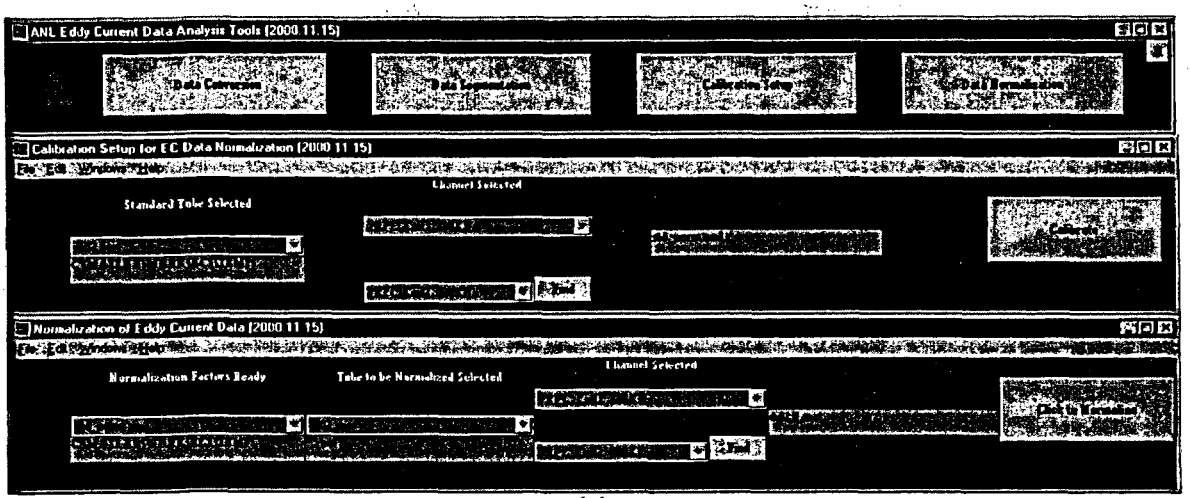

(a)

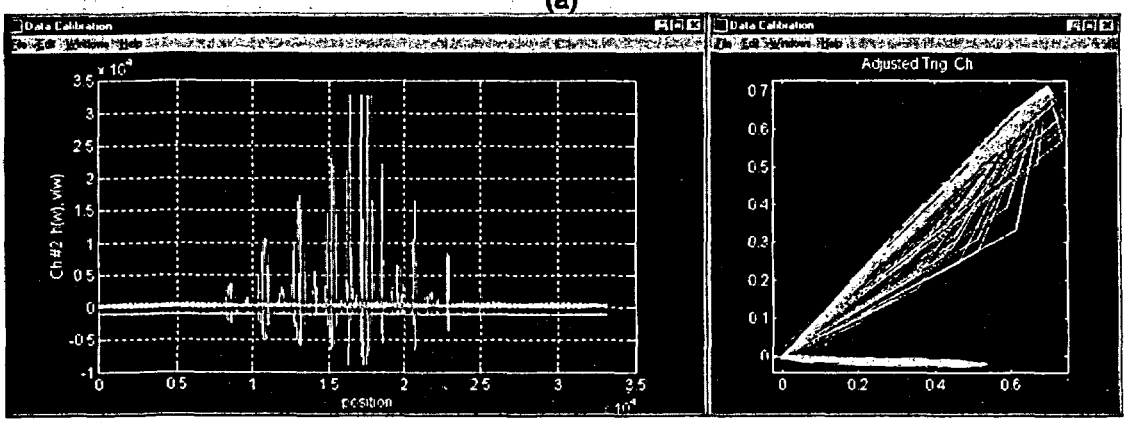

(b)

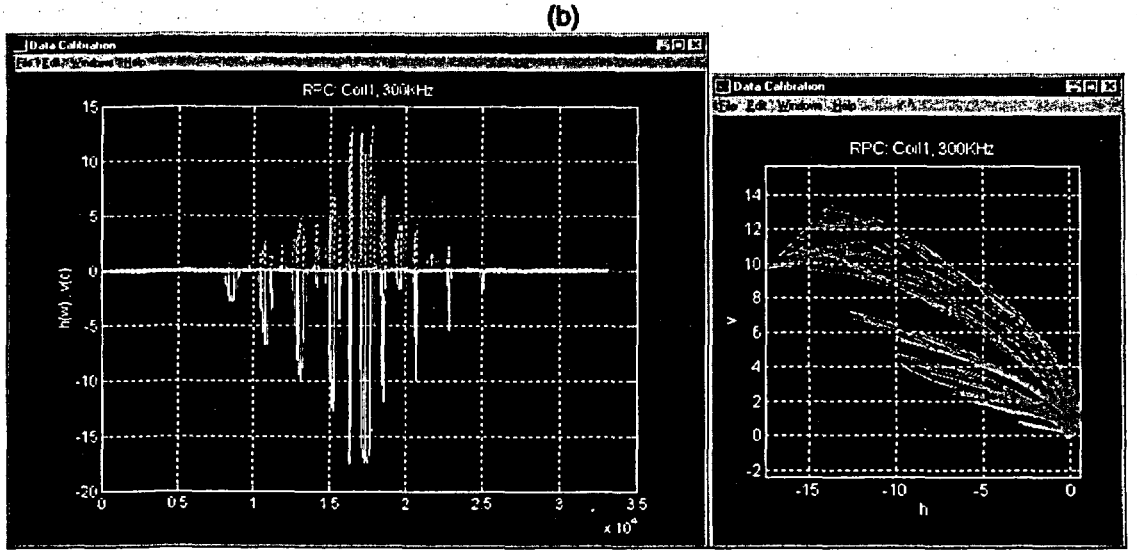

(c)

Figure 3.11. Displays of GUIs for (a) main ECTool menu with data calibration submenus, (b) raw data and trigger channel, and (c) calibrated data in strip chart and Lissajous display format. Eddy current data were acquired on a 18–notch standard with a 2.92–mm (0.115–in.)–diameter primary pancake coil of a three–coil rotating probe.

3.3.3 Signal Processing, Data Analysis, and Display Routines

In reference to Fig. 3.10, the data analysis section (shown by blocks 3–6) has three basic stages: pre–processing, flaw detection and identification, and post–processing of data. These blocks consist of various scripts that successively perform the calculation of S/N ratios for all channels, apply filters for pre– and post–processing of data, and ultimately combine multiple–frequency information from all processed channels to provide an estimate of flaw depth for the entire tubing test section. Both frequency and spatial domain filters are incorporated for signal conditioning, baseline reduction, and resolution enhancement. Initially, the S/N ratio is calculated from a user–defined approximate location along the trace baseline and minimum detectable amplitude from a calibration standard tube. Subsequently, this information is used to implement a series of filters that perform suppression of artifacts, baseline fluctuations, and signal enhancement or restoration. The filter characteristics take into account both the coil configuration and the sampling frequency of the inspection data. The identification of flaws and their origin, i.e., OD or ID, is done through a series of rules that are applied to the multiple–frequency EC data. Both amplitude and phase relationships among the processed channels are used at this stage of the process. Finally, the phase information at multiple frequencies is combined to calculate the flaw depth for the tube test section in reference to known indications on a calibration standard tube. Multivariate analysis using the available information from multiple channels is used for estimating the NDE depth profile of the tube.

A series of algorithms has been implemented as MATLAB scripts to provide the profile of flaw depth in an SG tube test section from NDE inspection results. These codes are executed through a user interface tool to automatically process the EC data. Figure 3.12 shows the main window of the GUI tool *ETProf*, which incorporates various algorithms for the processing of raw EC data. Figure 3.12 also shows several forms of graphics currently in place for the visualization of data at various stages of analysis. Subsequent to calculation of the relative depth profile, estimated values are converted to percent of tube wall thickness. Reconstruction of helically scanned data into C–scan format allows for the observation of sizing results from any azimuth and elevation view angle and for any axial or circumferential cross section of the tube. Scaling of data in axial and circumferential directions permits direct deduction of the flaw extent along the tube.

3.3.3.1 Signal Conditioning

Pre– and post–conditioning of data are some of the most fundamental operations in any signal processing application. The aim of such data manipulations is to minimize the contribution from known sources of signal distortion. Coherent noise that is present at multiple channels occurs commonly in EC testing of SG tubing. Low–frequency baseline fluctuations and high–frequency noise are also always present, to various degrees, in any EC inspection data. Typical sources of low–frequency signals, particularly for absolute impedance coils, are probe wobble, probe wear, temperature fluctuations, and gradual dimensional and geometry changes of the tube. Tube ID conditions and electronic noise, on the other hand, are typical sources of high–frequency noise. For both these sources of signal degradation, frequency domain filters can be designed to effectively suppress unwanted signals. Two types of filtering have been incorporated into the data analysis routine to reduce the level of such noise. They consist of standard Fourier domain filters and the more elaborate finite–impulse

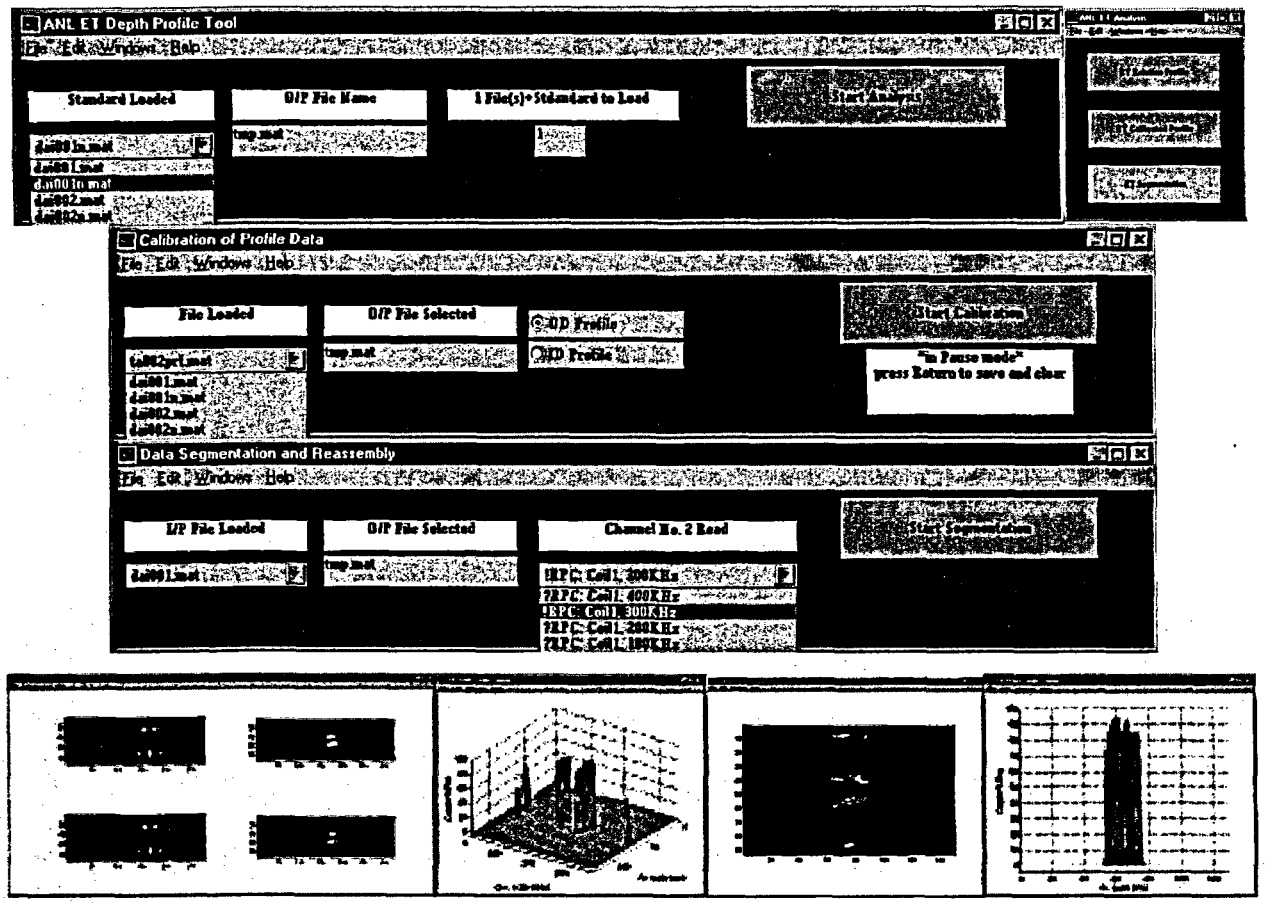

Figure 3.12. Series of MATLAB–based GUI tools (top four rows) for computer-aided analysis of EC inspection results acquired with standard commercial instruments. Also shown (bottom two rows) are several graphical display formats such as image, terrain, and cross–sectional NDE profiles of tube test section at various stages of analysis.

response (FIR) filters. Filter characteristics are determined from the data sampling rate and the frequency content of noise. The FIR filters used to serve the same purpose are briefly described below.

Frequency domain bandpass FIR filters are nonrecursive filters that offer certain advantages and limitations over recursive infinite–duration impulse response (IIR) filters. The primary advantages are their linear phase, stability, finite–duration transients, and efficiency of implementation. FIR filters are always stable, but require longer sequences to meet the same requirements as their IIR counterparts. This latter property, a direct consequence of their simpler transfer function, often translates into more computation time for nonrecursive filters. As with all frequency–domain filters, when conditions are not ideal, the increase in S/N ratio gained by the filtering process is always accompanied by some degree of perturbation of the amplitude and phase of the original signal.

The time–domain difference equation for a linear filter with input sequence $x(k)$ and output sequence $y(n)$ could be written in a general form as

$$y(n) = \sum_{k=0}^{M} b(k)\,x(n-k) + \sum_{k=1}^{N} a(k)\,y(n-k), \tag{3.4}$$

in which the coefficients a and b define the filter response. The transfer function of the IIR filter in z domain, which is the z-transform of the time-domain difference Eq. 3.4, can be described by

$$H(z) = \frac{Y(z)}{X(z)} = \frac{\sum_{k=0}^{M} b(k)z^{-k}}{a_0 + \sum_{k=1}^{N} a(k)z^{-k}}, \tag{3.5}$$

where $a_0 = 1$ for the case of a FIR filter, and the summation in the denominator of Eq. 3.5 vanishes. The difference between the two filtering types can be seen by examining the filter frequency response, which is a rational function in z^{-1} for an IIR filter and represents a discrete Fourier transform for an FIR filter. Regardless of filter type, unless the data sequence in the Fourier domain is composed of sinusoidal components of the desired signal and noise that are well separated, the amplitude and phase of the filtered signal will always experience perturbation with respect to those of the original signal. This is of particular concern in the case of EC signals in which the frequency content of the entire data sequence is often closely spaced and thus requires very sharp (high-order) filters to separate real signals from background fluctuations. Filters for EC signal conditioning often require a sharper transient and, consequently, a larger number of coefficients, because much of the useful information from the Fourier domain spectrum is at the low-frequency end. Studies so far have suggested that frequency domain filters are generally more suitable for improving detection probability. Phase angle perturbations that are a result of filter application can often lead to more complex impedance-plane trajectories, which may complicate conventional data analysis procedures.

3.3.3.2 Signal Enhancement and Restoration

Two basic approaches for improving data quality are the signal enhancement and signal restoration methods. Signal enhancement refines the quality of data without requiring knowledge of the degradation phenomenon. Signal restoration, on the other hand, is founded on the assumption that the degradation source is well understood so that an inverse process could be implemented to recover the true response. The principal objective in both cases is to treat the data so that the result is more suited for a specific application than the original data. Although the two approaches are clearly differentiated in most standard data restoration applications, distinction between the two becomes less apparent in practical applications associated with the EC testing of SG tubing. This is because of the difficulty in accurately modeling the underlying degradation phenomenon, which arises from the combined influence of many factors, and because of the blurring effect of the coil impulse response. Both data enhancement and approximate restoration schemes have been incorporated into the multiparameter data analysis algorithm. Comparable results can be achieved by the two techniques for the processing of EC rotating probe data. Signal restoration, referred to here as approximate deconvolution or inverse filtering, is implemented in the frequency domain, while

signal enhancement is implemented directly in the original spatial domain. Although deconvolution-based methods are generally expected to produce more accurate results, they are also computationally more intensive.

Deconvolution techniques are used in a wide range of signal processing applications, primarily to recover signals distorted by the sensing environment. In EC inspection applications, pseudoinverse filters could be effective for enhancement of spatial resolution that is degraded by the finite spread of the coil-induced field. Better separation of flaw indications from extraneous signals could, in turn, improve the estimation of flaw depth determined from the phase-angle information of multifrequency data. Frequency-dependent signal restoration could also help reduce differences in probe response at different frequencies. This could be particularly beneficial for multifrequency mixing techniques in which the differences in the coil impulse response at the base and auxiliary frequencies could significantly contribute to the level of mix residuals.

Data enhancement and restoration techniques in application to EC signals are limited because the flow of current in a conducting medium is governed by a diffusion-type equation. Distortion is not simply a modulation of signal amplitude. Instead, the wave form could undergo a complete alteration of structure that is not linearly dependent on its original form. Another factor that could significantly influence the degree to which a signal can be recovered is the lack of separation between the spectral content of flaw indications and extraneous signals. Internal/external artifacts and design discontinuities (conducting and magnetic deposits, tube dimensional variations, external support structures, etc.) can produce signal trajectories with spectral components that are close to those from flaw indications. Furthermore, practical sampling rates that are typically used for acquisition of ISI data with rotating probes do not yield the continuous smooth signals that are essential for optimal restoration by inverse-filtering schemes. Finally, it is important to note that physically realizable optimal inverse filters are often unstable. For this reason, approximate deconvolution algorithms may provide the best alternative for real-time restoration of EC flaw signals for practical ISI applications.

Signal Enhancement– When the exact form of the degradation process can only be approximated, signal enhancement techniques are often the first choice for the treatment of data. Because such techniques can be implemented directly in the original domain, they are computationally efficient. Data enhancement is achieved by applying pre-stored kernels to the EC C-scan data. Both smoothing and peak restoration are attained in this manner. The kernels, in effect, perform least-squares polynomial fitting of the data. Because of the availability of information around any center pixel, a symmetric convolution process is applied. Test case results on signal restoration by 2-D kernels are shown in the following discussion.

Signal Restoration– Degradation of the probe's spatial resolution in two dimensions could, in general, be described by a discrete convolution model. With prior knowledge of the distortion model, the original signal may then be recovered through deconvolution, either directly by polynomial division in the spatial domain, or by transformation into the frequency domain.

Test Case Results on Signal Restoration for Machined Specimens– Preliminary evaluation of the 2-D deconvolution scheme that is integrated into the multiparameter data analysis algorithm was carried out by using a subset of laser-cut notch specimens. The geometry of all

the available laser–cut specimens and associated flaw dimensions is discussed in detail in Ref. 16.

Figures 3.13 and 3.14 display the results of inverse filtering on two samples from the subset of laser–cut tubes with one or both types of 2–D Lorentzian kernels. In all cases, the restored data show improved spatial resolution and reduction of the baseline level. It is important to note that the primary objective of the proposed deconvolution scheme as a preprocessing tool for multiparameter analysis of EC inspection results is to maximize the separation between crack–like indications and extraneous signals with minimum loss of information from the original data. For all test cases shown here, the results also indicate less ambiguity in the measurement of the phase angle of restored indications in comparison to those from the original readings. A more detailed description of analyses of EC inspection results using bobbin and +Point™ probes, as well as multiparameter data analysis, was provided in our earlier report [16].

Test Case Results on Signal Restoration for Laboratory–Grown SCC Specimens– Eddy current readings on a collection of 22.2–mm (0.875–in.)–diameter Alloy 600 tubes with laboratory–produced cracking were analyzed with the multiparameter data analysis scheme described in this report. Flaws in this small set of six samples consisted primarily of OD axial cracking and circumferential cracking in the free-span and roll–transition regions, respectively, plus a single specimen with axial ID cracking at a dented TSP region. Multiple–frequency NDE data used in this study were acquired with a standard three–coil rotating probe containing a 2.92–mm (0.115–in.) pancake, a mid–range +Point, and 2.03–mm (0.080–in.) high–frequency pancake coil. The primary pancake coil readings were utilized for analyses. The calibration standard contained 18 EDM notches of axial and circumferential orientation originating from the OD and ID of the tube and ranging in depth from 20% to 100% TW. All notches were 6.35 mm (0.25 in.) in length. Data analysis results are presented as an isometric display of the relative depth for the flawed region of the tube. Estimated flaw sizes are shown both with and without signal restoration by inverse filtering.

Figure 3.15 shows the results of analyses for an axial ODSCC with estimated maximum depth of ≈80% TW. Comparison of the restored sizing data in Fig. 3.15(b) with that in Fig. 3.15(a) suggests the crack to be composed of a series of axial segments with the one segment being nearly separated from the rest. Similar results are shown in Fig. 3.16 for another specimen with an axial ODSCC flaw. Terrain plots of the relative depth, however, suggest the orientation of the crack to be approximately at 45° with respect to the tube axis. Maximum flaw depth in this case was estimated to be ≈ 80% TW.

Processed data from other examples [16] clearly indicate complete suppression of the roll transition, which is the dominant signal feature in the amplitude trace. The terrain plots of the restored data in one case suggested two circumferential cracks, both composed of multiple segments. The results of analysis for an ID axial crack in a dented region at the TSP intersection were also provided. In this case, a terrain plot of the defected segment was constructed from the estimated ID flaw size. Some improvement of spatial resolution followed signal restoration. Once again, suppression of the TSP and dent signals was clearly evident in both cases [16].

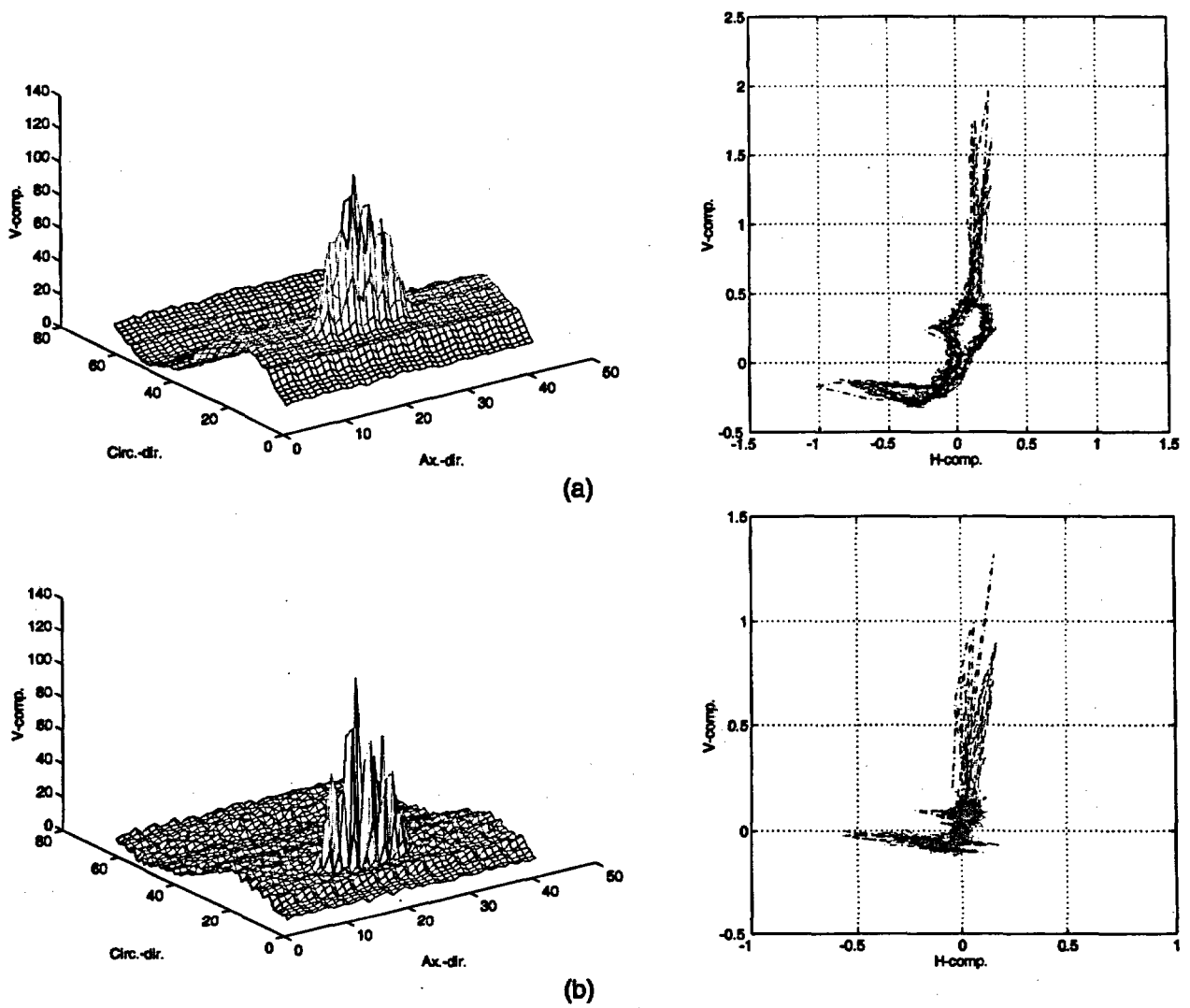

Figure 3.13. (a) Original and (b) restored signal for Type–3 laser–cut specimen #5528–3–3 with nominal OD flaw depth of 40% TW. NDE maximum depth estimates were 42% by bobbin coil (phase–angle) and 61% by multiparameter analysis of RPC (2.92–mm [0.115–in.] pancake) data.

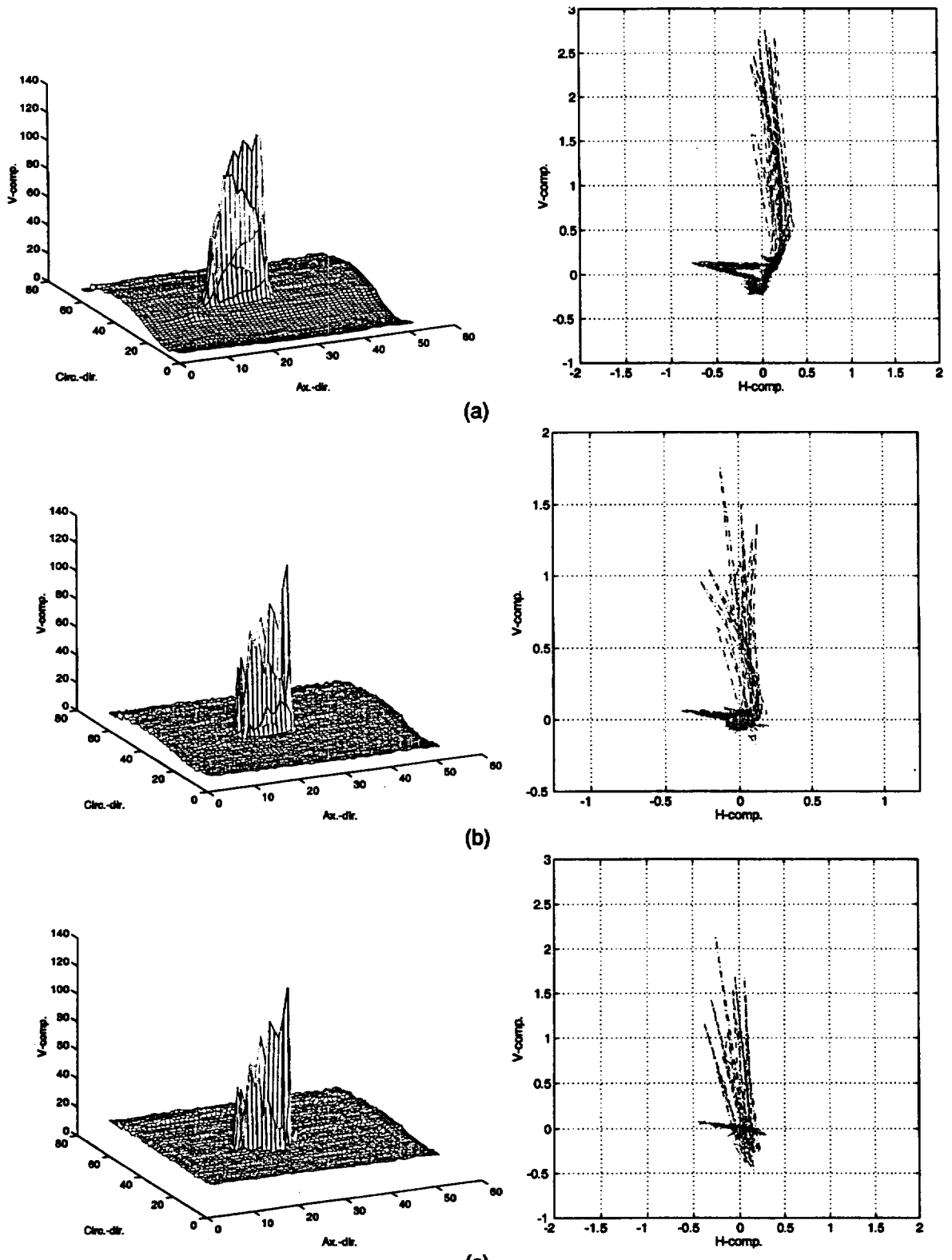

Figure 3.14. (a) Original and (b)–(c) restored signals with 2–D Lorentzian kernels for Type–4 laser–cut specimen #5469–2–1 with nominal OD flaw depth of 80% TW. NDE maximum depth estimates were 45% by bobbin coil (phase–angle) and 74% by multiparameter analysis of RPC (2.92–mm [0.115–in.] pancake) data.

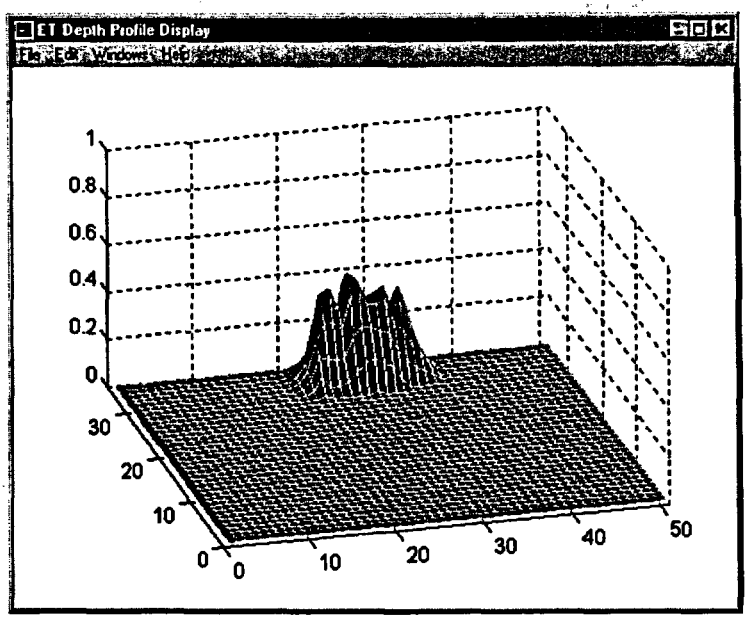

(a)

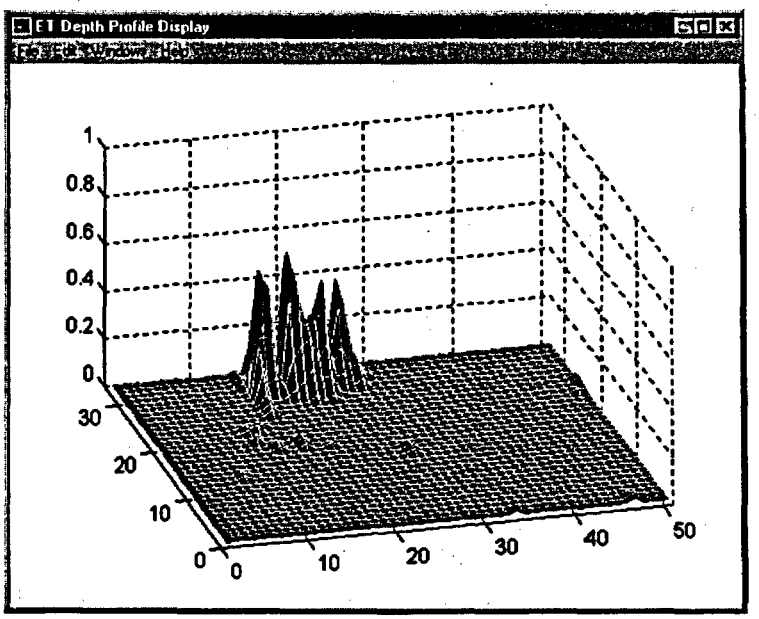

(b)

Figure 3.15. Data analysis results for laboratory-grown specimen with longitudinal ODSCC showing (a) terrain plot of relative OD depth for cracked zone and (b) restored data by inverse filtering. Maximum crack depth is estimated to be ≈80% TW. Isometric display of results shows finer details in restored data.

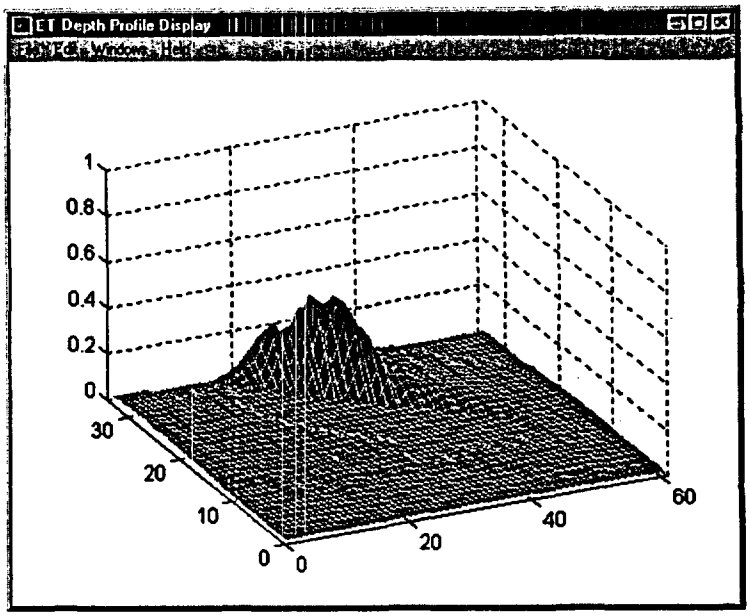

(a)

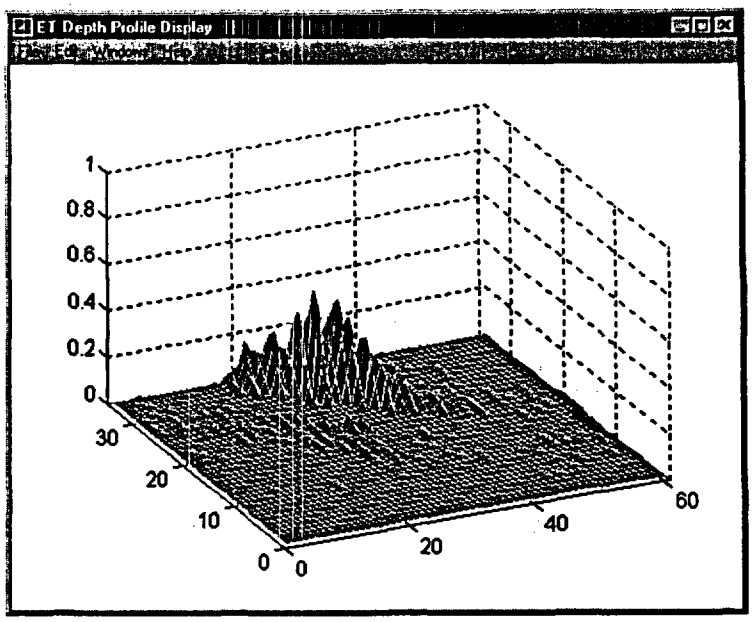

(b)

Figure 3.16. Data analysis results for laboratory-grown specimen with skewed ODSCC showing (a) terrain plot of relative OD depth for cracked zone and (b) restored data by inverse filtering. Maximum crack depth is estimated to be ≈80% TW. Isometric display of results shows finer details in restored data.

3.3.4 Multiparameter Data Analysis

Multivariate data analysis algorithms serve as the foundation for various operations in the processing of EC data. Three algorithms were investigated in this program and have been adapted for use in various areas of research associated with the EC testing of SG tubing. They consist of multiple linear regression (MLR), principal component regression (PCR), and partial least squares (PLS) techniques. Conventional least-squares-based regression has been used primarily in standard artifact suppression schemes, commonly referred to as mixing algorithms. The more versatile PLS algorithm has been used in a wider range of applications, including more sophisticated suppression schemes and predictive models.

3.3.4.1 Least Squares Regression and Factor-Based Techniques

Multivariate analysis techniques are often utilized to explore unknown trends in large quantities of data. The two basic stages in such analyses are generally referred to as calibration and prediction. In the calibration stage, a data matrix is constructed from the probe response at various time or frequency slots for a given set of calibration samples. The calibration phase produces a model that relates the probe response to known values of the parameters to be estimated. In the prediction stage, the matrix of coefficients and weights that describes the system response (input-output relationships) is used to estimate the parameters of interest in new measurement test sets. Having the response matrix [X] and the parameter matrix [Y], MLR develops a linear combination of variables in [X] that minimizes the errors in reproducing [Y]. This is accomplished by constructing a relationship between [X] and [Y] such that

$$[Y] = [X][\beta] + [E], \tag{3.6}$$

where $[\beta]$ is the matrix of regression coefficients, and $[E]$ is the matrix of errors associated with the MLR model. The matrix $[\beta]$ is found by linear regression to minimize the difference between the true and estimated elements of the parameter matrix in a least-squares sense as

$$[E] = \sum_{n=1}^{N}\sum_{m=1}^{M}(y_{mn} - \hat{y}_{mn})^2 = \sum_{n=1}^{N}\sum_{m=1}^{M}\varepsilon_{mn}^2 \tag{3.7}$$

MLR attempts to use all of the available information in the independent variable matrix for model construction. Both relevant (signal) and irrelevant (noise) information are weighted equally by this method when input-output relations are constructed. To overcome this limitation, the two factor-based techniques (PCR and PLS) have also been examined. The factors are linear combinations of the original variables. Factor-based models attempt to use a minimal set of factors that best describe the true relationship between the independent and dependent variable matrix. Because factor-based models do not attempt to directly invert the covariance matrix, potential colinearities in data can be accommodated without causing singularities.

PLS was chosen to construct a multivariate regression model for the EC data. For the PLS algorithm, a general model would consist of a regression between the scores of the

relationships for the dependent variable [Y] and independent variable [X]. The outer relationships can be written in matrix form as

$$[X] = [T][P] + [E] = \sum_{n=1}^{N} t_n p_n + [E] \tag{3.8}$$

$$[Y] = [U][Q] + [F] = \sum_{n=1}^{N} u_n q_n + [F], \tag{3.9}$$

with the inner relation defined by

$$\hat{u} = b_n t_n, \tag{3.10}$$

where [T], [U], [P], and [Q] are the eigenvectors and eigenvalue matrices, and [B] is the vector that contains the inner relationships. The principal components are simultaneously calculated for both blocks. The intention is to minimize $\|F\|$ (i.e., *Norm*([F])) and, hence, to construct a useful relationship between [X] and [Y].

3.3.4.2 Multifrequency Mixing Techniques

Processed channel information from multiparameter mixing is commonly utilized in analyzing multifrequency EC inspection data. So-called mixing techniques, originally implemented electronically on analog signals by using rotation, scaling, and subtraction, were devised to enhance detection of EC signals of interest by suppressing the effect of unwanted signals such as background fluctuations and artifacts. Mix frequencies are chosen so as to provide independent information on the signal to be eliminated. Current mix algorithms generally use a linear least squares method in which the output (mix channel) signal is a weighted linear combination of horizontal and vertical components of input signal components at different frequencies. Because independent mix coefficients can be calculated for each signal to be suppressed (often based on simulated artifacts on a calibration standard), in theory an unwanted signal could be eliminated by successive implementation of different sets of mix coefficients. However, except under ideal conditions, the mix signal will always contain residual signals from unwanted artifacts, and the mixing process could affect, to different degrees, both the amplitude and phase of the signal from defects of interest.

Direct (independent) and indirect (dependent) mixing algorithms have been examined for suppressing multiple unwanted indications from composite signals. In an indirect mix, regression coefficients are determined by using a data segment from a simulated artifact such as a TSP ring on a reference standard tube, which is expected to closely resemble those present in the actual SGs. The aim of the regression model is to best reproduce the primary/base frequency signal by combining signal components from auxiliary frequency channel(s). This is the conventional approach used for the analysis of EC ISI results. Alternatively, independent mix procedures have the potential to suppress unwanted signals by using multiple-frequency readings on the same tube. This approach, primarily suggested for suppression of dominant signal features, is of particular interest when tube standards with simulated artifacts that resemble field-induced signals are not readily available.

Various two- and three-frequency regression fits have been investigated. Preliminary results indicated that two-frequency mixes are generally more consistent, so the approach was to sequentially apply two-frequency mixes for suppression of two unwanted indications at the same axial location. To improve the mix outcome, several modifications were made to our standard mix algorithm. These consisted of energy-scaling each trace, resampling in the frequency domain, and phase-angle referencing. Frequency resampling was done to increase the number of available independent variables. Phase-angle tracking was done to help reduce phase ambiguity from multiple application of linear regression coefficients. Based on cases tested so far, the amplitude renormalization consistently exhibited improved quality of mix outputs. This finding is believed to be a result of the weighting introduced by the energy-scaling process.

3.3.4.3 2-D Suppression of Unwanted Signals

Multifrequency mix procedures that involve combining the information from a primary/base frequency and one or two auxiliary frequency channels have been fairly effective for the processing of bobbin coil readings. However, mix algorithms developed for 1-d bobbin coil signals are not as effective for the processing of higher-resolution rotating-probe inspection results. Unlike the situation for the bobbin coil, mixes for rotating-probe C-scan data are quite subtle and routinely fail to produce consistent outcomes. Also, when mix coefficients are applied to the entire signal trace, significant distortion of both the amplitude and phase-angle information of the original readings could result. To improve rotating-probe mixes, specially designed simulated TSP rings (e.g., a 270° ring as opposed to an axisymmetric 360° ring used for bobbin mixes) are often utilized. Nevertheless, the mix results could vary substantially, depending on the selected portion of signal for the calculation of mix coefficients. For this reason, mix channel information is not currently used for reporting rotating-probe inspection results.

Potential alternatives to 1-D conventional mix procedures for RPC data have been evaluated. Two approaches based on 2-D factor analysis techniques were considered. Both methods utilize spectral decomposition, also referred to as singular value decomposition (SVD) or outer product expansion. However, they differ significantly in their analysis of factors. The first method is based on a standard decomposition at a single frequency and subsequent selection of appropriate coefficients. The second method uses a least-squares (LS) regression approach with two frequencies.

Spectral decomposition methods serve as the fundamental numerical technique in a wide range of applications from solution of a linear system of equations to problems in signal and image processing such as restoration, compression, denoising, pattern recognition, and feature extraction. Such transformation algorithms basically attempt to decompose an often ill-conditioned data matrix to an outer product expansion of left- and right-hand unitary matrices of orthonormal eigenvectors with a matrix of pseudo-eigenvalues. With the underlying assumption that the basis functions that span the signal and noise subspaces are orthogonal, this mapping should then provide improved separation of relevant signal features from inconsequential trends. Following the decomposition, selection of appropriate factors allows for the preservation of relevant signal features and, in effect, elimination of background noise.

In practice, selection of appropriate factors often poses the greatest challenge when spectral decomposition alone is used. This is particularly true for the EC inspection results with rotating probes because flaw and artifacts at one frequency are often described by common factors. As a result, it is not always possible to select a set of factors that reasonably separate consequential indications from artifacts and background fluctuations. Therefore, factors cannot be applied blindly, and some form of discretion is necessary in deciding which factors to keep. For this reason, the method of multiple-frequency LS-based factor analysis provides a more robust and systematic approach to suppression of unwanted signals in rotating-probe data.

Single-frequency spectral decomposition and a two-frequency decomposition with LS-based regression were initially tested on simulated composite signals from RPC readings on a 22.2-mm (7/8-in.)-OD tube standard with machined notches and a 270° support plate slip ring. Various combinations of OD and ID notches within the TSP region were produced by vectorial addition of data segments at various frequencies with notches with the TSP data segment. The nonaxisymmetric geometry of the TSP ring used here poses a greater challenge to any signal suppression scheme than do axisymmetric drilled support plates. However, it is expected that such nonuniform and overwhelming EC indications could be encountered in the field from external structures such as broached support plates.

Suppression of TSP indications at a single frequency by using a standard SVD algorithm did not produce acceptable results. In several test cases it was impossible to achieve a reasonable degree of suppression of TSP indications without substantial degradation of the flaw signal. The method of two-frequency LS-based factor analysis was able to suppress TSP indications with acceptable degradation of flaw signals. Figures 3.17 and 3.18 show results for two test cases. In both cases, single and multiple flaws that were arbitrarily placed within the TSP region were recovered with a high level of suppression of TSP indications. Selection of primary and auxiliary frequencies for 2-D suppression is analogous to that used by standard 1-D mix procedures. As with conventional 1-D mix procedures, multiple unwanted indications could be suppressed by successive application of this method.

3.3.4.4 Multivariate Analysis for Estimation of NDE Profile

Multivariate analysis is also used in the final stage of data analysis for estimation of the flaw depth. Phase-angle information from multiple channels is used to construct a model that correlates the NDE results to flaw size and origin. The flaw size and origin are assumed to be related to the phase-angle information at the different frequencies. Eddy current measurements on a calibration standard tube are used to determine the regression coefficients in the relation.

The reliability of a predictive correlation depends heavily on the data used to construct that model. Both the range and composition of data play crucial roles. With regard to the analysis of EC data, this means the adequacy of the results is strongly dependent on the range of flaw size, type, and origin in the calibration standard tube. Sizing accuracy is also strongly dependent on the availability of multiple frequency data. A minimum of two frequencies is required for a two-parameter model, but our work has shown that three frequencies generally produce more consistent results. Although incorporation of a larger number of channels is theoretically feasible and desirable, acquiring rotating probe data at a greater number of frequencies is generally prohibitive for practical ISI applications.

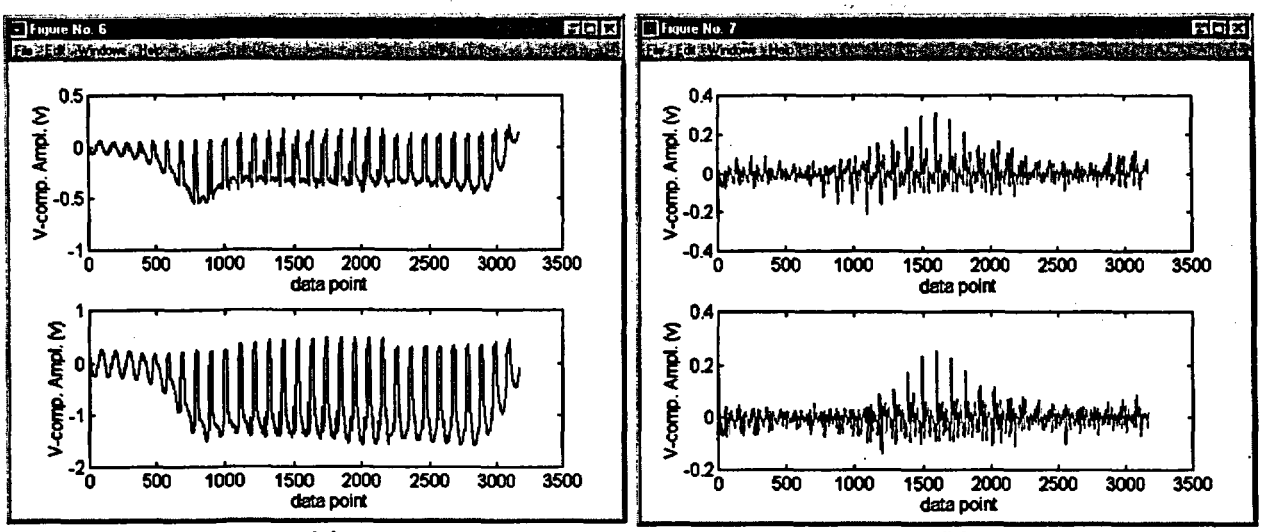

(a) (b)

Figure 3.17. Demonstration of 2–D signal suppression on RPC traces of (a) simulated raw data at 400 kHz (top) and 200 kHz (bottom) frequencies composed of a 40% TW axial OD notch at an arbitrarily selected location within a 270° tube support ring and (b) processed data using 400 kHz primary and 200 kHz auxiliary frequency (top) and 300 kHz primary and 100 kHz auxiliary frequency (bottom). In both cases, the processed data indicate substantial improvement of S/N ratio over original readings.

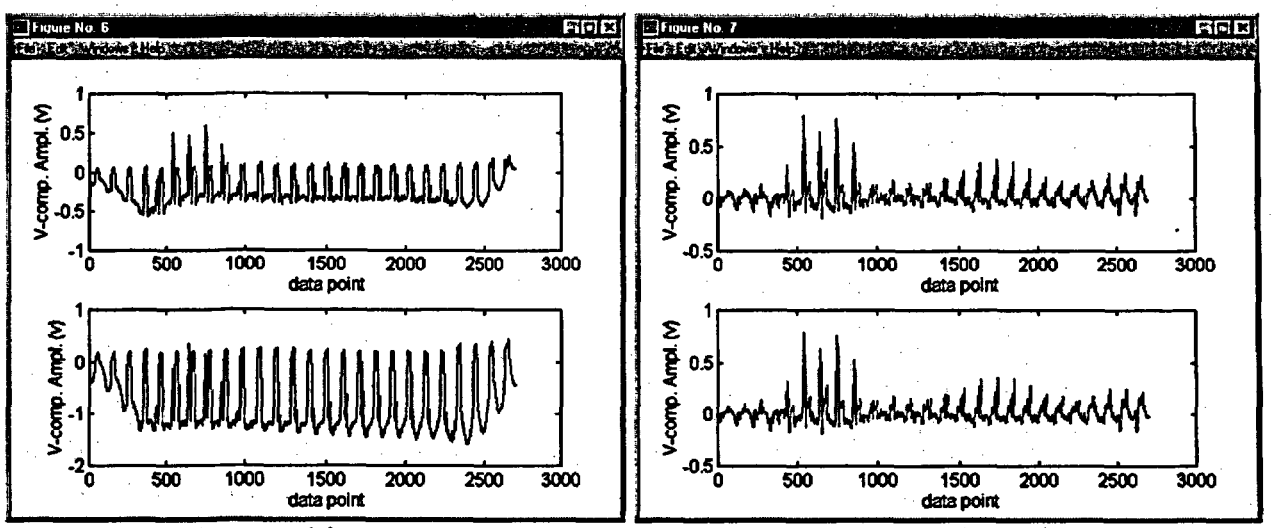

(a) (b)

Figure 3.18. Demonstration of 2–D signal suppression on RPC traces of (a) simulated raw data at 400 kHz (top) and 200 kHz (bottom) frequencies composed of a 40% TW axial OD and 40% TW circumferential ID notch at arbitrarily selected locations within a 270° tube support ring and (b) processed data using 400 kHz primary and 200 kHz auxiliary frequency (top) and 300 kHz primary and 100 kHz auxiliary frequency (bottom). In both cases, the processed data indicate substantial improvement of S/N ratio over the original data.

3.3.5 Rule-based Flaw Identification

In conventional EC data analysis of SG tubing, human analysts are trained to differentiate flaw-induced signals from artifacts by analysis of the behavior of signals, typically extracted from their impedance plane trajectory and signal amplitude, through application of a series of rules. For example, clockwise (CW) and counter-clockwise (CCW) rotation of the impedance plane signal trajectory is commonly used to determine the flaw origin. When the phase angles at all frequencies from a TW flaw are set to a fixed value, indications of OD origin exhibit CCW rotations, and those of ID origin have smaller CW rotations. In addition to such well-defined rules for interpretation of signal behavior developed from a fundamental understanding of the effect of flaws on EC signals, empirical rules based on past experience and historical lessons learned in dealing with similar SG units are also used.

Analogous to the manual analysis of EC inspection data, computer-aided data analysis algorithms can be developed based on analysis of characteristic behavior of EC signals as a function of frequency. Because all available information can be examined rather than a selected subset in the case of a manual analysis, such algorithms allow more effective identification of subtle forms of degradation. Computer-based algorithms that imitate some form of the human decision-making process are generally labeled as expert systems.

The automated identification of flaws and their origin through application of a series of rules is shown in block 4 of Fig. 3.10. The rules are coded as a series of conditional statements (i.e., IF-THEN) that are sequentially applied to the data. Calculation of S/N from the earlier stages of the data analysis is used to set a threshold for sorting of signals that are to be examined. Combined amplitude and phase-based rules are used to better discriminate between potential flaws and noise. The rules are set to be generally conservative for identification of flawed regions of the tube. As a tradeoff between conservatism and sensitivity, they can be adjusted to some degree based on the S/N value for a particular test section. The current set of rules is valid for a specific coil configuration and range of frequency.

3.3.6 Data Quality

Because eddy current testing is a comparative NDE method, success is highly dependent on the consistency of data acquisition parameters and proper calibration results. Although the quality of data affects both detection and sizing, this issue is of particular concern when quantitative estimates of flaw size are needed. Minimum requirements for acceptable data acquisition parameters are documented in various EPRI examination technique specification sheets and NRC generic letters for ISI of SG tubing. These guidelines generally define the instrumentation setup (coil excitation frequencies, gain setting, cable length, sampling rate, probe speed, etc.) and calibration procedures to achieve a certain probability of detection (POD) for a given probe (e.g., bobbin, rotating, and array probes). These techniques have been primarily aimed at ensuring attainment of an acceptable POD. The requirements on data quality, for example, in connection with the use of rotating probes for estimation of flaw size are less well defined. Industry is attempting to define a suitable set of parameters that could be used to judge data quality. One such parameter is the S/N for a particular section of SG tubing. Because initial detection of potential flaw signals during manual analysis of EC data is based on visual identification, defining a particular value or range of values for the S/N may be appropriate for manual analysis for the purpose of detection. However, data quality that may be appropriate for detection may not be adequate for reliable estimation of the flaw size.

For instance, degradation of S/N arising from baseline fluctuations and semiperiodic signals from tube deformations that could significantly reduce visual flaw identification can be generally dealt with by numerical processing of data. On the other hand, degradation of S/N in the form of acquisition-related corruption of data and insufficient sampling rate that may not substantially affect detection may significantly influence the sizing results. Recovery of signal peaks in a digitized data stream is governed by the Nyquist sampling rate. The relationship between sample interval Δx and maximum observable frequency f_{max} according to the Nyquist theorem is given by

$$f_{max} = \frac{1}{2\Delta x} \tag{3.11}$$

For rotating probes, sufficient sampling rates should be acquired in both axial and circumferential directions in accordance with the rotational and push/pull speed of the probe. Although lack of sampling can be remedied to some degree through interpolation of the data, significant undersampling will always result in loss of information.

3.4 Multiparameter Data Analysis Results

The effectiveness of the multiparameter algorithms for the computer-aided analysis of EC NDE data has been evaluated in studies on EDM notches, laboratory-grown flaws, and in-service flaws. Additional examples are found in Ref. [16]. A more detailed description of sizing results is provided in Section 3.4.2.

3.4.1 Graphical Display of Multiparameter Analysis of NDE Data

Figures 3.19 and 3.20 compare conventional data displays, e.g., Eddynet™ isometric plots, with the graphical displays generated by multiparameter analysis to demonstrate enhancement in spatial resolution provided by the analysis. The multiple-frequency EC data were acquired with a standard three-coil rotating probe that incorporates a 2.92-mm (0.115-in.) pancake, a mid-range +Point™, and 2.03-mm (0.080-in.) high-frequency pancake coil. The isometric plots are amplitude responses from the +Point coil at a single channel. The processed results are estimated depth profiles obtained by analysis of multifrequency data from the mid-range pancake coil. Comparison of estimated profiles with destructive results also shows improved sizing accuracy by the multiparameter analysis [16]. For the test cases shown here, conventional analysis of original data generally resulted in underestimates of the maximum depth.

Figure 3.21 displays the multiparameter analysis results for laboratory-grown circumferential ODSCC. The analysis results indicate the presence of multiple circumferential cracks with maximum depths exceeding 60% TW. Figure 3.21(a) shows the flaw image at different stages of the process. Figure 3.21(b) shows a terrain plot of the estimated flaw depth from an arbitrarily chosen azimuth and elevation angle. Figure 3.21(c) and (d) show axial and circumferential projections of the flaws.

Figure 3.22 shows similar results for a specimen with a single axial ODSCC. Figure 3.23 shows another example with two deep axial cracks. The dominant indications are two parallel axial cracks with maximum depths estimated to be ≈90% TW.

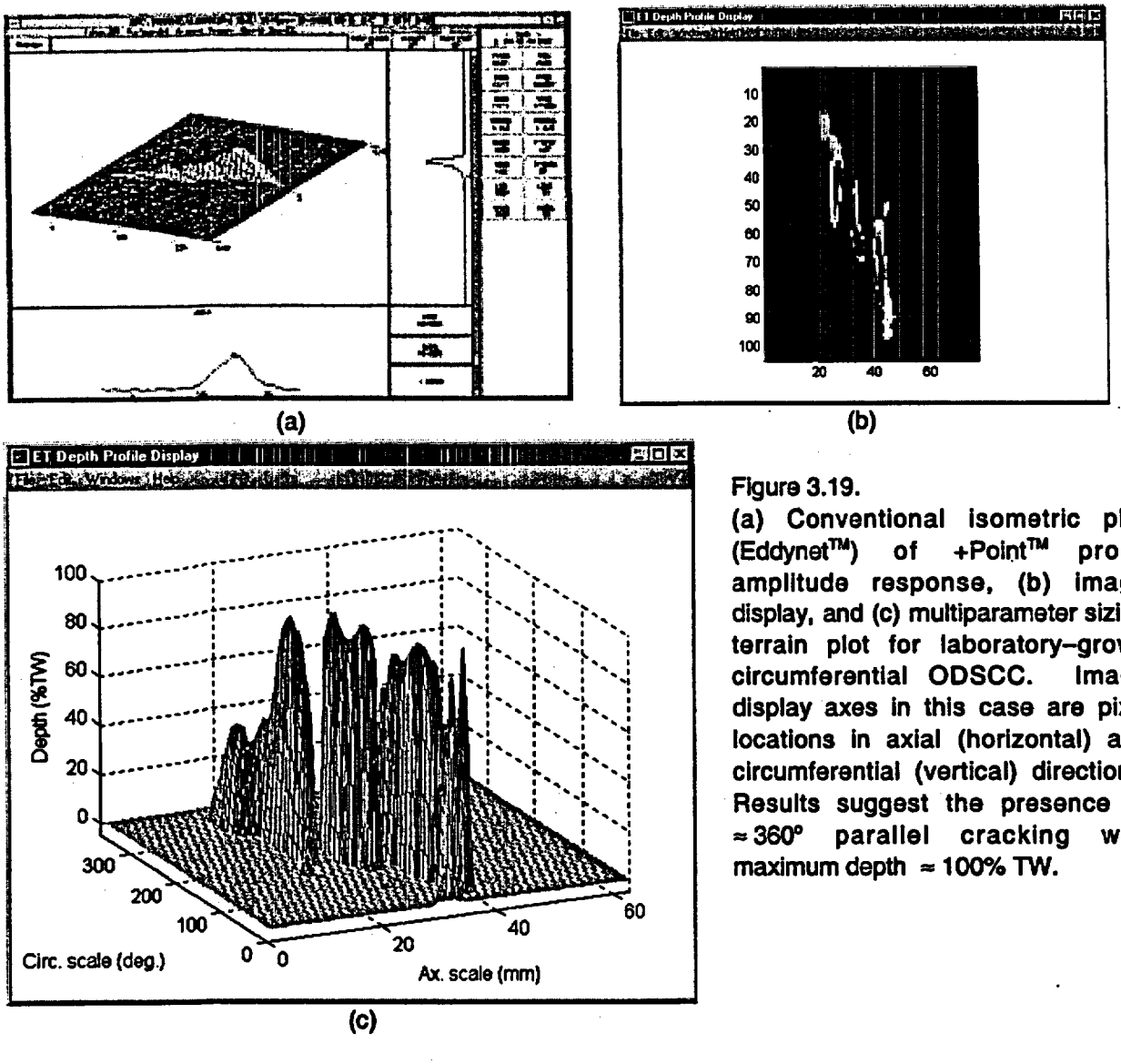

Figure 3.19.
(a) Conventional isometric plot (Eddynet™) of +Point™ probe amplitude response, (b) image display, and (c) multiparameter sizing terrain plot for laboratory-grown circumferential ODSCC. Image display axes in this case are pixel locations in axial (horizontal) and circumferential (vertical) directions. Results suggest the presence of ≈360° parallel cracking with maximum depth ≈ 100% TW.

3.4.2 Assessment of Sizing Accuracy in Presence of Artifacts

In the study to assess the effect of various artifacts on flaw signals, data on laboratory-degraded specimens were collected with and without the removable collars that simulate artifacts such as the TSP, sludge, and magnetite deposits that may be present to various degrees during field inspections. Eddy current data for each test case of a simulated OD artifact were collected separately, each time scanning the entire batch of tubes. Acquisition frequencies represent typical primary and auxiliary channels that are used for the inspection of thin-wall SG tubing. Studies so far suggest that the degree of signal distortion depends primarily on the artifact geometry and composition, as well as signal amplitude at a given excitation frequency. Sizing results for the case of plain tube and TSP simulation are in good agreement. For the data set used in this study, the estimated maximum depth of cracks varied by <10% of tube-wall thickness for all the test cases considered. As expected, the effect of OD simulated collars is less for larger amplitude signals and more significant for the smaller amplitude portions of the flaw.

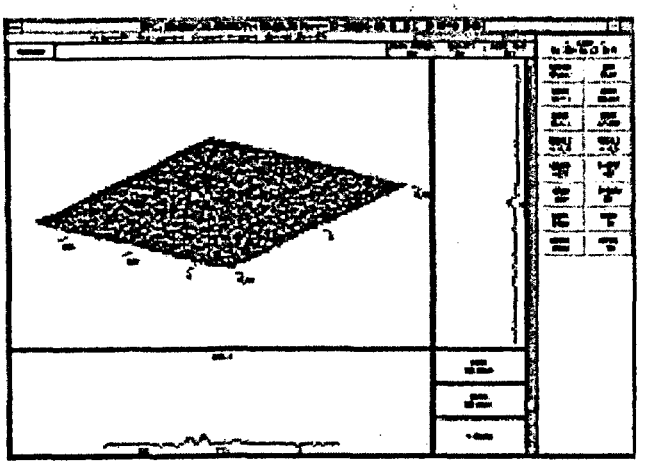

(a)

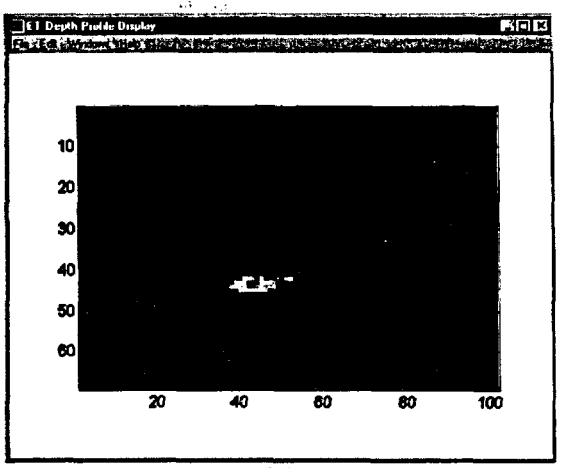

(b)

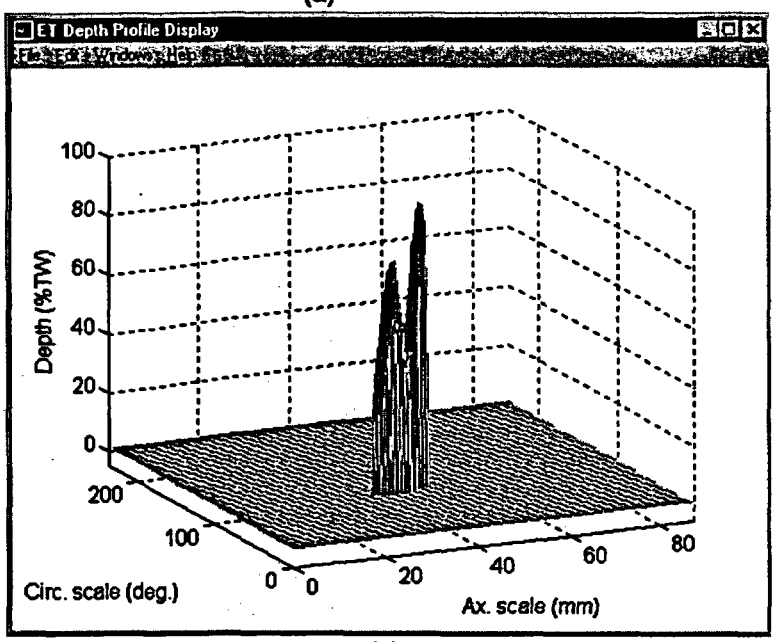

(c)

Figure 3.20.
(a) Conventional isometric plot (Eddynet™) of +Point™ probe amplitude response, (b) image display, and (c) multiparameter sizing terrain plot of same specimen with laboratory-grown axial ODSCC. The image display axes in this case are pixel locations in axial (horizontal) and circumferential (vertical) directions. NDE results suggest the presence of axial cracking with max. depth > 90% TW. Flaw exhibited no bobbin and uncharacteristically low rotating probe amplitude response.

A batch of 31 tubes containing various crack types and sizes has also been utilized to further assess the capability of computer-aided data analysis algorithms. Flawed tubes in this set have been augmented with blank specimens having no visible damage, to better test the techniques. Eddy current readings on these tubes were acquired with and without simulated artifacts such as the TSP, sludge, magnetite, and copper deposits. The effect of tube dimensional variations on detection and sizing of indications is also simulated by producing flaws within the transition zone of mechanically rolled tube sections. Eddy current inspection results from samples show a wide range of complexity in flaw geometries, varying from single axial/circumferential to multiple and mixed-mode cracks. A more detailed description of NDE results on this set is provided in Ref. [16].

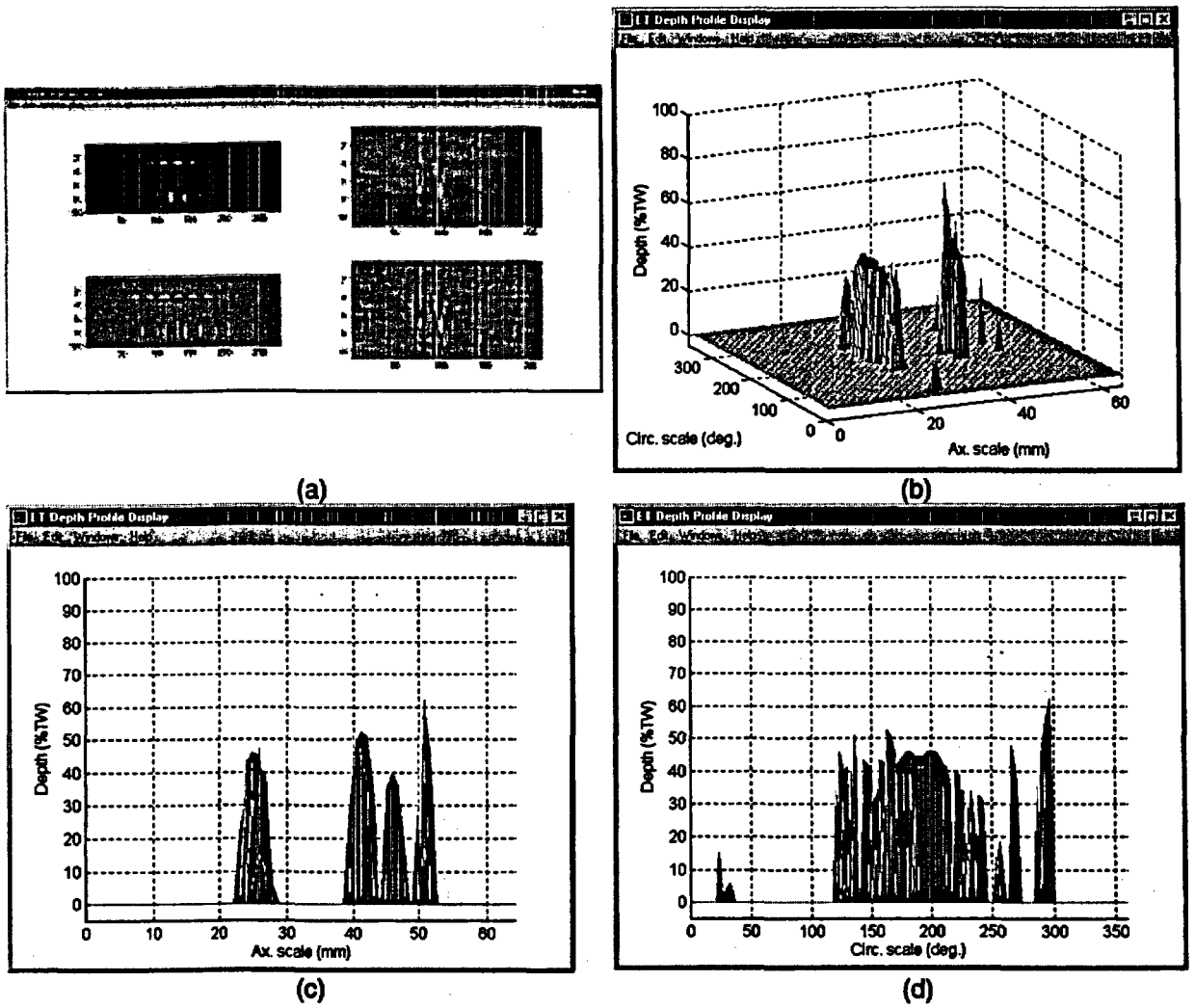

Figure 3.21. Representative display of data analysis results for specimen with laboratory–grown ODSCC degradation showing (a) image display, (b) terrain plot, (c) axial projection, and (d) circumferential projection. Results indicate multiple cracks at several axial locations around circumference, with maximum depth >60% TW.

3.4.4 Analysis of Field–Degraded Tubes

Eddy current data from a set of six pulled tube sections that were removed from a retired McGuire SG were analyzed. Pre– and post–pull inspections identified all flaws as ODSCC at dented TSP intersections. Data were collected with both a bobbin and 3–coil rotating probe containing a mid–range pancake, +Point™, and a high–frequency pancake coil. The tubes were first decontaminated and then were scanned in a glove box with and without a simulated TSP ring. In addition to an ASME standard, an in–line EDM 18–notch standard was used. This standard contains a series of 9.52–mm (0.375–in.)–long notches of axial and circumferential orientation, varying in depth from 20% to 100% TW, originating from both the tube ID and OD. Both bobbin and rotating probe data were acquired with procedures similar to those used during the field inspections. Additional data at intermediate frequencies were also obtained for

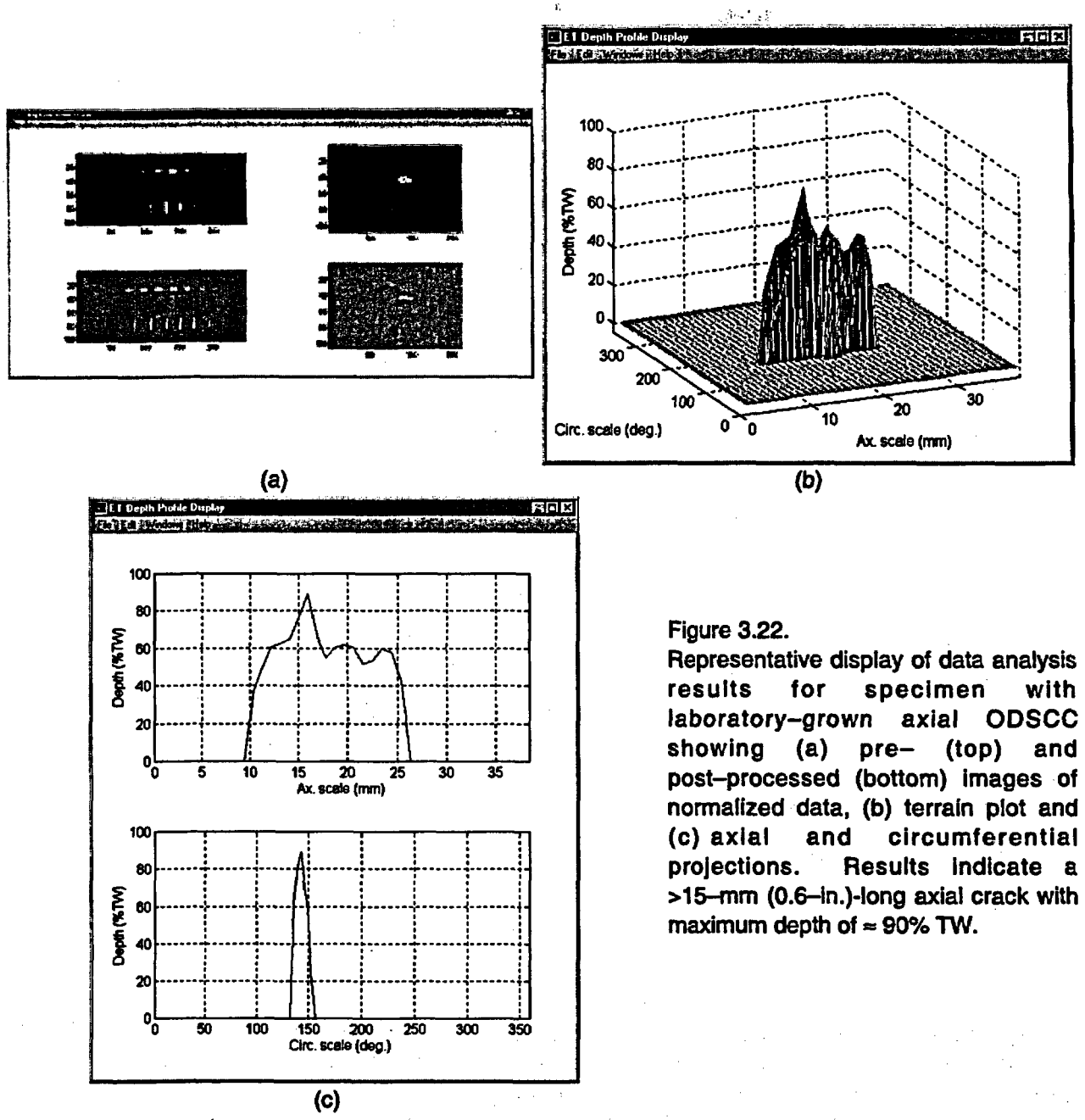

Figure 3.22.
Representative display of data analysis results for specimen with laboratory–grown axial ODSCC showing (a) pre– (top) and post–processed (bottom) images of normalized data, (b) terrain plot and (c) axial and circumferential projections. Results indicate a >15–mm (0.6–in.)-long axial crack with maximum depth of ≈ 90% TW.

further assessments. The multiparameter analysis routines were modified to analyze EC data from 19.0-mm (0.75–in.)–diameter tubing with a nominal wall thickness of 1.09 mm (0.043 in.). The flaw depth and extent were also estimated by conventional analysis of the data using the Eddynet™ software. Initial results from the conventional and multiparameter analyses of the NDE data are discussed here.

Flaw depth estimates by bobbin coil were obtained using the 550/130 kHz mix process channel. Estimates of flaw maximum depth and extent by rotating probe were made using the 300 kHz channel. The probe gain had to be reduced during acquisition to avoid saturation of

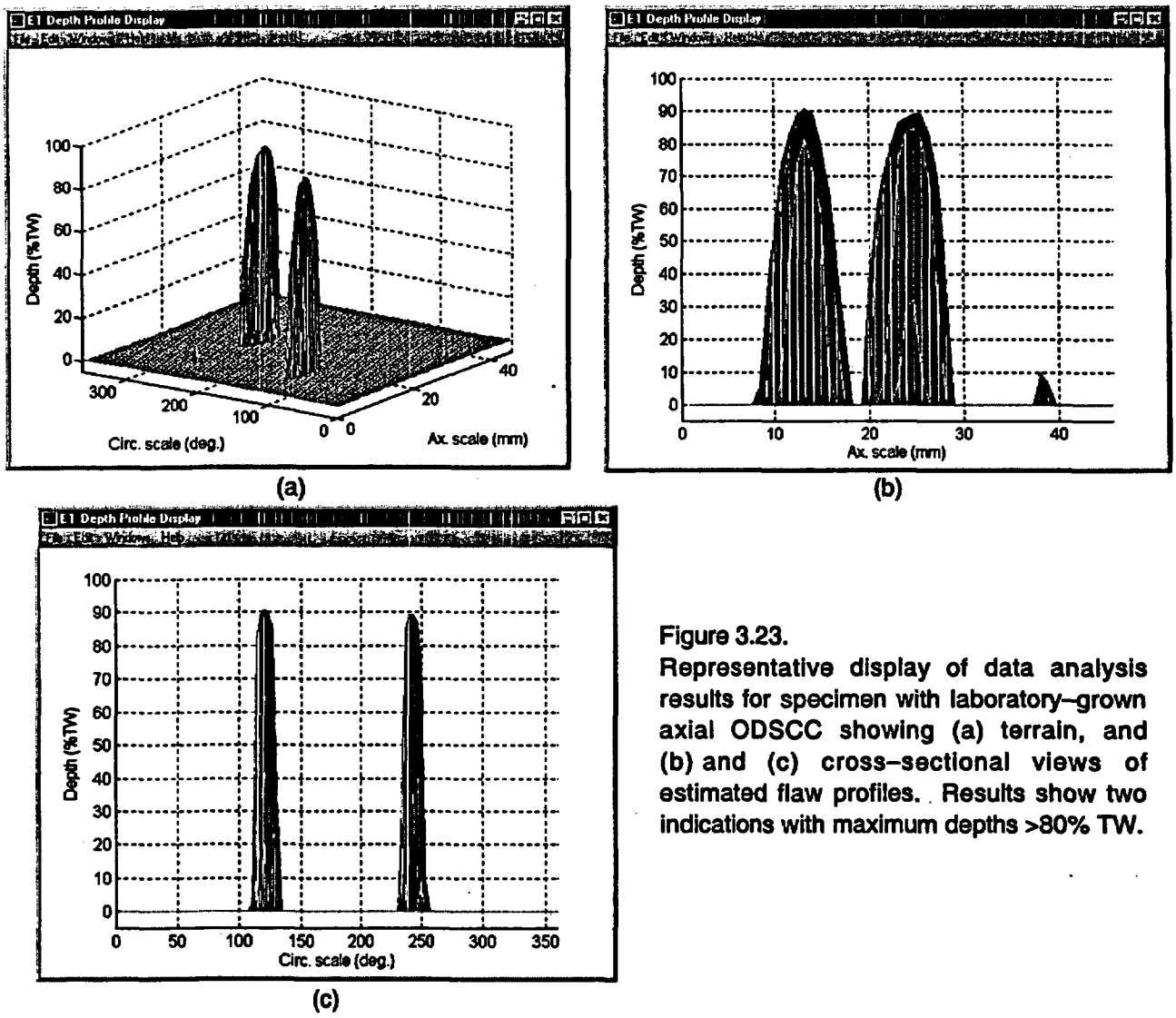

Figure 3.23.
Representative display of data analysis results for specimen with laboratory–grown axial ODSCC showing (a) terrain, and (b) and (c) cross–sectional views of estimated flaw profiles. Results show two indications with maximum depths >80% TW.

the pancake coil signal from 100% TW EDM notches. The noise levels in all the pulled tube test sections were significantly higher (i.e., lower S/N ratio) than in laboratory–produced specimens. The noise was primarily ID–originated. Comparison of the S/N ratios from all coils showed that the +Point™ signal was the least affected by the presence of the noise.

Except for one case, all the flaws detected by the surface–riding coils of the rotating probe were also detected by the bobbin coil. In the one exception (a single test section with no detectable degradation by bobbin coil), the rotating probe indicated a >50% TW flaw where a large signal from a tube deformation appears to have masked the flaw signal for the bobbin coil. In the cases where a flaw was detected by the bobbin coil, no apparent correlation was found between flaw depth and the BC signal magnitude (peak–to–peak voltage), which varied from 0.75 V to >4 V. Maximum flaw depths estimated by +Point™ varied from < 10% TW to < 90% TW, with axial crack lengths from ≈3.5 mm (0.13 in.) to ≈10 mm (0.40 in.). The shortest axial flaw had the largest circumferential extent based on the rotating-probe C–scan display. In tubes without the simulated TSP collar, there was reasonable agreement between bobbin and

rotating probe estimates of maximum crack depth based on phase-angle information for the majority of detectable flaws.

Flaw depth estimates were also obtained by multiparameter analysis of mid-range pancake coil data. The minimum necessary modifications of the algorithms, which have been used to date for 22.2-mm (0.875-in.)-diameter tubing, were made to allow sizing of flaws in 19.05-mm (0.75-in.)-diameter tubing. The rotating probe data were resampled off-line to produce approximately equal digitization rates in axial and circumferential directions. Figures 3.24–3.29 show the data analysis results for all the tube sections examined so far. Terrain plots of flaw size are shown for a small zone around the degraded region of each tube. Except for one case, the maximum depth estimates are generally in agreement (i.e., to within +/–20%) with those from the +Point™ coil. It is more difficult to estimate the flaw sizes in 1.09-mm (0.043-in.)-thick wall tubing than in thicker wall 1.27-mm (0.050-in.) tubing. This effect is due to fundamental limitations that are independent of the coil design and the analysis method. As a direct consequence of the skin depth effect, the same upper and lower frequency limits for thinner wall tubing result in smaller ID–OD phase separation at each frequency as well as a smaller variation of phase angle between the primary and auxiliary frequency channels. This smaller dynamic range, in effect, reduces the sizing accuracy and increases the ambiguity in determination of flaw origin.

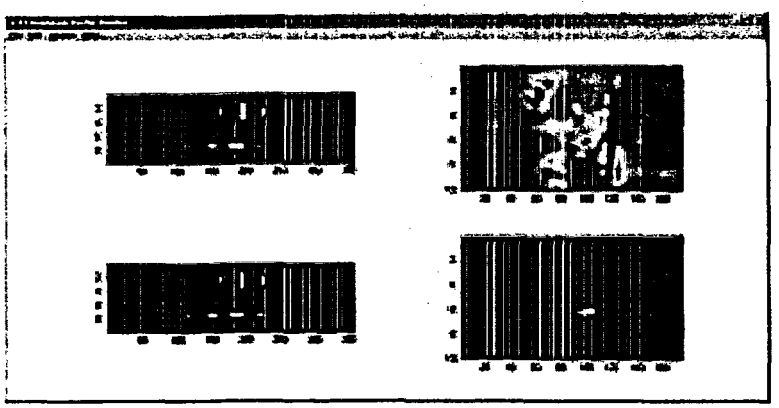

(a)

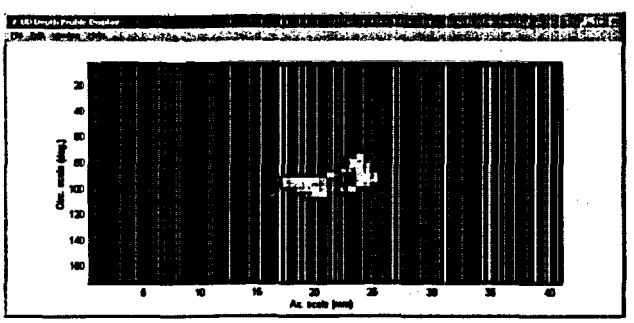

(b)

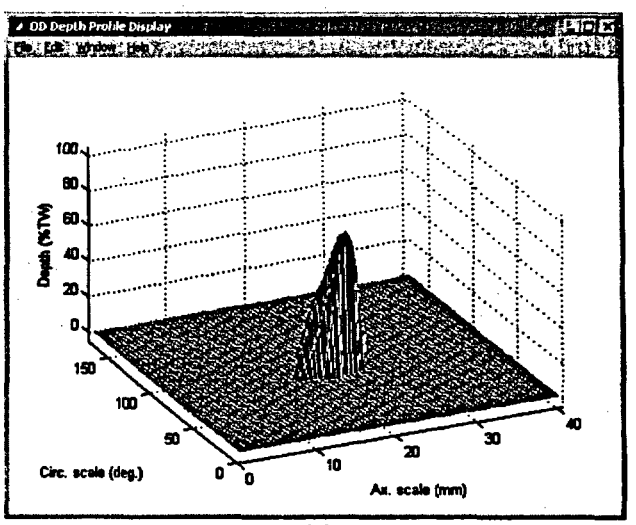

(c)

Figure 3.24.
Data analysis results for McGuire pulled tube section with axial ODSCC degradation at dented TSP intersection. Maximum flaw depth is estimated to be <80% TW. Graphics shows (a) amplitude image display of the standard and flawed tube at different stages of the process, and (b) flaw image, and (c) terrain plot of sizing data.

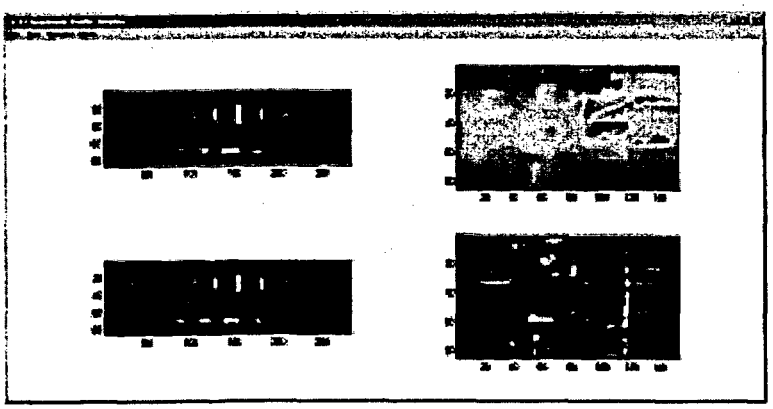

(a)

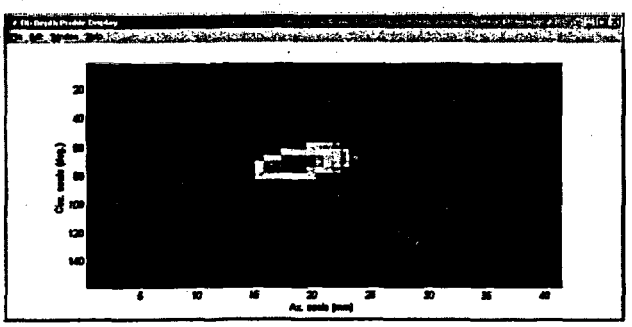

(b)

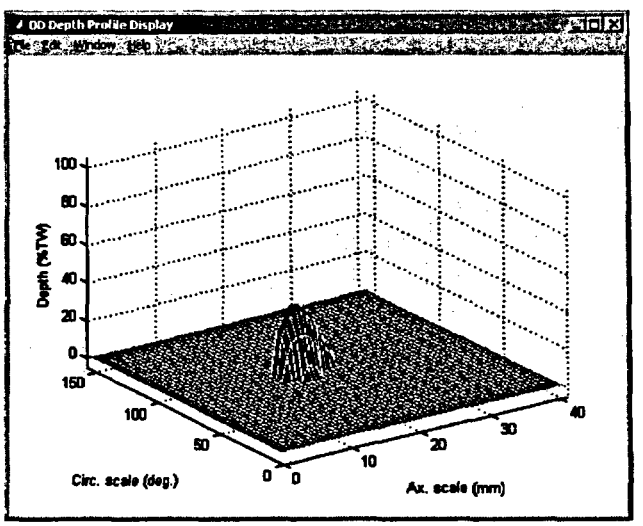

(c)

Figure 3.25.
Data analysis results for McGuire pulled tube section with axial ODSCC degradation at dented TSP intersection. Maximum flaw depth is estimated to be <40% TW. Graphics shows (a) amplitude image display of the standard and flawed tube at different stages of the process, (b) flaw image, and (c) terrain plot of sizing data.

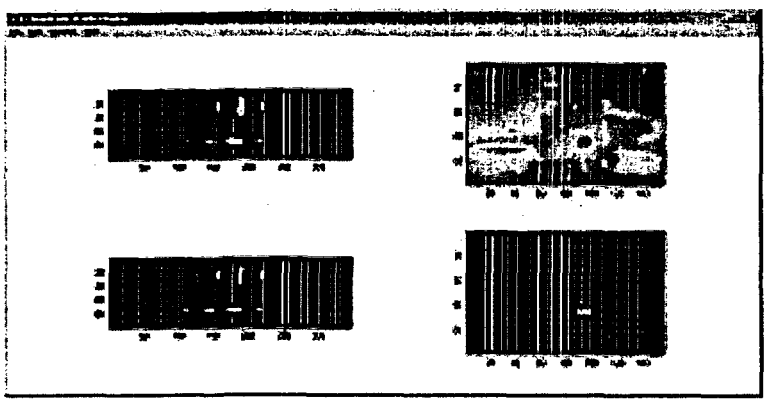

(a)

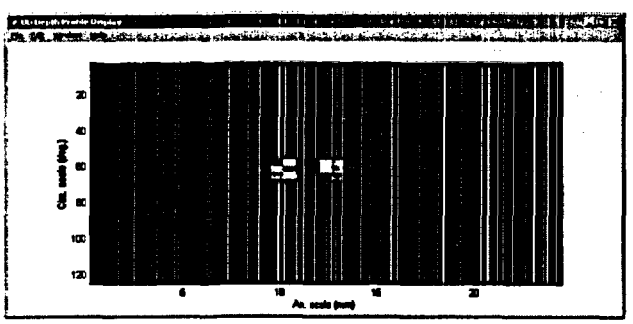

(b)

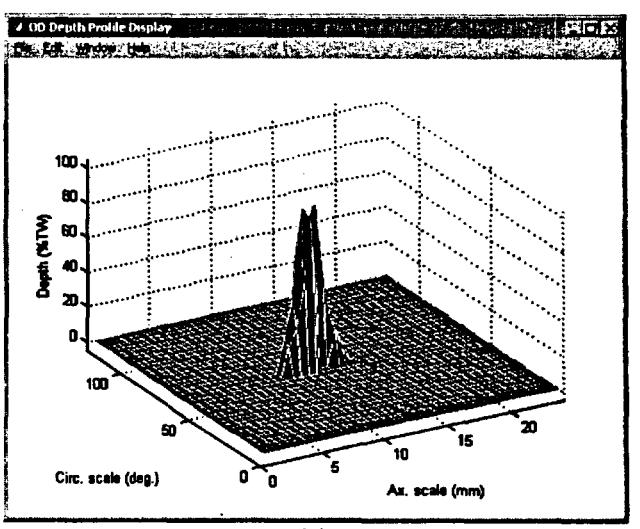

(c)

Figure 3.26.
Data analysis results for McGuire pulled tube section with axial ODSCC degradation at dented TSP intersection. Maximum flaw depth is estimated to be > 90% TW. Graphics shows (a) amplitude image display of the standard and flawed tube at different stages of the process, (b) flaw image, and (c) terrain plot of sizing data.

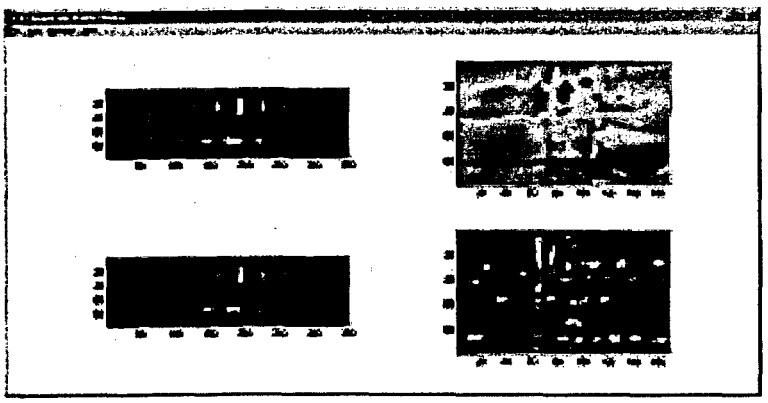

(a)

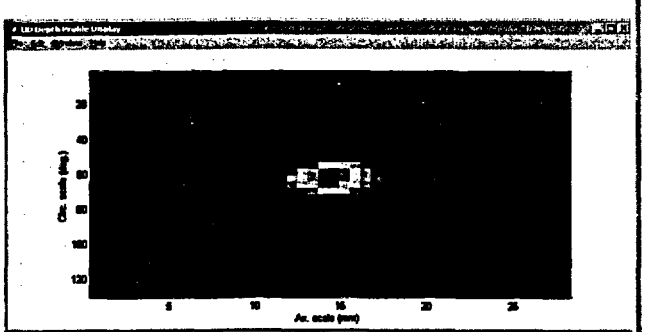

(b)

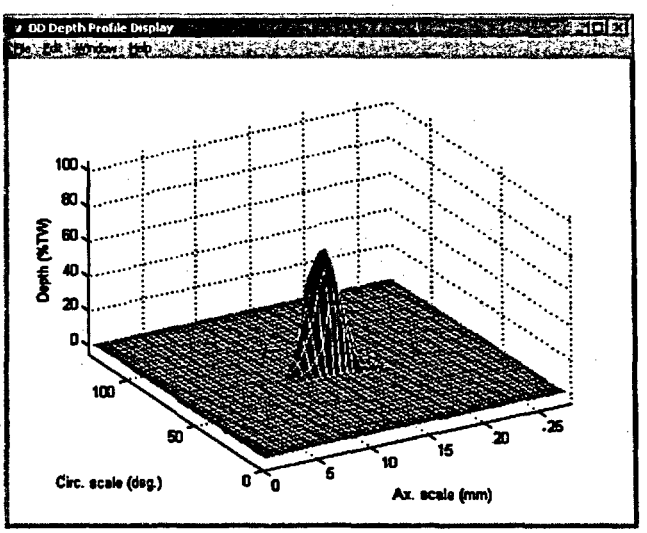

(c)

Figure 3.27.
Data analysis results for McGuire pulled tube section with axial ODSCC degradation at dented TSP intersection. Maximum flaw depth is estimated to be <70% TW. Graphics shows (a) amplitude image display of the standard and flawed tube at different stages of the process, (b) flaw image, and (c) terrain plot of sizing data.

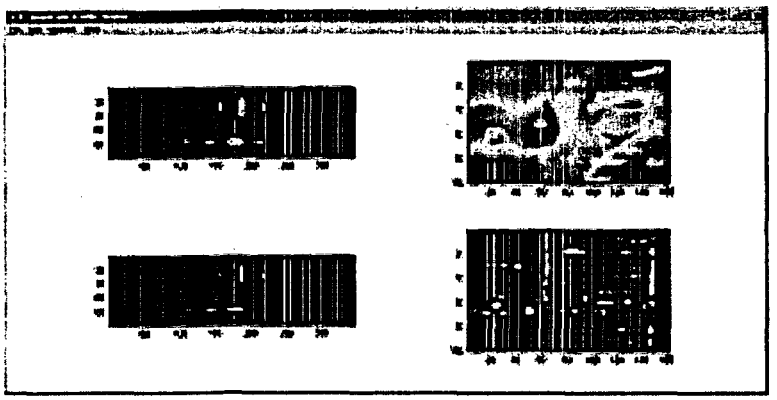

(a)

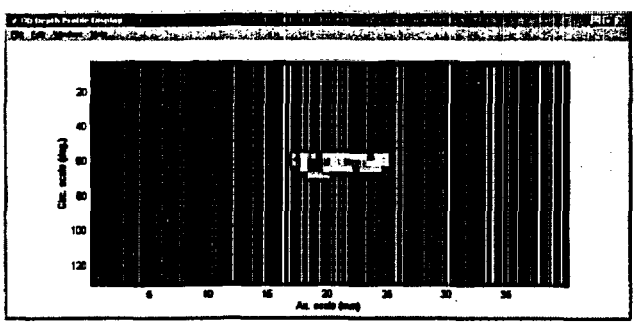

(b)

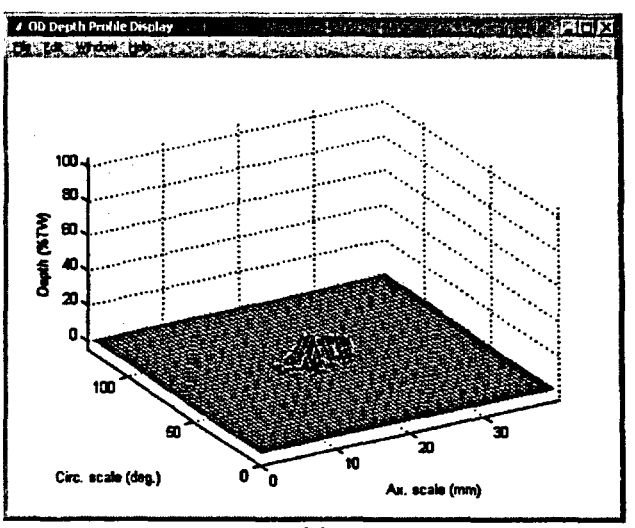

(c)

Figure 3.28.
Data analysis results for McGuire pulled tube section with axial ODSCC degradation at dented TSP intersection. Maximum flaw depth is estimated to be <20% TW. Graphics shows (a) amplitude image display of the standard and flawed tube at different stages of the process, (b) flaw image, and (c) terrain plot of sizing data.

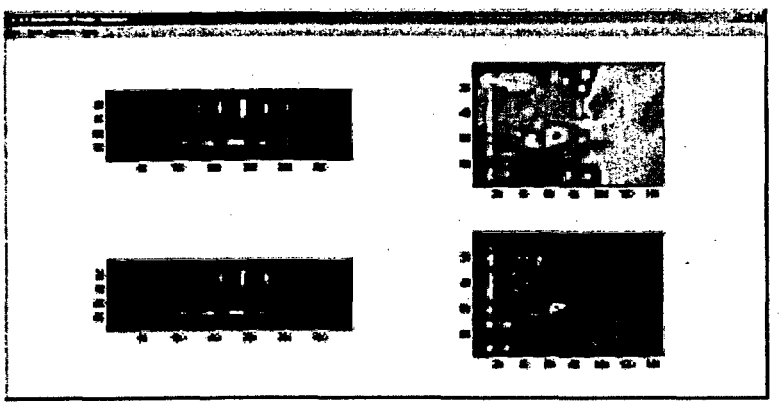

(a)

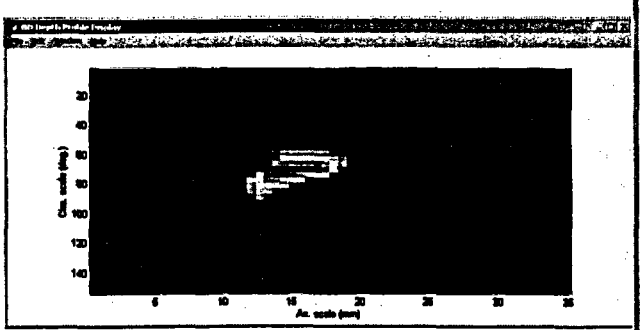

(b)

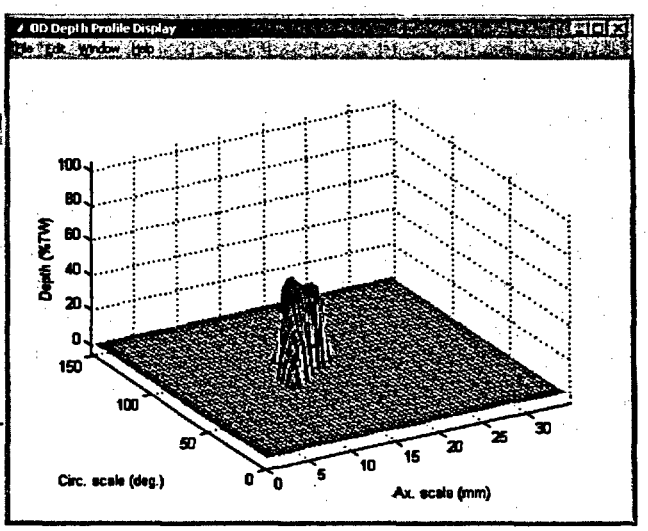

(c)

Figure 3.29.
Data analysis results for McGuire pulled tube section with axial ODSCC degradation at dented TSP intersection. Maximum flaw depth is estimated to be > 50% TW. Graphics shows (a) amplitude image display of the standard and flawed tube at different stages of the process, (b) flaw image, and (c) terrain plot of sizing data.

4. Research on Degradation Modes and Integrity (D. R. Diercks, K. E. Kasza, S. Majumdar, J. Y. Park, and W. J. Shack

4.1 Production of Laboratory-Degraded Tubes and Characterization of Flaws

Because degraded tubing from operating or retired SGs is difficult and expensive to obtain and the availability of such tubing is limited, it is necessary to produce prototypical degradation in tubes as a part of this program. These tubes are to be used to evaluate NDE equipment and techniques in the SG mock-up and to conduct pressure and leak-rate testing. Techniques for Alloy 600 tubes have been developed to produce SCC degradation of various sizes, depths, and orientations that are prototypical of field-degraded SG tubes. Flaws in tube specimens were destructively examined and compared with the results of EC NDE.

4.1.1 Materials Properties of Alloy 600

As the test material for the program, Alloy 600 tubing with diameters of 19.1 mm (0.750 in.) and 22.2 mm (0.875 in.) has been obtained from four sources. Valinco supplied 19.1-mm (0.750-in.) tubing (Heat NX8524) in the as-fabricated ("cold-worked") condition, and 22.2-mm (0.875-in.) (Heat NX8520 and NX8527) tubing in the mill-annealed condition. Heat NX8520 was supplied with two mill-annealing processes: 3 min at 980°C (1796°F) for a low temperature annealing or 2 min at 1060°C (1940°F) for a high temperature annealing. Material with the low-temperature annealing is designated as NX8520L, and material with the high-temperature annealing is designated as NX8520H. Heat NX8527 was mill-annealed for 3 min at 940°C. PNNL provided ≈110 m (360 ft) of 22.2-mm (0.875-in.) tubing in 3.7-m (12-ft) lengths. PNNL was unable to identify the heat number, but the tubing was labeled "EX-82-1/2675" on all but one piece, which was labeled "HT #9829/1L-102." PNNL also provided cold drawn and annealed 22.2-mm (0.875-in.) tubing (Teledyne Columbia-Summeril Heat NX7968). EPRI provided 22.2-mm (0.875-in.) tubing (Heat 96834 M-81) that was mill-annealed at 927°C(1700°F). This material (Heat 96834) was mainly used for the crack evolution studies described in Section 4.2.

Heat analyses were provided by the vendors, and a check chemical analysis was performed on a sample from the PNNL tubing. These analyses are shown in Table 4.1. In all cases, the tubing conforms to specification ASTM B 163 for Alloy 600. Room-temperature tensile properties, hardness, and grain size data were provided by the vendors. However, additional tests were also conducted by ANL and by an outside vendor. The results, summarized in Table 4.2, show that, although the ultimate tensile strengths are comparable, the ductility of the 22.2-mm (0.875-in.) tubes is significantly greater than that of the 19.1-mm (0.750-in.) tubes. The room-temperature harnesses and grain size of the Alloy 600 tubing are also included in Table 4.2. The average grain size is ASTM 8.0 (average linear intercept, 20 μm) for the 19.1-mm (0.750-in.) tubing (Heat NX8524) and ASTM 8.6 (average linear intercept 16 μm) for the 22.2-mm (0.875-in.) tubing and PNNL ID EX-82-1/2675.

Table 4.1. Elemental analysis (wt. %) of Alloy 600 tubing material. Diameters of 19.1–mm [0.750–in.] (heat NX8524) and 22.2–mm [0.875–in.] (heats NX8520, NX8527, NX7968, 96834, and PNNL ID EX–82–1/2675).

Element	Specifications ASTM B163	NX8520	NX8524[a]	NX8524[b]	NX8527	NX7968	96834	EX–82–1[c]
Ni	72.0 min.	75.63–75.77	74.66	74.95	74.85–75.20	75.44	74.81	75.05
Cr	14.0–17.0	15.28–15.40	15.21	14.84	15.33–15.51	15.58	15.85	15.21
Fe	6.0–10.0	7.96–8.03	9.16	9.11	8.49–8.68	8.38	8.16	8.30
Mn	1.0 max.	0.19	0.20	0.20	0.21	0.24	0.27	0.18
Cu	0.5 max.	0.02	<0.01	0.01	<0.01	0.18	0.01	0.17
C	0.15 max	0.022	0.022	0.023	0.023–0.025	0.040	0.037	0.035
S	0.015 max.	<0.001	<0.001	<0.001	<0.001	0.001	0.001	0.001
Si	0.5 max.	0.18–0.21	0.20	0.17	0.13– 0.16	0.14	0.30	0.23
Al	d	0.21	0.24	0.22	0.23–0.25	d	d	0.15
Ti	d	0.26–0.34	0.29	0.35	0.30–0.36	d	d	0.18
Co	d	0.02	0.01	0.02	0.01–0.02	d	d	0.03
P	d	0.004	0.003	0.005	0.004–0.005	d	d	0.009
B	d	0.002–0.004	0.004	0.002	0.001–0.003	d	d	0.002
N	d	<0.01	<0.01	<0.01	<0.01	d	d	0.004

[a]Top of ingot.
[b]Bottom of ingot.
[c]Check analysis for tubing from PNNL with a label, EX–82–1/2675.
[d]Not specified, not measured, or not reported.

Table 4.2. Room–temperature tensile properties, hardness and grain size of Alloy 600 tubing. Diameters of 19.1–mm [0.750–in.] (heat NX8524) and 22.2–mm [0.875–in.] (heats NX8520, NX8527, NX7968, 96834, and PNNL ID EX–82–1/2675)

Heat No.	Spec. No.	Diam (mm)	σ_y (MPa)	Ave. σ_y (MPa)	σ_u (MPa)	Ave. σ_u (MPa)	ε_t (%)	Ave. ε_t (%)	Grain Size ASTM	Hardness
NX8520	L[a]	22.2	d	d	d	696	d	d	d	VH 162
	H[b]	22.2	d	d	d	641	d	d	d	VH 146
NX8524	6–1	19.1	296	d	679	d	25.5	d	d	d
	6–2	19.1	314	d	682	d	25.5	d	d	d
	6–3	19.1	315	308	682	681	24.5	25.2	8.0	VH 173±8
NX8527	2–1	22.2	267		629		40.0			
	2–2	22.2	275		648		41.0			
	2–3	22.2	270	271	625	634	41.5	40.8		
	SGMC	22.2		317±14		696±14				VH 179
	SGMC[c]	22.2		179±14		600±14				VH 148
NX7968		22.2		296		639		51.6	–	–
96834		22.2		359		734		38.0	9.0	RB 85.0
EX–82–1	15–1	22.2	356		689		44.0			
	15–2	22.2	356		681		44.5			
	15–3	22.2	358	357	678	683	41.0	43.1	8.6	VH 184±9

[a]Low temperature mill–annealed at 980°C (1796°F) for 3 min.
[b]High temperature mill–annealed at 1060°C (1940°F) for 2 min.
[c]Mill–annealing plus 1100°C 10 min, and 600°C 48–h heat treatment.
[d]Not specified, not measured, or not reported.

4.1.2 Production of Laboratory Cracked Tubes

Stress corrosion cracks have been produced in 22.2-mm (7/8-in.)-diameter specimens (Heats NX7968, NX8527, NX8520L, and NX8520H). Cracking is accomplished using a 1 M aqueous solution of sodium tetrathionate ($Na_2O_6S_4 \cdot 2H_2O$) at room temperature and atmospheric pressure. The material was first mill-annealed for 3 min at 940°C for Heat NX8527, 3 min at 980°C (1796°F) for Heat NX8520L, and 2 min at 1060°C (1940°F) for Heat NX8520H. Heat NX8524 was in the as-fabricated (cold-drawn) condition. Before exposure to the tetrathionate solution, the specimens were heat treated at 600°C (≈1100°F) for 48 h to produce a microstructure that is susceptible to cracking [18]. Various techniques, including localized environmental exposure, low applied load, and controlled electrochemical potential, have been applied in an effort to produce segmented SCCs. During the course of the program, about nine-hundred 22.2-mm ($^7/_8$-in.)-diameter Alloy 600 tubes were processed to produce axial ODSC and IDSCC, circumferential ODSCC andl IDSCC, and SCCs in skewed orientations. Some of the specimens were produced with multiple cracks or combinations of multiple cracks of different orientations. Most of the specimens were straight tubes, but some were roll-expanded, dented, or ovalized. Some of the heat-treated tubes have been installed as uncracked blanks in the NDE SG tube mock-up. The current cracking facility is able to handle ten individual tube specimens to produce axial SCCs and three specimens for circumferential SCCs.

To accelerate cracking, some specimens from Heat NX8527 were additionally solution-heat-treated at 1010-1100°C (1850-2012°F) for 10-20 min before the sensitization heat treatment at 600°C for 48 h. Cracking time ranged from 10-1000 h. The specimens that received the high-temperature treatment cracked in shorter times than those without it. However, this solution treatment causes grain growth and a reduction in hardness and flow stress. Tensile tests were performed and showed the flow stress of the material to be reduced by ≈20% due to the heat treatments.

The sensitization heat treatment at 600°C (1112°F) for 48 h did not weaken the material. Tensile tests were performed for the 22.2-mm ($^7/_8$-in.) Alloy 600 tube material from NX8520H and NX8520L.

The solution and sensitization heat treatments may also change the magnetic properties of the alloy and influence EC measurements. To examine this, two 22.2-mm ($^7/_8$-in.) Alloy 600 tubes (Heat NX8527) with EDM notches have been treated with the solution and sensitization heat treatments, and EC results were compared before and after the heat treatments. It was found that sensitized sections (i.e., those containing flaws) could be distinguished from blank (non-sensitized) sections, unless magnetically biased probes were used. When magnetically biased probes were used, the signals from sensitized and non-sensitized sections were indistinguishable.[1]

To examine the influence of oxide films on Alloy 600 tube specimens on EC response, 10 cracked tubes were oxidized in high-temperature water environments. Of these, five tubes (SGL114, 159, 170, 182, and 187) were oxidized in deionized high-purity water with 8 ppm dissolved oxygen at 290°C (554°F) and 8.8 MPa (1280 psi) for 1680 h. Five additional tubes (SGL127, 149, 169, 189, and 197) were oxidized in deionized high-purity water with 3 ppm dissolved oxygen at 290°C (554°F) for 120 h, then in a simulated primary water environment (1200 ppm B and 2 ppm Li) at 320°C (608°F) and 12.4 MPa (1800 psi) for 1400 h. Eddy

current NDE was performed before and after the oxidation treatment. Results from the EC examinations of these specimens are described in Ref. [19].

In the early stages of the program, SCCs were produced in Alloy 600 tube specimens in a caustic solution using a high-pressure autoclave system. Fifteen 19.1-mm (0.750-in.) tubes (Heat NX8524) and fourteen 22.2-mm (0.875-in.) tubes (Heat NX8527) were cracked by this technique. The concept, design, and operational procedures of the autoclave system are described in Refs. [13] and [20]. Tube specimens were exposed at PWR SG operating temperatures (or slightly higher to accelerate cracking) to aggressive solution containing ≈60% NaOH plus CuO and Cu, which are known to induce stress corrosion cracking in Alloy 600. Components in the facility that operate in contact with the aggressive water chemistry were fabricated of Hastelloy C-276 or stainless steel (SS). The results of the degradation experiments for 29 tubes in the autoclave system are summarized in Ref. [19]. Use of this high pressure technique was discontinued since the development of the low temperature technique that is simpler and more convenient, and the majority of the tube specimens for the program were produced by the low-temperature sodium tetrathionate technique. The BC voltages were found to increase significantly for the oxidized tubes, though the shape of the Lissajous figures remained unchanged. In contrast, the results for the +Point coil were inconclusive.

4.1.3 Characterization of Laboratory-Cracked Tube Specimens: Specimen Set for Control and Verification

Twenty-seven laboratory-cracked Alloy 600 tube specimens were characterized by destructive means, and the results were compared with the EC/NDE measurements. All twenty-seven specimens are the nominal 22.2-mm ($^{7}/_{8}$-in.)-diameter tubing. The cracks were destructively opened by fracture and examined macroscopically and with scanning electron microscopy. The specimens were heat tinted prior to fracturing to permit discrimination of the SCC and fracture opening surface. The heat tinting is accomplished for 1/2-1 h at 600°C (1112°F) in an air atmosphere. This tinting makes the SCC appear in darker contrast to the fracture area. Details of the method used for the destructive examination and comparisons with the EC/NDE crack profile are given in Ref. [16]. Figures 4.1 through 4.6 are the results of destructive examination and comparison with the EC NDE evaluation for the 27 laboratory-produced cracks. The EC/NDE evaluations are overall in good agreement with the destructive examination for cracks deeper than about 50% TW, while poorer agreements is observed for shallow cracks.

4.1.4 Characterization of Laboratory-Cracked Tube Specimens: Mock-up Specimens

Seven ANL mockup tube specimens were characterized by destructive means, and the results were compared with the EC/NDE measurements. All seven specimens were the nominal 22.2-mm ($^{7}/_{8}$-in.)-diameter tubing. Four specimens were produced by ANL using the technique described in the previous section, and three specimens were provided by PNNL/West. The cracks were destructively opened by fracture and examined macroscopically and with scanning electron microscopy. The EC/NDE crack profile was obtained using the multi-parameter analysis technique. Figures 4.7-4.13 show the results of the destructive examination and comparison with the EC NDE profiles. The EC/NDE measurements are overall in good agreement with the destructive examination. However, EC/NDE noticeably underestimated the crack size for specimen PNNL/W 4-02 (Fig. 4.11), and a minor crack in specimen PNNL/W 4-05 was not resolved (Fig. 4.13).

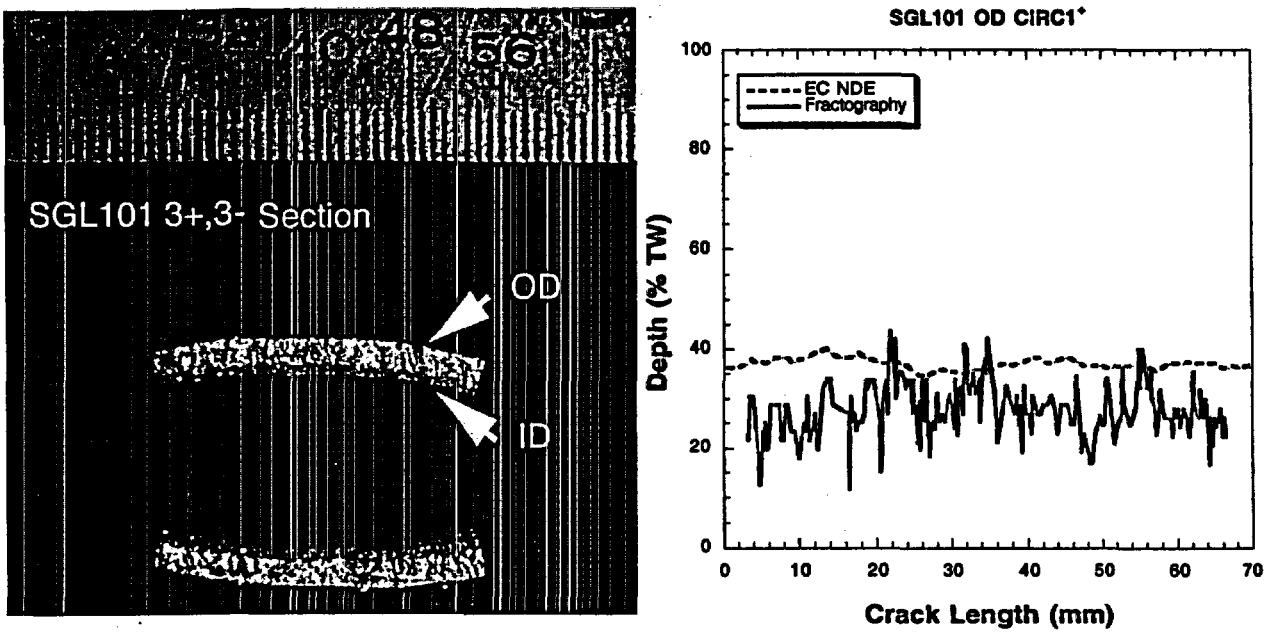

(a) (b)

Figure 4.1. Fractography profile and NDE for circumferential IDSCC 1 in specimen SGL101.

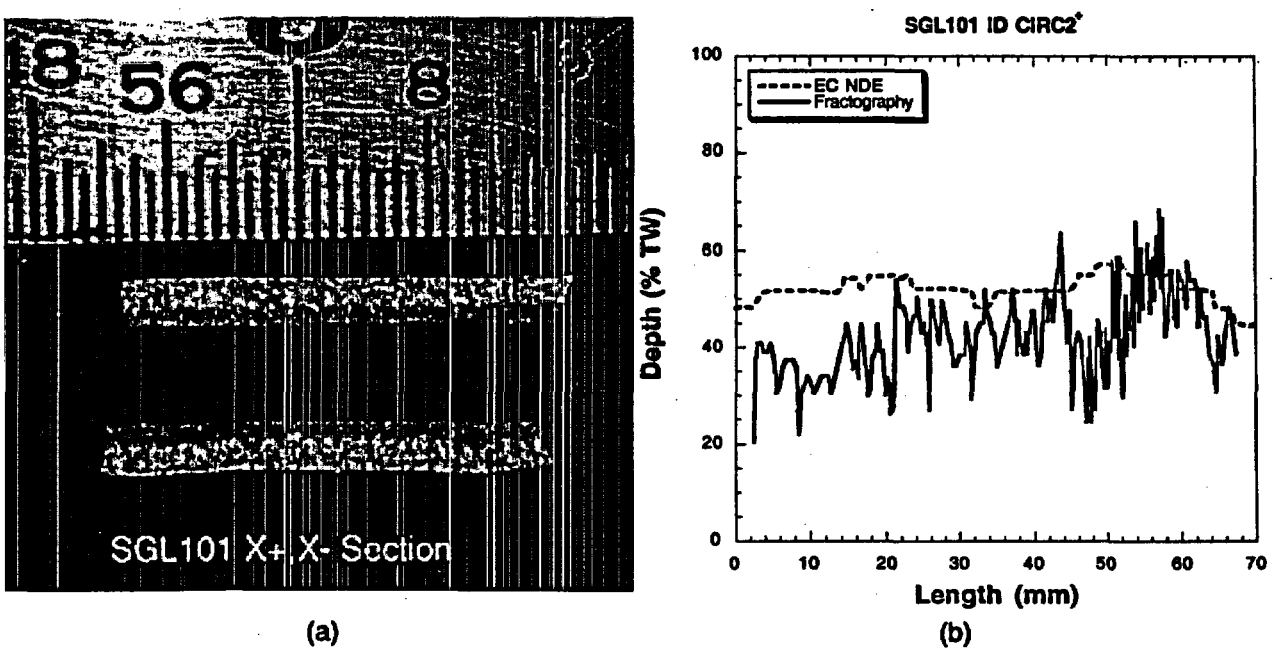

(a) (b)

Figure 4.2. Fractography profile and NDE for circumferential IDSCC 2 in specimen SGL101.

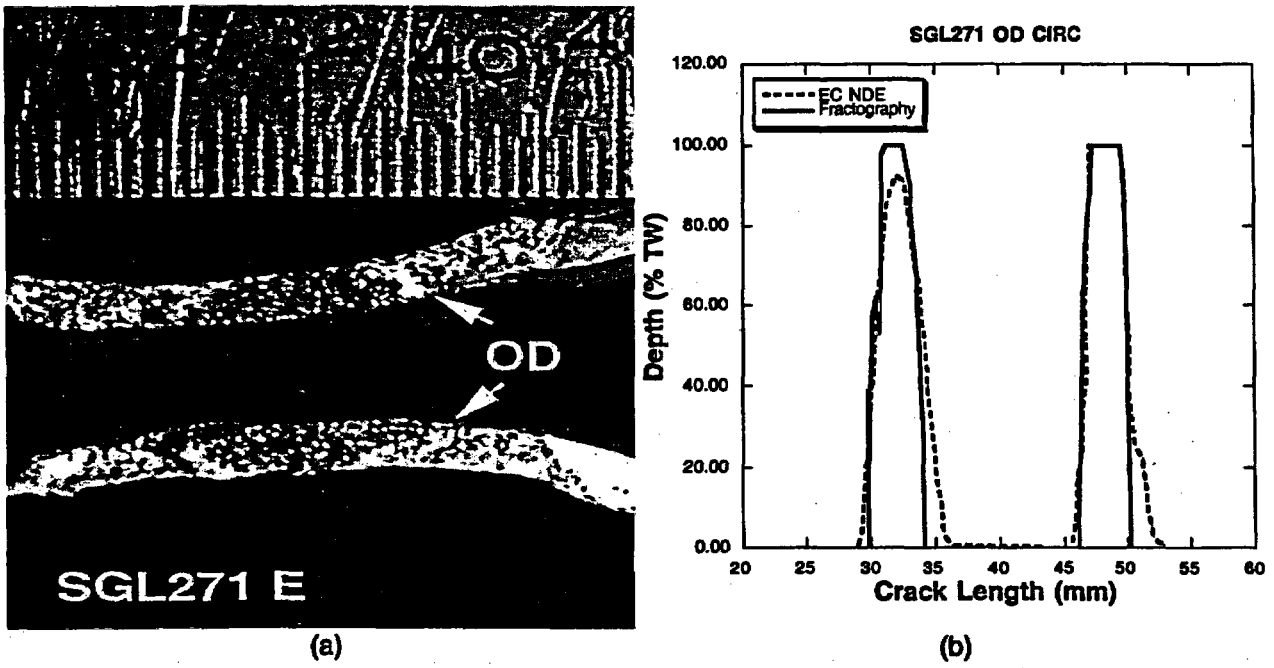

(a) (b)

Figure 4.3. Fractography profile and NDE for circumferential ODSCC in specimen SGL271.

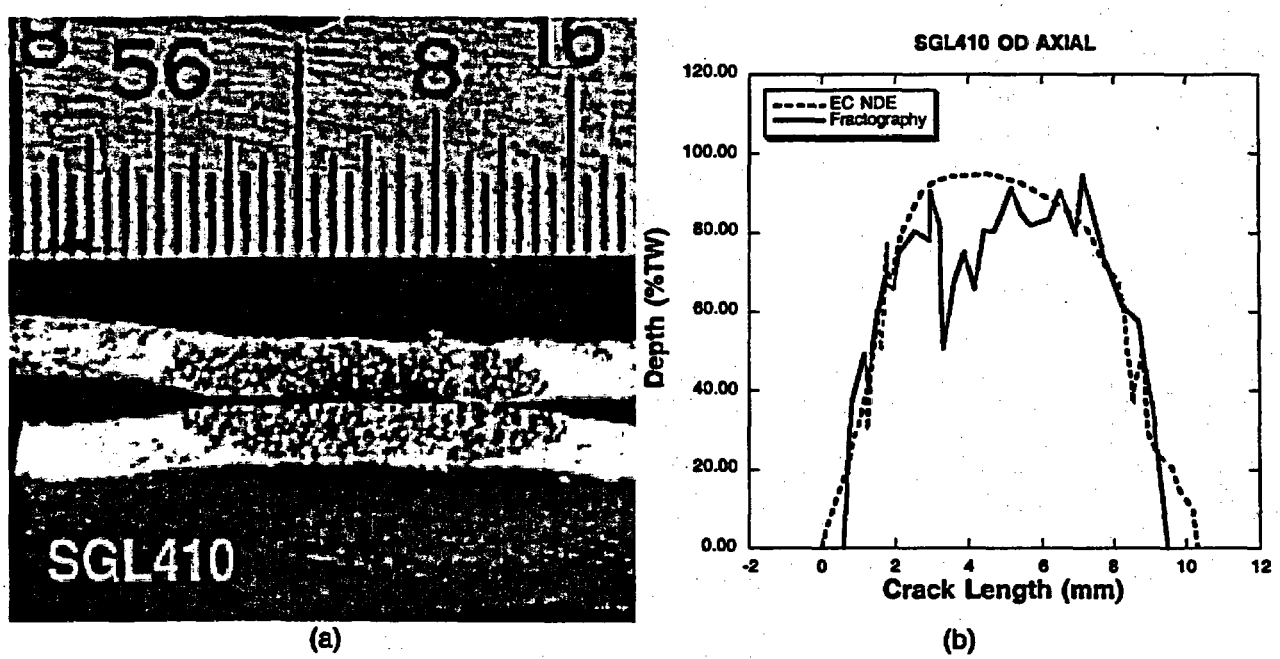

(a) (b)

Figure 4.4. Fractography profile and NDE for axial ODSCC in specimen SGL410.

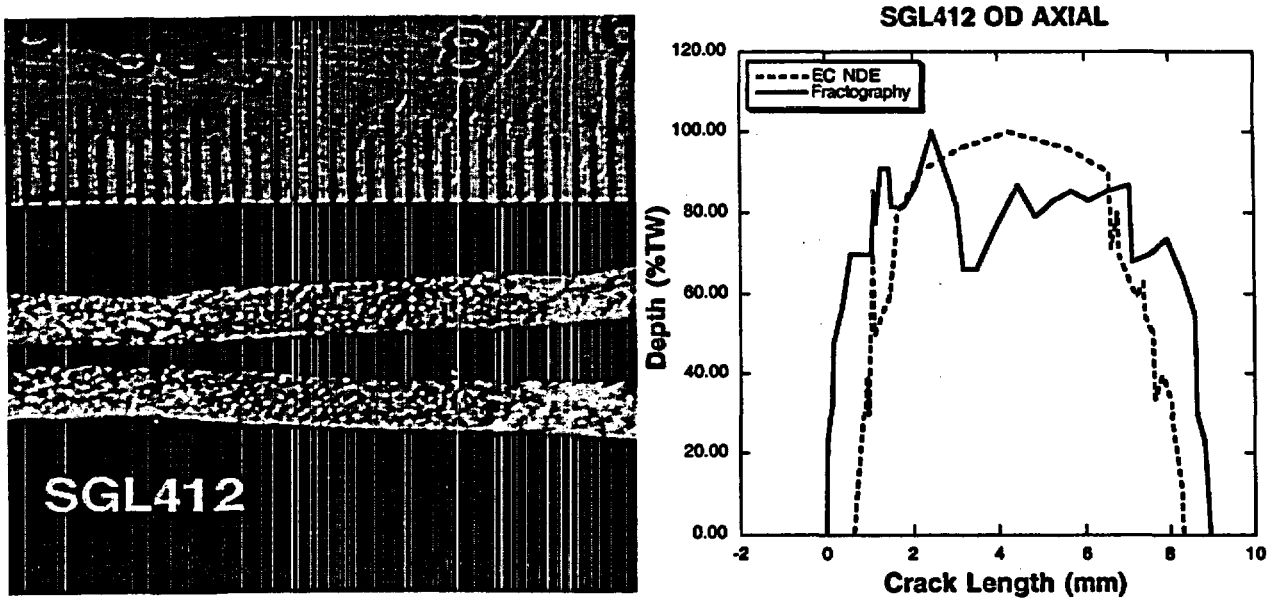

(a) (b)

Figure 4.5. Fractography profile and NDE for axial ODSCC in specimen SGL412.

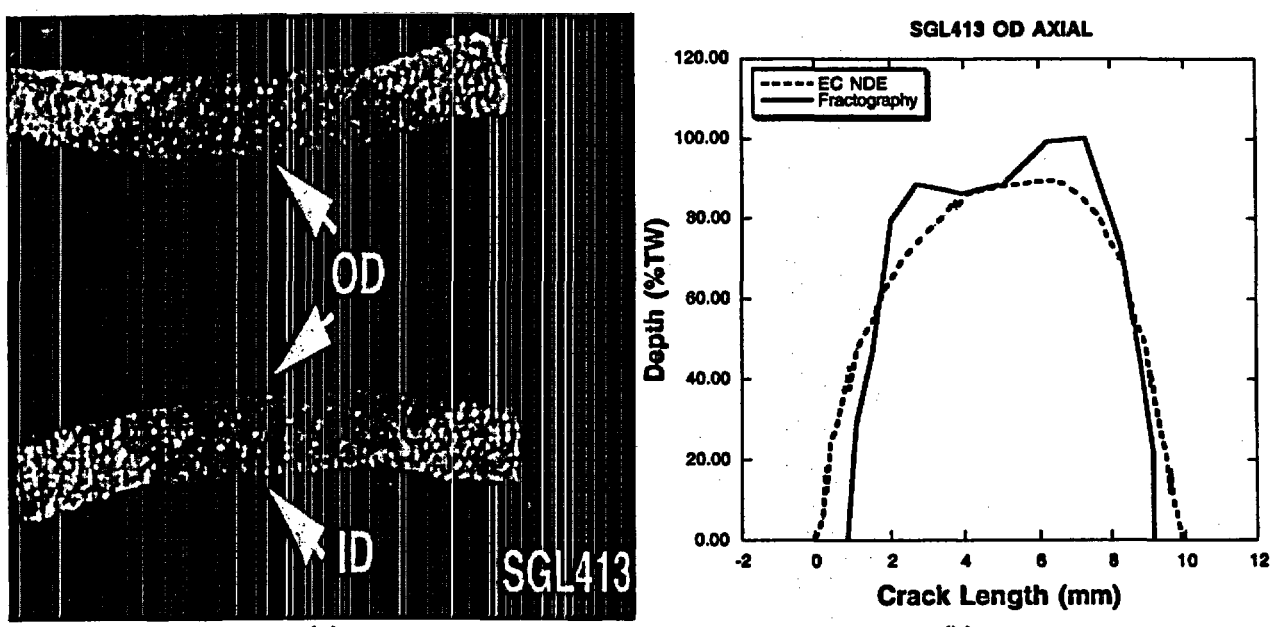

(a) (b)

Figure 4.6. Fractography profile and NDE for axial ODSCC in specimen SGL413.

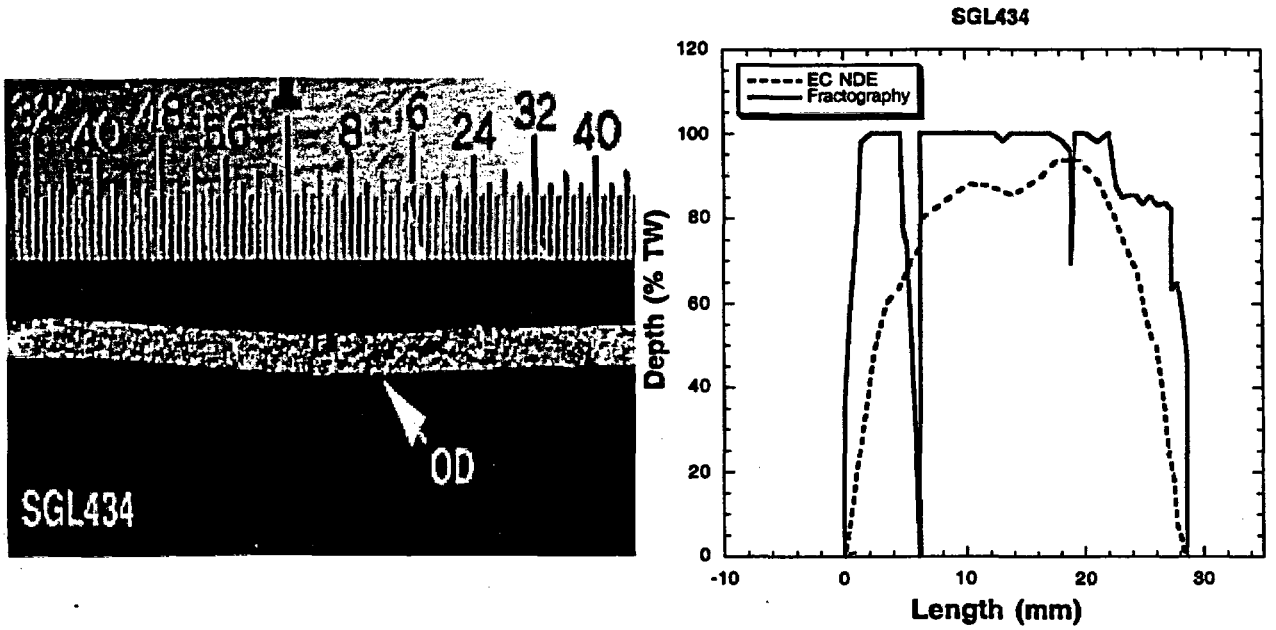

Figure 4.7. Fractography profile and NDE for axial ODSCC in specimen SGL434.

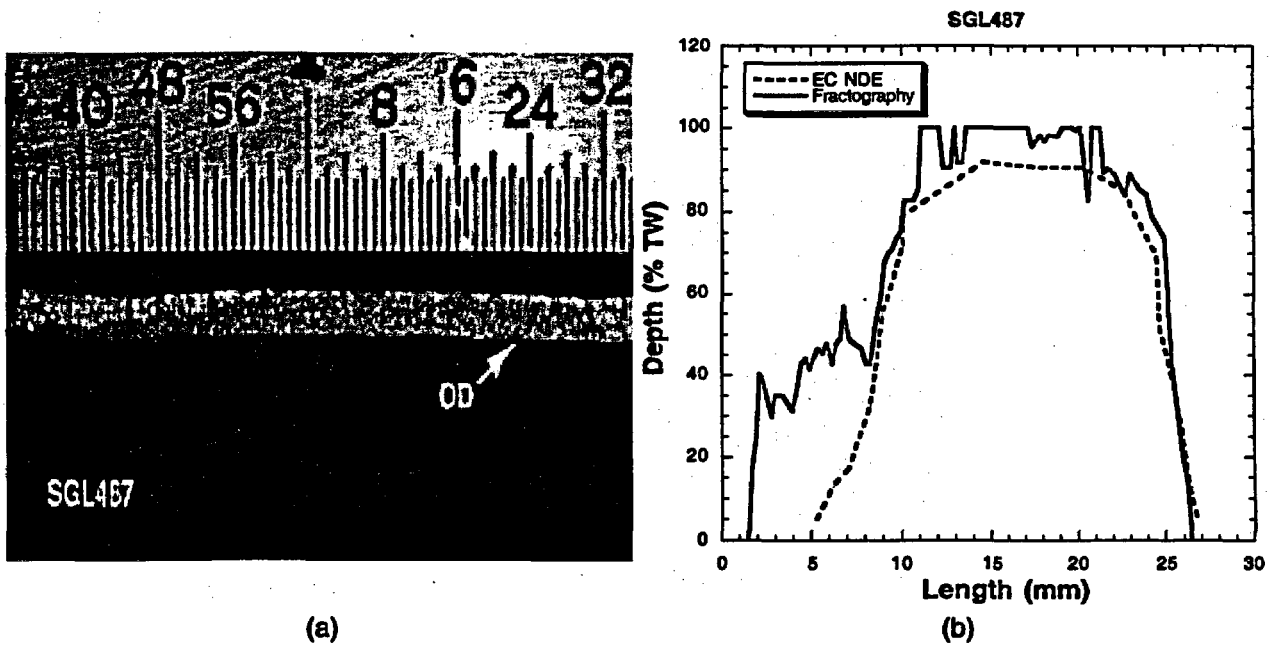

Figure 4.8. Fractography profile and NDE for axial ODSCC in specimen SGL487.

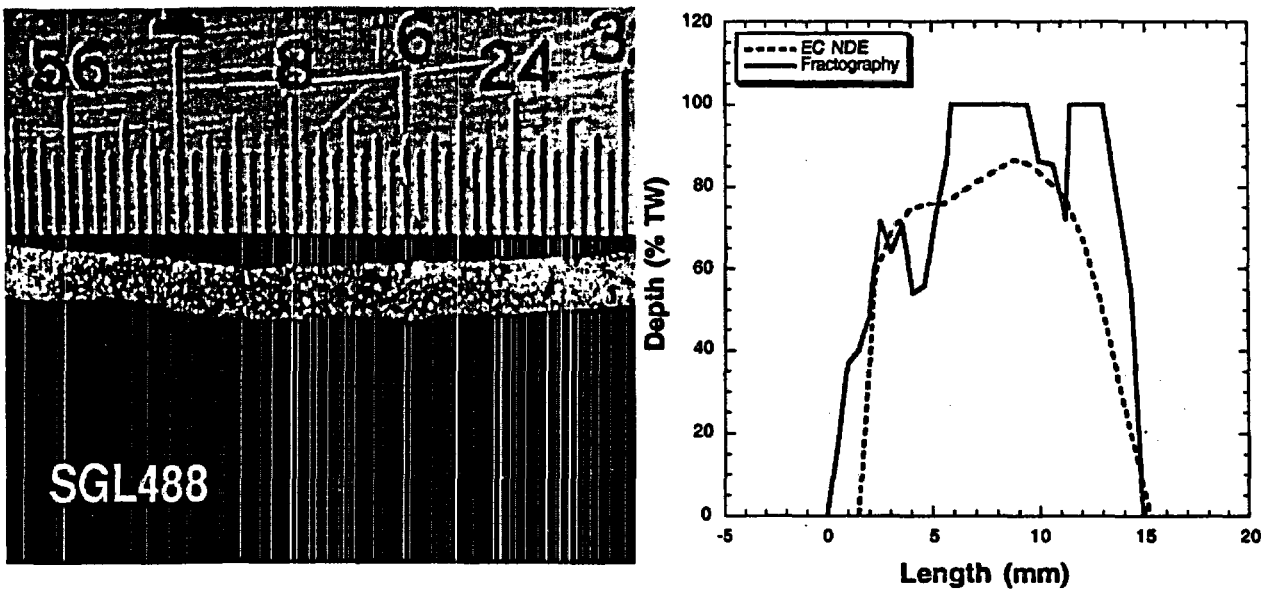

(a) (b)

Figure 4.9. Fractography profile and NDE for axial ODSCC in specimen SGL488.

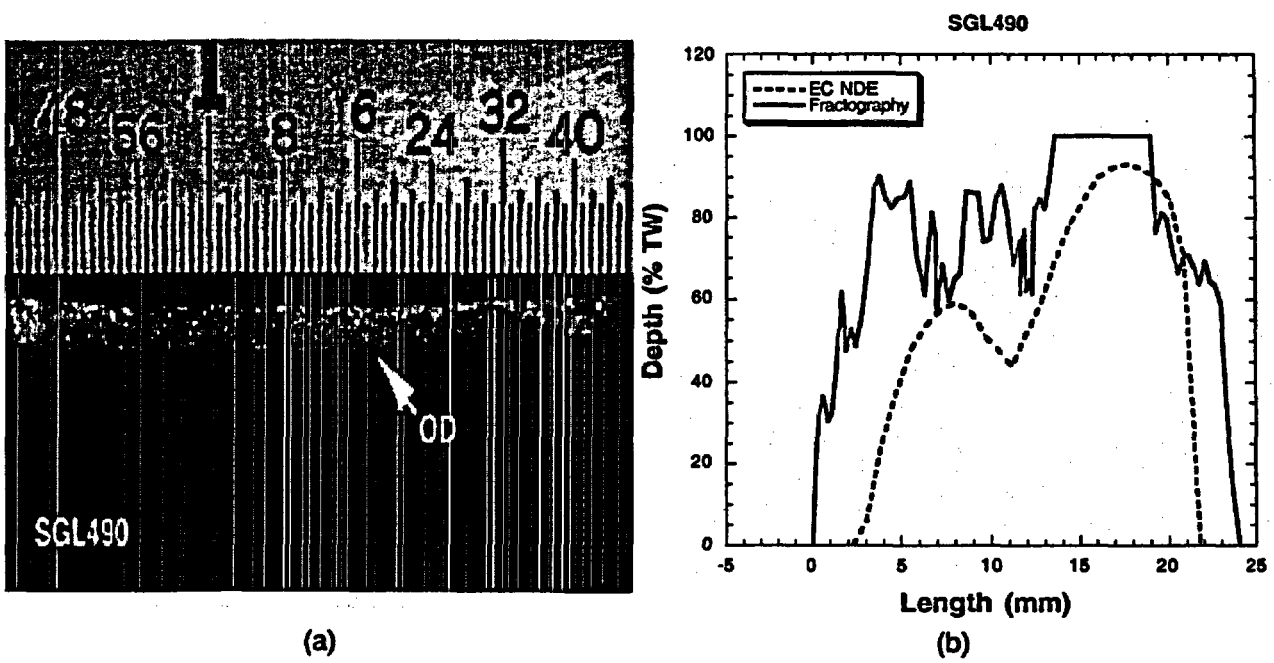

(a) (b)

Figure 4.10. Fractography profile and NDE for axial ODSCC in specimen SGL490.

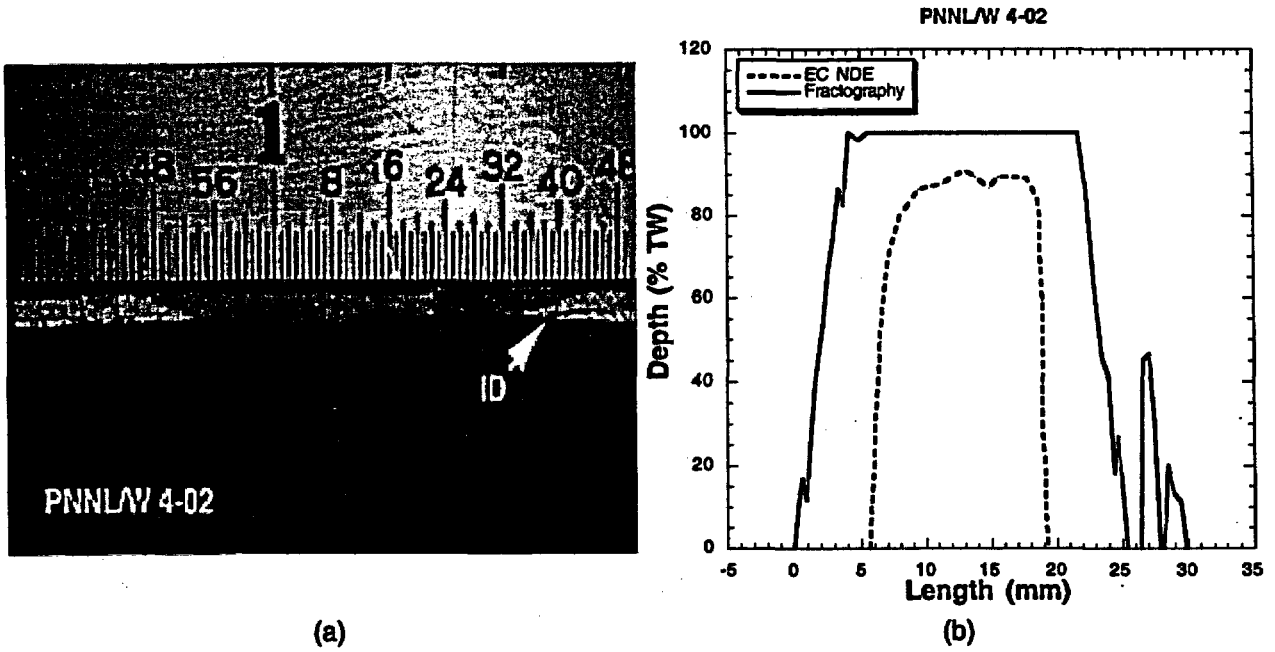

Figure 4.11. Fractography profile and NDE for circumferential ODSCC in specimen PNNL/W 4–02.

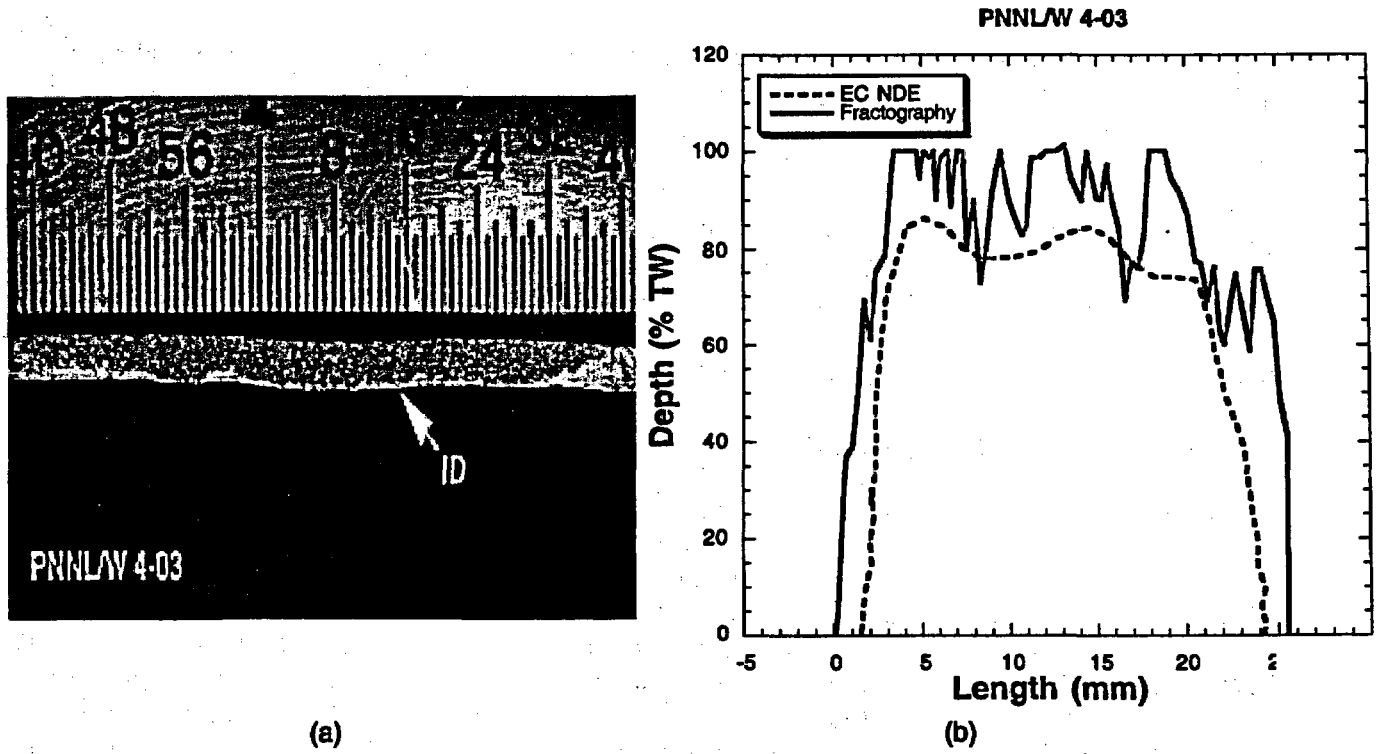

Figure 4.12. Fractography profile and NDE for circumferential ODSCC in specimen PNNL/W 4–03.

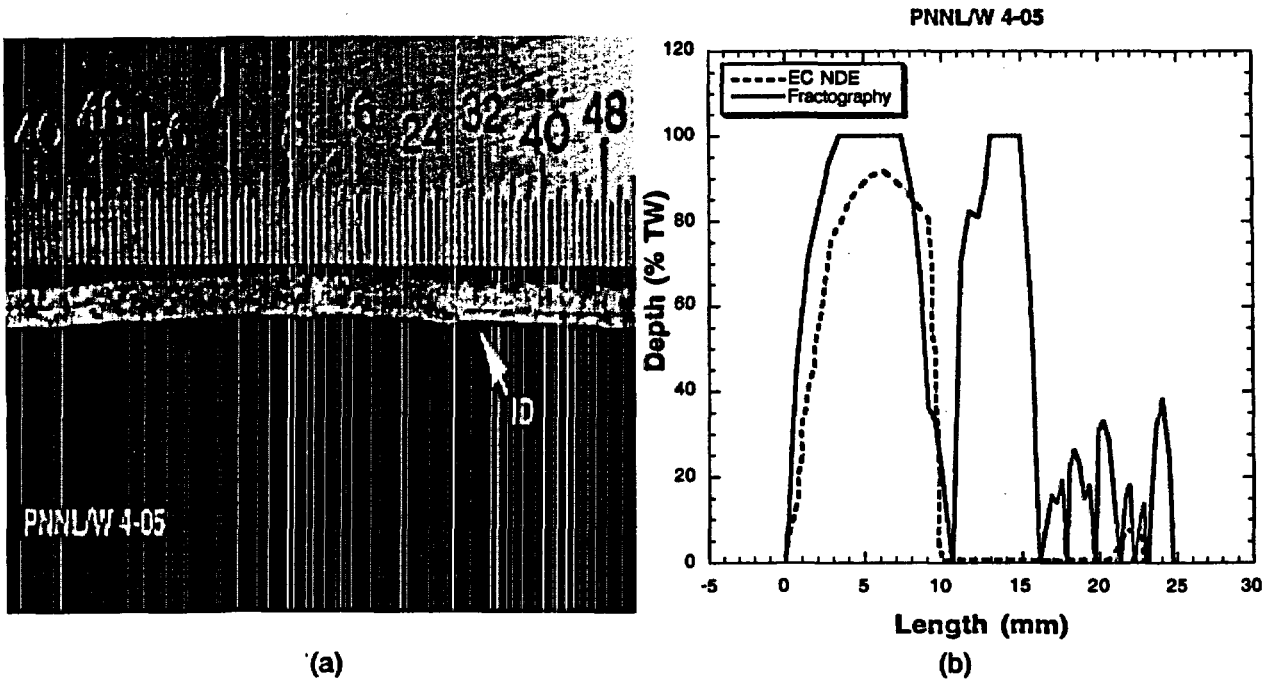

Figure 4.13. Fractography profile and NDE for circumferential ODSCC in specimen PNNL/W 4–05.

4.1.5 Characterization of Field–Serviced Tube Specimens: McGuire SG Tubes

Six tube specimens from the retired McGuire SG were characterized by destructive examination, and the results were compared with the EC/NDE results. The nominal diameter of the tube specimens is 19.1 mm (0.750 in.). The cracks were destructively opened by fracture and examined macroscopically and with scanning electron microscopy. Figures 4.14–4.17 show the results of destructive examination and comparison with EC NDE profiles for tube specimen 4–43–2, 5–51–2, 7–24–3, and 14–55–3. The EC/NDE crack profile was obtained using the multi–parameter analysis technique, although this technique is still under development for 19.1–mm (0.750–in.) diameter tubing. The EC/NDE results are overall in good agreement with the destructive examination, except for specimen 5–51–2 (Fig. 4.15).

4.1.6 Characterization of Laser-Notched Tube Specimens

Destructive analyses were performed for 22.2–mm (0.875–in.) Alloy 600 tube specimens with laser–cut notches of various geometries. The notches were destructively opened during pressure and leak tests, and by subsequent fracture of ligaments.

Digitized profiles of the laser–cut notches in tube specimens were obtained from fractography and compared with eddy current NDE measurements. The results for specimen 5528–1–1, 5528–1–2, and 5528–2–1 are shown in Figures 4.18–4.21. Specimen 5528–1–1, 5528–1–2, and 5528–2–1 contain a single–segment axial flaw in each specimen. The average depth at the mid–section of the laser–cut notch is 70, 75, and 68% TW for specimen 5528–1–1, 5528–1–2, and 5528–2–1, respectively. Specimen 5528–3–2 has a 6–segmented axial cut. The average depth at the mid–section of the laser–cut notch is 65% TW. The EC/NDE measurements slightly underestimated the depths of the laser–cut notches, although they are

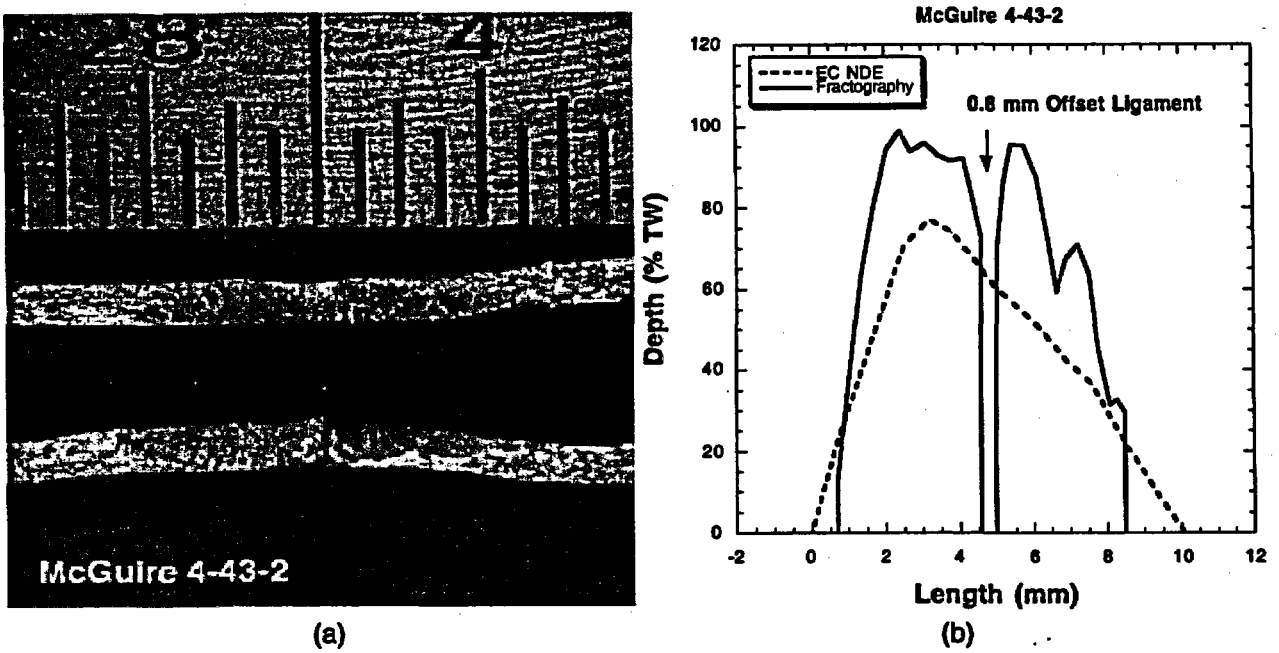

Figure 4.14. Fractography profile and NDE for axial ODSCC in McGuire tube specimen 4–43–2.

generally in good agreement with the fractographic results. During pressure and leak tests, the thickness of the tube is reduced due to plastic deformation. However, in the present analyses, an assumption was made that reduction of the thickness at the laser–cut notch face in the tube is small and can be neglected. This may explain some of the discrepancy between the NDE and fractographic results.

The laser–cuts are significantly deeper at the end of notch segments. For all the specimens, the ends of the laser–cut segments are cut much deeper than the average depth at the mid–section, i.e., 100% TW. This is probably caused from longer dwell times at the end of the segments during the traverse of the laser beam. NDE does not resolve these pin–hole defects.

4.2 Crack Evolution Studies

An SCC testing facility was constructed for experimental investigation of Pb–induced cracking in Alloy 600 and Alloy 690 steam generator materials. The system consists of two 8–L Hastelloy C276 autoclaves, a Hastelloy C276 small-diameter pipe autoclave, loading mechanism, and electrochemical measurement instruments. The 8–L Hastelloy autoclaves are rated for a maximum pressure of 13.1 MPa (1900 psi) at 350°C (662°F) and are ASME Code stamped. These 8–L autoclaves will be used for c–ring type static SCC and high-temperature electrochemistry tests (Fig. 4.22). The small diameter pipe autoclave will be used for the constant extension rate tests (CERT) (Fig. 4.23). Testing material will be the tubing that has been used in the other tasks in this program. However, the Electric Power Research Institute (EPRI) provided some additional materials: 5 m each of 22.2–mm ($^7/_8$–in.)–diameter Alloy 600 tubes of Heat no. 96834 M81 (annealed at 927°C) and 96834 (annealed at 1024°C), and 5 m of 22.2–mm ($^7/_8$–in.)–diameter Alloy 690TT of Heat no. D2A2201 (annealed at 579°C and aged at 700°C [1292°F] for 15 h). A potentio/galvanostat system was installed that operates

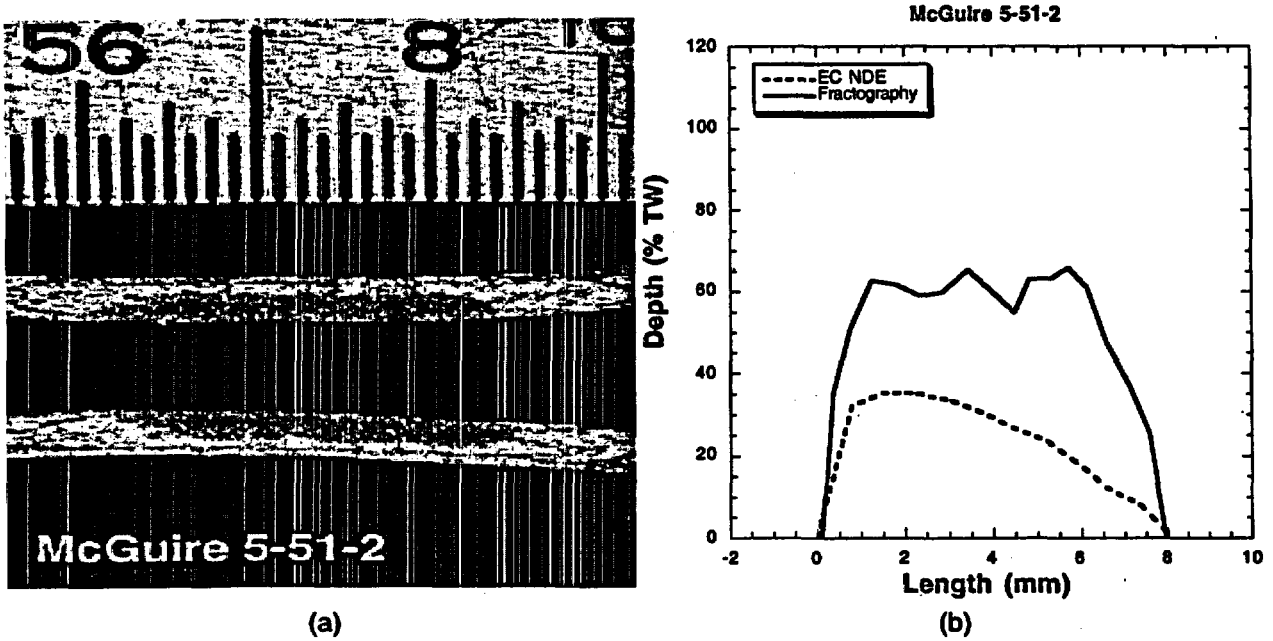

Figure 4.15. Fractography profile and NDE for axial ODSCC in McGuire tube specimen 5–51–2.

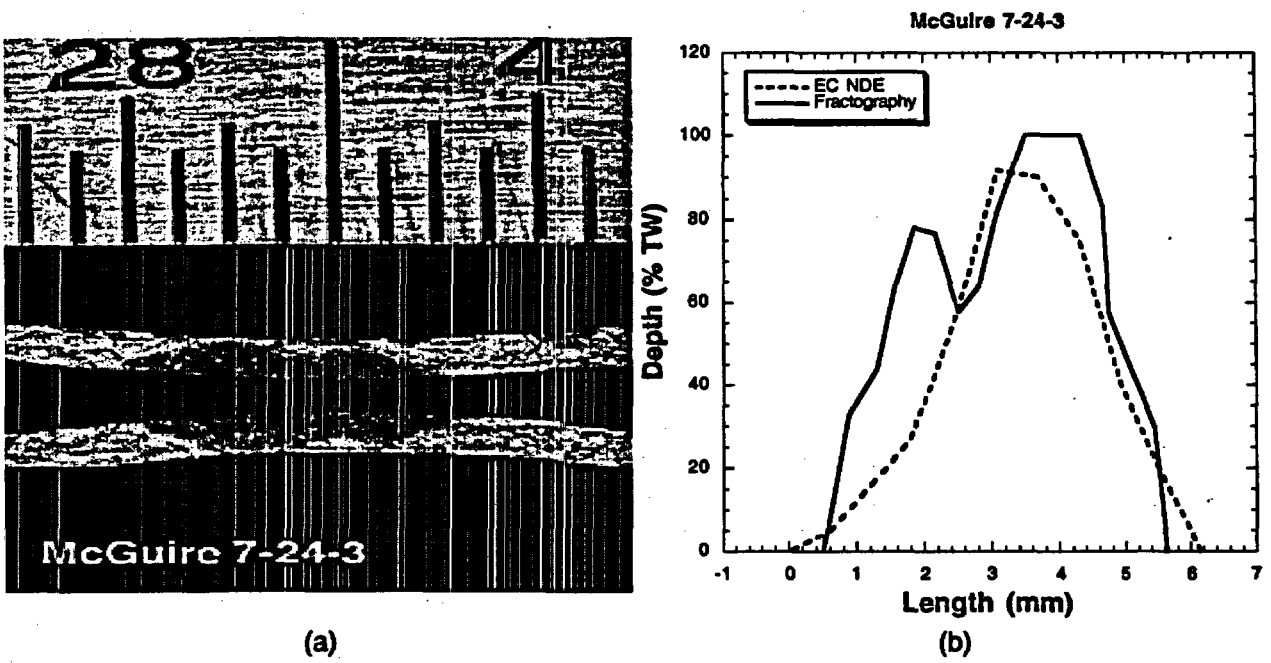

Figure 4.16. Fractography profile and NDE for axial ODSCC in McGuire tube specimen 7–24–3.

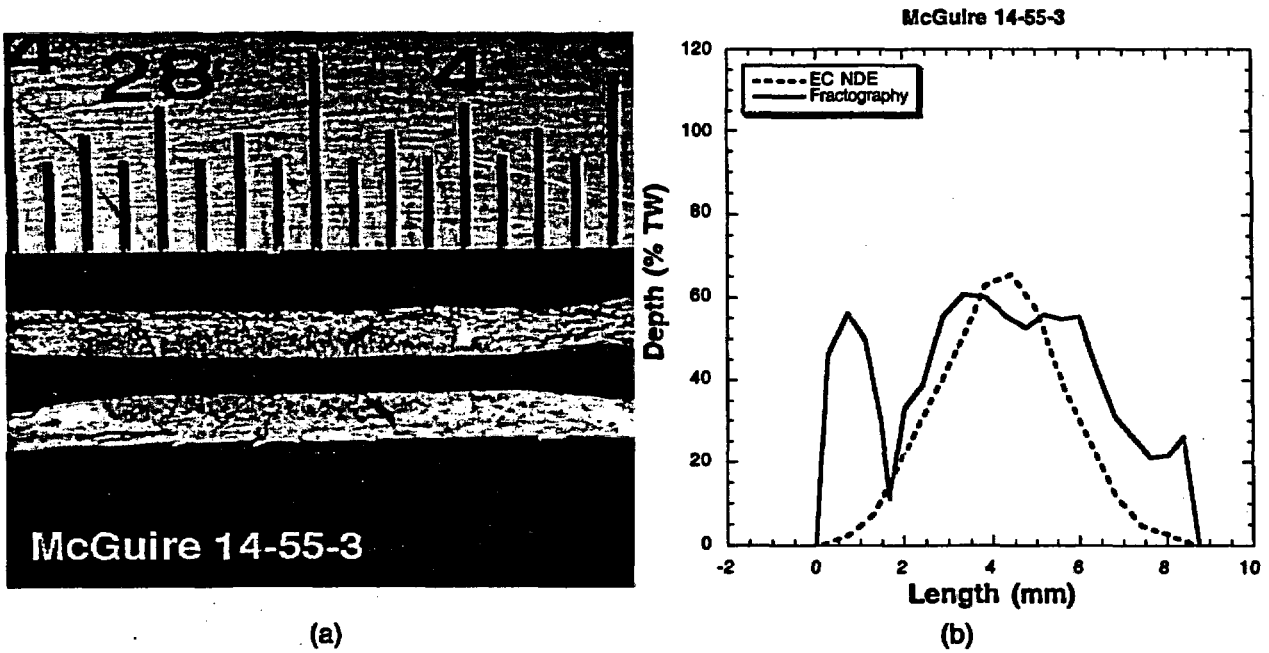

(a) (b)

Figure 4.17. Fractography profile and NDE for axial ODSCC in McGuire tube specimen 14–55–3.

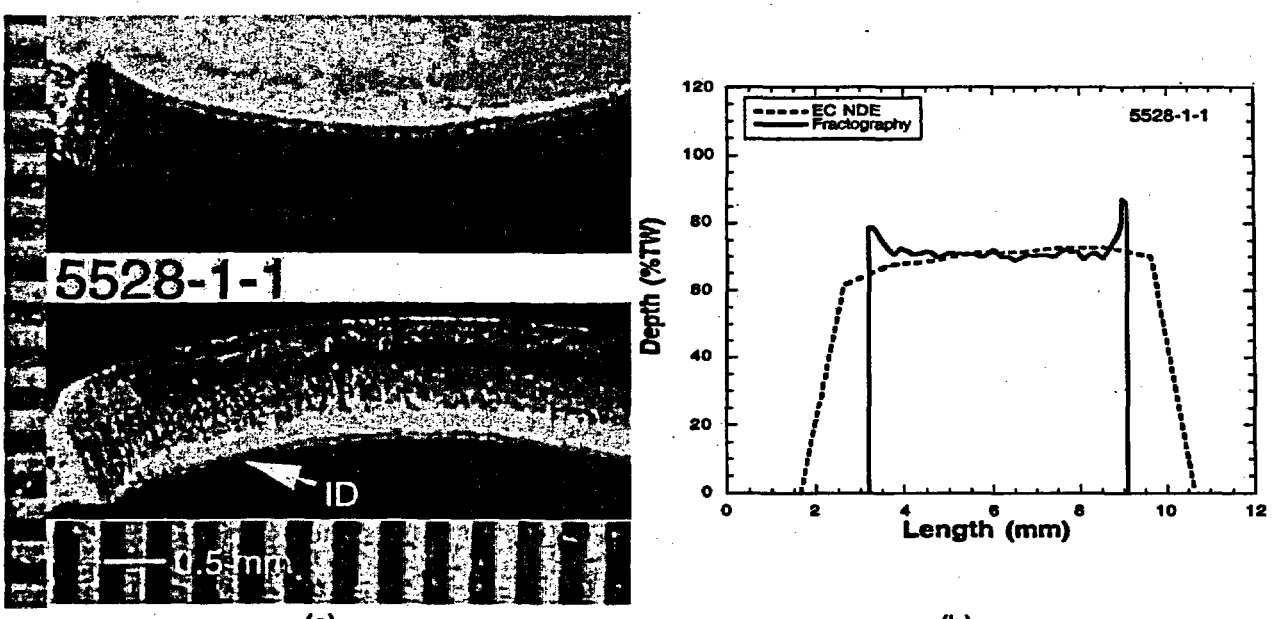

(a) (b)

Figure 4.18. Fractography of axial laser–cut 5528–1–1 and profiles determined by EC/NDE and fractography.

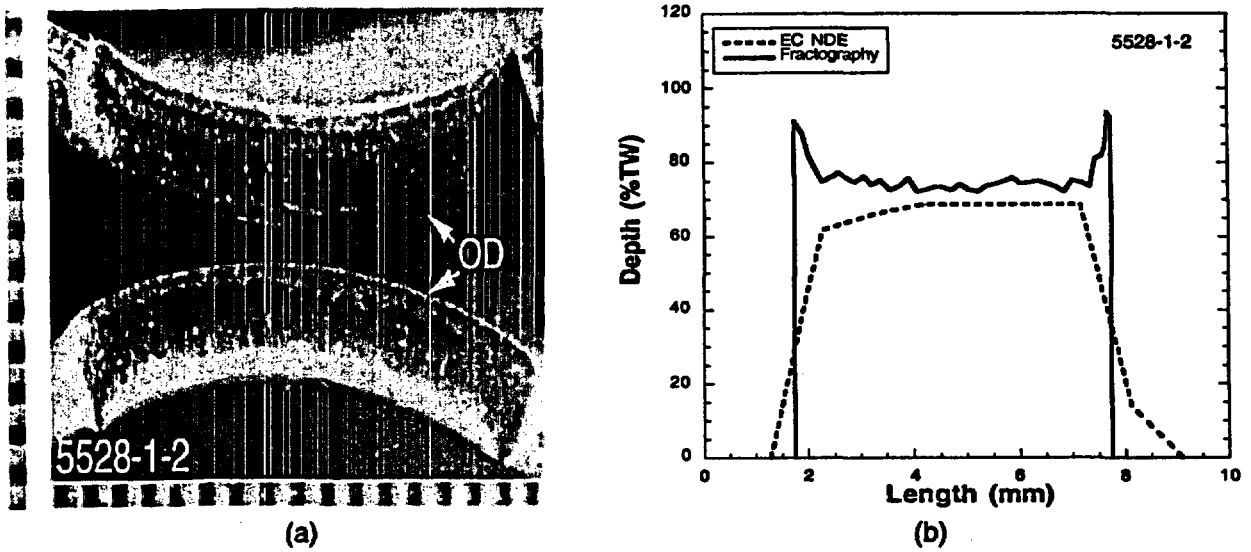

(a) (b)

Figure 4.19. Fractography of axial laser–cut 5528–1–2 and profiles determined by EC/NDE and fractography.

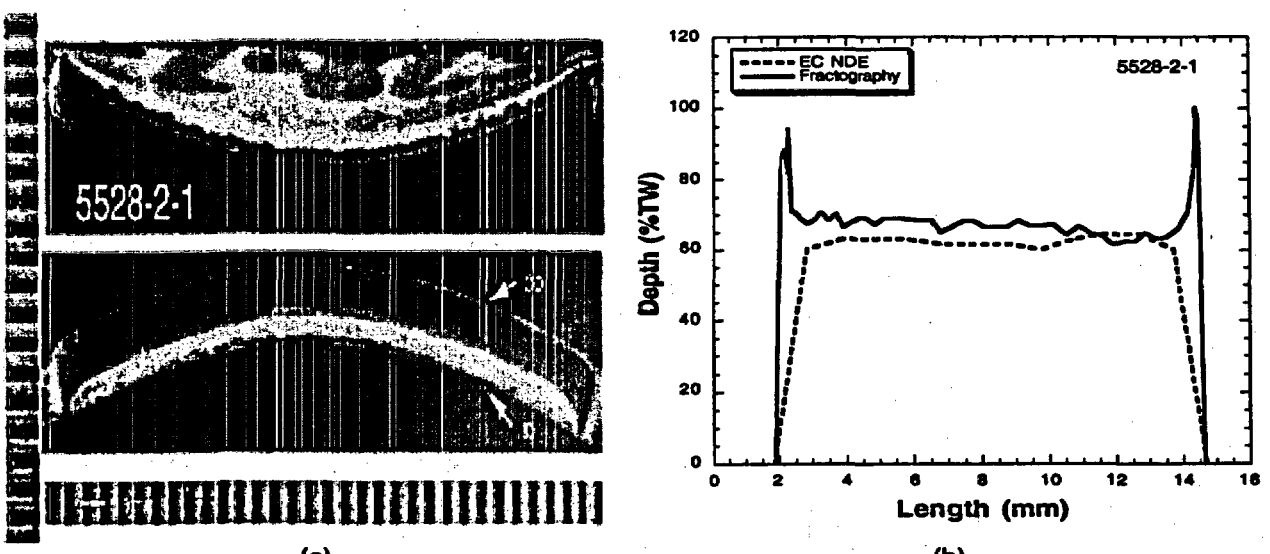

(a) (b)

Figure 4.20. Fractography of axial laser–cut 5528–2–1 and profiles determined by EC/NDE and fractography.

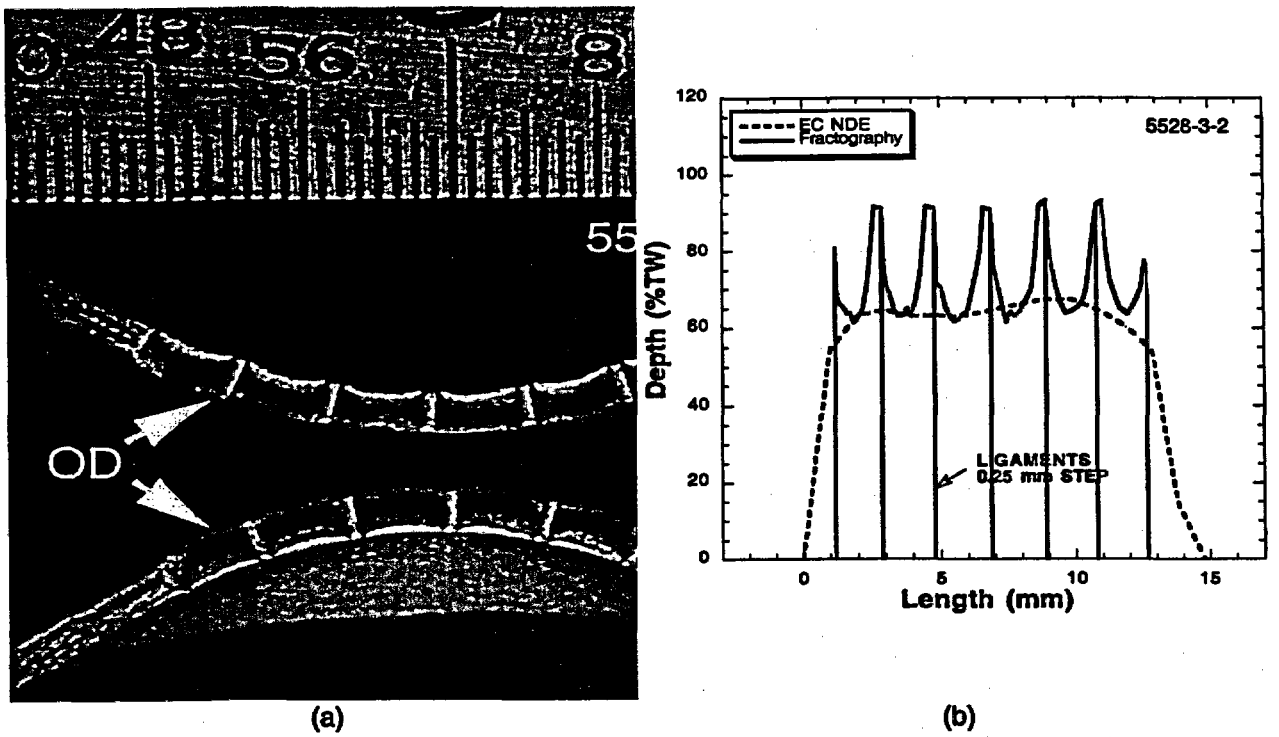

Figure 4.21. Fractography of axial laser–cut 5528–3–2 and profiles determined by EC/NDE and fractography.

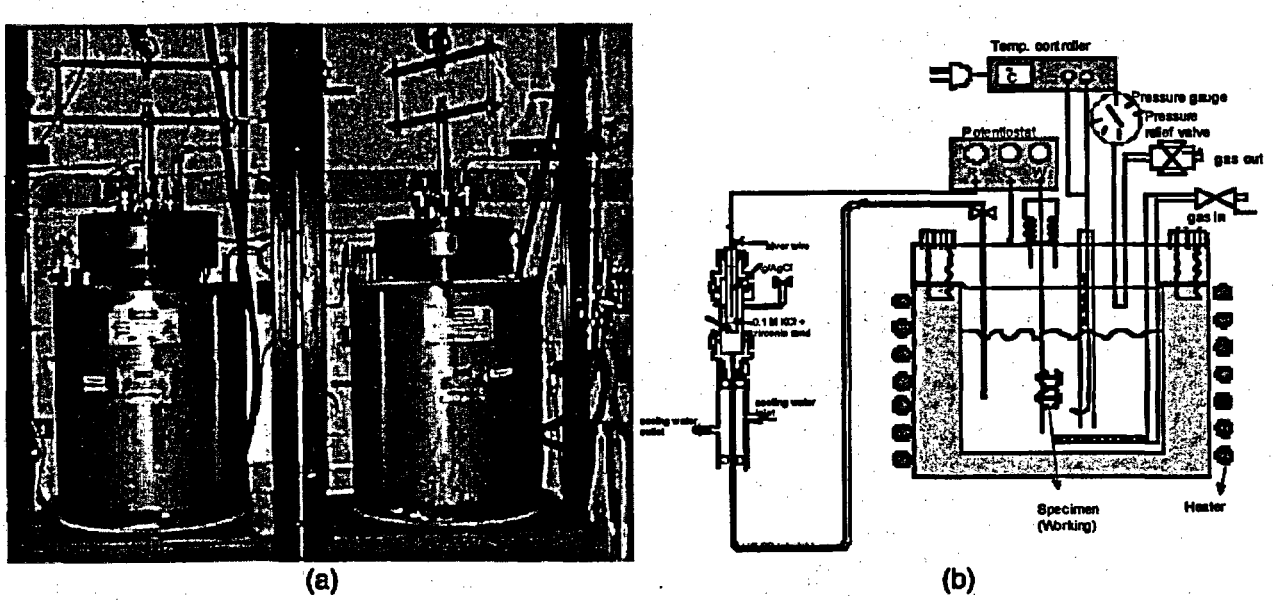

Figure 4.22. Eight-L autoclaves used for c–ring type static SCC and high-temperature electrochemistry tests.

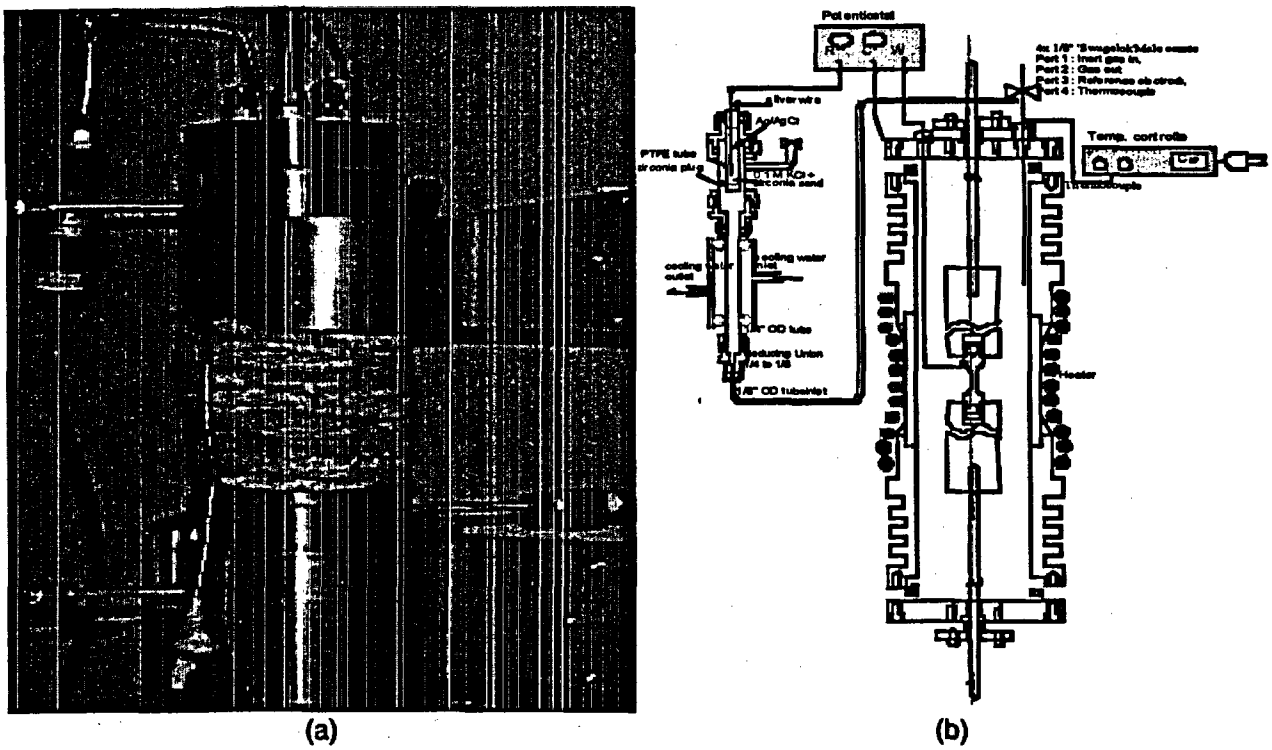

Figure 4.23. Small-diameter Hastelloy pipe autoclave system used for CERT.

electrically isolated signals from the ground. Preliminary functional tests have been performed for the systems. Silver–silver chloride reference electrodes were fabricated. Accuracy and stability of the reference electrode were evaluated by measuring the potential with respect to a standard calomel electrode (SCE) at room temperature. A reference electrode that was fabricated with a 32 mA/mm^2 oxidation current outperformed the others. The measured potential remained stable within 4.4% (2 mV) for about 850 h at room temperature (Fig. 4.24).

As part of functional tests, electrochemical polarization tests were performed for Alloy 600 tube specimens (Heat No. 96834 M81) in a near neutral (pH = 6.0) aqueous solution of 0.4 M sodium sulfate at 25°, 100°C, and 250°C (77, 212, and 482°F). Figure 4.25 shows the results of the polarization tests. The polarization curve, in general, shifts to higher potential and current ranges as the temperature of the solution increases. The corrosion potential is about –0.6, –0.4, and –0.1 V normal hydrogen electrode (NHE) at 25°, 100°C, and 250°C, respectively. The potential range for anodic passivation is significantly reduced at higher temperatures. Anodic polarization tests were performed for specimens from a reference Alloy 600 (Heat 96834 M81) in aqueous solutions of 0.4 M Na_2SO_4 at pH 3 and pH 6.8 at room temperature (Fig. 4.26). The corrosion potential is –2.57 V standard hydrogen electrode (SHE) in acidic solution (pH 3.0) and –0.60 V SHE in near neutral solution (pH 6.8), respectively. The primary activation current is 10^{-3} A/cm^2 in pH 3.0 and 3×10^{-4} A/cm^2 in pH 6.8 solution. Electrochemical impedance (ECI), which provides information for characterization of the corrosion and passive layer at the specimen surface [21, 22], was measured for the Alloy 600 (Heat 96834 M81) specimens in a near-neutral (pH = 6.8) 0.4 M Na_2SO_4 at room temperature. The measurements were performed in a frequency range of 10^{-3}–10^5 Hz. Impedance and current versus electrochemical potential are plotted for 0.02 and 100 Hz (Figs. 4.27 and

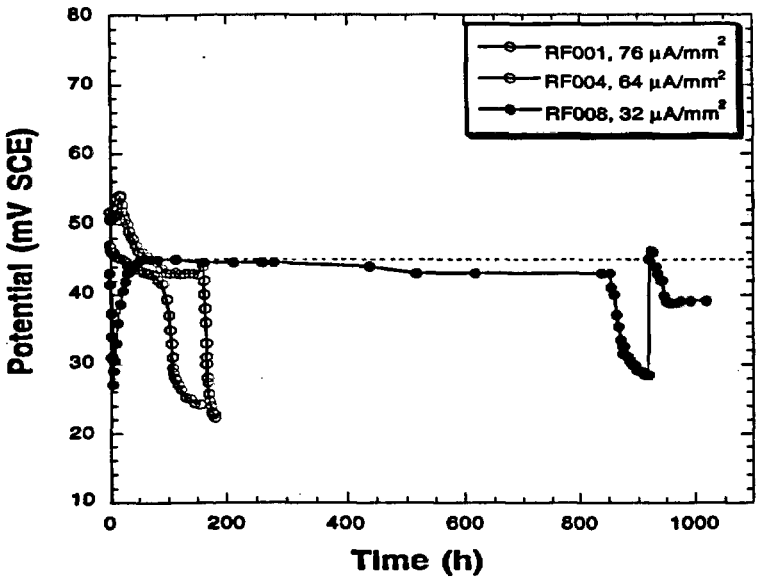

Figure 4.24.
Accuracy and stability of Ag/AgCl reference electrodes that were manufactured with different oxidation current.

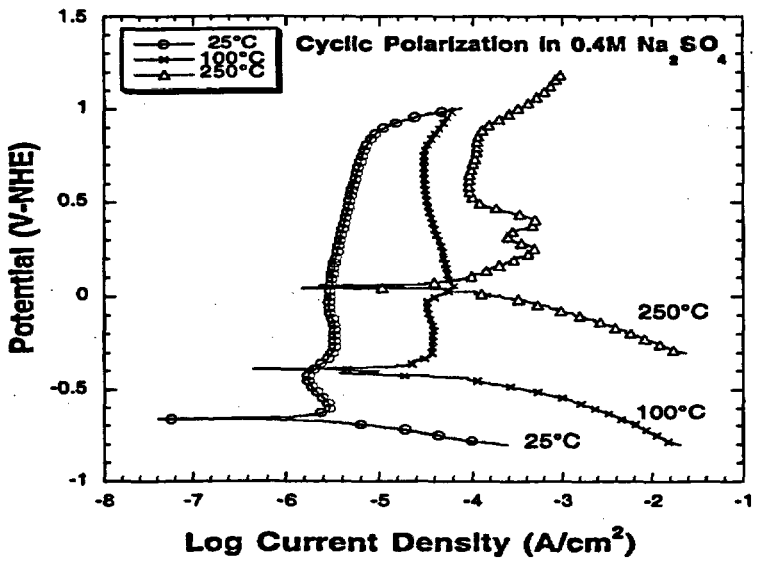

Figure 4.25.
Electrochemical polarization curve for Alloy 600 specimen (Heat No. M81) in 0.4 M sodium sulfate aqueous solution at 25, 100, and 250°C.

4.28). High and the maximum impedance are observed in the passive range potentials at both 0.01 and 100 Hz. Additional ECI measurements will be performed at the other environmental conditions (potential, pH, Pb concentration, and temperature), along with electrochemical polarization tests.

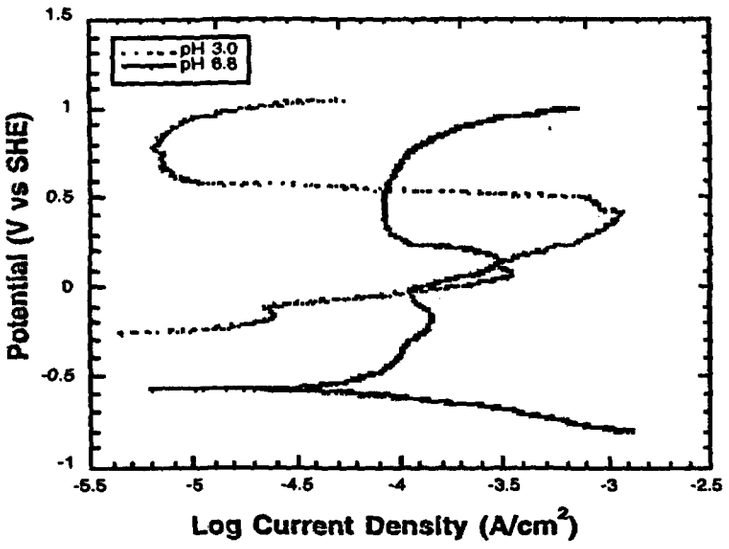

Figure 4.26.
Anodic polarization of Alloy 600 (Heat 96834 M81 annealed at 926.7°C) in 0.4 M Na_2SO_4 at pH 3.0 and pH 6.8.

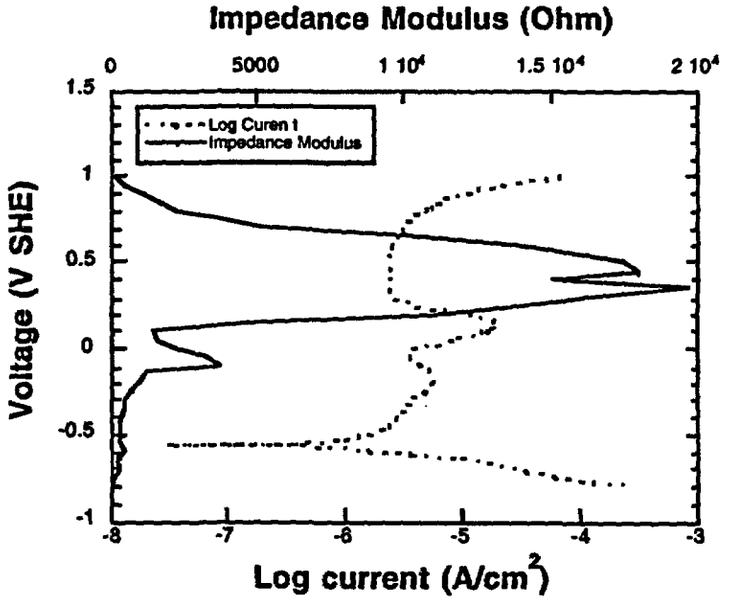

Figure 4.27.
Electrochemical impedance and current at 0.02 Hz for Alloy 600 (Heat 96834 M81 annealed at 926.7°C) in pH 6.8 and 0.4 M Na_2SO_4 aqueous solution at room temperature.

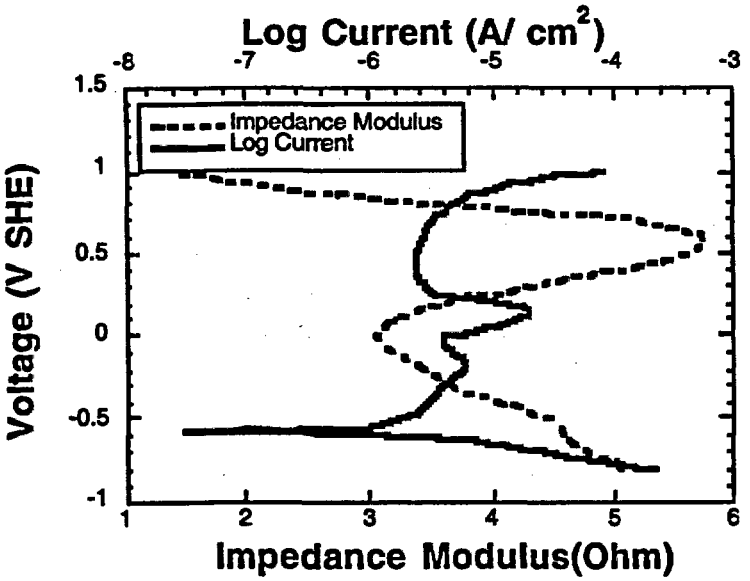

Figure 4.28.
Electrochemical impedance and current at 100 Hz for Alloy 600 (Heat 96834 M81 annealed at 926.7°C) in pH 6.8 and 0.4 M Na_2SO_4 aqueous solution at room temperature.

4.3 Tube Integrity Tests under Design Basis Conditions

Two facilities capable of testing steam generator tubes under design-basis conditions were constructed as part of the program. One of these is a high-temperature Pressure and Leak-Rate Test Facility (temperatures up to 343°C [650°F], pressures of up to 21 MPa [3000 psi], and pressurized-water flow rates up to 1520 L/min [400 gpm]) for conducting tube failure and leak-rate tests under prototypical SG operating conditions. The other is a room-temperature High-Pressure Test Facility (pressures up to 52 MPa [7,500 psi] and flow rates up to 48.4 L/min [12.8 gpm]) that operates at high pressures to determine the structural margins associated with flawed tubes. The High-Pressure Facility was also expanded to include a containment module designed for testing radioactively contaminated field-pulled tubes.

4.3.1 High-Temperature Pressure and Leak-Rate Test Facility

The ANL High-Temperature Pressure and Leak-Rate Test Facility is used to obtain data on the failure pressures, failure modes, and leak rates of flawed tubing at temperatures up to 343°C (650°F), pressures of up to 21 MPa (3000 psi), and pressurized-water flow rates up to 1520 L/min (400 gpm). This facility was designed to be able to maintain pressures up to those expected in design-basis accidents for flow rates approaching 1000 L/min (250 gpm). More details on the design and operation of the facilities are given in Ref. 23.

The facility has a large heated blowdown vessel with water inventory of ≈760 L (200 gal) that is able to provide high flow rates; piping and valves sized to minimize pressure drop in the supply line to the flawed tube; nitrogen cover-gas pressurization in the blowdown vessel with computer feedback control to maintain pressure even at high flow rates; a downstream back-pressure regulator valve to control tube pressure differential, thereby minimizing non-prototypical two-phase flow from entering the tube and permitting rapid pressure control; and a tube test module containment vessel. This test module can hold tubes of ≈0.15-1.0 m (6–40 in.) in length and can also be fitted with support stings to simulate support plate constraints on flawed tubes. A photograph of the facility is shown in Fig. 4.29.

Diagrams of the facility and test module are shown in Figs. 4.30 and 4.31, respectively. The pressurized and heated blowdown vessel holds ≈760 L (200 gal) of water and thereby provides adequate water inventory for ramping the tube pressure differential P1-P2 and testing tube specimens that contain preexisting throughwall flaws. Tube pressure differential ramp-up is produced through a back-pressure regulator valve (V6) located downstream from the test module containment vessel. The pressure differential can also be ramped up by increasing the gas overpressure in the blowdown vessel. Both modes of operation can be carried out under manual or computer control. In the computer-controlled mode, the pressure can be programmed to simulate a prototypical transient pressure history. During a test, the blowdown vessel is maintained at a constant pressure P3 up to 21 MPa (3000 psi) by use of regulated nitrogen cover gas pressurization from a 30-MPa (4400-psi) tank system of 0.9659 ML (34,110 standard ft^3) capacity. The differential pressure P1-P2 across the specimen wall is ramped up in a series of quasi-steady plateau increases through feedback control of valve V6, which controls pressure P2. The pressure P2 can also be increased linearly with time at differing rates. The flow rate Q, the pressure differential P1-P2, and the temperature are recorded as a function of time.

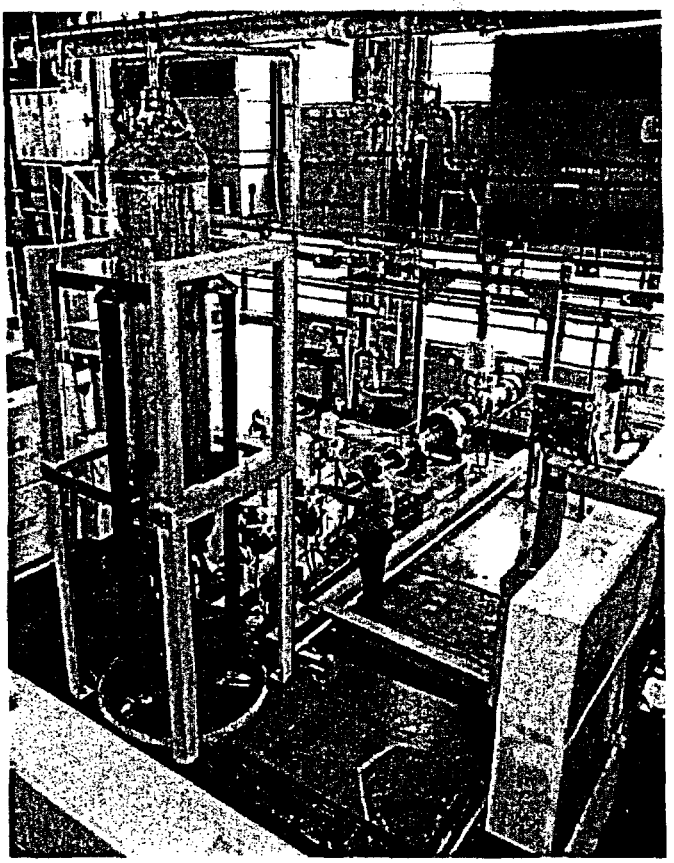

Figure 4.29
ANL Pressure and Leak-Rate Test Facility.

A turbine flow meter is located immediately upstream of the test module to monitor the leak rate. Load cells in the support legs of the blowdown vessel are used to monitor the mass of the water in the blowdown vessel as a function of time, thereby providing a backup to and cross check of the flow meter. Any flow through a flaw is routed outdoors through a large pipe to minimize back pressure and is discharged into a large muffler for noise suppression.

Tests in this facility do not use bladders. The flow capacity is adequate to test axial flaws as large as 25-38 mm (1.0-1.5 in.) in overall length and to drive them open by increasing pressure while the flaw is opening up. The differential pressure across the specimen is controlled by changing the back pressure on the tube. The pressure in the blowdown vessel during a test is always maintained sufficiently above the saturation pressure associated with the desired water temperature to prevent water flashing to steam in the water supply piping upstream of the test specimen. For flaws that do not leak initially or leak at a very low rate, the pressure difference across the specimen is raised in 0.34-1.38 MPa (50-200 psi) increments with a 5-10 s hold at each pressure plateau. If the leak rate increases, the pressurization rate is correspondingly increased. In general, the pressurization rate will not exceed 0.69 or 1.38 MPa/s (100 or 200 psi/s). If major ligament tearing occurs for a large flaw with a sudden jump in flow rate to 380 L/min (100 gpm) or more, the test pressure is then set to a constant value. The actual pressure will initially vary, but a steady-state pressure and corresponding flow rate can be obtained through feedback control of the computerized gas pressurization valves. The test is shut down automatically when the vessel water inventory drops to a minimum level.

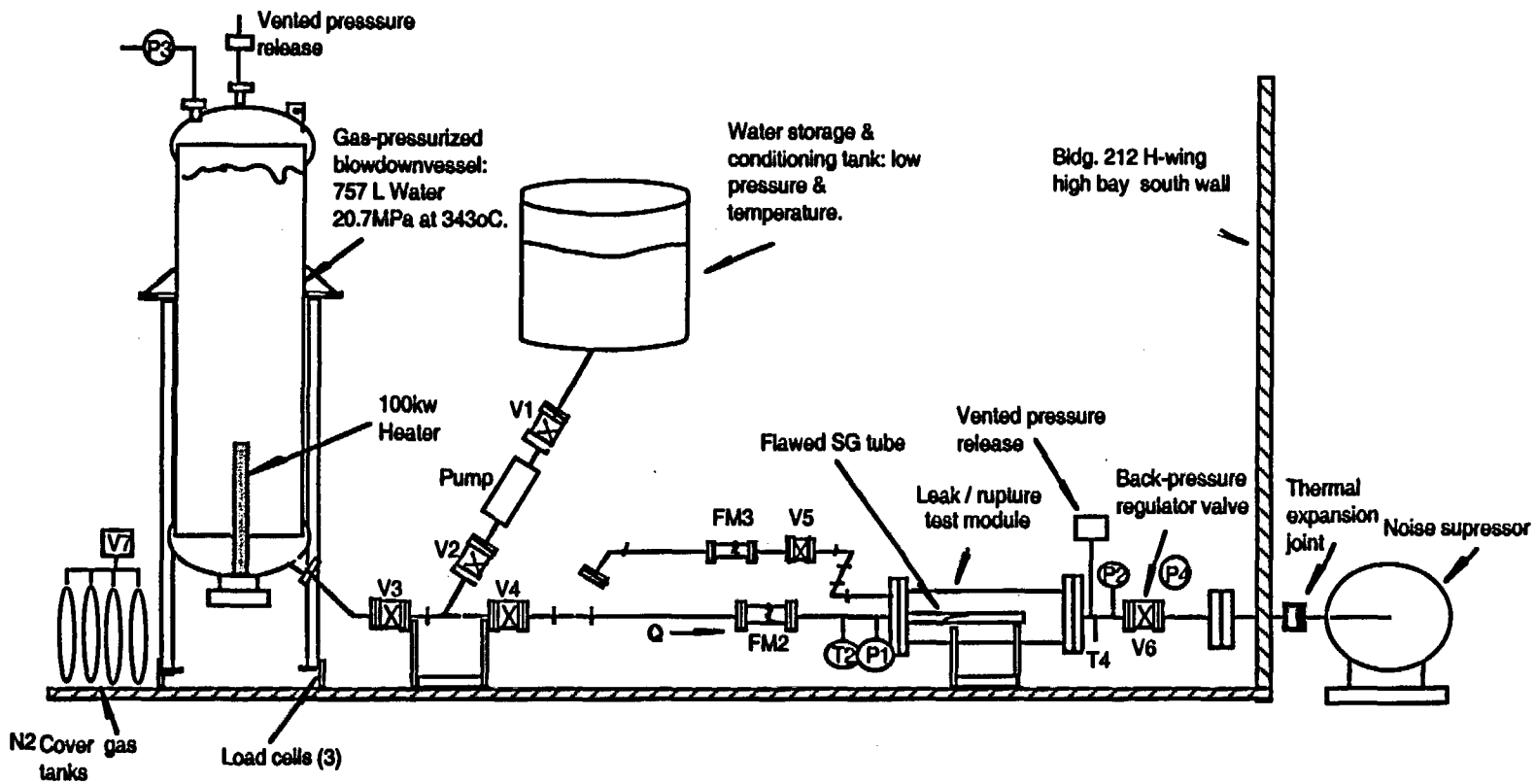

Figure. 4.30. High-Temperature Pressure and Leak-Rate Test Facility.

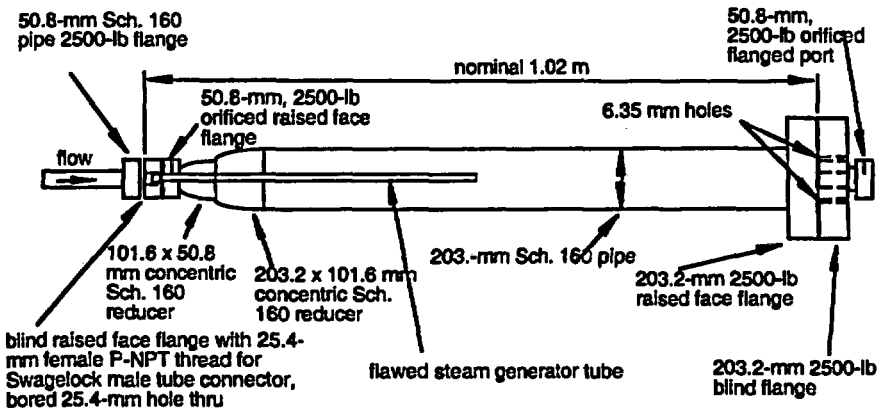

Figure 4.31. Tube test module for Pressure and Leak-Rate Test Facility.

Another type of test is conducted to determine whether flaws will exhibit time-dependent opening under constant temperature and pressures associated with normal and main steam line break (MSLB) conditions. In this test, a 8.3 MPa (1200 psi) pressure differential is held from one to several hours (depending on leak rate and water inventory), and the flaw is monitored for signs of leak initiation or increased flow rate. After this hold period, the tube pressure differential is increased in 0.69 or 1.38 MPa (100 or 200 psi) increments up to MSLB pressure. At each step, the pressure is held constant for a period of a few seconds to several minutes, depending upon the flow rate. After the MSLB pressure is reached, the pressure is held for an extended time (dictated by remaining water inventory), and the leak rate monitored.

4.3.2 Room-Temperature High-Pressure Test Facility

The Room-Temperature High-Pressure Test Facility can produce pressures up to 51.7 MPa (7500 psi) and is used to investigate the design margin associated with flawed tubes. Because the facility has a 48.4 L/min (12.8 gpm) flow capability at 51.7 MPa (7500 psi), tubes with small throughwall flaws can be tested without the use of a bladder. For somewhat larger cracks for which bladders and foils are required to maintain pressure, the small leaks that may occur during tube pressurization are less likely to result in an aborted test.

This facility can also be used for long-duration tests of crack stability and for jet-impingement erosion tests on adjacent tubes, since water can be continuously supplied from an outside source during a test. The apparatus is also capable of measuring very low flow rates (considerably less than the 0.04 L/min [0.01 gpm] lower limit for the Pressure and Leak-Rate Test Facility) through the use of flaw leak collection and timed measurement of water mass. Additionally, real-time ultra-high-speed video recording (2000-12,000 frames per second) of crack and jet dynamic behavior can be done during testing. A special containment module for testing radioactively contaminated field-pulled tubes has also been built.

A schematic diagram of the facility is shown in Fig. 4.32, and a photograph of the facility is shown in Fig. 4.33. Pressure is provided by a constant-rpm, single-acting triplex, constant-displacement pump driven by a 60-hp electric motor that provides a constant 48.4 L/min (12.8 gpm) flow of water at up to 51.7 MPa (7500 psi). Pump-generated pressure pulsation is <0.34 MPa (<50 psi). The pump has two overpressurization protection safety relief valves, one located on the pump, and the other on the 139-L (40-gal) water accumulator suction tank. The

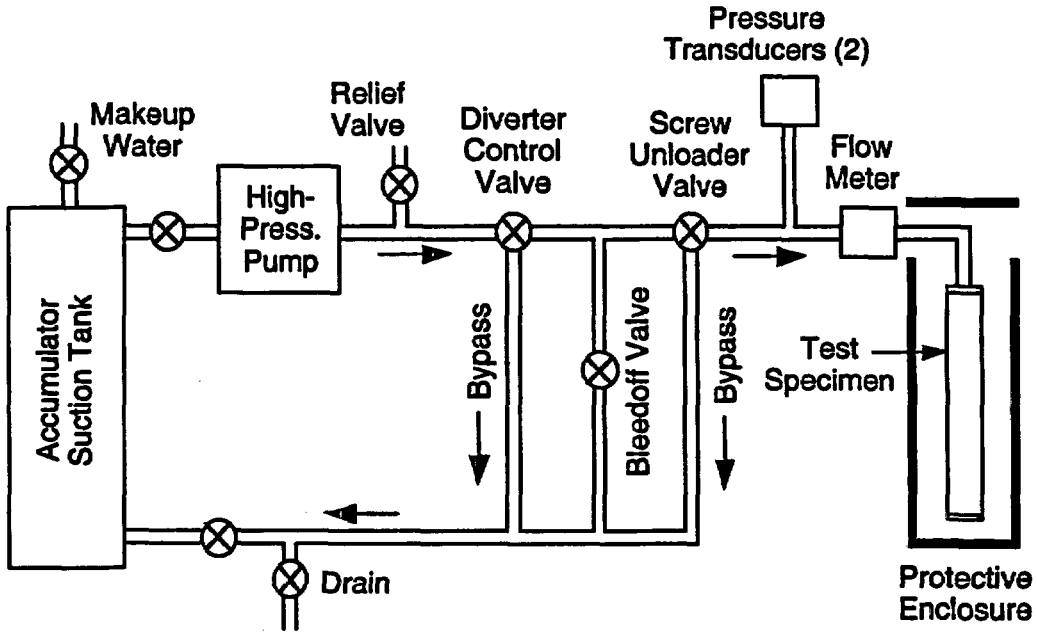

Figure 4.32. Schematic diagram of High-Pressure Test Facility pressurizer and associated components.

lever operated hydro-diverter control valve originally supplied with the pressurizer was modified to work in series with a screw unloader valve that allows more positive, finer control of pressurization. The pressurizer water pump system can operate with a continuous supply of water from the building water system.

The tube pressurization rate can be varied from quasi-steady-state (<0.7 MPa/s or <100 psi/s) to 7-21 MPa/s (1000-3000 psi/s), which encompasses the rates given in EPRI guidelines for burst testing to 70 MPa/s (10,000 psi/s). Pressurization over the full range of the system, 0-52 MPa (0-7500 psi), is possible at all of these pressurization rates.

The module for testing of clean tubes (Fig. 4.32) consists of a 0.46-m (18-in.)-diameter x 1.02-m (40-in.)-long stainless steel pipe with transparent Lexan™ plates at the ends of the module to confine the water jet spray produced by a leaking tube.

Figure 4.34 shows a schematic of the containment module for testing field-pulled tubes. This module is also supplied with pressurized water and controlled from the High-Pressure Facility. It is essentially a 380 L (100 gal) stainless steel holding tank that captures all the water that flows through the tube and flaw under test. Thus, any particulate contamination released from the tube will be captured. Upon completion of a test, the water in the tank is filtered to trap any particulate before the water is released. A breather/overflow vent prevents module pressure buildup during testing and is fitted with a filter to prevent any release of particulate contamination. A level sensor alarm in the containment module is used to indicate that the maximum water fill level has been reached, and the test should be terminated.

Whenever possible, tests are performed without bladders or reinforcing foils and under quasi-steady pressurization rates to avoid complications in interpreting data and to maximize information on flaw behavior. If flaws do not fail unstably in the initial test without a bladder,

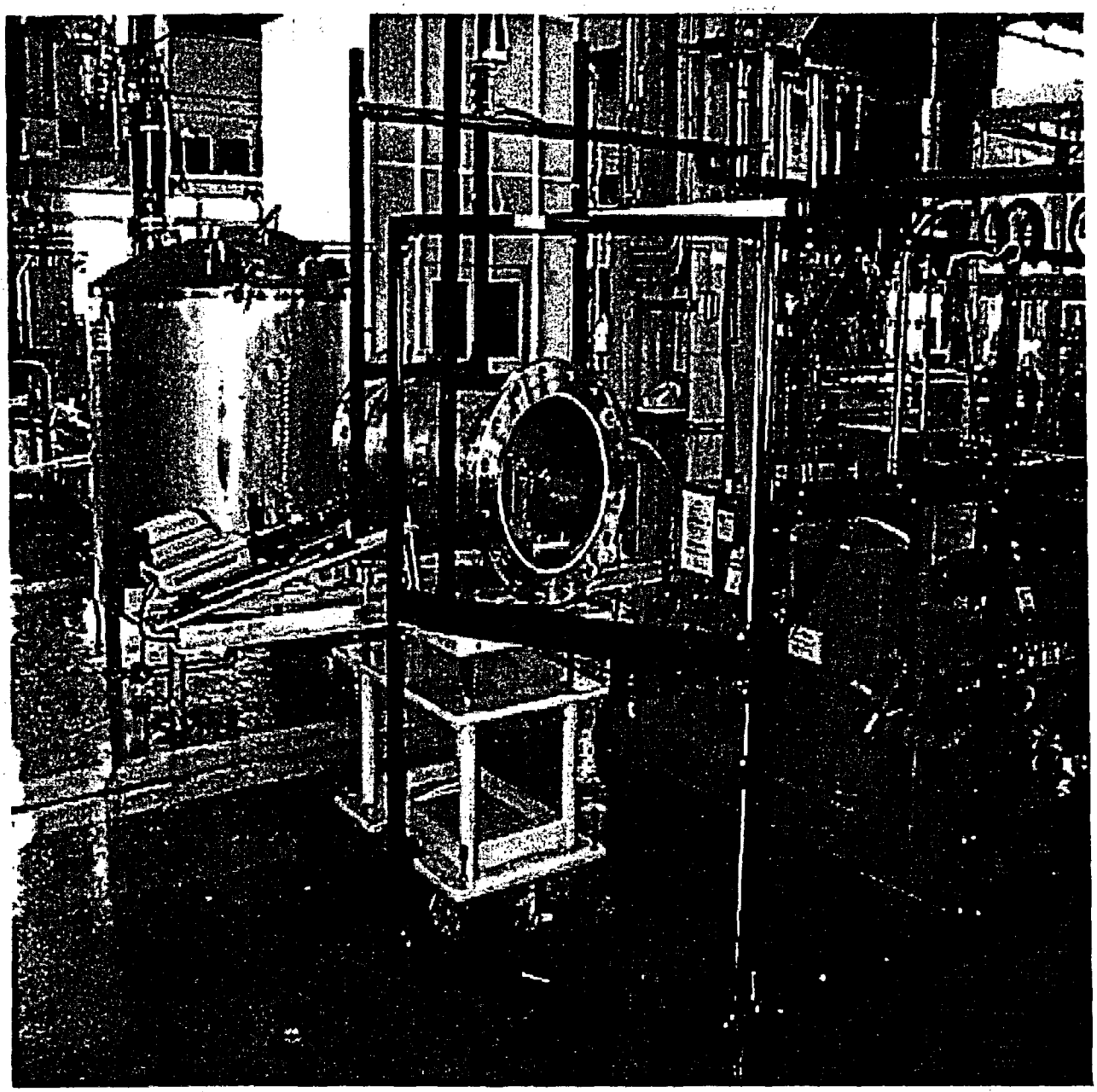

Figure 4.33 Overall view of major components of High-Pressure Test Facility. Visible are the water pump pressurizer, test module, tube support, video system, and 3000-L (800-gal) tank for conducting tests on field-pulled tubes. Also shown is Lexan™ personnel-protection barrier.

a bladder and possibly a backup foil are inserted in the tube to permit continuation of the test. The most commonly used bladder is hard Tygon tubing with a 3.2-mm (1/8-in.) wall thickness. The tubing is slightly smaller than the inside diameter of the specimen and is slipped inside the flawed tube and sealed in each end with a Teflon plug (Figs. 4.35 and 4.36). For cracks longer than 12.7 mm (1/2 in.), Stage II tests usually also require a 0.13-mm (0.005-in.)-thick brass foil to be inserted between the inner wall of the SG tube and the outer surface of the bladder. The foil extends 6.3 mm (0.25-in.) beyond the extremities of the flaw. The foil and

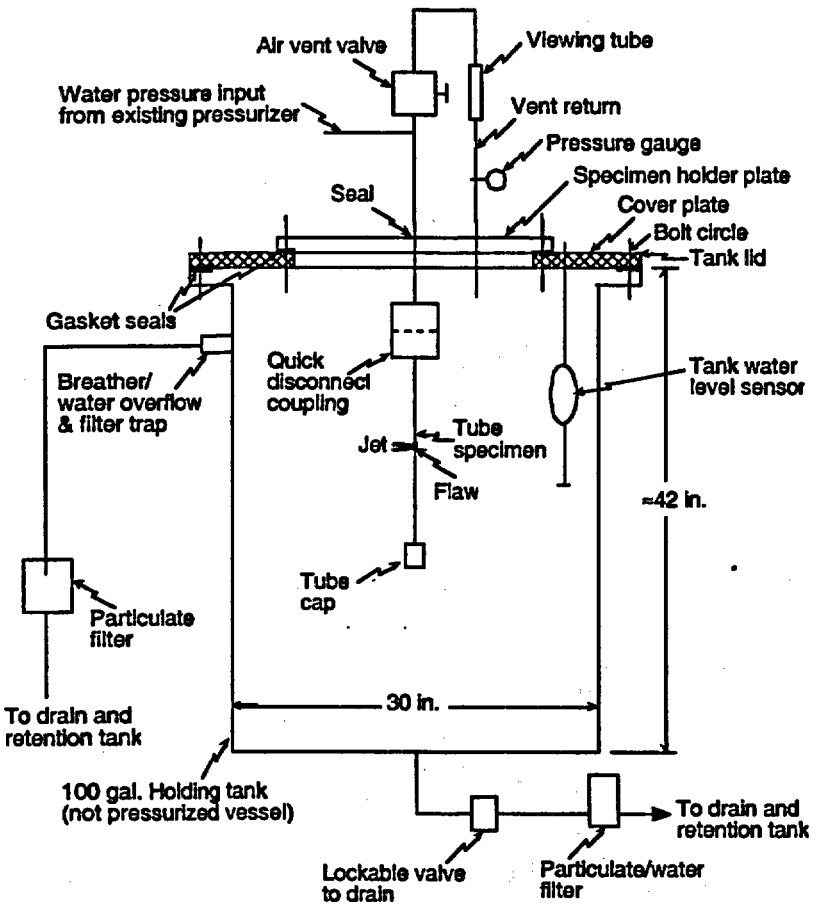

Figure 4.34. Containment module for testing radioactively-contaminated field-pulled tubes.

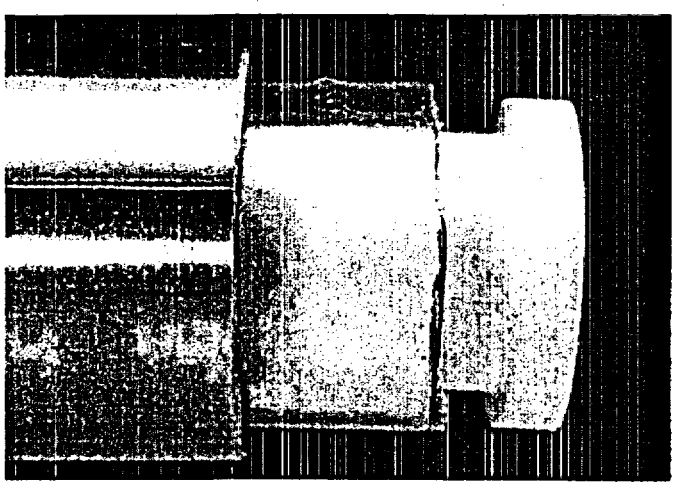

Figure 4.35.
Side view of tube with bladder and bored plug seal being installed.

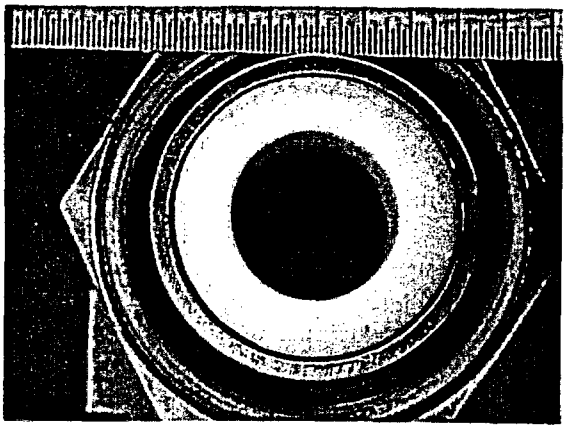

Figure 4.36.
End view of tube with bladder and plug installed.

bladder are lubricated with a multipurpose spray lubricant to reduce friction between the foil and the SG tubing. To avoid extrusion of the bladder/foil through the flaw, the tube is pressurized at a rate of 3.5–7 MPa/s (500–1000 psi/s).

4.3.3 Test Results for Machined Flaws

All machined flaws were fabricated from 22.2-mm (7/8-in.)-diameter Alloy 600 SG tubing. Electro-discharge machining and laser cutting were used to fabricate single notches (both axial and circumferential), circular holes, and multiple flaw geometries of various types. Laser cutting generates tighter flaws than can be achieved with EDM.

The flawed tubes were all 0.56-m (22-in.) long, with the flaw centered at 0.15 m (6 in.) from the end of the tube fitted with a welded plug. The unplugged end of the tube was held in place in the test module vessel of the Pressure and Leak-Rate Test Facility or the High-Pressure Test Facility by a Swagelok fitting with a hole that permits flow to enter the flawed tube.

4.3.3.1 EDM Circular Holes

A series of tests was conducted on 22.2-mm (7/8-in.)-diameter SG tubes in the Pressure and Leak-Rate Test Facility using room- and high-temperature water. The tubes had EDM sharp-edged, circular throughwall holes The tests covered hole sizes with diameters ranging from 0.40-6.35-mm (1/64-1/4-in.) and were initially used to check out the facility in bringing it online.

Leakage from the SG tubes occured over a wide range of ratios of crack length (L) to crack opening widths (h), as shown in Fig. 4.37. Most of the database used in formulating and validating the current multiphase models for crack leak rate comes from tests simulating flow-through SCCs in thick-wall piping. In these cases, L/h is typically >100. As shown in Fig. 4.37, under MSLB conditions for cracks in steam generator tubes longer than about 6 mm (0.25 in.), L/h is <100, i.e., these cracks are more open than SCCs in piping. The work of Amos and Schrock [24] and others shows that L/h strongly influences whether choking can occur and also the importance of friction and roughness effects. In addition, flashing of a metastable liquid depends on a relaxation time, which implies that the actual wall thickness as well as L/h may be important in determining when flashing occurs within the crack. For flows through a relatively large orifice such as a 0.79-mm (1/32-in.)-diameter hole at 17.2 MPa (2500 psi), the mean velocity of the jet is ≈120 m/s (≈400 ft/s). Thus, the flow through the

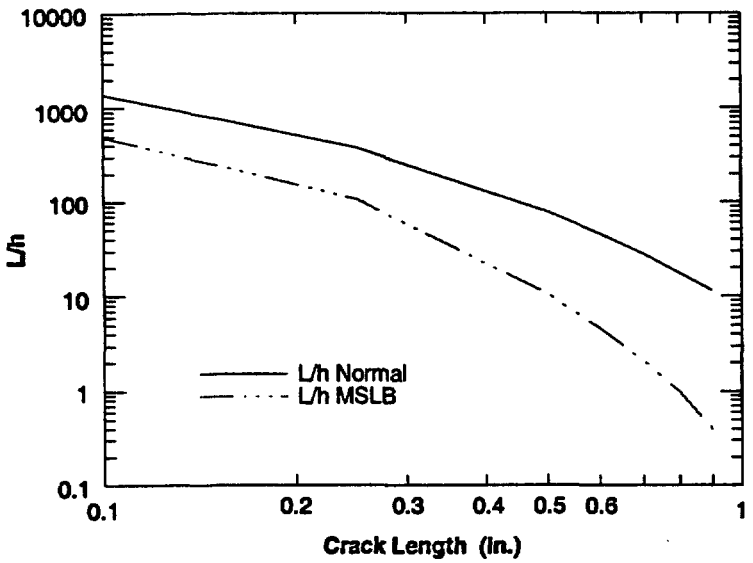

Figure 4.37.
Variation of the ratio of flow path length to the crack opening width with crack length for normal operating and main steam line break conditions.

tube wall requires ≈1 x 10^{-5} s. The time to travel across the 6.35 mm (0.25 in.) gap to the adjacent tube is ≈5.2 x 10^{-5} s. Because these times are short, in some cases, flashing may not occur within the crack or possibly not even completely in the gap between tubes.

The flow rates for the 0.794-, 3.175-, and 6.35-mm ($^1/_{32}$-, $^1/_8$- and $^1/_4$-in.)-diameter orifices at the nominal differential pressure of 17.2 MPa (2500 psi) were 2.76, 56.0, and 216 L/min (0.73, 14.8, and 57.0 gpm), respectively. The average jet velocity through the 3.175-mm ($^1/_8$-in.)-diameter orifice at 17.2 MPa (2500 psi) was 112 m/s (366 ft/s). Such jet velocities can produce significant lateral thrust, and the specimen with a 6.35-mm ($^1/_4$-in.)-diameter orifice was bent ≈10° from its axis as a result of this thrust. No bending was observed for the specimens with smaller orifices.

The standard correlation for incompressible flow through a sharp-edged circular orifice is,

$$Q = C \cdot A \cdot \left(\frac{\Delta p}{\rho}\right)^{1/2}, \qquad (4.1)$$

where Q is the flow rate, C is the orifice discharge coefficient, A is the cross-sectional flow area, Δp is the pressure difference across the orifice, and ρ is the density of the fluid. Room-temperature flow rates were predicted quite well using a value of 0.6 for C. The orifice model predicts a temperature effect on flow rate through the dependence of fluid density on temperature. The density of water at 21 and 282°C (70 and 540°F) is 1.00 and 0.745 g/cm^3 (62.3 and 46.51 lb/ft^3), respectively. In two separate tests, the same tube tested at a pressure differential of 8.72 MPa (1265 psi) and a temperature of 282°C (540°F) exhibited a flow rate of 3.03 L/min (11.45 gpm). With C = 0.6, Eq. (4.1) predicts a flow rate of 3.04 L/min (11.51 gpm), in very good agreement with the experimental value. The orifice correlation predicts a flow rate of 37.7 L/min (9.95 gpm) for this same 3.175-mm (1/8-in.)-diameter hole under the same pressure differential for room-temperature water, in good agreement with the experimental value of 37.1 L/min (9.8 gpm).

For the 0.79,- 3.18-, and 6.35-mm ($^1/_{32}$-, $^1/_8$-, and $^1/_4$-in.)-diameter orifices tested at a pressure difference of 17.2 MPa (2500 psi) and room temperature, the orifice model predicts flow rates of 3.33, 53.0, and 212 L/min (0.88, 14.0, and 56.0 gpm), respectively, which are again in good agreement with the experimental values.

Additional tests were performed with orifice diameters of 3.18, 1.59, 0.79, and 0.40 mm ($^1/_8$, 1/16, $^1/_{32}$, and $^1/_{64}$ in.) at room temperature (21°C or 70°F) and elevated temperature (282°C or 540°F) for pressure differences of 0-17.2 MPa (0-2500 psi). The ratio of the flow path length (L) (wall thickness of the tube =1.27 mm [0.05-in.]) to hole diameter (h) for these hole sizes is 0.4, 0.8, 1.6, and 3.2, respectively. Even the smallest of the orifices is still very open compared to most cracks.

For the elevated-temperature tests, the internal tube pressurization was held at 17.2 MPa (2500 psi), and the back pressure on the outside of the tube was varied from zero to a few MPa (several hundred psi) to determine if the flow was choked. For all four orifice sizes, changes in the back pressure produced changes in hole flow rate, indicating no choking. The orifice flow model predicts the flow rates to within 8% of the experimental values in all the tests. In the high-temperature tests, the water does not appear to flash to steam until after it exits the orifices.

4.3.3.2 Axial EDM OD Notches

A series of tests on tubes with single 38.1-, 25.4-, 12.7-, and 8.9-mm (1.5-, 1.0-, 0.5-, and 0.35-in.)-long axial EDM OD notches of various depths was performed at room and elevated temperatures in the Pressure and Leak-Rate Test Facility. All flaws were nominally 0.20 mm (0.0075 in.) wide.

Three tubes (T3EA80X1.5, T4EA80X1.5, and T7EA80X1.5) with geometrically identical EDM flaws were tested at room temperature. These axial OD flaws were 38.1-mm (1.5 in.)-long, 0.20-mm (0.0075-in.)-wide, and 80% TW. Two of these tubes had the same as-received heat treatment, and the remaining tube was sensitized (solution heat treated at 1100°C for 10 min and aged at 600°C for 48 h) before testing.

The behavior of the three tubes was quite similar, and test details are therefore presented only for tube T4EA80X1.5. For this tube, the pressure difference across the tube wall was increased in a series of pressure steps starting at 0.69 MPa (100 psi) in increments of 1.38 MPa (200 psi) up to 10.3 MPa (1500 psi), then in increments of 0.69 MPa (100 psi) up to 13.8 MPa (2000 psi), and finally in increments of 0.34 MPa (50 psi). At ≈17.22 MPa (2497 psi), the flow through the flaw abruptly increased from zero to a sustained leak rate of ≈1470 L/min (388 gpm) in less than 1 s. The ANL ligament failure correlation[4] predicted a failure pressure of 17.24 MPa (2500 psi) for this flaw. The facility automatically shut down because of low water inventory in the blowdown vessel. The facility was originally designed to sustain a leak rate of at least 760 L/min (200 gpm), and this design limit was exceeded in this test. Upon removal from the test module, the tube was found to have been bent by the jet thrust, and the crack had opened up to a large hole.

Table 4.3 summarizes the failure pressures, flow rates, and posttest rupture geometries for tests T3EA80X1.5, T4EA80X1.5, and T7EA80X1.5. The rupture geometries were obtained by an analyses of digital photographs of the failures that project the actual three-dimensional

Table 4.3. Results from pressure and leak-rate tests on tubes with 38.1-mm (1.5-in.)-long 80% TW axial EDM flaws. Tube T3EA80X1.5 was subjected to a sensitization heat treatment before testing, and the remaining two tubes were tested in as-received mill-annealed condition.

Tube ID	Failure Pressure, MPa [psi]	Flow Rate, L/min [gpm]	Opening Area, cm^2 [$in.^2$]	Overall Length, cm/ [in.]	Maximum Width, cm/ [in.]
T3EA80X1.5	13.8 [2000]	1605 [424]	8.31 [0.507]	3.30 [1.30]	1.83 [0.72]
T4EA80X1.5	17.2 [2497]	1469 [388]	7.41 [0.452]	3.35 [1.32]	1.60 [0.63]
T7EA80X1.5	16.5 [2398]	1453 [384]	7.24 0.442]	3.38 [1.33]	1.57 [0.62]

geometry onto a plane. The failure pressures, leak rates, and rupture geometry data for the two tubes with the same heat treatment (T4EA80X1.5 and T7EA80X1.5) are in close agreement. The sensitized tube (T3EA80X1.5) exhibited a reduced failure pressure, an increased flow area, and a larger opening. This heat treatment, which was used in the initial stages of this program to increase susceptibility to SCC, clearly weakens tubes. The failure behavior is consistent with the lower flow stress observed for this heat treatment [25].

Forty-two tests were performed on shorter EDM OD notches. These notches were all 0.19 mm (0.0075 in.) wide and had four axial lengths, namely 6.35, 12.7, 19.1, and 25.4 mm (0.25, 0.5, 0.75, and 1.0 in.). Flaws depths explored were 60, 80, 90, and 100% TW.

Room-temperature tests were run on specimens with 12.7-mm (0.5-in.) and 19.1-mm (0.75-in.)-long, 80 and 100% TW flaws without a bladder, with a bladder, and with a bladder plus backup foil to help understand the effects of bladders and foils on failure pressures. These tests are summarized in Table 4.4. For Specimen OM120, which was tested without a bladder, the throughwall ligament failed at a pressure of 26.9 MPa (3900 psi), which is in good agreement with the predicted value of 25.5 MPa (3700 psi). No discernible unstable tearing occurred at the notch ends. A 2.4-mm ($^3/_{32}$-in.) or 3.2-mm (1/8-in.)-thick hard Tygon bladder was used for the tests with a bladder.

Tests with bladders were performed for specimens with 80% TW flaws of 12.7 mm (0.5 in.) (OM121; Fig. 4.38) and 19.1 mm (0.75-in.) (OM123) lengths, respectively. The tests were conducted at a nominal pressurization rate of 13.8 MPa/s (2000 psi/s). Clearly, both flaws experienced significant tearing at both ends of the original notches. The experimental/predicted unstable burst pressures were 29.0/30.3 MPa (4200/4400 psi) and 21.9/22.8 MPa (3180/3300 psi), respectively.

A 12.7-mm (0.5-in.)-long 60% TW flaw, unlike an 80% TW flaw of the same length, will exhibit unstable tearing or bursting simultaneous with the failure of the throughwall ligament. Such flaws can be tested with and without a bladder to assess the effect of bladders on burst data. Tube OM113 was tested without a bladder. The flaw burst unstably without a bladder at

Table 4.4. Summary of room-temperature pressurization tests conducted using High-Pressure Test Facility on tubes with axial EDM notches to determine effect of internal Tygon tube bladder and 0.13-mm (0.005-in.)-thick brass backup foil on failure pressure. All tests with internal bladders were conducted at a pressurization rate of 13.8 MPa/s (2000 psi/s); the remaining tests were conducted at a quasi-steady-state pressurization rate.

Spec. ID	Flaw Geometry		Internal Bladder and Backup Foil	Unstable Burst Pressure	
	Length, mm (in.)	Depth, % TW		Experimental, MPa (psi)	Predicted, MPa (psi)
OM120	12.7 (0.5)	80	None	26.9[a] (3900)	25.5[a] (3700)
OM121	12.7 (0.5)	80	2.4-mm (3/32-in.)-thick bladder, no foil	29.0 (4200)	30.3 (4400)
OM123	19.1 (0.75)	80	2.4-mm (3/32-in.)-thick bladder, no foil	21.9 (3180)	22.8 (3300)
OM113	12.7 (0.5)	60	None	40.7 (5900)	38.6 (5600)
OM112	12.7 (0.5)	60	2.4-mm (3/32-in.)-thick bladder, no foil	41.4 (6000)	38.6 (5600)
OM102	12.7 (0.5)	100	2.4-mm (3/32-in.)-thick bladder, no foil	29.6 (4300)	30.3 (4400)
OM101	12.7 (0.5)	100	3.2-mm (1/8-in.)-thick bladder, no foil	29.6 (4296)	30.3 (4400)
OM133	12.7 (0.5)	100	3.2-mm (1/8-in.)-thick bladder plus foil extending 6.35 mm (0.25 in.) beyond notch	30.0 (4350)	30.3 (4400)
OM134	12.7 (0.5)	100	3.2-mm (1/8-in.)-thick bladder plus foil extending circumferentially 90° to either side of notch	30.7 (4450)	30.3 (4400)

[a]Pressure for failure of throughwall ligament; tube not tested to unstable burst.

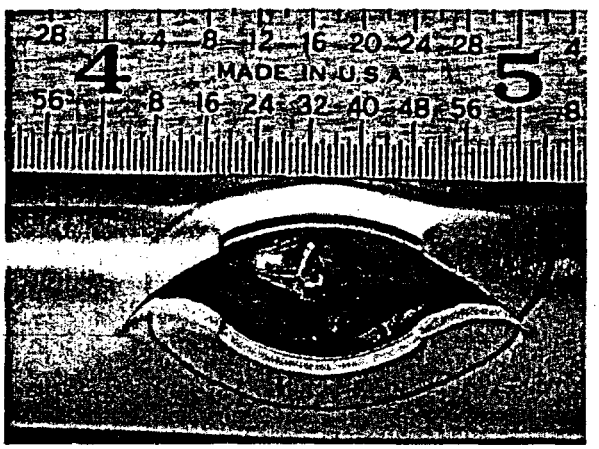

Figure 4.38.
Posttest appearance of specimen OM121 (12.7-mm [0.5-in.]-long 80% TW axial EDM notch), tested with bladder at a pressurization rate of 13.8 MPa/s (2000 psi/s). Flaw burst occurred at 29.0 MPa (4200 psi), as compared to the predicted failure pressure of 30.3 MPa (4400 psi).

40.7 MPa (5900 psi), as compared to the predicted burst pressure of 38.6 MPa (5600 psi). Tube OM112 had the same flaw geometry, but was tested with a bladder. The tube failed at 41.4 MPa (6000 psi), which is close to the predicted value of 38.6 MPa (5600 psi) and to the failure pressure observed in the test without a bladder. Use of the bladder caused significantly more unstable tearing of the notch ends than in Tube OM113.

Tests were also performed on tubes with 12.7-mm (0.5-in.)-long 100% TW EDM axial notches. Such flaws cannot be unstably burst in the High-Pressure Test Facility without the use of a bladder. This flaw geometry was tested with two different bladders. Tube OM102 was tested with a 2.4-mm ($^3/_{32}$-in.)-thick bladder, and tube OM101 was tested with a 3.2-mm ($^1/_8$-in.)-thick bladder. The bladder was extruded through the flaw opening. The tube burst at 29.6 MPa (4300 psi), close to the predicted value of 30.3 MPa (4400 psi), but only a very slight amount of unstable tearing occurred.

Tube OM101 (Fig. 4.39) was tested with the thicker bladder. The thicker bladder did not extrude through the flaw, in contrast to tube OM102, and significantly more flaw bulging and unstable tearing took place at the notch ends. Tube OM101 burst at 29.6 MPa (4296 psi), which is good agreement with the predicted value of 30.3 MPa (4400 psi), despite the more extensive tearing with the thicker bladder. Thus, the proper use of bladders produces a unique value for the unstable burst pressure for a given flaw geometry, irrespective of the extent of tearing. However, the resulting leak areas can be drastically different.

Backup foils are sometimes used to prevent premature bladder extrusion through throughwall flaws and resulting excessive water leakage that would prevent pressurization to a sufficient level to burst a tube. To evaluate the influence of foil backups, two tubes with identical flaw geometries (axial notch 12.7-mm [0.5-in.] long and 100% TW) were tested at a pressurization rate of 13.8 MPa/s (2000 psi/s) with 3.2-mm (1/8-in.)-thick bladders and two designs of 0.13-mm (0.005-in.)-thick brass foil backups. Specimen OM133 (Fig. 4.40) had a foil that extended 6.35 mm (0.25 in.) beyond the defining dimensions of the axial notch, in conformance with EPRI guidelines. Specimen OM134 had a larger foil that extended circumferentially 90° to either side of the notch and 12.7 mm (0.5 in.) beyond the ends of the notch. The use of a larger foil can be advantageous when dealing with SCC flaws that cover a large tube area and have additional secondary cracking that makes a precise determination of flaw extent by pretest NDE or dye penetrant uncertain. In both cases, the internal tube surface was lubricated with a multipurpose spray lubricant to reduce friction between the foil and the tube.

Test OM133 was performed with a small foil, and OM134 with a large foil. Both flaws exhibit more unstable tearing than test OM101, which used only a bladder (see Fig. 4.39). However, the burst pressures of 30.0 MPa (4350 psi) for Specimen OM133 and 30.7 MPa (4450 psi) for Specimen OM134 are close to the observed failure pressure of 29.6 MPa (4296 psi) for Specimen OM101 tested without the foil. Even though these tests show that the foil coverage area has not influenced the failure pressure, this behavior could change if larger foils were used or tubes that fail at considerably lower pressures were tested, in which case the greater extent of foil might produce local strengthening and erroneous flaw-opening pressure data. Likewise, thicker foils or foils made of stronger material such as stainless steel could also produce unreliable data.

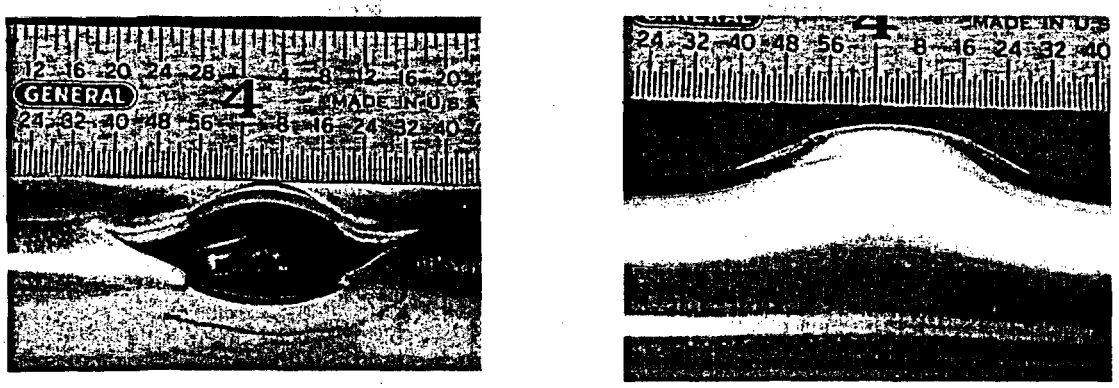

Figure 4.39 Top (left) and side (right) views of tube OM101 with a 12.7-mm (0.5-in.)-long 100% TW EDM axial OD notch, tested with a 3.2-mm (1/8-in.)-thick bladder at a pressurization rate of 13.8 MPa/s (2000 psi/s).

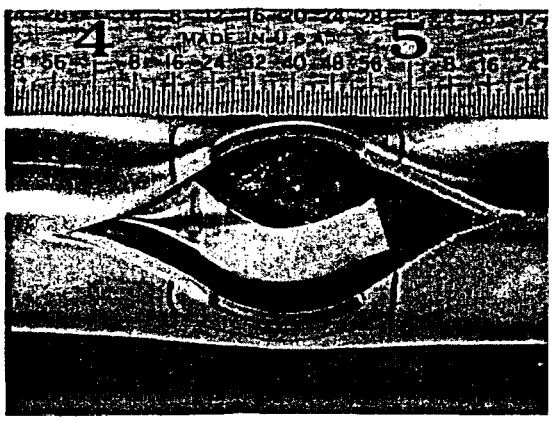

Figure 4.40.
Specimen OM133 with 12.7-mm (0.5-in.)-long 100% TW OD axial EDM notch tested with 3.2-mm (1/8-in.)-thick hard bladder and small backup foil at a pressurization rate of 13.8 MPa/s (2000 psi/s). Failure pressure was 30.0 MPa (4350 psi).

Room-temperature failure tests were also conducted on nine tubes with the same short-length (6.35-mm [0.25-in.] long) EDM OD axial notches having depths of 60, 80 and 90% TW. The tests were conducted with and without bladders and foil backups at various pressurization rates. The results from the nine tests are summarized in Table 4.5. The 60% TW flaws (Specimens OM118 and OM119) were tested at fast pressurization rates without and with a bladder, respectively, and the flaws opened within 2.1 MPa (300 psi) of each other. These flaws were predicted to burst unstably at 45.4 MPa (6600 psi) before tearing, but the actual failure pressures were found to be somewhat higher. In addition, Specimen OM118 exhibited no unstable tearing, but OM119 (tested with a bladder) exhibited significant tearing many times longer than the original flaw length. This effect of the bladder on the flaw opening area is in agreement with the observations for Specimens OM113 and OM112 described above.

Specimens OM116 and OM117, both of which had 80% TW flaws, were tested at low and high pressurization rates without and with bladders, respectively. Specimen OM116 exhibited no unstable burst and opened at 37.7 MPa (5475 psi), whereas OM117 tested with a bladder exhibited unstable burst at 43.1 MPa (6252 psi). This flaw geometry was predicted to tear at 37.2 MPa (5400 psi) and to go unstable at 45.5 MPa (6600 psi). Specimen OM116, which could not be pressurized sufficiently rapidly to induce unstable burst because of the absence of a bladder, tore near the predicted value. Specimen OM117, tested with a bladder went unstable at a pressure ≈2.4 MPa (350 psi) lower than the predicted value for unstable burst. Again, the flaws exhibit greatly different flaw opening areas.

Table 4.5 Test results for flawed tubes containing 6.35-mm (0.25-in.)-long EDM OD axial notches.

Specimen ID	Flaw Depth, (% TW)	Pressurization Rate, MPa/s (psi/s)	Initial Flaw Tearing Pressure, MPa (psi)	Initial Flaw Tearing Leak Rate, L/min (gpm)	Unstable Burst Pressure, MPa (psi)	Unstable Burst Leak Rate, L/min (gpm)	Predicted Ligament Tear/Burst Press., MPa (psi)
OM118	60	13.6 (1970)	49.6 (7200)	46.9 (12.8)	d	d	48.3 (7000)/ 45.5 (6600)
OM119[a]	60	20.7 (3000)	47.6[a] (6900)[a]	>49[a] (13)[a]	47.6[a,e] (6900)[a,e]	>49[a,e] (>13)[a,e]	48.3 (7000)/ 45.5 (6600)
OM116	80	Quasi-steady	37.7 (5475)	12.5 (3.31)	d	d	37.2 (5400)/ 45.5 (6600)
OM117[a]	80	21.4 (3110)	43.1[a] (6252)[a]	>49[a] (13)[a]	43.1[a,e] (6252)[a,e]	>49[a,e] (>13)[a,e]	37.2 (5400)/ 45.5 (6600)
OM138	90	Quasi-steady	30.0 (4350)	4.2 (1.1)	42.7[d] (6200)[d]	45.0[d] (11.9)[d]	27.6 (4000)/ 45.5 (6600)
OM139	90	5.2 (750)	28.3 (4100)	2.8 (0.75)	43.8[d] (6356)[d]	45.4[d] (12.0)[d]	27.6 (4000)/ 45.5 (6600)
OM140	90	22.1 (3200)	33.8 (4900)	-	44.8[d] (6492)[d]	45.4[d] (12.0)[d]	27.6 (4000)/ 45.5 (6600)
OM141[b]	90	4.9 (705)	30.3[b] (4400)[b]	4.5[b] (1.2)[b]	45.0[b,e] (6520)[b,e]	48.4[b,e] (12.8)[b,e]	27.6 (4000)/ 45.5 (6600)
OM142[c]	90	6.3 (916)	27.6[c] (4008)[c]	4.9[c] (1.3)[c]	41.5[c,e] (6026)[c,e]	48.4[c,e] (12.8)[c,e]	27.6 (4000)/ 45.5 (6600)

[a]Tested with 2.38-mm (3/32-in.)-thick bladder.
[b]Tested with 3.18-mm (1/8-in.)-thick bladder.
[c]Tested with 3.18-mm (1/8-in.)-thick bladder with foil backing.
[d]No unstable burst.
[e]Unstable burst.

Three of the five 90% TW flaws (Specimens OM138, OM139, and OM140) were tested without bladders at progressively increasing pressurization rates of quasi-steady-state, 5.2, and 22.1 MPa/s (750 and 3200 psi/s), respectively. None of these flaws exhibited unstable burst. This flaw geometry was predicted to first tear at 27.6 MPa (4000 psi) and then to go unstable at 45.5 MPa (6600 psi). The specimens actually tore open at pressures of 30.0, 28.3, and 33.8 MPa (4350, 4100, and 4900 psi), respectively. Thus, the results for the tests conducted at the two lower pressurization rates were in good agreement with the predicted values, but the specimen tested at the highest pressurization rate tore open at 6.2 MPa (900 psi) above the predicted value. This dependence of flaw opening pressure on pressurization rate has also been observed in testing of 19.1-mm (0.75-in.)-long axial notches, as described at the end of this section. For all three specimens, the leak rates upon flaw opening were below the facility maximum of nominally 45 L/min (12.8 gpm), and the flaws were therefore pressurized to higher levels of 42.7, 43.8, and 44.8 MPa (6200, 6356, and 6492 psi), respectively. At this point, the flow rates reached the facility maximum, and further pressurization to unstable burst (≈45.5 MPa or 6600 psi) could not be achieved.

This same flaw geometry was tested with a bladder (Specimen OM141) and a bladder/foil combination (Specimen OM 142). Both of these specimens went unstable and exhibited greatly increased flaw opening areas. Both of these flaws first tore open near the predicted valued of 27.6 MPa (4000 psi) and were then pressurized to higher levels. Specimen OM141, tested with only a bladder, exhibited unstable burst at 45.0 MPa (6520 psi), which is very near the predicted value of 45.4 MPa (6600 psi). However, Specimen OM142, which used a foil backup, burst at 41.5 MPa (6026 psi). The reason for this behavior is not clear.

To supplement the preceding on the influence of pressurization rate on a short flaw, three identical 80% TW, 19.1-mm (0.75-in.)-long axial notches (OM107, OM122, and OM109) were tested in three different pressurization scenarios. A low quasi-steady-state pressurization rate resulted in ligament tearing at 21.4 MPa (3100 psi), pressurization at 13.8 MPa/s (2000 psi/s) produced ligament tear at 24.2 MPa (3510 psi), and pressurization at 48.3 MPa/s (7000 psi/s) produced ligament tear at 26.4 MPa (3830 psi). The predicted ligament tearing pressure for this flaw geometry is 20.7 MPa (3000 psi), which is in good agreement with the quasi-steady pressurization rate test OM107. All three initially identical flaws exhibited ligament tearing but no discernible unstable tearing at the notch ends. In addition to the increase in ligament tear pressure with pressurization rate, the flaws exhibit a slight increase in maximum notch opening width with increasing pressurization rate. This behavior is similar to that for the 6.35–mm (0.25-in.)-long axial notches presented above.

A nine-tube set of 22.2-mm (7/8-in.)-diameter Alloy 600 tubes was prepared with pairs of EDM 6.35 or 12.7-mm (0.25 or 0.5-in.)-long axial notches and was tested in the High-Pressure Test Facility. The flaws were either 70% (for tube OM153) or 80% (remaining eight tubes) TW separated by various full-wall-thickness ligaments of lengths 0.25, 1.25, and 2.5 mm (0.010, 0.050, and 0.100 in.), all with an initial width of 0.19 mm (0.0075 in.). The flaws were either in axial alignment or shifted circumferentially parallel to each other to give the required ligament size.

Table 4.6 summarizes the results on the pairs of flaws. Data on the pressure at initiation of throughwall leakage and unstable burst, if obtained, are presented. Figures 4.41–50 show posttest photographs for some of the flaws. The flaws were first tested without bladders using quasi-steady pressurization consisting of raising the pressure in 0.69 MPa (100 psi) increments with a 5 s hold at each pressure plateau. The testing was stopped when the flaw first opened, as indicated by the abrupt onset of flow. None of the flaws experienced unstable tearing at the end of the quasi-steady pressurization testing. Most of the flaws exhibited simultaneous tearing of the part–through ligaments at the base of the notch and of the ligament separating the segments in the first phase of testing. In specimens OM152, OM159, and OM162, the part–through ligaments failed, but the separating ligament remained intact (see Figs. 4.44 and 4.47).

All the flaws consisting of two 12.7-mm (0.5-in.)-long notches leaked the maximum 48.8 L/min (12.9 gpm) capacity of the facility upon opening. Hence, pressurization could not be sustained after the flaws opened. In contrast, the 6.35-mm (0.25-in.)-long flaws when opened in Phase 1 testing were capable of sustained pressurization because the flow rates were less than the facility maximum. The sustained flow rate and pressure for these flaws are presented in Table 4.7.

Table 4.6 Pressures at first flaw opening and unstable burst for a nine-tube set of 22.2-mm (7/8-in.)-diameter Alloy 600 tubes containing pairs of 6.35- or 12.7-mm (0.25- or 0.5-in.)-long axial EDM notches of 70 and 80% TW separated by various lengths of full-wall-thickness ligaments.

Specimen No.	Flaw Geometry: Notch Lengths, mm (in.)	Flaw Geometry: Ligament Length, mm (in.)	Flaw Geometry: Flaw Depth, % TW	Pressure at First Leak, MPa (psi)	Pressure at Unstable Burst, MPa (psi)
OM149	12.7 (0.5)	2.5 (0.10)	80	27.0[a] (3920)	-
OM150	12.7 (0.5)	0.25 (0.01)	80	19.0[a] (2760)	-
OM151	12.7 (0.5)	1.25 (0.05)	80	23.0[a] (3340)	-
OM152	12.7 (0.5)	2.5 (0.10)	80	18.9 [a,b,c](2744)	23.5 (3405)
OM153	6.35 (0.25)	0.25 (0.01)	70	34.8[a] (5048)	-
OM159	6.35 (0.25)	2.5 (0.10)	80	34.8[a,b,c] (5050)	38.3 (5550)
OM160	6.35 (0.25)	1.25 (0.05)	80	32.3[a] (4675)	-
OM161	6.35 (0.25)	0.25 (0.01)	80	28.3[a] (4100)	-
OM162	6.35 (0.25)	1.25 (0.05)	80	31.4[a,b,c] (4560)	32.5 (4710)

[a]No unstable tearing at this pressure.

[b]Only bottom of notches tore open; no ligament tearing.

[c]Flaw was retested with bladder and 13.8 MPa/s pressurization rate to cause unstable tearing.

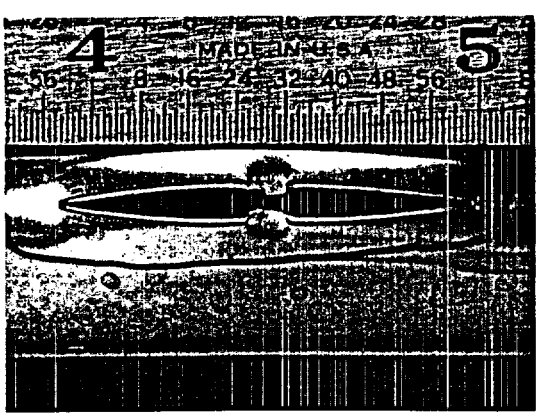

Figure 4.41.
Specimen OM149 with two aligned axial notches [12.7-mm (0.5 in.) long, 2.54-mm (0.100-in.) ligament, 80% TW] after Phase 1 testing.

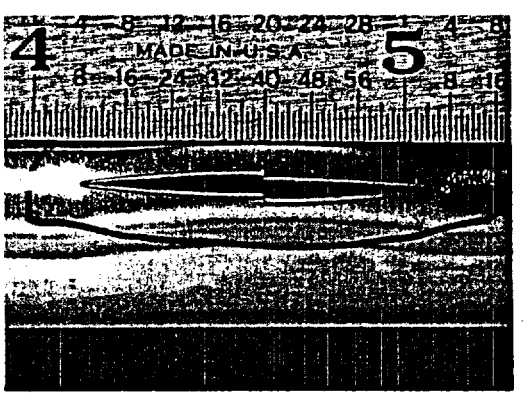

Figure 4.42.
Specimen OM150 with two shifted axial notches [12.7-mm (0.5-in.) long, 0.25-mm (0.010-in.) ligament, 80% TW] after Phase 1 testing.

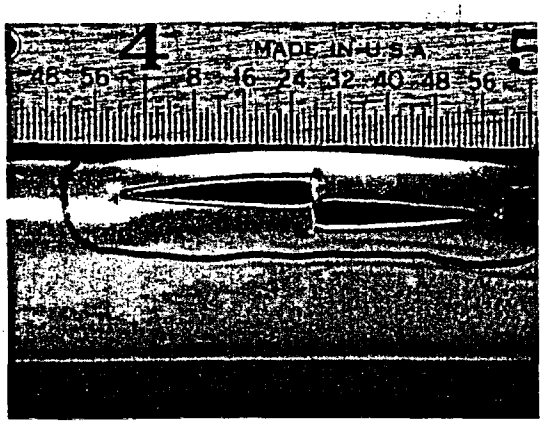

Figure 4.43.
Specimen OM151 with two shifted axial notches [12.7-mm (0.5 in.) long; 1.27-mm (0.050-in.) ligament, 80% TW] after Phase 1 testing.

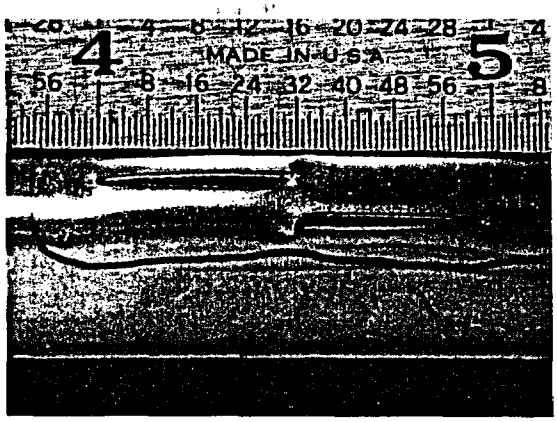

Figure 4.44.
Specimen OM152 with two shifted axial notches [12.7-mm (0.5 in.) long; 2.54-mm (0.100-in.) ligament, 80% TW] after Phase 1 testing.

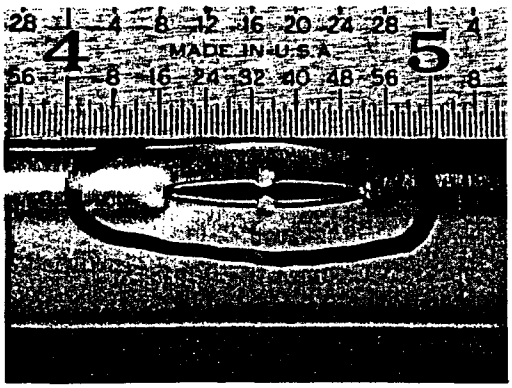

Figure 4.45.
Specimen OM160 with two aligned axial notches [6.35-mm (0.25-in.) long, 1.27-mm (0.050-in.) ligament, 80% TW] after Phase 1 testing.

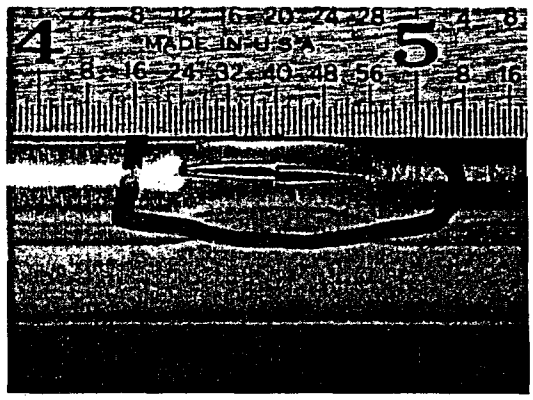

Figure 4.46.
Specimen OM161 with two shifted axial notches [6.35-mm (0.25-in.) long, 0.25-mm (0.010-in.) ligament, 80% TW] after Phase 1 testing.

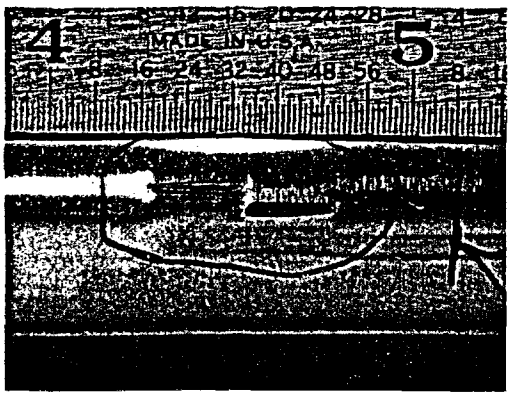

Figure 4.47.
Specimen OM162 with two shifted axial notches 6.35-mm (0.25-in.) long, 1.27-mm (0.050-in.) ligament, 80% TW] after Phase 1 testing.

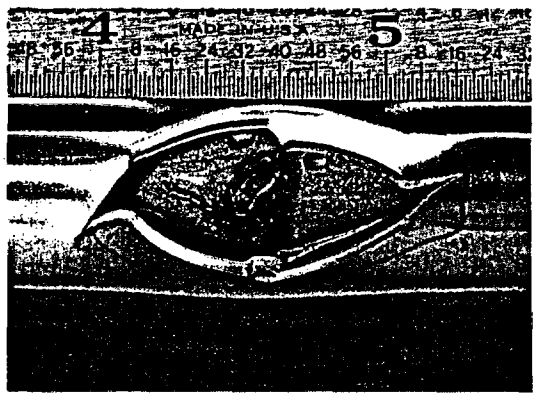

Figure 4.48.
Specimen OM152 with two shifted axial notches 12.7-mm (0.50-in.) long, 2.54-mm (0.100-in.) ligament, 80% TW] after Phase 2 burst testing.

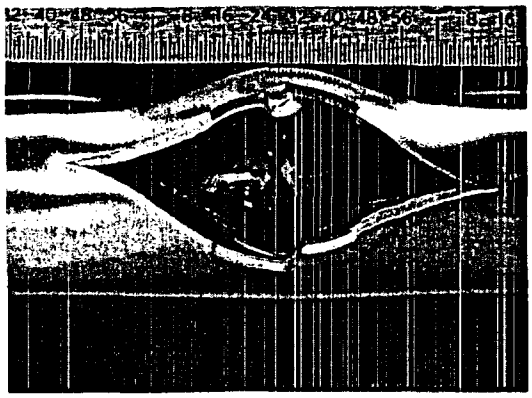

Figure 4.49.
Specimen OM159 with two shifted axial notches [6.35-mm (0.25-in.) long, 2.54-mm (0.100-in.) ligament, 80% TW] after Phase 2 burst testing.

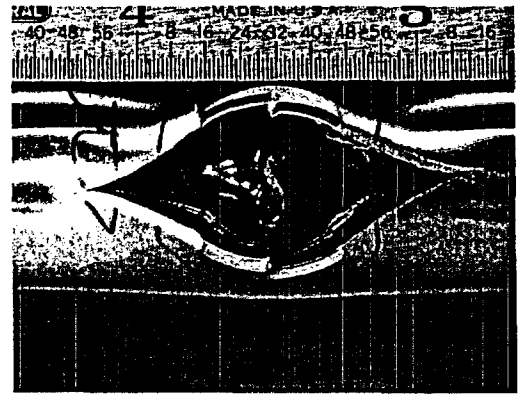

Figure 4.50.
Specimen OM162 with two shifted axial notches [6.35-mm (0.25-in.) long, 1.27-mm (0.050-in.) ligament, 80% TW] after Phase 2 burst testing.

Table 4.7. Sustained pressure and leak rate during Phase 1 testing after flaw opening of two paired 6.35-mm (0.25-in.)-long axial notches.

Specimen No.	Flaw Geometry: Notch Lengths, mm (in.)	Flaw Geometry: Ligament Length, mm (in.)	Flaw Geometry: Flaw Depth, % TW	Sustained Pressure, MPa (psi)	Sustained Leak Rate, L/min (gpm)
OM153	6.35 (0.25)	0.25 (0.01)	70	5.4 (780)	47.69 (12.60)
OM159	6.35 (0.25)	2.5 (0.10)	80	33.2 (4820)	26.08 (6.89)
OM160	6.35 (0.25)	1.25 (0.05)	80	3.9 (560)	48.45 (12.80)
OM161	6.35 (0.25)	0.25 (0.01)	80	13.8 (2000)	46.29 (12.23)
OM162	6.35 (0.25)	1.25 (0.05)	80	29.0 (4200)	32.89 (8.69)

In a second phase of testing, Specimens OM152, OM159, and OM162 were retested with a bladder and a 13.8 MPa/s (2000 psi/s) pressurization rate to obtain information on unstable burst pressure. Figures 4.48–4.50 show the burst flaw openings.

The data in Table 4.6 furnish some insight on how pairs of part-TW axial notches separated by a ligament interact. The data for Specimens OM149 (27.0 MPa) and OM152 (23.5 MPa) show that, for 12.7-mm-long flaws with 2.5-mm ligaments, the axially aligned flaws are stronger than the circumferentially shifted notches with ligaments of the same size. Similarly, for paired 6.35-mm-long notches with 0.25-mm ligaments, i.e., Specimens OM153 (34.8 MPa) and OM161 (28.3 MPa), the axially aligned flaws are stronger. The same behavior is also seen for paired 6.35-mm-long notches with 1.25-mm ligaments, i.e., Specimens OM160 (32.3 MPa) and OM162 (31.4 MPa).

Table 4.8 shows data for six tests from Table 4.6 selected to illustrate the effect of ligament width on the failure pressures. As can be seen, the opening pressure for each flaw length increases to a value that is increasingly less sensitive to ligament size. This finding

Table 4.8. Opening pressures of six flaws as a function of separating ligament size for paired 6.35- and 12.7-mm (0.25- and 0.50-in.)-long interacting circumferentially shifted axial notches, all 80% TW.

Specimen No.	Individual Notch Length, mm (in.)		Ligament Size, mm (in.)		Opening Pressure, MPa (psi)	
OM161	6.35	(0.25)	0.25	(0.01)	28.3	(4100)
OM162	6.35	(0.25)	1.27	(0.05)	31.4	(4560)
OM159	6.35	(0.25)	2.54	(0.10)	34.8	(5050)
OM150	12.7	(0.50)	0.25	(0.01)	19.0	(2760)
OM151	12.7	(0.50)	1.27	(0.05)	23.0	(3340)
OM152	12.7	(0.50)	2.5	(0.10)	23.5	(3405)

implies that the flaws are interacting less. Furthermore, the limiting pressure for each flaw length is approaching the predicted opening pressures for single flaws of 6.35- and 12.7-mm length, which are 34.5 and 20.7 MPa (5000 and 3000 psi), respectively.

4.3.3.3 Laser-Cut Notches

Additional data on flaw interaction were obtained from tests on twenty-four 22.2-mm (7/8-in.)-diameter Alloy 600 tubes with a variety of laser-cut OD flaws consisting of simple single axial and circumferential notches, as well as complex OD patterns of axial and circumferential notches separated by various ligament sizes. Ten generic flaws were tested with the geometries shown in Figs. 4.51 and 4.52. The laser-cutting technique permits considerably more complex flaws to be fabricated than are possible using EDM. The laser-cut flaws are also considerably tighter than the minimum 0.19-mm (0.0075-in.)-wide notches that can be achieved by EDM.

The 24 laser-cut flaws were tested in two stages. The first stage consisted of pressurizing at a quasi-steady-state rate without the use of internal bladders. The pressurization protocol consisted of starting at an internal pressure of 0.34 MPa (50 psi) and increasing the pressure in 0.69 MPa (100 psi) increments after a 10 s dwell at each pressure plateau. This process continued until ligament tearing occurred, and the resultant increases in flow made it impossible to continue the tests. The specimens that exhibited only stable ligament tearing and opening in the first-stage tests were retested with a bladder and foil backups, if necessary.

The results from the 24 Stage 1 tests are summarized in Table 4.9. Pre- and post-test photographs of some representative flaws of the ten types are shown in Figs. 4.53–55. Table 4.9 also gives pretest EC estimates of the maximum flaw depth. All of the laser-cut flaws exhibited pinhole laser burn-through at the ends of each notch. These pinholes were too small to be detected by EC techniques, but they leaked water at 0.34 MPa (50 psi). At a pressure of 6.9 MPa (1000 psi), the leak rate through these pinholes was typically in the range of 0.04-0.4 L/min (0.01-0.1 gpm or 14.4-144 gal per day).

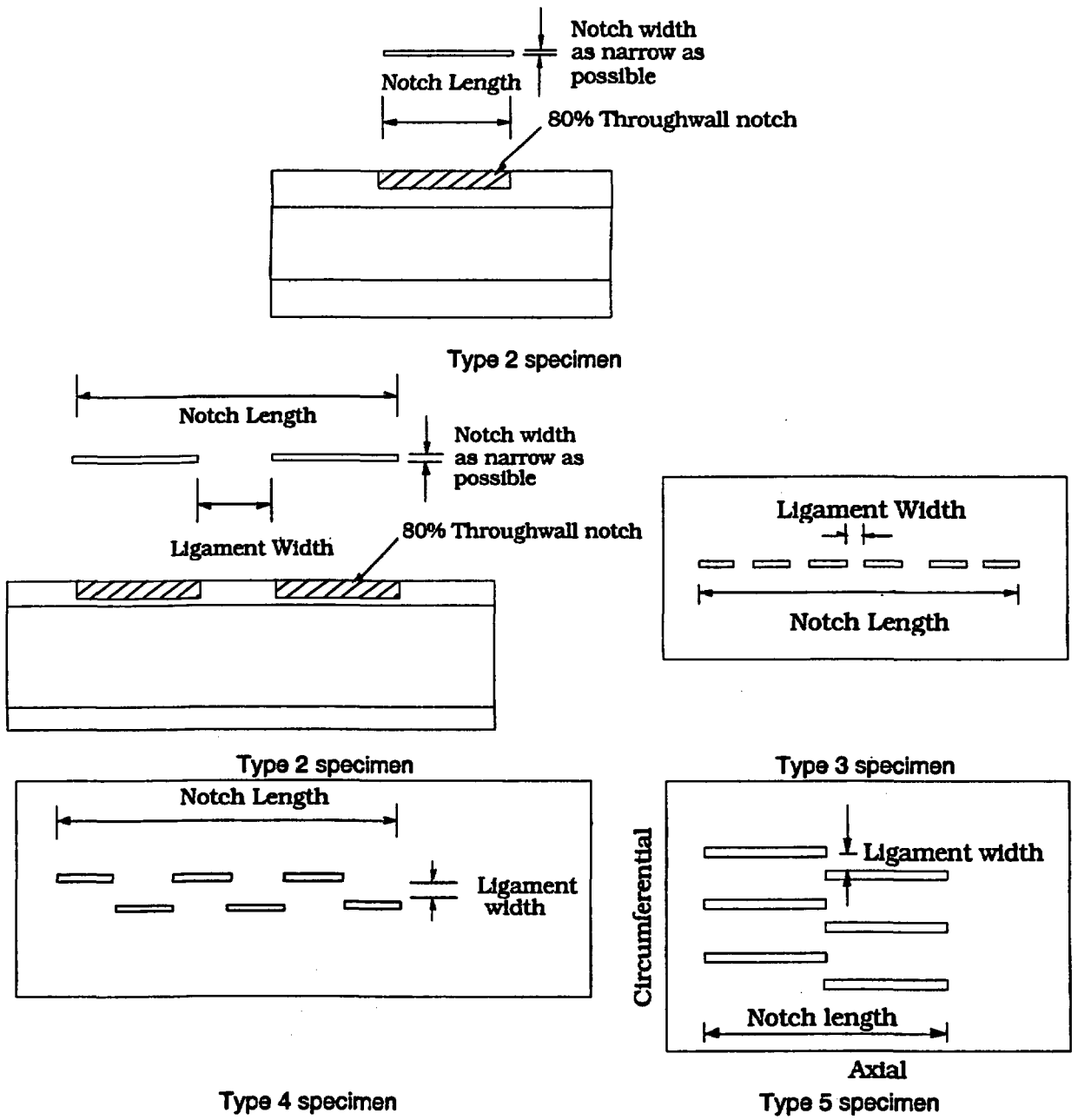

Figure 4.51. Configurations of notches in various types 1-5 of laser-cut tube specimens.

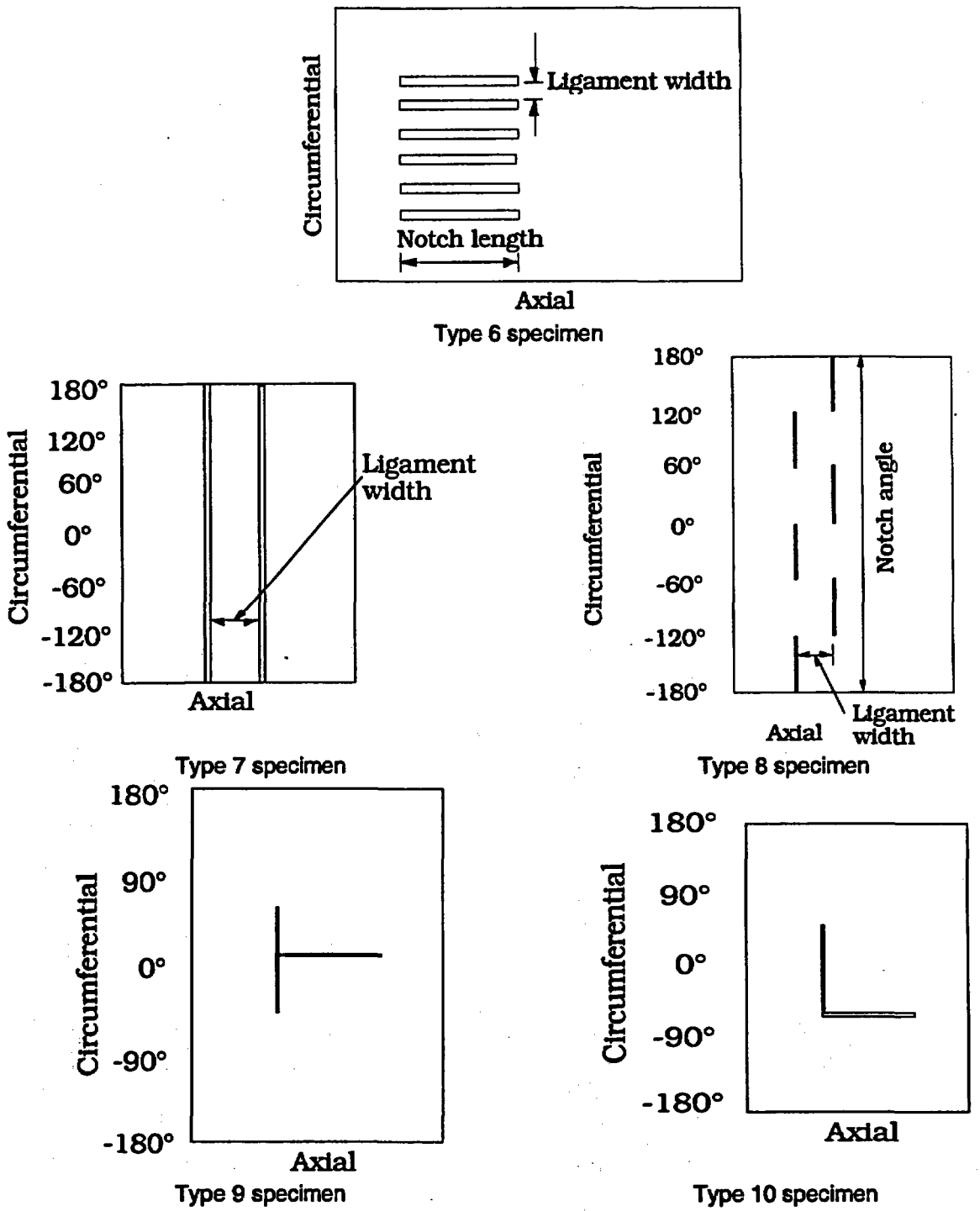

Figure 4.52. Configurations of notches in various types 6-10 of laser-cut tube specimens.

Table 4.9. Test results from Stage 1 quasi-steady-state testing of flawed tubes containing OD laser-cut notches (without bladders). All notches had nominal depths of 80% TW except for Specimens 5528-3-3 and 5469-2-2, which had nominal depths of 40% TW. All tubes leaked water through laser burn pinholes at the ends of the laser-cut notches at 0.34 MPa (50 psi) except Specimen 5528-2-2.

Specimen Number	Flaw Type	Number of Notches	NDE Flaw Depth (% TW)	Nominal Flaw Length, mm (in.)	Ligament Width, mm (in.)	Max. Pressure at Ligament Tearing, MPa (psi)	Sust. Press. after Ligament Tearing, MPa (psi)	Flow Rate after Lig. Tearing, L/min (gpm)
5528-1-1	1	1	75	6.35 (0.25)	NA	36.6 (5310)	36.5 (5300)	18.1 (4.78)
5528-1-2	1	1	74	6.35 (0.25)	NA	37.1 (5380)	37.0 (5360)	13.8 (3.65)
5528-1-3	1	1	76	8.89) (0.35	NA	31.7 (4600)	29.8 (4320)	32.6 (8.6)
5528-1-4	1	1	73	8.89) (0.35	NA	32.4 (4700)	31.2 (4530)	30.5 (8.05)
5528-2-1	1	1	69	12.7 (0.5)	NA	34.5 (5000)	3.5 (500)	48.1 (12.7)
5528-2-2	1	1	61	12.7 (0.5)	NA	38.6[b] (5600)[b]	1.4 (200)	48.4 (12.8)
5516-4-3	2	2	72	12.7 (0.5)	0.25 (0.01)	33.8 (4900)	7.2 (1040)	48.1 (12.7)
5516-4-2	2	2	70	12.7 (0.5)	0.13 (0.005)	33.8 (4900)	6.5 (940)	48.1 (12.7)
5528-3-1	3	6	70	12.7 (0.5)	0.13 (0.005)	29.0 (4200)	10.7 (1550)	48.1 (12.7)
5528-3-2	3	6	73	12.7 (0.5)	0.25 (0.01)	30.0 (4350)	8.5 (1240)	48.1 (12.7)
5528-3-3[a]	3	6	61	12.7 (0.5)	0.25 (0.01)	35.2 (5100)	3.7 (540)	48.4 (12.8)
5528-3-4	4	6	76	12.7 (0.5)	0.13 (0.005)	35.9 (5200)	2.7 (390)	48.4 (12.8)
5469-2-1	4	6	74	12.7 (0.5)	0.25 (0.01)	32.8 (4750)	6.0 (870)	48.4 (12.8)
5469-2-2[a]	4	6	60	12.7 (0.5)	0.25 (0.01)	37.6 (5450)	3.8 (550)	48.4 (12.8)
5469-2-3	5	6	79	12.7 (0.5)	0.25 (0.01)	33.5 (4860)	2.1 (800)	48.4 (12.8)
5469-2-4	5	6	78	12.7 (0.5)	0.51 (0.02)	39.3[b] (5700)[b]	1.0 (150)	48.4 (12.8)
5469-3-1	6	6	80	12.7 (0.5)	0.25 (0.01)	28.3 (4110)	13.3 (1930)	46.9 (12.4)
5531-3-1	6	6	79	12.7 (0.5)	0.51 (0.02)	34.3 (4980)	5.2 (760)	48.4 (12.8)
5469-3-3	7	2	75	360°	0.13 (0.005)	51.4 (7450)	0.4 (60)	49.2 (12.99)
5469-3-4	7	2	74	360°	0.25 (0.01)	51.7 (7500)	did not fail	did not fail
5469-4-1	8	6	70	360°	0.13 (0.005)	39.2 (5680)	0.3 (50)	48.8 (12.9)
5469-4-2	8	6	70	360°	0.25 (0.01)	38.3 (5550)	0.3 (50)	48.8 (12.9)
5469-4-3	9	2	69	180° x 0.5	NA	30.8 (4475)	0.7 (100)	48.8 (12.9)
5469-4-4	10	2	72	180° x 0.5	NA	31.3 (4540)	0.7 (100)	48.8 (12.9)

[a]Laser-cut notches had nominal depths of 40% TW.

[b]Specimen exhibited unstable tearing without internal bladder.

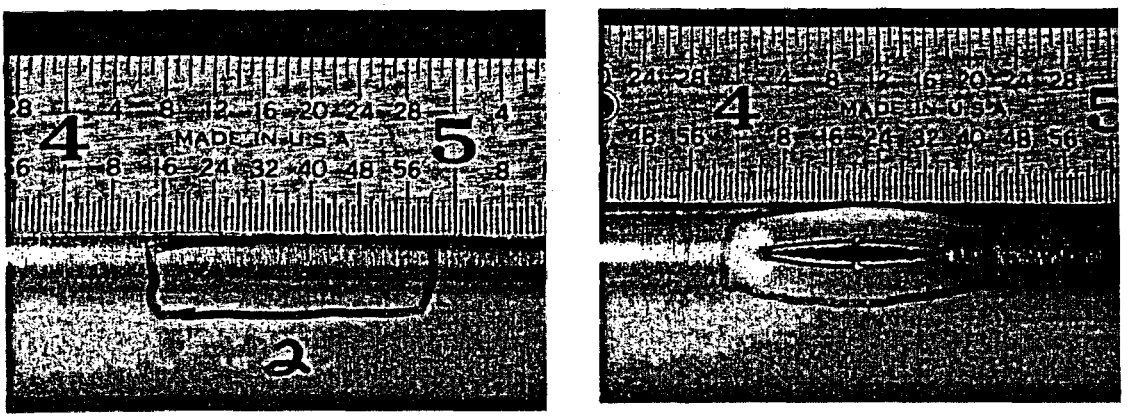

Figure 4.53. Appearance of Specimen 5516-4-3 with Type 2 flaw before (left) and after (right) Stage 1 testing.

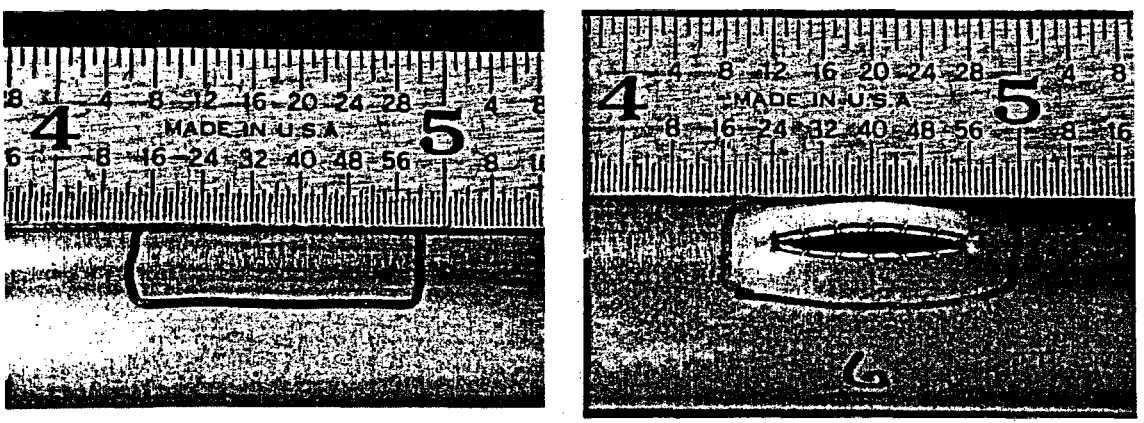

Figure 4.54. Appearance of Specimen 5528-3-3 with Type 3 flaw before (left) and after (right) Stage 1 testing.

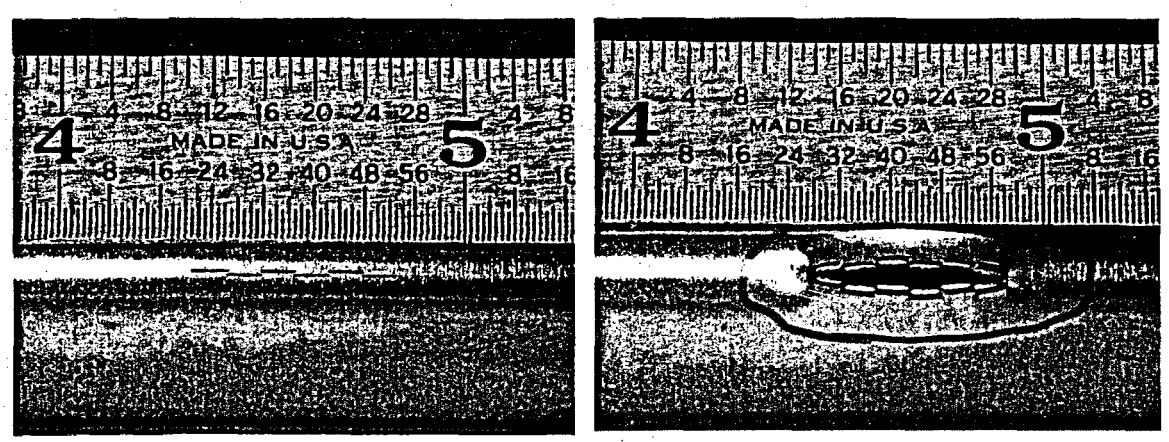

Figure 4.55. Appearance of Specimen 5469-2-2 with Type 4 flaw before (left) and after (right) Stage 1 testing.

The six Type 1 flaws (Fig. 4.51) were single axial notches of three lengths (6.35, 8.9, and 12.7 mm [0.25, 0.35, 0.5 in.]), and all were nominally 80% TW. The two Type 2 flaws (Fig. 4.51) consisted of two aligned axial notches, each 6.35 mm (0.25 in.) in length and 80% TW, separated by a complete wall thickness ligament of lengths 0.25 or 0.13 mm (0.010 or 0.005 in.). During testing, progressive sequential tearing was not evident; both types of ligaments tore simultaneously at 33.8 MPa (4900 psi).

The three Type 3 flaws (Fig. 4.51) consisted of six aligned equal-length axial notches separated by complete-wall-thickness ligaments. The total length of the composite flaw (notches plus ligaments) was 12.7 mm (0.5 in.). For two of the tubes, the flaws were 80% TW, and the interspersed ligaments were 0.13 or 0.25 mm (0.005 or 0.010 in.) in length. For the third tube, the six notches were only 40% TW, and the interspersed ligaments were 0.25-mm (0.010-in.) long. Again, in the tests on these specimens, progressive sequential tearing of the ligaments was not evident. For this type of flaw and the dimensions tested, the length of the ligaments separating the notches had little influence on failure pressure, but the depth of the notches exerted a noticeable influence.

The three Type 4 flaws (Fig. 4.51) consisted of six nonaligned, side-step, equal-length, axial notches in two axial rows of three aligned flaws, each separated by complete-wall-thickness ligaments. The overall length of the composite flaw was 12.7 mm (0.5 in.). In two of the three tubes, the individual notches were 80% TW, and the interspersed ligaments were 0.13 or 0.25 mm (0.005 or 0.010 in.) in length. In the third tube, the individual notches were only 40% TW, and the interspersed ligaments were 0.25-mm (0.010-in.) long. Figure 4.55 show the pre- and post-test flaw appearances of Specimen 5469-2-2, which had the 40% TW flaw depth. The post-test photograph indicates no unstable tearing at the notch ends and shows that the ligaments between the notches and those at the bottom of each notch have torn. Again, all of the ligaments tore simultaneously at the failure pressure of 37.6 MPa (5450 psi), and the depth of the notches exerted a stronger influence on the failure pressure than did the length of the interspersed ligaments.

The two Type 5 flaws (Fig. 4.51) were composed of six individual notches of equal length in two parallel offset rows of three notches each. The laser-cut notches in both specimens were 80% TW, and the ligament lengths were either 0.25 or 0.51 mm (0.010 or 0.020 in.). Figure 4.56 show the pre- and posttest appearances of Specimen 5469-2-4, which had the 0.51-mm (0.020-in.) ligaments. The post-test photograph shows that ligament tearing occurred along only one of the unaligned axial rows, and in contrast to the previous tests, unstable tearing also occurred at the ends of flaw. This unstable tearing occurred without the use of an internal bladder. Progressive sequential tearing was not evident during testing; all ligaments tore simultaneously at 39.3 MPa (5700 psi). The other flaw of this type (Specimen 5469-2-3) with the thinner (0.25-mm [0.010-in.] ligament between notches did not tear unstably, and it opened at the considerably lower pressure of 33.5 MPa (4860 psi).

The two Type 6 flaws (Fig. 4.51) consisted of six axial parallel notches of equal 12.7-mm (0.50-in.) length and 80% TW depth with ligament widths of 0.25 or 0.51 mm (0.010 or 0.020 in.). For Specimen 5531-3-1, which had the 0.51-mm (0.020-in.)-long ligaments, ligament tearing occurred in only one of the parallel notches, and no unstable tearing occurred at the ends of notch. The flaw tore open at 34.3 MPa (4980 psi). The other flaw of this type (Specimen 5469-3-1) with the thinner (0.25-mm [0.010-in.])-long ligament between the notches behaved similarly but opened at the considerably lower pressure of 28.3 MPa (4110 psi).

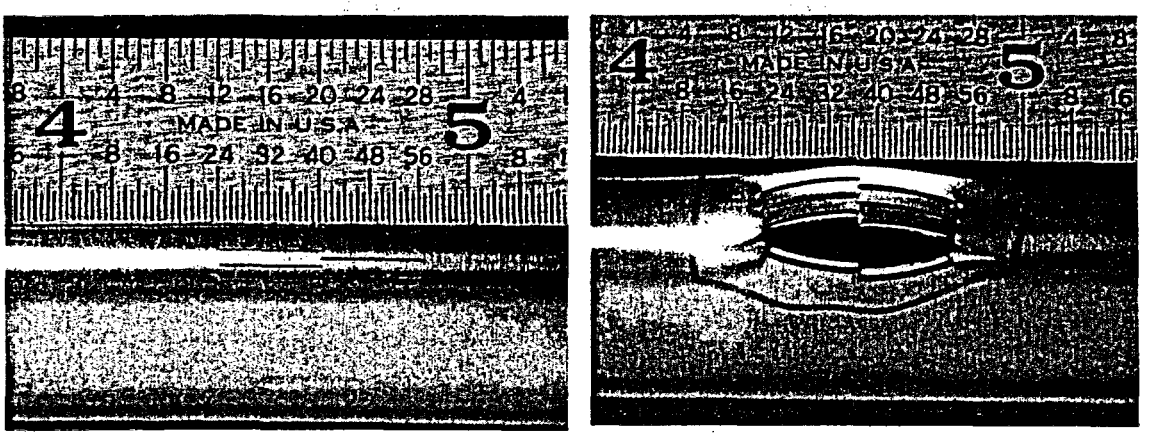

Figure 4.56. Appearance of Specimen 5469-2-4 with Type 5 flaw before (left) and after (right) Stage 1 testing.

The two Type 7 flaws (Fig. 4.51) consisted of two parallel 360° continuous circumferential notches of 80% TW depth separated by ligament widths of 0.13 or 0.25 mm (0.005 or 0.010 in.). Specimen 5469-3-3 had the thinner 0.13-mm (0.005-in.) ligament, and ligament tearing occurred around the entire tube circumference, resulting in complete separation of the tube into two pieces. Failure occurred at 51.4 MPa (7450 psi), which is near the maximum 53.1 MPa (7700 psi) operating pressure of the facility. The other flaw of this type (Specimen 5469-3-4) had the thicker (0.25-mm [0.010-in.]) ligament and could not be opened at the maximum facility pressure of 53.1 MPa (7700 psi).

The two Type 8 flaws (Fig. 4.51) consisted of six equal-length circumferential notches of 80% TW depth in two circumferential parallel rows having three notches each, separated by ligaments widths of 0.13 or 0.25 mm (0.005 or 0.010 in.). In Specimen 5469-4-1, which had the thicker (0.25-mm [0.010-in.]) ligament, ligament tearing occurred around the entire tube circumference, resulting in complete separation of the tube into two pieces. Failure occurred at 39.2 MPa (5680 psi). The other flaw of this type (Specimen 5469-4-2) with the thinner (0.13-mm [0.005-in.]) ligament opened at the slightly lower pressure of 38.3 MPa (5550 psi).

The single Type 9 flaw (Fig. 4.51) consisted of two intersecting notches, one extending 180° around the circumference and the second perpendicular notch extending 12.7 mm (0.5 in.) in the axial direction. The two notches were 80% TW and formed a tee. Ligament tearing occurred primarily along the 12.7-mm (0.5-in.)-long axial notch and only slightly along the circumferential notch. The flaw tore open at 30.9 MPa (4475 psi).

The single Type 10 flaw (Fig. 4.51) consisted of two intersecting notches similar to those in the Type 9 flaw. However, the notches in the Type 10 flaw were configured to form an el rather than a tee. For this geometry, ligament tearing again occurred primarily along the 12.7-mm (0.5-in.)-long axial notch and only slightly along the circumferential notch. The flaw tore open at 31.3 MPa (4540 psi), very near the failure pressure for the Type 9 flaw.

Most of the tubes from the 24-tube set were subjected to Stage 2 testing after the above Stage 1 tests were completed. Initially, the Stage 2 tests were conducted with only a bladder (3.2-mm [1/8-in.]-thick Tygon tubing) and no foil backup. Seven tubes were tested in this fashion, namely Specimens 5528-1-1, 5528-1-2, 5528-1-3, 5528-1-4, 5518-3-1, 5516-4-2, and

5516-4-3. All flaws after this were tested with a similar bladder and a 0.13-mm (0.005-in.)-thick brass foil backup. The results of the Stage 2 testing are summarized in Table 4.10.

4.3.3.4 Pressurization of Flaws to Obtain Specified Openings

The Paul Sherrer Institute (PSI) of Switzerland requested that ANL produce axial fish-mouth flaw openings of specified sizes in Type 304 stainless steel (SS) tubes for subsequent testing at the Institute. Although only three fish-mouth specimens were needed, PSI provided 10 tubes to permit experimentation in developing the appropriate production technique. Each of the tubes had an OD of 18.8 mm (0.741 in.) and an ID of 16.6 mm (0.655 in.) and contained 100% TW EDM notches with an initial 0.20-mm (0.0075-in.) width. Four of these ten tubes had a notch length of 20 mm (0.8 in.), three had a length of 33 mm (1.3 in.), and three had a length of 48 mm (1.9 in.). ANL was to expand these flaw openings to maximum widths of 10, 5.6, and 4.4 mm (0.4, 0.22, and 0.17 in.), respectively, by internal pressurization. Producing "flaws to order" provided a unique test of the capability to predict crack opening and failure behaviors.

The pressurization tests were carried out using internal bladders to prevent excessive leakage through the flaw and reinforcing circumferential brass foils, typically extending 270° around the circumference, to prevent extrusion of the bladder through the flaw opening during pressurization. Figure 4.57 shows that the calculated crack opening displacements (CODs) were in reasonable agreement with test data for the 20.3- and 33.0-mm (0.8- and 1.3-in.)-long notches. The COD for the 48.3-mm (1.9-in.)-long notch was significantly overestimated. However, since the COD vs. pressure curves are fairly steep for all three notches, the final pressures recommended were quite close to the actual pressures applied during the tests. Overall, the values for the target notch width were met within reasonable limits (Table 4.11).

4.3.4 Laboratory-Grown SCC

In contrast to rectangular machined notches of constant depth, laboratory-grown SCCs are irregular in shape and have variable depths along their lengths. They often consist of a family of crack segments in different planes rather than consisting of a single planar crack. Nineteen leak and burst tests have been performed on laboratory-grown SCC flaws. Flaw geometries include ID and OD axial and ID and OD circumferential flaws. The crack geometries for the flaws were estimated prior to testing by multiparameter and conventional EC analysis. Where possible, post-test fractography was also performed to confirm the NDE estimates, but in cases where the burst pressure was high, the resultant large deformations of the tube made the post-test analysis difficult. An additional 31 tube set, which was used for detailed studies on the accuracy of NDE crack sizing and characterization, was also tested. The purpose of the tests on these tubes was not to characterize the failure and leakage behavior of the tubes, but to moderately pressurize the tubes to slightly open the flaws. This step simplified destructive examination of the specimens and allowed accurate profiles of the cracks undistorted by the large deformations that often occur when tubes are tested to failure.

The initial tests on laboratory-grown SCC flaws were performed on five 22.2-mm (7/8-in.)-diameter Alloy 600 tubes with laboratory-produced axial ODSCC of nominal length 12.7 mm (0.5 in.). Four of the tubes, SGL-177, SGL-195, SGL-104, and SGL-219, were cracked at ANL in an aqueous solution of sodium tetrathionate. The fifth tube (W 2-10)

Table 4.10. Test results from Stage 2 testing of flawed tubes containing OD laser-cut notches. All notches had characteristics that existed after Stage 1 testing (from Table 4.9).

Test Number	Flaw Type	Pressurization Rate MPa/s (psi/s)	Burst (Yes/No)	Maximum Pressure, MPa (psi)
5528-1-1	1	12.6 (1823)	Y	41.2 (5980)
5528-1-2	1	13.9 (2023)	Y	40.3 (5850)
5528-1-3	1	12.9 (1865)	Y	33.4 (4850)
5528-1-4	1	14.4 (2084)	Y	32.1 (4660)
5528-2-1	1	No Stage 2	-	-
5528-2-2	1	No Stage 2	-	-
5528-3-2[a]	3	13.3 (1928)	Y	30.4 (4409)
5528-3-3[a,b]	3	10.0 (1450)	Y	28.6 (4146)
5528-3-4[a]	4	12.2 (1776)	Y	30.0 (4346)
5469-2-1[a]	4	13.4 (1950)	Y	31.9 (4630)
5469-2-2[a,b]	4	10.3 (1497)	Y	33.4 (4850)
5469-2-3[a]	5	13.3 (1925)	Y	32.2 (4669)
5469-2-4[a]	5	13.3 (1930)	Y	26.8 (3893)
5469-3-1[a]	6	13.5 (1953)	Y	32.2 (4675)
5531-3-1[a]	6	13.2 (1909)	Y	29.0 (4200)
5469-3-3	7	Stage1 opened	-	-
5469-3-4[c]	7	14.2 (2066)	N	53.1 (7700)
5469-4-1	8	Stage1 opened	-	-
5469-4-2	8	Stage1 opened	-	-
5469-4-3	9	Stage1 opened	-	-
5469-4-4	10	Stage1 opened	-	-

[a]Specimen tested in Stage 2 with internal bladder plus foil. All other Stage 2 tests were conducted with an internal bladder only, except for Specimen 5469-3-4, which was tested in Stage 2 with neither a bladder nor a foil.
[b]Specimen exhibited unstable tearing in Stage 1 testing without internal bladder.
[c]Specimen did not open in Stage 1 testing, and therefore was tested in Stage 2 with neither a bladder nor a foil. It did not fail at the maximum system pressure in Stage 2.

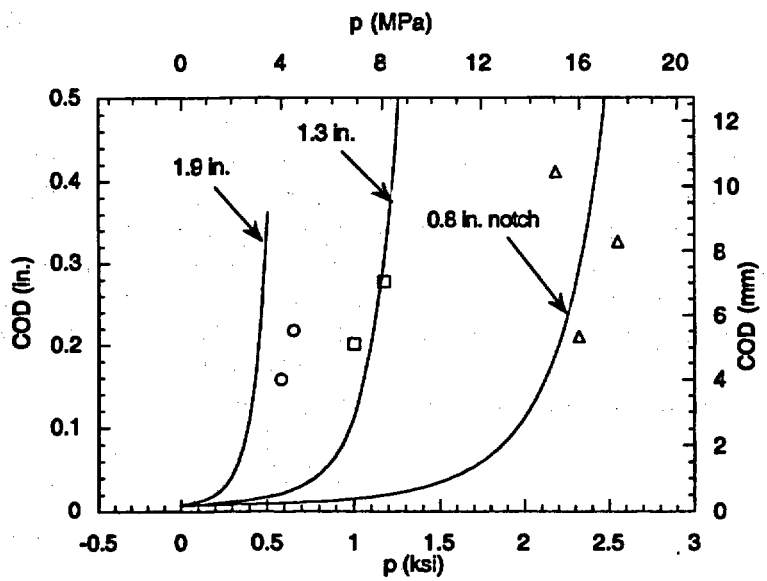

Figure 4.57. Calculated variations of crack opening displacements with pressure. Symbols denote measured COD values after the tests.

Table 4.11. Flaw opening widths and internal pressures for PSI tubes.

Test No.	Notch Length, mm (in.)	Crack Opening Displacement, mm (in.)		Internal Pressure[a], MPa (ksi)		Remarks
		Target	Actual	Calculated	Actual	
1	20 (0.8)	-	-	16.8[b] (2.43)	17.6 (2.55)	Intentionally pressurized to unstable burst
2	20 (0.8)	10.0 (0.4)	8.3 (0.326)	16.9 (2.45)	17.6 (2.55)	Slight tearing
3	20 (0.8)	10.0 (0.4)	5.3 (0.210)	16.9 (2.45)	16.0 (2.32)	
4	20 (0.8)	10.0 (0.4)	10.4 (0.411)	16.9 (2.45)	15.0 2.18	Slight tearing
5	33 (1.3)	5.6 (0.22)	-	7.9 (1.15)	11.6[c] (1.68)	Inadvertently tested to large unstable tearing
6	33 (1.3)	5.6 (0.22)	7.0 (0.277)	7.9 (1.15)	8.1 (1.17)	
7	33 (1.3)	5.6 (0.22)	5.1 (0.201)	7.9 (1.15)	6.9 (1.00)	
8	48 (1.9)	4.4 (0.17)	5.5 (0.218)	3.1 (0.45)	4.5 (0.65)	
9	48 (1.9)	4.4 (0.17)	4.0 (0.158)	3.1 (0.45)	4.0 (0.58)	
10	48 (1.9)	4.4 (0.17)	-	3.1 (0.45)	-	Not tested

[a]Calculated internal pressure to produce target COD and actual internal pressure applied to produce observed COD.

[b]Calculated internal pressure required to produce unstable burst.

[c]Actual internal pressure applied to produce inadvertent unstable burst.

contained an axial ODSCC flaw produced by Westinghouse using a doped steam procedure. Tubes SGL-177 and SGL-195 were tested at room temperature, and tubes SGL-104 and SGL-219 were tested at 282°C (540°F). The Westinghouse tube W 2-10 was tested at both temperatures.

Dye-penetrant test results on the flaws are shown in Figs. 4.58–4.61. Eddy current examinations indicated that all four ANL-produced SCC flaws had variable crack depths along their lengths, with maximum depths of 75-95%. The Westinghouse tube exhibited a similar crack depth profile. All the flaws have small TW regions, which were identified by bubble testing. They were not seen by EC techniques because of their tightness and very small axial extents, and the dye-penetrant inspections revealed flaw branching for all of the flaws. The EC BC voltages indicated that the five flaws fell into two categories. The EC BC voltage for the Westinghouse tube was 4.5 V, very close to the 4.0 V exhibited by the ANL tube in Test SGL-177. The other three ANL tubes had higher EC voltages, in the range of 6-10 V.

The test results on these five tubes are summarized in Table 4.12. Although all the specimens showed gas leakage under very low pressures, measurable leakage of water was not observed until the pressures reached 13.3 MPa (1928 psi) or greater. This is reported in

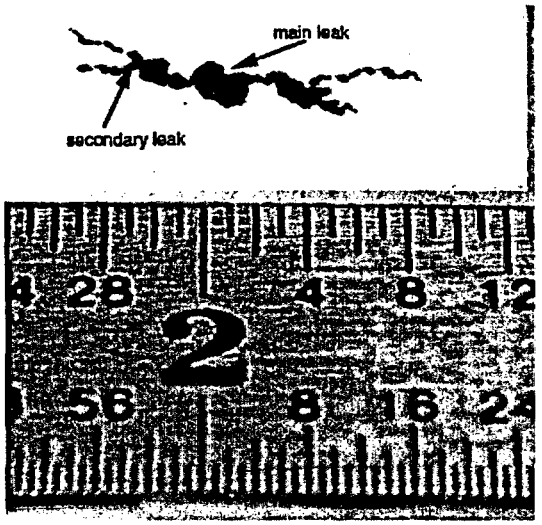

Figure 4.58.
Pre-test image of Specimen SGL-177 with flaw highlighted by dye penetrant and digital image processing. Two regions of TW penetration are indicated by bubble testing.

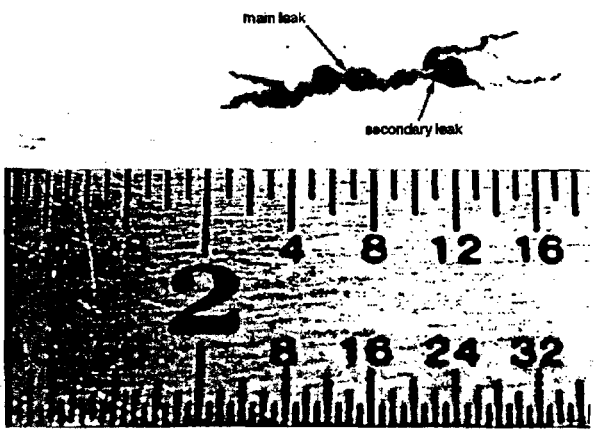

Figure 4.59.
Pre-test image of Specimen SGL-195 with flaw highlighted by dye penetrant and digital image processing. Two regions of TW penetration are indicated by bubble testing.

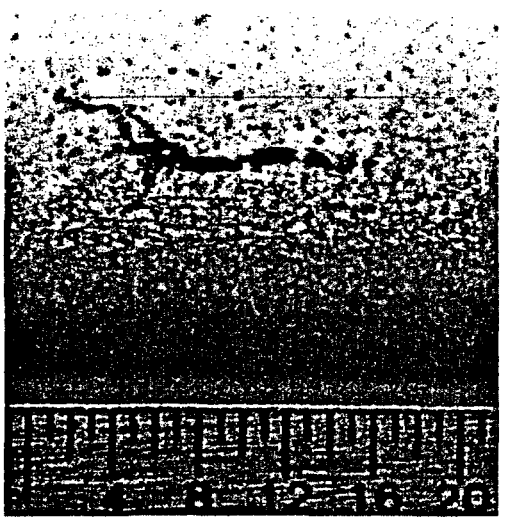

Figure 4.60.
Pre-test image of Specimen SGL-219 with flaw highlighted by dye penetrant and digital image processing. A single region of throughwall penetration was indicated by bubble testing.

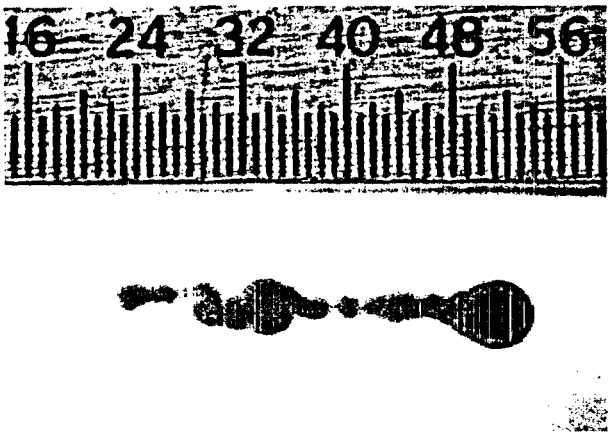

Figure 4.61.
Pre-test dye-penetrant digital image of Westinghouse ODSCC tube produced using doped steam (Test T505CATW2-10).

Table 4.12 Summary of results from tests on four Argonne tubes and Westinghouse tube with axial ODSCC cracks.

Spec. Number	Overall Flaw Length, mm	Test Temp, °C	Pretest Air Leak at 0.28 MPa	Initial Leak Pressure/Final Test Pressure, MPa	Constant Tearing pressure, MPa	Flow Rate at Initial/Final Opening Pressure, L/min.
SGL-177	12.2	R.T.	yes	16.9/19.3	16.9	0.04-0.26/ 1.67
SGL-195	13.7	R.T.	yes	14.7/15.5	14.7	<0.04/32.6
SGL-104	10.4	282	yes	16.2/17.2	no tearing	21.2/23.5
SGL-219	14.0	282	yes	13.3/16.2	16.2	3.7/ 14.0-39.0
W 2-10	12.4	R.T.	yes	17.2/18.6	17.2	0.04- 0.068/0.12
W 2-10	12.4	282	yes	18.6	18.6	0.30-0.72

Table 4.12 as the "initial leak pressure." Another phenomenon that was observed in most of the tests was an increase in the leakage while the flaw was held at a constant pressure. This occurred even in room temperature tests and shows that, with irregular crack geometries, time-dependent failure of some portion of the crack ligament is possible. The pressures at which time dependent increases in the leakage rates were observed are reported in Table 4.12 as the "constant tearing pressure." Post-test photographs of Specimens SGL-195 and -177 are shown in Figs. 4.62 and 4.63.

Additional tests were performed on 14 tubes that contained a wider range of flaw geometries, including OD axial and circumferential cracks and combinations of these types, as well as OD flaws in the roll transition.

Table 4.13 summarizes the results from the 14 tests, all on tubes with OD flaws. Specimens SGL-226 and SGL-363 contained complex flaws with combinations of axial and

Figure 4.62.
Photograph of failed region of Specimen SGL-195 after testing.

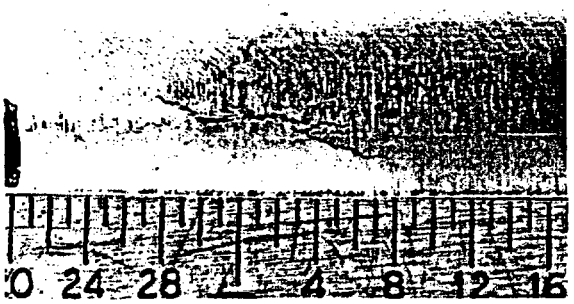

Figure 4.63.
Photograph of failed region of Specimen SGL-177 after testing.

circumferential cracks, including cracking in the roll transition for Specimen SGL-363. Specimens SGL-413, -425, -480, -493, -494, -719, -728, -730, -731, and -734 contained axial flaws, and Specimens SGL-099 and 158 contained circumferential cracks, based on dye-penetrant determinations. The tabulated maximum depths and the EC voltages represent pretest characterizations using standard EC signal analysis procedures and software.

The information on pressure at first leak comes from visual observation of the flawed tube through observation windows for the first signs of water leakage. For Specimens SGL-158, -413, -425, -480, -493, -728, -731, -226, and -363, first leak occurred in the form of one drop of water issuing from the flaw over a period of several minutes. The frequency of drop formation increased with increasing pressure, and the leaks often passed through being a small droplet spray, followed by a continuous leak stream. The tests were terminated when the flaw opened enough that the flow reached the maximum 48.4 L/min (12.8 gpm) capacity of the pressurizer pump. The tabulated maximum pressure for the tests represents the pressure at which the flow capacity of the facility was reached.

For Specimens SGL-099, -494, -719, and -734, the pressure at first leak and maximum pressure achieved were the same or differed only slightly. These tests were characterized by

Table 4.13. Results from pressure tests on 14 SCC flaws

Test No.	Flaw Type	Max. Flaw Depth, %	BC Voltage	Pressure at First Leak, MPa (psi)	Max. Pressure Attained, MPa (psi)
099	OD/Circ	20	3.25	51.0 (7400)	51.0 (7400)
158	OD/Circ	60	4.32	24.8 (3600)[a,b]	31.4 (4560)
413	OD/Axial	90	1.57	12.4 (1800)[b]	24.6 (3570)
425	OD/Axial	0	2.14	16.6 (2400)[b]	30.3 (4350)
480	OD/Axial	0	3.08	6.2 (900)[b]	15.2 (2200)
493	OD/Axial	0	3.84	0.55 (80)[b]	17.6 (2550)
494	OD/Axial	0	0.54	31.7 (4600)	33.7 (4880)
719	OD/Axial	55	0.83	29.0 (4200)	29.7 (4300)
728	OD/Axial	90	1.97	14.5 (2100)[b]	20.7 (3000)
730	OD/Axial	100	1.10	37.9 (5500)	41.7 (6050)
731	OD/Axial	90	3.12	0.28 (40)[a,b]	21.4 (3100)
734	OD/Axial	55	1.71	34.5 (5000)	36.5 (5300)
226	OD/Axial/Circ	90	-	12.1 (1750)[b]	26.2 (3800)
363	OD/Axial/Circ/ Roll Trans.	90	-	18.6 (2700)[b]	24.7 (3580)

[a]Pre-test air bubble leak test at 0.28 MPa (40 psi) indicated throughwall pinhole.
[b]First leak occurred as one drop of water issuing from the flaw over a period of several minutes.

essentially no leak prior to sudden rapid flaw opening, yielding a leak rate >48.4 L/min (12.8 gpm). All of the flaws tested in this 14-tube series exhibited significant tearing, with varying degrees of secondary cracking evident. Some tubes also exhibited evidence of unstable tearing without the use of bladders.

Specimen SGL-226 contained an ODSCC flaw that exhibited both axial and circumferential cracking, based on pretest dye-penetrant and NDE examinations. A posttest photograph of the flaw opening (Fig. 4.64) shows a ≈6.35-mm (0.25-in.)-long axial crack intersected by a ≈25-mm (1-in.)-long circumferential crack. This flaw first began to leak at 12.1 MPa (1750 psi), with a rate of approximately one drop every few minutes. By the time the pressure had reached 20.7 MPa (3000 psi), the leak rate had increased to 4.39 L/min (1.16 gpm). The test was terminated at 26.2 MPa (3800 psi) when the flaw suddenly opened and the flow rate exceeded the facility capacity.

Specimen SGL-363 contained an ODSCC flaw at a roll transition that, based on pretest dye-penetrant and NDE examinations, was made up of a complex series of axial/circumferential cracks. Figure 4.65 shows the posttest photograph of the flaw opening, a large hole with both circumferential and axial ligament tearing and considerable secondary cracking. This flaw began to leak at 18.6 MPa (2700 psi), with a rate of approximately one drop every few minutes. The flaw abruptly opened at 24.7 MPa (3580 psi), and the flow rate again exceeded the facility capacity.

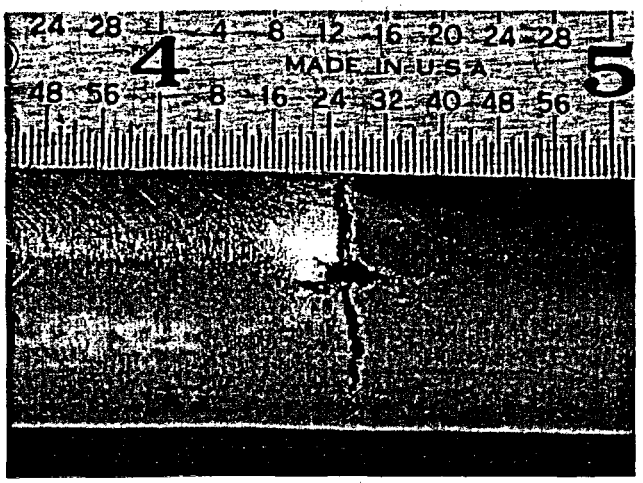

Figure 4.64.
Post-test appearance of complex ODSCC flaw in Specimen SGL-226 exhibiting both axial and circumferential cracking.

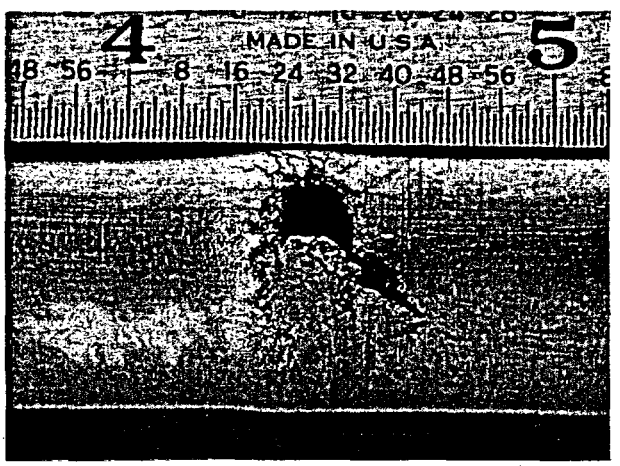

Figure 4.65.
Post-test appearance of complex ODSCC flaw in Specimen SGL-363 exhibiting a large opening resulting from both axial and circumferential cracking.

4.3.5 SCC from Operating Reactors

Pressure and leak-rate tests were performed on six McGuire tubes that were decontaminated and inspected using EC NDE. These tubes are designated 7-24-3, 5-51-2, 4-43-2, 14-55-3, 14-55-5, and 39-57-2. The NDE results identified short ODSCC flaws in the TSP region. The tubes were tested in the High-Pressure Test Facility using room-temperature water without bladders under a quasi-steady pressurization rate consisting of successive 0.7 MPa (100 psi) pressure increases with interspersed 5-s dwell periods up to the facility maximum pressure of 51.7 MPa (7500 psi).

The results for these tests are presented in Table 4.14. Four of the six flaws did not burst nor was any leak detected, and testing was terminated near the facility maximum pressure. Note that there was no access to the tubes to observe if very small leakage (e.g., single drops at the tube OD surface) was occurring. Flaws in two of the tubes, Tubes 4-43-2 and 39-57-2, opened suddenly and yielded significant flow rates at the pressures indicated in Table 4.14. These failures occurred at pressures lower than estimated by structural analysis based on the NDE estimates of flaw size.

Table 4.14. Results from pressure and leak-rate tests on tubes from McGuire SG. All flaws were in the TSP region.

Tube ID	Pressure at First Leak, MPa (psi)	Leak Rate at Max. Pressure, L/min @ MPa (gpm @ psi)	Predicted Opening Pressure, MPa (psi)	Visual Flaw Characteristics
7-24-3	(no leak)	0.0 @ 51.6 (0.0 @ 7.490)	62.0 (9,000)	Bulge; hairline circ. crack 6.35-mm (0.25-in.) long; secondary cracks.
5-51-2	(no leak)	0.0 @ 51.0 (0.0 @ 7,400)	66.2 (9,600)	Bulge; hairline axial crack 6.35-mm (0.25-in.) long; secondary cracks.
4-43-2	49.0 (7,100)	32.2 @ 49.0 (8.5 @ 7,100)	54.5 (7,900)	Bulge, 2 axial cracks with ligament between; total length 10 mm (3/8 in.).
14-55-3	(no leak)	0.0 @ 51.2 (0.0 @ 7,425)	64.8 (9,400)	No bulge; hairline axial crack 5-mm 3/16-in.) long; secondary cracks.
14-55-5	(no leak)	0.0 @ 50.9 (0.0 @ 7,380)	72.4 (10,500)	No bulge; axial crack 6.35-mm (0.25-in.) long.
39-57-2	36.2 (5,250)	28.0 @ 36.2 (7.4 @ 5,250)	61.4 (8,900)	Bulge; hairline axial crack 10-mm (3/8-in.) long; secondary cracks.

A preliminary posttest visual examination of Tube 7-24-3 showed a puckered, or raised, area on the outside of the tube in the TSP region. The puckered area was oriented circumferentially and had associated small secondary cracks, also with circumferential orientatations. The overall extent of the puckered region was nominally 6.35 mm (0.25 in.). Tube 5-51-2 exhibited a fine hairline axial crack, ≈6.35-mm (0.25-in.) long, in the TSP region, with less puckering and some small secondary cracking. All of the other tube flaws were axial. The flaw in Tube 4-43-2, which opened suddenly at a pressure of 49.0 MPa (7,100 psi) and exhibited a leak rate of 32.2 L/min (8.5 gpm), had two axial flaws separated by a ligament, with an overall length of ≈10 mm (3/8 in.). All of the flaws except that in Tube 39-57-2 did not leak or open up until the internal pressure exceeded the 3ΔP safety margin. Also, each flawed region consisted of a main flaw plus secondary flaws that also apparently contributed to the overall behavior. This finding is similar to that observed for the short laboratory-grown SCC flaws. These flaws have been destructively examined, and the results have been reported in Section 4.1.3.

4.4 Jet Erosion Under Design Basis Conditions

Two basic erosion damage mechanisms, droplet impact and cavitation, are believed to be associated with fluid jets. In the case of jets comprised of water droplets, the impact of the droplet gives rise to fluctuating stresses in the target, which produce fatigue damage. In the case of cavitation, bubbles form in the liquid stream and then collapse on impact, again producing fluctuating stresses and fatigue in the target.

Tests have been conduced to determine the susceptibility of steam generator tubes to erosive damage from impacting jets of superheated water or steam leaking from adjacent tubes. Most of the tests were performed using jets leaking from circular holes, though a few tests also used leaking tubes with laboratory-produced SCC flaws. In all cases, the distance between the leaking tube and the target tube was 6.35 mm (0.25 in.), and the tubes were oriented to produce an impact angle of 90° on the target tube. All tests were conducted in the high-temperature Pressure and Leak-Rate Test Facility. The test duration was generally based on the hole leak rate, which is a function of the hole area and the pressure. Test times are constrained by the 760 L (200 gal) blowdown vessel capacity, though longer test times can be achieved by shutting down the facility, refilling the blowdown vessel, and restarting.

The target specimens were fabricated from 22.2-mm (7/8-in.)-diameter Alloy 600 tubing with a nominal wall thickness of 1.27 mm (0.050 in.). A cold-discharge machining method was used to avoid any mechanical or thermal working of the material. The target specimens were 6.35-mm (0.25-in.) wide and 38.1-mm (1.5-in.) long, with four legs that attach to the leaking flawed tube to hold the target at a distance of 6.35 mm (0.25 in.) from the jet exit. Each leg is fastened to the flawed tube by four spot-welded fastening straps, and the escaping jet impacts the concave surface of the target specimen (Fig. 4.66).

Erosion tests were performed using jets from 1.59-, 0.79-, and 0.40-mm ($^1/_{16}$-, $^1/_{32}$- and $^1/_{64}$-in.)-diameter EDM circular holes. The jets were produced using a tube internal pressure of 17.2 MPa (2500 psi). The external pressure for most of the tests was zero, approximating MSLB conditions, but a few tests were performed with other external pressures. The test duration was typically ≈2 h. A range of water temperatures was used to assess the influence of degree of subcooling on erosion behavior.

The jet impact zone of a test with a 0.79-mm ($^1/_{32}$-in.)-diameter hole, a temperature of 282°C (540°F), an internal pressure of 16.7 MPa (2428 psi), and a back pressure of 3.7 MPa (530 psig) is shown in Fig. 4.67. Erosion of the hole in the leaking tube was also verified. High-magnification SEM examinations of the jet impact zone verified the presence of erosion suggested in this optical photograph. The depth of material removed can be estimated using a scanning phase-shift three-dimensional surface profiler microscope. This instrument produces an image in which color or shading represents height or depth relative to a reference location. Figure 4.68 shows the phase-shift image of the jet impact zone in Fig. 4.67. The depths of various features for each scan referenced relative to the uneroded surface of the specimen are rendered in different shades in the photograph. The deepest erosion penetration is found to be 260 μm, or ≈21% of the tube wall thickness.

The results for the erosion tests on circular orifices are summarized in Tables 4.15-4.17. The tests in Table 4.15 involved a significant amount of subcooling. An additional 16 erosion

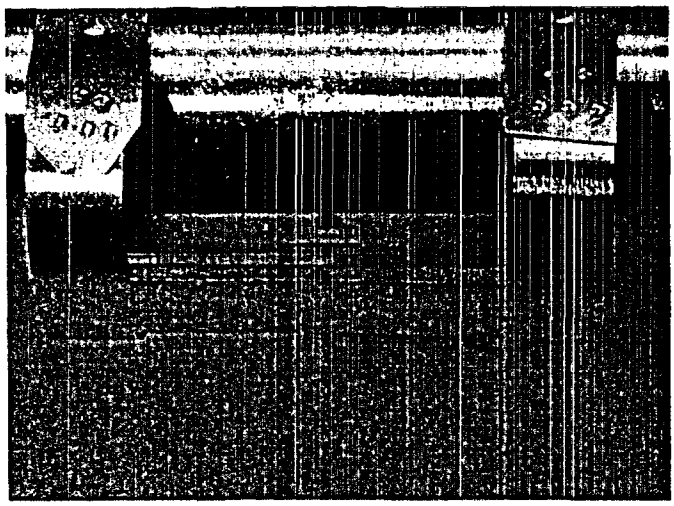

Figure 4.66.
Setup for jet-impact erosion test showing EDM hole in Alloy 600 tube and Alloy 600 impact specimen fastened by spot-welded straps to the tube. There is a 6.35-mm (0.25-in.) gap between the jet exit and the impact specimen.

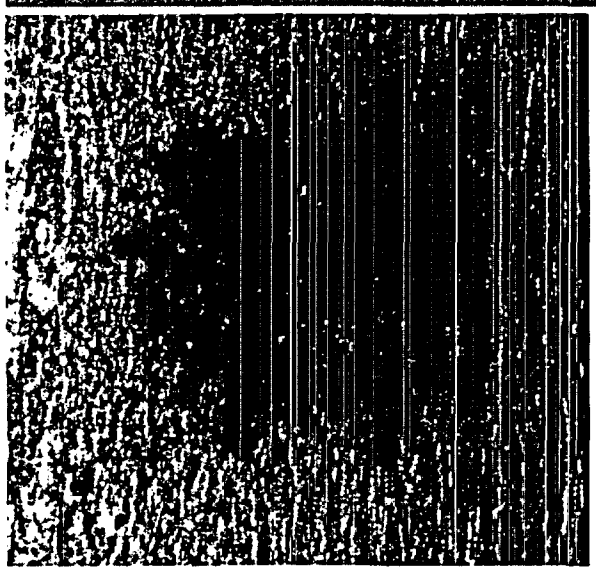

Figure 4.67.
Close-up view of 0.79-mm (1/32-in.) hole in jet-impact specimen after 265 min of testing at 282°C (540°F) and 17.2 MPa (2500 psig) with 3.7 MPa (530 psig) back pressure.

tests were conducted with 0.79 and 0.40-mm ($^1/_{32}$- and $^1/_{64}$-in.)-diameter hole sizes (Tables 4.16 and 4.17, respectively), to more thoroughly explore the parameters influencing jet-impingement erosion under prototypical conditions. The tests featured reduced levels of subcooling using water temperatures of 135-308°C (275-587°F). Most of the tests were of 2 h duration, but two of the 0.79-mm ($^1/_{32}$-in.)-diameter-hole tests lasted 4 and 6 h, respectively.

Figure 4.69 shows a plot of jet-induced erosion depth as a percent of specimen wall thickness as a function of temperature for both hole sizes. For the sake of completeness, a data point from testing a 1.59-mm ($^1/_{16}$-in.)-diameter hole with 282°C (550°F) water, which yielded 3.2% coupon penetration depth, is included. This plot indicates that impact erosion depth varies with water temperature, and the erosion rate is substantially reduced with decreasing and increasing subcooling on either side of the peak damage temperature range. Examination of the jet impact zones shows that, as expected, for large amounts of subcooling, the impact zone is about the same diameter as the jet. For very small amounts of subcooling, the size of the impact zone is substantially larger than the initial jet diameter, indicating that flashing has occurred. The zone of peak erosion corresponds to a situation in which the

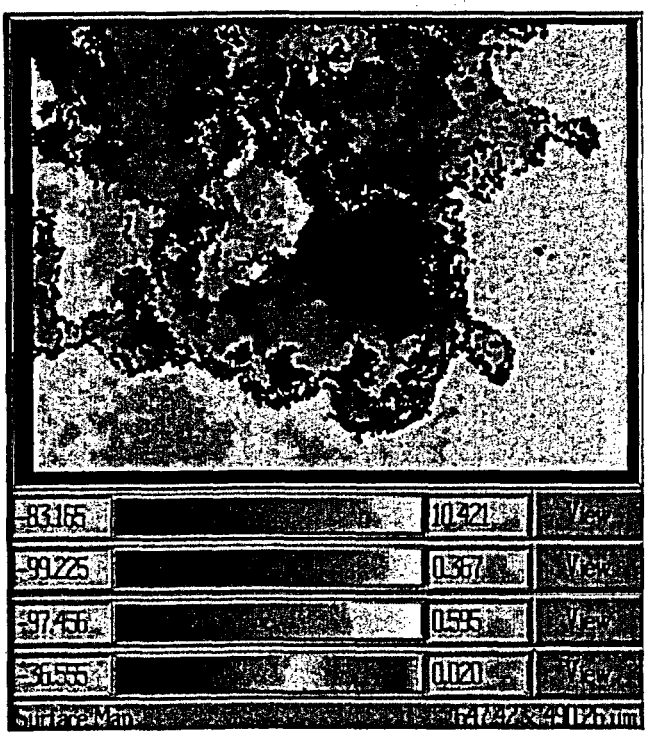

Figure 4.68.
Depth of the erosion zone shown in Fig. 4.67, as determined using interferometric techniques.

Table 4.15. Erosion data from jet-impact erosion tests utilizing jets from various sizes of EDM holes impacting Alloy 600 erosion coupons positioned 6.35-mm (0.25-in.) from the hole exit at 282°C and room temperature.

Jet Hole diameter mm (in.)	Water Temperature, °C (°F)	Tube Internal/External Pressure, MPa (psig)	Test Duration, min	Erosion Depth, % Wall Thickness
1.59 (1/16)	282 (540)	16.7/0.04 (2428/6)	34.1	(slight surface burnishing)
0.79 (1/32)	21 (70)	17.2/0 (2500/0)	240	(slight surface burnishing)
0.79 (1/32)	282 (540)	16.7/3.7 (2428/530)	265	21
0.40 (1/64)	282 (540)	17.3/0 (2502/0)	198	9

impact zone is the same diameter as the jet. This suggests that the primary mechanism for erosion is cavitation due to vapor bubble formation at the onset of two-phase conditions. Erosion rates are low in the purely single phase regime (large subcooling) and in the two-phase region where flashing occurs either in the tube wall or in the region between the tube and the target (small subcooling).

Table 4.16. Erosion data from jet-impact erosion tests utilizing jets from 0.40-mm (1/64-in.)-diameter EDM holes impacting Alloy 600 erosion coupons positioned 6.35-mm (0.25-in.) from the hole exit for various water temperatures. For all tests, the tube internal pressure was 16.8 MPa (2432 psig) with zero back pressure.

Coupon No.	Water Temp., °C	(°F)	Test Duration, min	Erosion Depth, % Wall Thickness
21	289	(553)	123	1.8
24	239	(463)	123	11.9
26	209	(408)	123	18.6
28	182	(360)	123	18.6
29	135	(275)	123	5.9

Table 4.17. Erosion data from jet-impact erosion tests utilizing jets from 0.79-mm (1/32-in.)-diameter circular EDM holes impacting Alloy 600 erosion coupons positioned 6.35-mm (0.25-in.) from the hole exit for various water temperatures. For all tests, the tube internal pressure was 16.8 MPa (2432 psig) with zero back pressure.

Coupon No.	Water Temp., °C	(°F)	Test Duration, min	Erosion Depth, % Wall Thickness
8	278	(532)	123	28.0
9	307	(586)	123	4.6
10	281	(537)	369	28.1
11	308	(587)	246	7.9
12	292	(558)	124	14.0
13	271	(519)	123	27.8
14	287	(548)	127	13.0
15	259	(499)	123	14.0
17	288	(550)	123	15.2
18	233	(451)	124	17.0
19	180	(356)	123	15.6

The temperature at which the peak erosion rate occurs varies with hole size. The peak erosion rate for the 0.40-mm (1/64-in.)-diameter hole occurs in the range of 182-210°C (360-410°F), while that for the 0.79-mm (1/32-in.)-diameter hole occurs in the range of 271-288°C (520-550°F). This behavior is consistent with the primary damage mechanism being cavitation and reflects the degree of flashing of water to steam in the hole, with the smaller-diameter hole producing more flashing at a given temperature and consequently lower erosion. In addition, the temperature at which flashing becomes significant is lower for the smaller-diameter hole.

For the orifice flows considered here, the erosion rates peak for degrees of subcooling typical of the cold leg, where, however, cracking is much less likely to occur. Erosion rates are much lower for conditions more typical of the hot leg. The trends observed with decreasing orifice size also suggest that the margin is even larger for actual stress corrosion cracks, since they typically would be even tighter than the 0.40-mm (1/64-in.)-diameter hole.

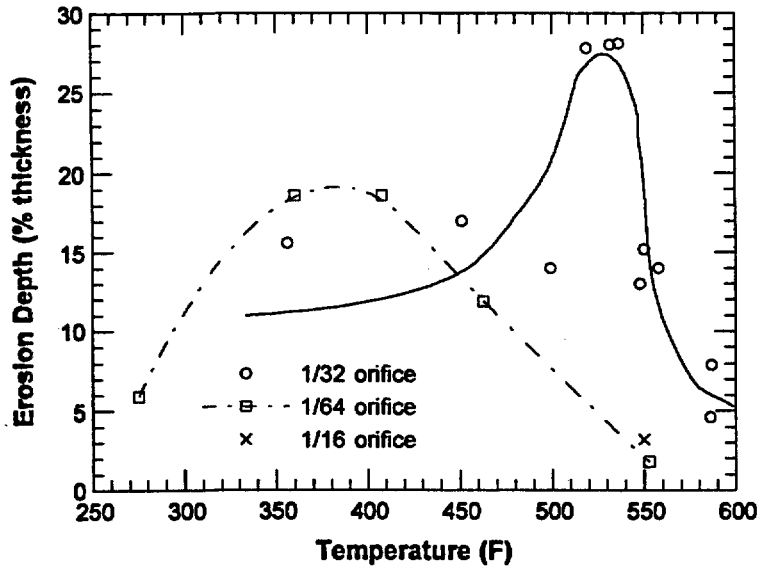

Figure 4.69.
Jet erosion penetration depth as a function of water temperature for 0.40- (triangles), 0.79-(circles), and 1.59-mm (cross) ($1/64$-, $1/32$-, and $1/16$-in.)-diameter EDM holes. For all tests, the tube internal pressure was 16.8 MPa (2432 psig) with zero back pressure. Most tests were 123-min duration.

Tests were planned to validate these results on more prototypical flaws, but to date only one test has been performed with a laboratory-produced ODSCC axial flaw (SGL-818). The flaws and the associated jets at 17.2 MPa (2500 psi) were first evaluated in the room-temperature High-Pressure Test Facility, where visual observation of the flaw jet behavior and very accurate determination of flow rate are possible.

Specimen SGL-818 was identified by NDE to be axial OD and nominally 10-mm (0.4-in.) long, with greater than 95% penetration. At 17.2 MPa (2500 psi) and room temperature, the leaking jet was fan-shaped and somewhat rotated out of axial alignment, with a base length at the tube of 3.2 mm ($1/8$ in.); at 6.35 mm ($1/4$ in.) above the tube surface (where the coupon would be located in the erosion test), its length had spread to 6.3 mm ($1/4$ in.). The jet was nonuniform over its breadth. The measured leak rate for the flaw was 1.1 kg/min (2.5 lb/min) or 1.1 L/min (0.3 gpm).

An erosion test at 288°C (550°F) and an internal pressure of 17.2 MPa (2500 psi) was then performed with this flaw. After 123 min of testing, no significant erosion of the target specimen was detected, with only very slight burnishing observed. Because this flaw was much tighter than the EDM holes, it would likely have higher frictional losses and, hence, a greater tendency for flashing under the same pressure and temperature conditions. Based on the orifice results, flashing results in a decreased erosion rate.

The SCC flaw in Specimen SGL 818 was opened in the High-Pressure Test Facility by subjecting it to a pressure of 21.7 MPa (3150 psi) to achieve a higher flow rate. It was then used in a jet-impact erosion test under the same conditions as previously. The erosion coupon showed more burnishing than in the first test, but the erosion depth was still <1%. It appears that the flaw remained tight enough that flashing is still occurring either in the tube wall or in the gap between tube and coupon or both.

4.5 Tube Failure Models under Design-Basis and Severe Accident Conditions

4.5.1 Characterization of Alloy 600 Tubing Material

4.5.1.1 Room-Temperature Mechanical Properties

Room-temperature tensile tests were conducted by two outside vendors on two heats of 22.2-mm (0.875-in.)-diameter Alloy 600 tubing, one purchased from Valinco (heat no. NX 8527) and a second heat obtained from PNNL. The results from these tests have been reported in detail in Ref. 13. The PNNL tube (ID EX-82-1/2675) is both stronger and more ductile than the Valinco tube (Heat No. NX 8527).

Alloy 600 tubes with diameters of 19.1-mm (0.750-in.)-diameter (Valinco heat no. NX 8524), 22.2-mm (0.875-in.)-diameter (Valinco heat no. NX 8527) and 22.2-mm (0.875-in.)-diameter (PNNL ID EX-82-1/2675) were sent to an outside vendor for pressure testing. Three unflawed tubes for each diameter were pressure tested with room-temperature water to failure. Results from pressure tests conducted at ANL are compared with those conducted at PNNL [26] in Table 4.18, which also includes the average tensile properties for the various heats. The failure pressure for the 19.1-mm (0.750-in.)-diameter Valinco tube is comparable to that of the 19.1-mm (0.750-in.)-diameter PNNL tube, although the PNNL tube has 16% higher yield strength. Both the failure pressure and tensile properties of the 22.2-mm (0.875-in.)-diameter PNNL heat EX-82-1/2675 are significantly higher than those of the other 22.2-mm (0.875-in.)-diameter PNNL heats. Tensile properties of the 22.2-mm (0.875-in.)-diameter Valinco tube are slightly lower than the PNNL heats, even though its failure pressure is about 5% higher than those reported by PNNL.

Elevated-Temperature Mechanical Properties

Elevated-temperature tensile and creep rupture data were collected from the literature. The flow stress (average of yield and ultimate tensile strengths in MPa as a function of temperature in °C) for the INEEL rod samples is given by [27]

$$\bar{\sigma} = \begin{cases} 564.4 - 0.4546T + 1.5055\times10^{-3}T^2 - 1.9907\times10^{-6}T^3 & \text{for } 20°C \le T \le 727°C \\ 4308.9 - 11.381T + 1.030\times10^{-2}T^2 - 3.1734\times10^{-6}T^3 & \text{for } 727°C < T \le 1100°C \end{cases} \quad (4.2)$$

A plot of the flow stress curve for various product forms is given in Fig. 4.70. Note that at high temperatures (>600°C), the flow stresses of various product forms tend to converge.

The Larson-Miller equation for creep rupture time is [13]

$$\log_{10}\sigma = 4.31\pm0.10 - 1.43 \times 10^{-4} P_{lm} \text{ for } \sigma \le 39.3 \text{ MPa} \quad (4.3a)$$

$$\log_{10}\sigma = 5.03\pm0.13 - 1.81 \times 10^{-4} P_{lm} \text{ for } \sigma > 39.3 \text{ MPa} \quad (4.3b)$$

where the time to rupture t_R is then given by

Table 4.18. Room-temperature failure pressures and axial tensile properties of unflawed Alloy 600 tubing tested by ANL [13] and PNNL [26].

Heat No.	Tested by	Diam., mm (in.)	Wall Thickness, mm (in.)	Avg. Fail. Press., MPa (ksi)	Avg. Yield Strength, MPa (ksi)	Avg. Ultimate Tensile Strength, MPa (ksi)
Valinco (NX 8524)	ANL	19.1 (0.750)	1.09 (0.043)	68.5 (9.94)	308 (44.7)	681 (98.8)
Heat C	PNNL	19.1 (0.750)	1.09 (0.043)	67.1 (9.73)	361 (52.4)	674 (97.8)
PNNL (EX-82-1/2675)	ANL	22.2 (0.875)	1.27 (0.050)	72.4 (10.50)	357 (51.8)	683 (99.1)
Heat B	PNNL	22.2 (0.875)	1.27 (0.050)	65.1 (9.44)	328 (47.6)	641 (93.0)
Heat E	PNNL	22.2 (0.875)	1.27 (0.050)	65.8 (9.54)	300 (43.5)	681 (98.8)
Heat F	PNNL	22.2 (0.875)	1.27 (0.050)	64.1 (9.30)	274 (39.7)	665 (96.4)
Valinco (NX 8527)	ANL	22.2 (0.875)	1.27 (0.050)	69.4 (10.07)	271 (39.3)	634 (92.0)

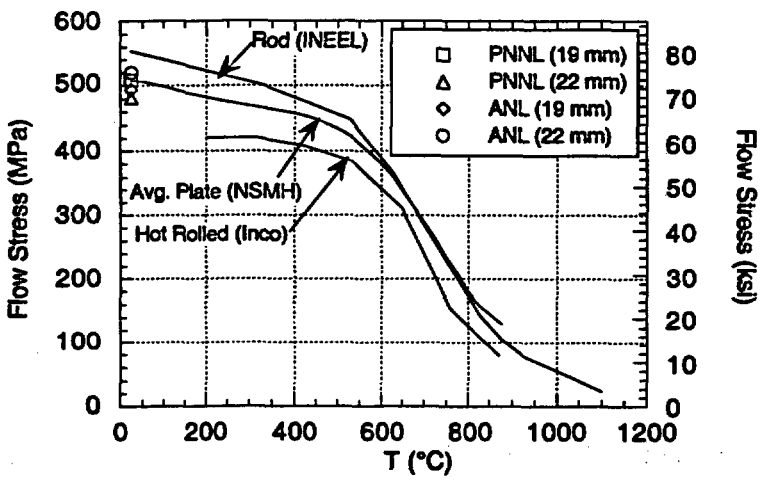

Figure 4.70.
Flow stress curves for various product forms of Alloy 600.

$$t_R = 10^{\frac{P_{lm}}{T} - 15} \qquad (4.4)$$

with t_R in h and T in K. The Larson-Miller plot is shown in Fig. 4.71.

4.5.2 Low-Temperature Failure Models

The failure pressure of unflawed tubes can be described in terms of a simple plastic collapse model:

$$P_b = \frac{h\bar{\sigma}}{R_m}, \qquad (4.5a)$$

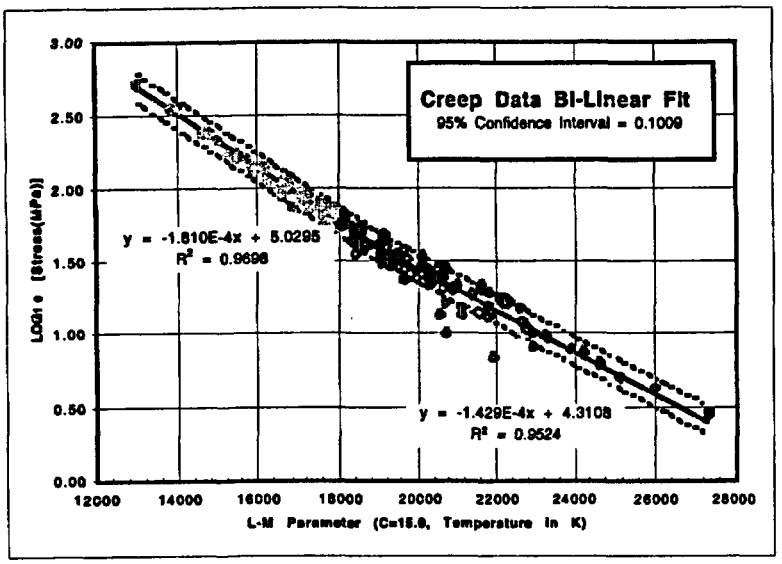

Figure 4.71.
Bilinear fit to existing creep data for Alloy 600. The three low outliers were not included in the statistical analysis.

where

$\bar{\sigma}$ = Flow stress = $k(S_u + S_y)$, (4.5b)

P_b = failure pressure of unflawed tube,

R_m = mean radius of tube,

h = wall thickness of tube,

k = flow stress factor,

S_u = ultimate tensile strength, and

S_y = yield strength.

Substituting the tensile and failure pressure data from Table 4.18 into Eqs. 4.5a and b yields the following the values of k for the three heats:

Valinco (19.1-mm diameter, heat no. NX 8524): k = 0.57,

Valinco (22.2-mm diameter, heat no. NX 8527): k = 0.63, (4.6)

PNNL (22.2-mm diameter, ID EX-82-1/2675): k = 0.57.

These are reasonably consistent with the k values for Alloy 600 reported in the literature, which vary between 0.5 and 0.6. The value of k for the 22.2-mm (0.875-in.)-diameter Valinco heat appears to be slightly on the high side.

4.5.2.1 Throughwall Axial Cracks

The most widely used model for predicting the pressure to cause unstable ductile (plastic collapse) failure of a tube with a throughwall axial crack is that originally proposed by Hahn et al. [28], later modified by Erdogan [29]:

$$p_{cr} = \frac{\bar{\sigma} h}{m R_m} = \frac{p_b}{m}, \tag{4.7a}$$

where

$$m = 0.614 + 0.481\lambda + 0.386\exp(-1.25\lambda), \tag{4.7b}$$

$$\lambda = \left[12(1-\nu^2)\right]^{\frac{1}{4}} \frac{c}{\sqrt{R_m h}} = \frac{1.82c}{\sqrt{R_m h}}, \tag{4.7c}$$

and p_b is the failure pressure of an unflawed tube (Eq. 4.5a) and 2c is the axial crack length.

4.5.2.2 Part-throughwall Axial Cracks

For part-throughwall axial cracks, the pressure required to fail the remaining through-thickness crack tip radial ligament can be calculated by an empirical equation (referred to as the BCL equation) developed by Kiefner et al. [30]:

$$p_{sc} = \frac{\bar{\sigma} h}{m_p R_m} = \frac{p_b}{m_p}, \tag{4.8a}$$

where

$$m_p = \frac{1 - \frac{a}{mh}}{1 - \frac{a}{h}}, \tag{4.8b}$$

and a is the crack depth. It should be emphasized that Eq. 4.8a gives only the pressure required to fail the remaining radial ligament. The stability of the resulting throughwall crack can be analyzed using Eq. 4.7a. If $p_{cr} > p_{sc}$, the throughwall crack is stable. Although the crack will leak, it will not increase in length without a further increase in pressure. If $p_{cr} < p_{sc}$, the resulting crack will be unstable and will rapidly increase in length without any additional increase in pressure.

Comparison with experiments shows that Eqs. 4.8a-b tend to underestimate the ligament rupture pressures of short and deep cracks [25]. Under the auspices of an NRC-sponsored steam generator integrity program, PNNL [26] conducted a series of pressure tests on Alloy 600 steam generator tubes containing part-through axial slots. The PNNL tube test data were re-analyzed (including re-measurements of the flaws by posttest fractography) by ANL, and the following equation was proposed for predicting ligament rupture pressure (referred to as the ANL equation) [25]:

$$m_p = \frac{1 - \alpha\frac{a}{mh}}{1 - \frac{a}{h}}, \tag{4.8c}$$

where

$$\alpha = 1 + \beta\left(\frac{a}{h}\right)^2\left(1 - \frac{1}{m}\right), \text{ and} \tag{4.8d}$$

β is a constant ≈ 1.

Except for short and deep cracks, Eq. 4.8c predicts similar failure pressures as Eq. 4.8b. The ANL equation has been validated for short and deep slots with a series of tests on Alloy 600 tubes with EDM slots (Fig. 4.3) and laser-cut slots (Fig. 4.4).

4.5.2.3 Throughwall Circumferential Cracks

Failure loads of tubes with a single circumferential crack depend critically on the bending constraint imposed externally on the tubes. The two extreme cases are the free-bending case and the fully constrained case. In most cases, the tube support plates (TSPs) offer substantial restraint against bending, and the failure loads are generally closer to the fully constrained case.

Ranganath and Mehta [31] calculated failure loads for throughwall circumferential cracks by plastic limit load (collapse) analyses, which were based on earlier work by Kanninen et al. [32]. For an unconstrained (free-to-bend) tube with a throughwall crack of angular length 2θ and no applied primary bending stress, the critical failure pressure is

$$p_{cr} = \frac{2\bar{\sigma}h}{R_m}\left(1 - \frac{\theta}{\pi} - \frac{2\beta}{\pi}\right), \tag{4.9a}$$

where the angular location of the neutral axis is given by

$$\beta = \sin^{-1}\left(\frac{\sin\theta}{2}\right) \tag{4.9b}$$

Equation 4.9a is applicable to the case where the tube is completely free to bend. In the opposite case of total constraint against bending, a criterion based on maximum shear stress in the net section as proposed by Cochet et al. [33] can be used to calculate the instability limit pressure:

$$p_{cr} = \frac{2(\gamma^2 - 1)(\pi - \theta)\bar{\sigma}}{2\pi + (\pi - \theta)(\gamma^2 - 1)}, \tag{4.10a}$$

where

$$\gamma = \frac{R_o}{R_i}. \tag{4.10b}$$

The following thin-shell, uniaxial approximation to Eq. 4.10a is often used for predicting failure of steam generator tubes that are fully constrained against bending:

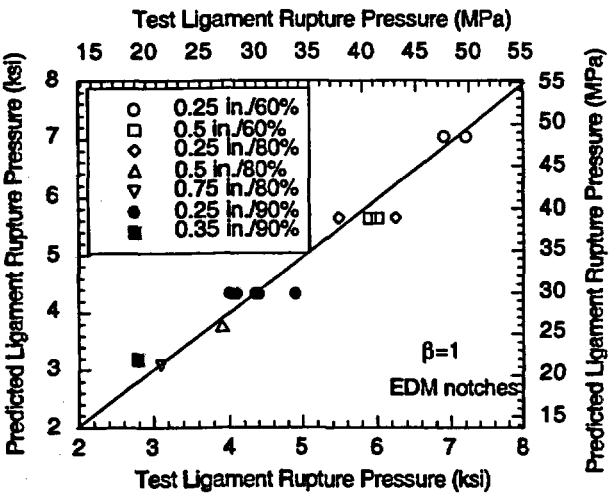

Figure 4.72.
Observed vs. predicted ligament rupture pressures for tubes with EDM notches using k = 0.55 and β = 1.

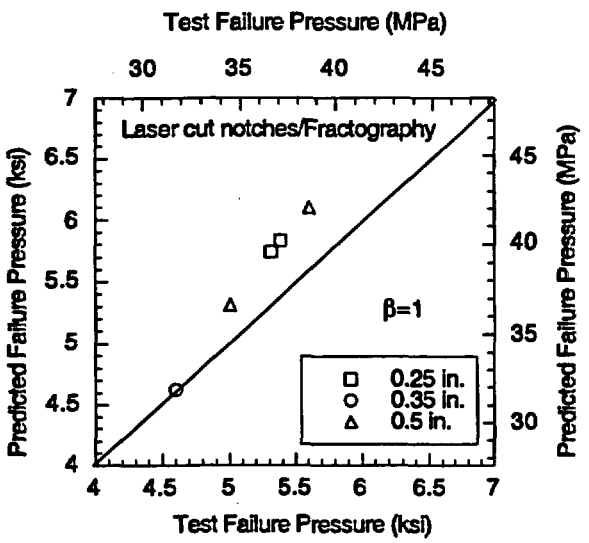

Figure 4.73.
Observed vs. predicted ligament rupture pressures for tubes with ≈80% deep laser-cut notches using k = 0.55 and β = 1.

$$p_{cr} = \frac{2\bar{\sigma}h}{R_m}\left(1-\frac{\theta}{\pi}\right). \qquad (4.10c)$$

As noted previously, the tube support plates offer a significant but not total restraint against bending. This condition tends to increase the failure pressure to somewhere between those predicted by Eqs. 4.9a and 4.10a (or 4.10c). A detailed analysis of the failure of a partially constrained tube with a throughwall circumferential flaw was presented in Ref. 34. It was shown that for a tubesheet-to-TSP span of 0.67 m (26 in.), which is typical of many generators, the critical pressure is much closer to the fully constrained case than the free-bending case.

4.5.2.4 Part Throughwall Circumferential Cracks

The pressure for through-thickness crack tip radial ligament rupture (p_{SC}) is generally expressed in terms of a stress magnification factor (m_p) and is obtained by equating the magnified axial stress in the ligament to the flow stress,

$$p_{sc} = \frac{2\bar{\sigma}h}{R_m m_p}. \tag{4.11}$$

As in the case of throughwall cracks, the ligament rupture pressure for circumferentially cracked tubes, i.e., the value of the magnification factor m_p, depends strongly on the degree of restraint against bending. The free bending and the completely constrained case are relatively easy to analyze (see below). The failure loads are expected to be much closer to the completely constrained case than the free bending case. The discussion here assumes that the tubes are either completely constrained or are completely free to bend.

Fully Constrained Case

This would also include the case for an unrestrained tube containing two symmetrical cracks. The whole section containing the crack (or cracks) is subjected to uniform axial tensile stresses with the ligament (or ligaments) being subjected to stress intensification. If the stress in the ligament (or ligaments) is expressed as 1/m times the stress in the rest of the section containing the crack (or cracks), the ligament stress (σ_{lig}) can be calculated from a simple equilibrium of axial forces,

$$\sigma_{lig} = \frac{pR_m}{2h} \frac{1}{\left[m + \left(\frac{n\theta}{\pi}\right)\left(1 - \frac{a}{h} - m\right)\right]}, \tag{4.12a}$$

where

$$n = \begin{cases} 1 \text{ for a single crack} \\ 2 \text{ for two symmetrical cracks} \end{cases}.$$

If we define m_p as the ratio between the ligament stress and the axial stress in the unflawed tube, m_p is given by

$$m_p = \frac{1}{\left[m + \left(\frac{n\theta}{\pi}\right)\left(1 - \frac{a}{h} - m\right)\right]}. \tag{4.12b}$$

Originally, Kurihara et al. [36] used an empirically obtained expression for m (with n = 1),

$$m = 1 - \left(\frac{a}{h}\right)^{\kappa}\left(\frac{n\theta}{\pi}\right)^{\mu}. \tag{4.13}$$

Since Eq. 4.13 does not have the correct limiting behavior (i.e., m does not tend to 0 when a/h tends to 1 for all θ), it was modified to have the same form as in the axial crack case, i.e. [4],

$$m = \frac{1 - \frac{a}{h}}{1 - \frac{a}{Nh}}, \tag{4.14a}$$

where

$$N = 1 + \lambda\left(\frac{n\theta}{\pi}\right)^{\gamma}. \tag{4.14b}$$

and λ and γ are fitting parameters. The test results on Type 304 stainless steel reported by Kurihara et al. [35] can be predicted fairly well by assuming $\lambda = \gamma = 0.2$ [4].

The original set of test data on four-point bending failure tests on pressurized part-through circumferentially cracked Type 304 stainless steel pipes at room temperature used by Kurihara et al. [35] are predicted (both failure modes and moments) somewhat better by the current model than by the Kurihara model [4].

Free-Bending Case

In this case a part of the section containing the crack will, in general, be subjected to compressive stress. As a result, Eq. 4.12a has to be replaced by

$$\sigma_{lig} = \frac{pR_m}{2h}\frac{1}{\left[m\left(1-\frac{2\beta}{\pi}\right)+\left(\frac{n\theta}{\pi}\right)\left(1-\frac{a}{h}-m\right)\right]}, \tag{4.15a}$$

where the angle β defining the location of the neutral axis is given by

$$\beta = \sin^{-1}\left[\frac{\sin\theta}{2}\left\{1-\frac{1}{m}\left(1-\frac{a}{h}\right)\right\}\right] \text{ for } \beta \le \pi - \theta, \tag{4.15b}$$

and Eq. 4.12b has to be replaced by

$$m_p = \frac{1}{\left[m\left(1-\frac{2\beta}{\pi}\right)+\left(\frac{n\theta}{\pi}\right)\left(1-\frac{a}{h}-m\right)\right]}, \tag{4.15c}$$

with m defined by Eq. 4.14a and n is the number of cracks.

4.5.2.5 Equivalent Rectangular Crack

So far the flaw has been considered a single crack that is rectangular in shape. In reality, stress corrosion cracks are multiple, nonplanar flaws that are complex in shape and have ligaments between the segments. To predict the through-thickness crack tip radial ligament rupture pressure (i.e., pressure beyond which leakage will occur) for complex-shaped multiple cracks, we have used the concept of an "equivalent rectangular crack." The procedure starts with a crack depth profile that has been determined either by eddy current or by fractography technique (e.g., Fig. 4.74, dashed line).

To determine the equivalent rectangular crack, a series of candidate equivalent rectangular cracks is considered with different lengths (e.g., Fig. 4.74, solid line). The

equivalent depth for the candidate equivalent rectangular crack is determined by computing the average depth contained within the crack length being considered and ignoring the depth profile outside (i.e., equating the hatched areas in Fig. 4.74). Out of all the candidate equivalent rectangular cracks, the one with the lowest ligament rupture pressure (i.e., highest m_p) is defined as the equivalent rectangular crack. Upon ligament rupture, leakage occurs through the 100% throughwall portion of the crack whose length is assumed to be equal to the length of the equivalent rectangular crack. The procedure has been automated in an Excel spreadsheet.

4.5.2.6 Multiple Notches

Tests were conducted for tubes with multiple notches in various configurations. Details are given in Ref. 36.

Two Part-Throughwall Axial EDM Notches

The through-thickness radial ligament rupture pressures for tubes with two part-throughwall axial notches, type 2 (axial ligament) and type 4 (circumferential ligament) as depicted in Fig. 4.75, were calculated by the equivalent rectangular approach for various notch lengths and inter-notch ligament widths. Tests were conducted in the High-Pressure Test Facility on specimens without bladders and were interrupted after the through-thickness ligament ruptured, as evidenced by onset of leakage (Stage 1). Comparison of predicted vs. experimental ligament rupture pressures, given in Figs. 4.76a and 76b, shows that the equivalent rectangular crack approach can predict the through-thickness ligament rupture pressures reasonably well. Except for the cases identified in Figs. 4.76a and 76b, the through-thickness radial ligament and the inter-notch ligament ruptured simultaneously. The inter-notch ligament width beyond which the two notches do not interact (from the viewpoint of pressure for through-thickness radial ligament rupture) depends on the notch depth as well as notch length. A 3-mm (0.1-in.)-wide ligament increases the through-thickness ligament rupture pressure by ≈30%, with the axial ligament having a slightly higher strengthening effect than the circumferential ligament. For smaller ligament widths, both types of ligaments (2 and 4) have comparable strengthening effect.

Two 100%-throughwall axial EDM notches

The pressures for inter-notch ligament rupture for two 100%-TW notches were calculated by nonlinear, finite deformation FEA. The calculated (by ANSYS and ABAQUS) variation of average ligament thickness vs. pressure for two 6-mm (0.25-in.)-long, 100% TW notches separated by a 2.5-mm (0.1-in.)-wide circumferential ligament is shown in Fig. 4.76a. Figure 4.77b shows the variation of calculated (axial ligament) and experimental ligament rupture pressure with ligament width for two 6-mm (0.25-in.) and two 13-mm (0.5-in.)-long, 100%-TW notches. Also shown in the figure by dashed lines are unstable burst pressures for 25-mm (1-in.) and 13-mm (0.5-in.)-long, 100%-TW notches. It is evident that the unstable burst pressures of a 13-mm (0.5-in.) and 25-mm (1-in.)-long, 100% TW notches are not increased by introducing a full thickness ligament with width less than about 1.3 mm (0.05 in.).

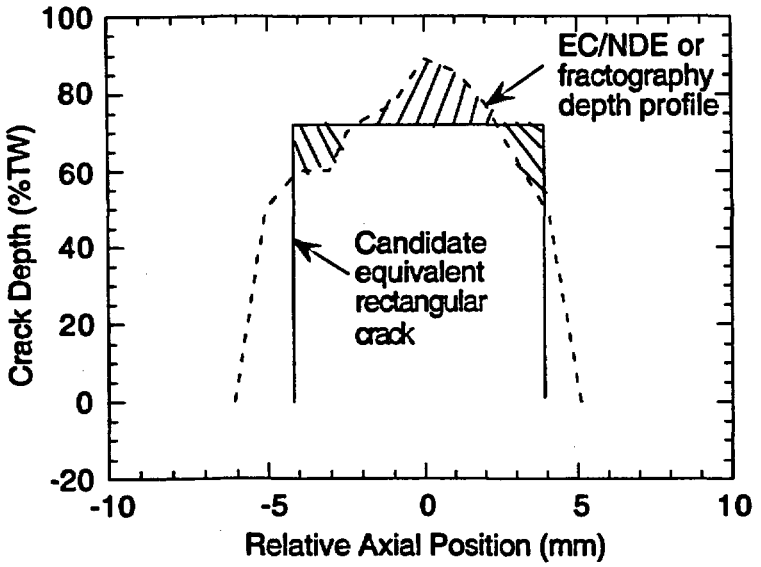

Figure 4.74.
Determination of equivalent rectangular crack.

Mutiple axial laser-cut notches

A series of tests was conducted on Alloy 600 tubes with 2 to 6 part-throughwall axial laser-cut notches in various configurations (Fig. 4.75). The ligament widths varied between 0.13 and 0.25 mm (0.005 and 0.010 in.). Predicted vs. observed pressures for through-thickness ligament rupture are shown in Fig. 4.78. Although the rupture pressures are reasonably predicted by the equivalent rectangular crack method for the case of two notches, they are overestimated by ≈30% for the case of six notches.

4.5.3 Leak Rate Models for Single-Phase Flow

The leak rate model based on simple orifice flow through a crack with an opening area A and a coefficient of discharge $C_d = 0.6$ is as follows:

$$Q = 0.6A\sqrt{\frac{2\Delta p}{\rho}}, \tag{4.16a}$$

where A is crack opening area, Δp is pressure differential, and ρ is mass density of water. This equation has been used successfully to predict leak rates in experiments conducted at room temperature and 282°C on specimens with EDM notches and stress corrosion cracks at ANL down to a leak rate of ≈0.44 L/min (≈0.1 gal/min). The correlation will break down at lower leak rates for very tight stress corrosion cracks, particularly at elevated temperatures where flashing may occur inside the cracks, but the conditions for such a limit have not yet been established. Expressing Q in L/min, A in mm^2, Δp in MPa, and ρ in kg/m^3,

$$Q = 50.9A\sqrt{\frac{\Delta p}{\rho}} \tag{4.16b}$$

or, using English units, i.e., Q in gpm, A in in^2, Δp in psi, and ρ in lb/ft^3,

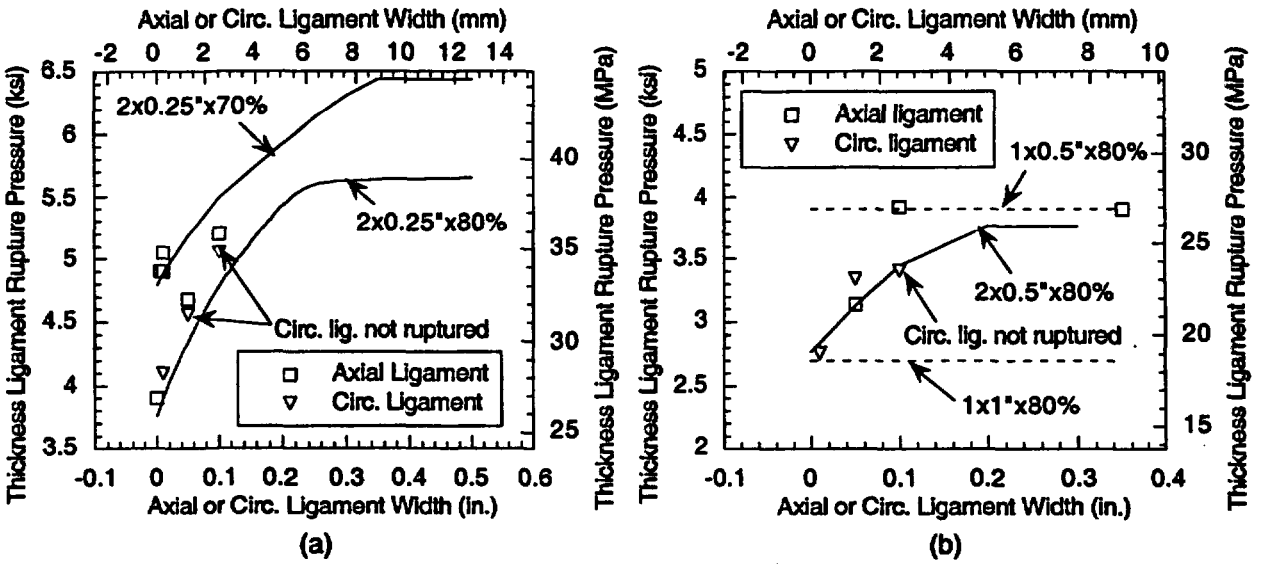

Figure 4.75. Predicted and observed rupture pressures for through-thickness ligaments as a function of axial or circumferential ligament widths for two part-throughwall EDM notches 6-mm (0.25–in.) and 13-mm (0.5-in.) long.

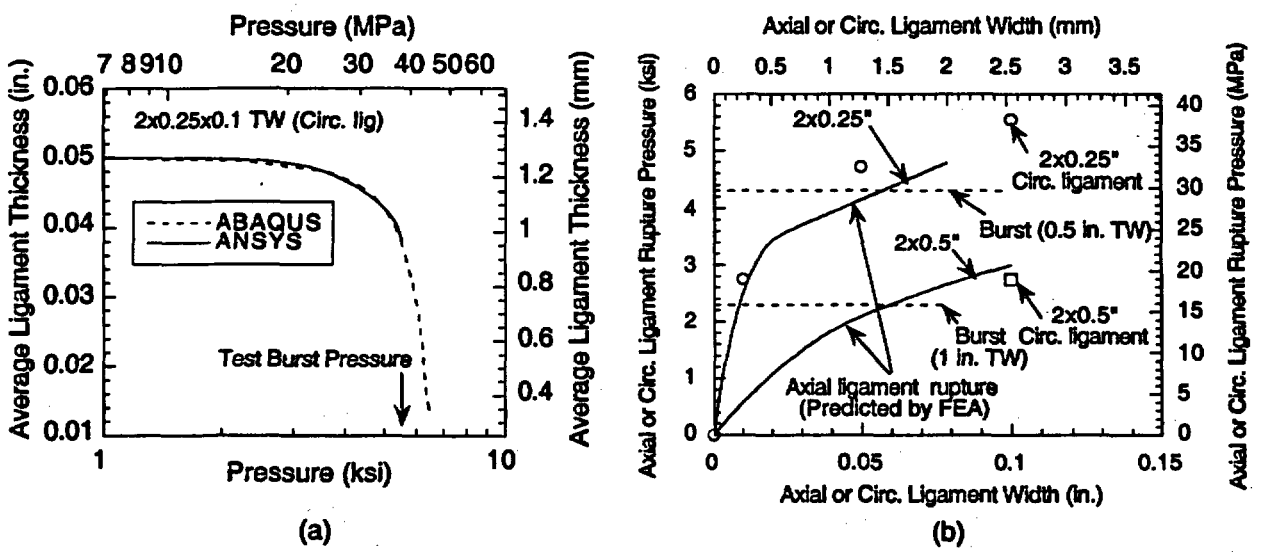

Figure 4.76. Variation of average ligament thickness with pressure for two 6-mm (0.25-in.)-long, 100% throughwall notches separated by 1.3-mm (0.05-in.)-wide ligament and variation of ligament rupture pressure with ligament width for two 13-mm (0.5-)-long and two 6-mm (0.25)-long, 100% throughwall notches.

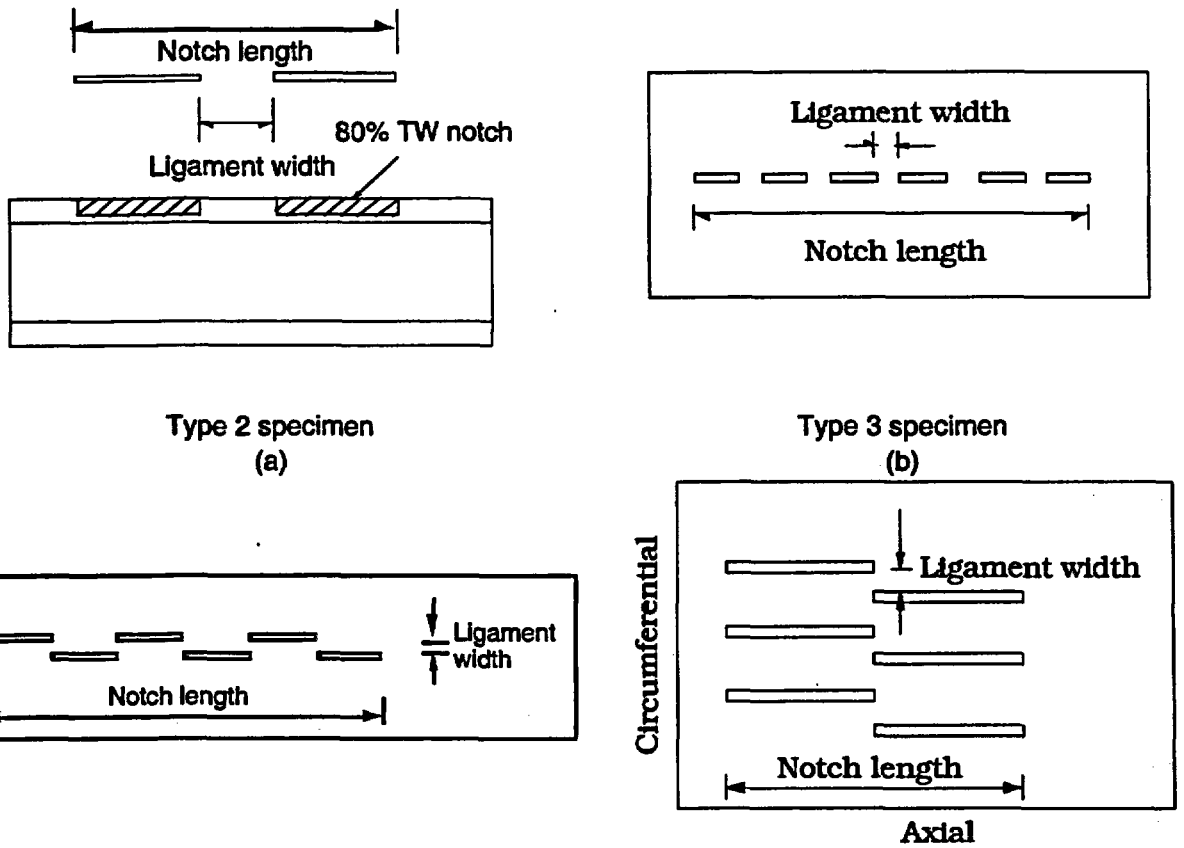

Figure 4.77. Geometries for multiple axial notch specimens.

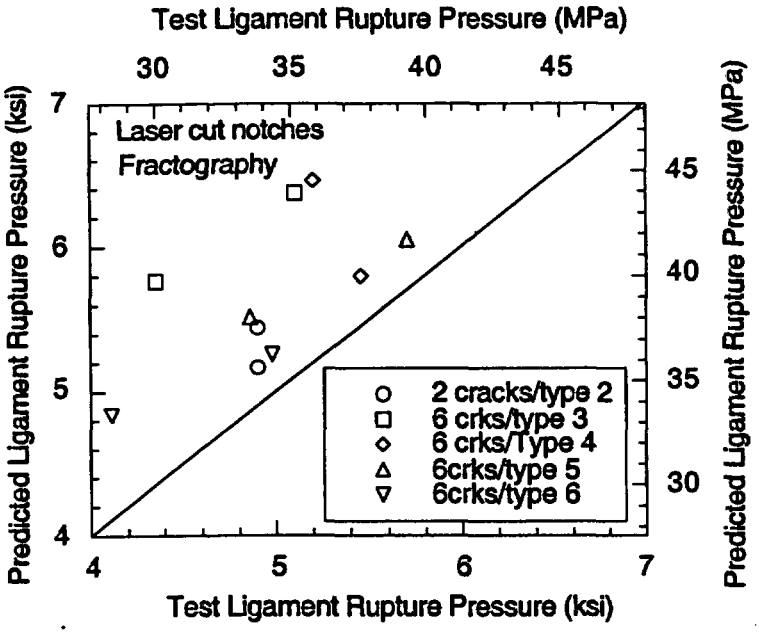

Figure 4.78.
Observed vs. predicted ligament rupture pressures for multiple laser-cut notches.

$$Q = 180.2A\sqrt{\frac{\Delta p}{\rho}}, \tag{4.16c}$$

The density of water is 997.5 kg/m^3 (62.27 lb/ft^3) at room temperature and 735.3 kg/m^3 (45.9 lb/ft^3) at 282°C.

4.5.3.1 Crack Opening Area

Axial cracks

Zahoor's model [37] for crack opening area A of an axial throughwall crack in a thin-walled tube is

$$A = 2\pi c_e^2 V_o \sigma / E, \tag{4.17a}$$

where

σ = hoop stress,

E is the Young's modulus,

$$V_o = 1 + 0.64935\lambda_e^2 - 8.9683\times10^{-3}\lambda_e^4 + 1.33873\times10^{-4}\lambda_e^6, \tag{4.17b}$$

$$\lambda_e^2 = c_e^2 / Rh,$$

R and h are the mean radius and thickness of tube, (4.17c)

$$c_e = c\left[1 + \frac{F}{2}\left(\frac{\sigma}{\sigma_y}\right)^2\right], \tag{4.17d}$$

$$F = 1 + 1.2987\lambda^2 - 2.6905\times10^{-2}\lambda^4 + 5.3549\times10^{-4}\lambda^6, \tag{4.17e}$$

$$\lambda^2 = c^2 / Rh, \tag{4.17f}$$

and σ_y is the yield strength, and c is the crack half-length.

The flaw opening area for an EDM notch was obtained by adding the initial flaw area (equal to flaw length multiplied by flaw width) to the crack opening area given by Eq. 4.17a. Crack opening areas calculated by Eq. 4.17a were found to agree well with FEA results [4]. The predicted leak rates are also in good agreement with experimentally measured leak rates at room temperature for the as-received tube (Fig. 4.79a) and heat-treated (flow stress reduced by 20%) tube (Fig. 4.79b). Continuously measured leak rates in 100% TW and 90% TW EDM notches are compared with predicted leak rates in Figs. 4.80a and 80b, respectively, at room temperature. Note that both the ligament rupture pressure and subsequent leak rates are predicted well for the 90% part-throughwall notch (Fig. 4.80b).

The results for a leak rate test at 282°C on an as-received tube with a 12.5-mm (0.5-in.)-long throughwall EDM notch are given in Fig. 4.81. Again the calculated leak rate is reasonably close to the measured value. Thus, the standard smooth-edge-orifice leak rate equation (Eqs. 4.16a-c) appears to predict the leak rates through EDM notches at room temperature and 282°C very well. The difference in leak rate between room temperature and 282°C can be accounted for simply by the difference in the density of water.

Circumferential cracks

The opening areas of circumferential cracks can be calculated from the Paris/Tada model [38]:

$$A = \frac{\pi\Delta p R^2}{E} B, \tag{4.18a}$$

where

$$B = \begin{cases} \lambda_e^2 + 0.16\lambda_e^4 \text{ for } 0 \le \lambda_e \le 1 \\ 0.02 + 0.81\lambda_e^2 + 0.30\lambda_e^3 + 0.03\lambda_e^4 \text{ for } 1 \le \lambda_e \le 5 \end{cases} \tag{4.18b}$$

$$\lambda_e = \theta_e\left(\frac{R}{h}\right)^{0.5} \tag{4.18c}$$

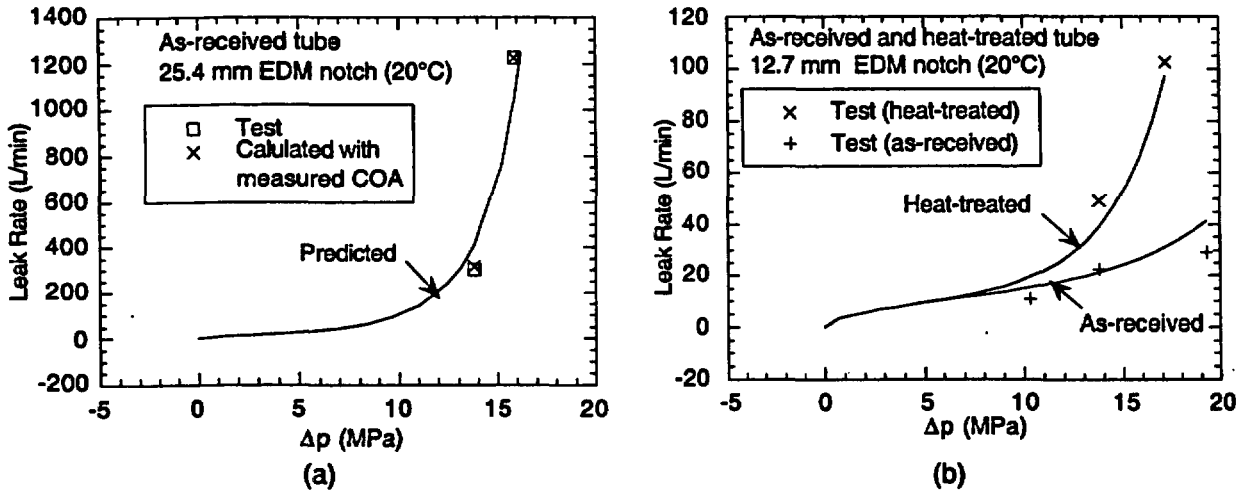

Figure 4.79. Calculated (solid line) and experimentally measured (symbols) leak rates at 20°C (68°F) for as-received and heat-treated 22-mm (0.875-in.)-diameter tubes with (a) 25.4 mm (1 in.) and (b) 12.7-mm (0.5-in.) throughwall axial EDM notches. Cross symbols (x) in Fig. 4.79a denote calculated leak rates using posttest measured crack opening areas.

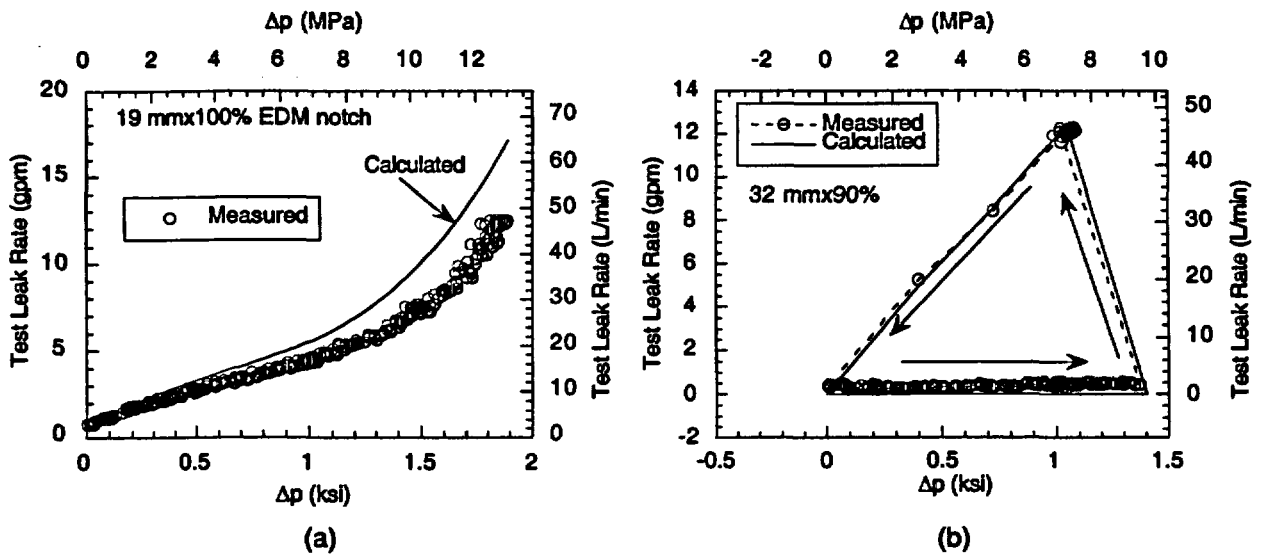

Figure 4.80. Calculated and measured pressure vs. leak rate plots for tests (a) OM169 (100% TW) and (b) OM171 (90% TW), both conducted on as-received tubes at 20°C.

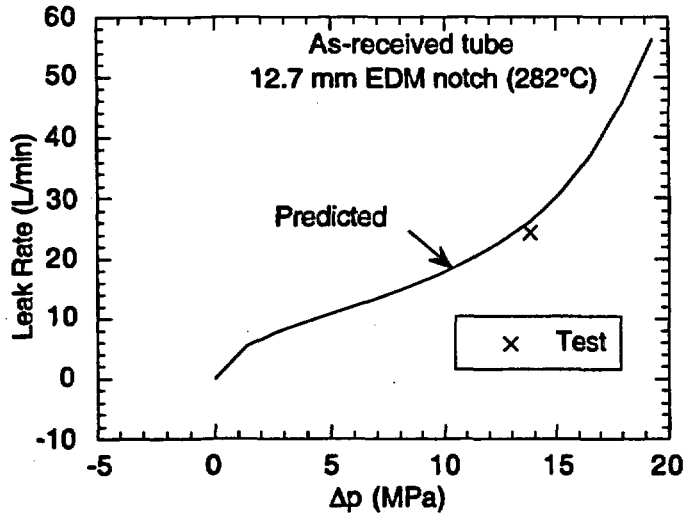

Figure 4.81.
Calculated (solid line) vs. experimentally measured (symbol) leak rates in as-received 22-mm (0.875-in.)-diameter tubes with a 12.7 mm (0.5 in.) flaw at 282°C (540°F).

$$\theta_e = \theta\left[1 + F_m^2 p^2 R^2 / \left(8h^2\sigma_y^2\right)\right] \tag{4.18d}$$

$$F_m = \begin{cases} 1 + 0.1501\lambda^{1.5} \text{ for } \lambda \le 2 \\ 0.8875 + 0.2625\lambda \text{ for } 2 \le \lambda \le 5 \end{cases} \tag{4.18e}$$

$$\lambda = \theta\left(\frac{R}{h}\right)^{0.5}. \tag{4.18f}$$

The Paris/Tada model [38] is restricted to small-scale yielding ($\lambda \le 5$) and does not account for the bending effects that become important at pressures that induce large-scale plasticity in the crack plane. As a result, the COA calculated by this model is independent of the span of the tube or support conditions.

4.5.4 Pressure and Leak Rate Tests on Specimens with Stress Corrosion Cracks

Pressure and leak-rate tests have been conducted on specimens with laboratory-generated SCCs and on tubes pulled from a retired McGuire SG. Crack depth profiles for all the specimens were estimated by pretest multiparameter NDE and, in some cases, were verified by posttest fractography. Equivalent rectangular crack lengths and depths were developed from both the NDE profiles and those determined by fractography and used to predict the ligament rupture pressure and leak rate. Because the remaining ligaments of part-TW SCCs rarely rupture along the full length of the crack during the initial ligament rupture event, specimens generally undergo incremental ligament rupture with increasing pressure before the cracks become unstable. We have tentatively generalized the equivalent crack approach to predict incremental ligament rupture after the initial ligament rupture event [39].

Laboratory-Generated Stress Corrosion Cracks

Two types of heat treatments were used for generating the stress corrosion cracks in the SG tubes. Early in the program, specimens were subjected to high-temperature annealing prior to introduction of the stress corrosion crack in the laboratory. This annealing treatment resulted in a loss of about 20% in flow stress. Later on, SCC specimens were not subjected to the high-temperature annealing treatment. As a result, the flow stresses of these specimens were virtually undiminished from those of the as-received tubes.

Crack depth profiles measured by pretest EC/NDE and posttest fractography for a specimen (SGL-480) with high-temperature annealing are shown in Fig. 4.82a. The predicted and measured leak rates at room temperature as a function of pressure for this specimen are shown in Fig. 4.82b. Crack depth profiles and leak rate vs. pressure plots for Specimen SGL-493, which also was exposed to high-temperature annealing and tested at room temperature, are shown in Figs. 4.83a and 4.83b, respectively. The predictions of leak rate based on fractography tend to be more accurate than those based on EC/NDE. The onset of leakage often occurs at a lower pressure than predicted.

Crack depth profiles and leak rate vs. pressure plots for Specimen SGL-731, which was not subjected to high-temperature annealing but was tested at room temperature, are shown in Figs. 4.84a and 4.84b, respectively. The corresponding plots for Specimen SGL-822 are shown in Figs. 4.85a and 4.85b. The predictions for SGL-822 are less satisfactory than the other cases. Although fractography indicated this crack to be very deep with several 100% TW segments, the crack behaved in a much stronger fashion than predicted.

4.5.5 High-Temperature Failure Models (Severe Accident Conditions)

Two types of failure models were used for predicting ligament rupture pressures of tubes with part-throughwall flaws under severe accident conditions, i.e., the flow stress model and the creep rupture model [25].

4.5.5.1 Flow Stress Model

In the flow stress model, it is assumed that, for any arbitrary history of stress $\sigma(t)$ and temperature $T(t)$, failure occurs at a temperature T and stress σ whenever the following failure equation is satisfied, independent of stress-temperature history:

$$\sigma = \frac{\overline{\sigma(T)}}{m_p}, \tag{4.19}$$

where $\overline{\sigma(T)}$ is the flow stress at temperature T, and m_p is a stress magnification factor that accounts for the crack.

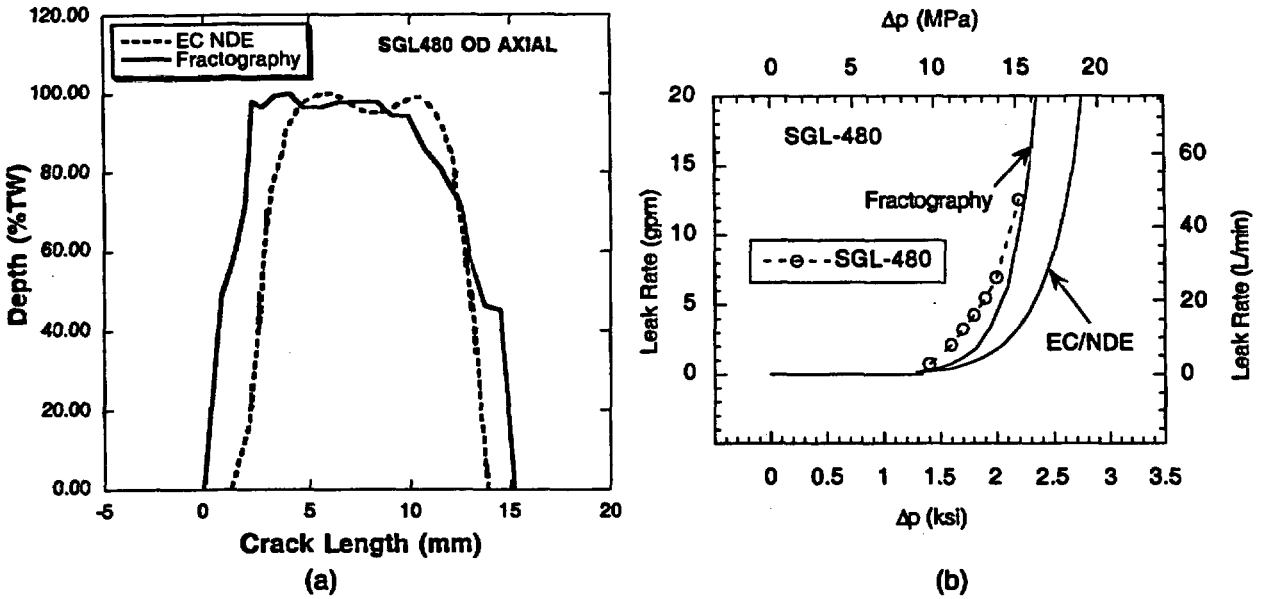

Figure 4.82. (a) Crack depth profiles (measured by pretest EC and posttest fractography), and (b) measured (symbols) and predicted (based on NDE and fractography depth) pressure vs. leak rate plots for Specimen SGL-480.

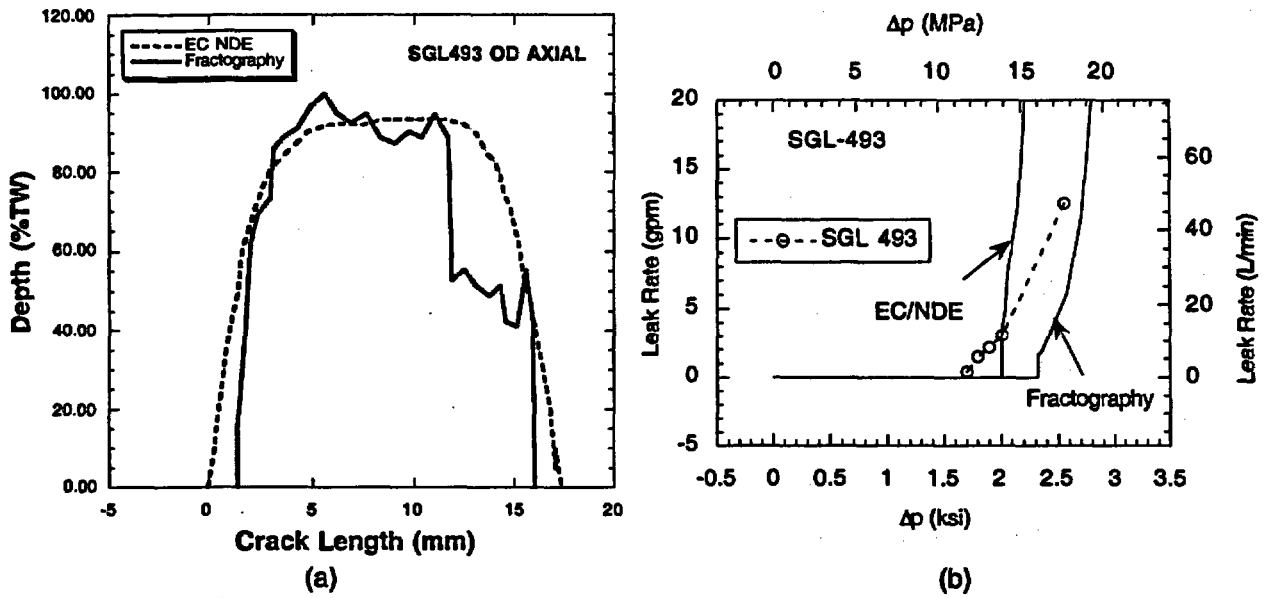

Figure 4.83. (a) Crack depth profiles (measured by pre-test EC and post-test fractography), and (b) measured and predicted (based on NDE and fractography depth) pressure vs. leak rate plots for specimen SGL-493.

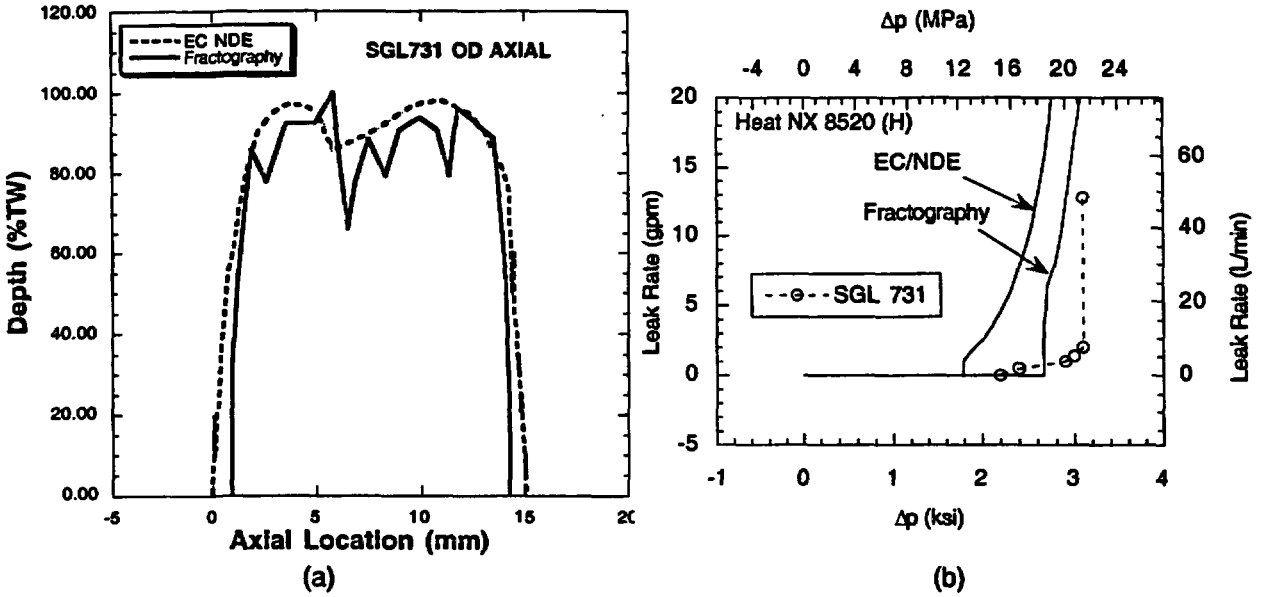

Figure 4.84. (a) Crack depth profiles (by EC/NDE and fractography) and (b) predicted and measured pressure vs. leak rate plots of Specimen SGL-731.

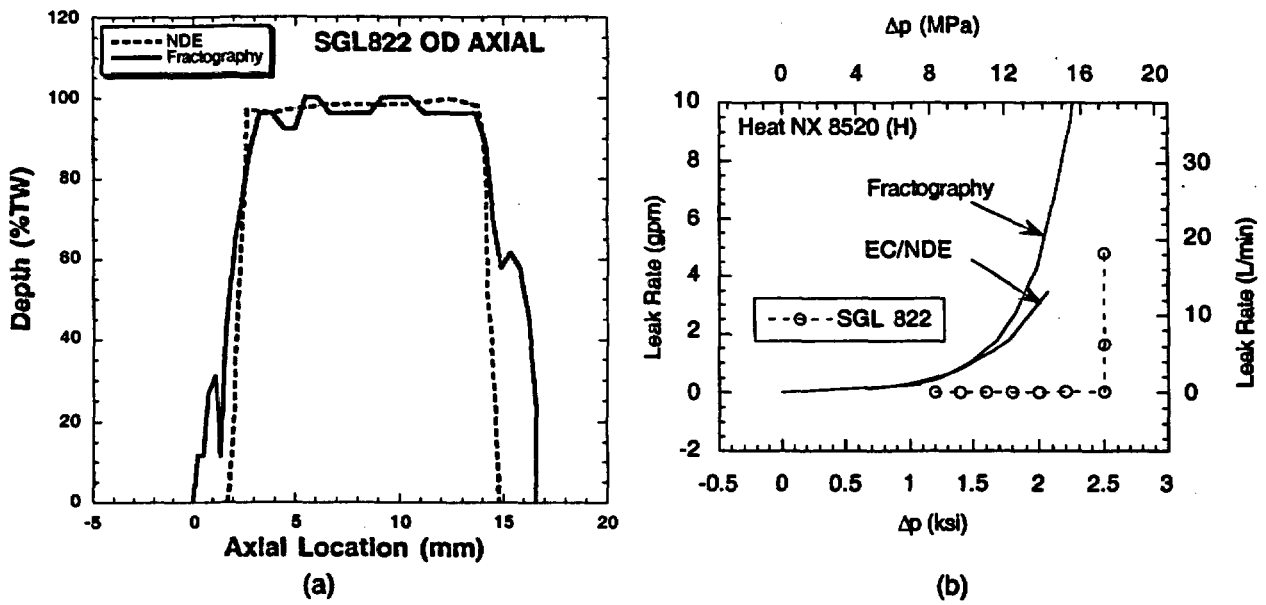

Figure 4.85. (a) Crack depth profiles (by EC/NDE and fractography) and (b) predicted and measured pressure vs. leak rate plots for Specimen SGL-822.

4.5.5.2 Creep Rupture Model

A rigorous creep rupture analysis of flawed tubes is very complex. Therefore, the approximate linear time fraction damage model (used in Section III of ASME Code) was extended to flawed tubing:

$$\int_0^{t_f} \frac{dt}{t_R(T, m_p\sigma)} = 1 \qquad (4.20)$$

Unlike the flow stress model, the predicted failure pressures by the creep rupture model are dependent on the time-temperature-stress history. The creep rupture model was validated by failure tests on specimens with part-through axial flaws of various lengths and depths conducted under constant and ramped internal pressure and temperature histories [25]. In all cases, predictions of the creep rupture model were closer to experimental results than those of the flow stress model.

4.5.5.3 Severe-Accident Test Conditions

The severe accident sequences that appear to produce the greatest risk of steam generator tube failure are those in which the reactor pressure vessel fails to depressurize, but depressurization does occur on the secondary side. Even in these cases, preliminary investigations suggest that failures are likely to occur in the hot-leg nozzle or the inlet surge-line nozzle, leading to depressurization of the reactor system, which prevents failure of steam generator tubes [40, 41]. However, such calculations are subject to large uncertainties, and the NRC is pursuing additional studies to better understand the progression of such sequences, the temperature of the steam generator tubes during such accidents, and the behavior of steam generator tubes (both unrepaired and repaired) at the high temperatures associated with such accidents. At these high temperatures, plastic deformation is likely to be much more extensive than at normal reactor operating temperatures, and creep effects may no longer be negligible.

4.5.5.4 Unrepaired Tubes

The behavior of flawed steam generator tubing during severe accidents has recently been considered in an INEEL [40] and an EPRI [41] report. The severe-accident scenario under investigation involves a total station blackout with a SG secondary-side atmospheric dump valve that has stuck open, resulting in loss of feedwater and secondary-side depressurization. The pressure difference across the SG tube wall remains relatively constant at 16.2 MPa (2.35 ksi). Estimates of the maximum tube temperatures presented in these reports are shown in Figs. 4.86 and 4.87. In these reports, the failure of unflawed tubing and other components such as the surge line nozzle is described in terms of creep damage failure. In contrast, both analyses assume that failure of flawed steam generator tubing in severe accidents can be described in terms of a flow stress model, Eq. 4.19, by taking the flow stress to be a function of temperature. With this assumption, the failure pressure of a flawed tube depends only on the flaw geometry and temperature and is independent of the loading rate or the detailed time/temperature history.

Although the flow stress model is a straightforward extension of a model that has been well verified at normal operating temperatures, the use of such a model at high temperatures

poses conceptual difficulties. Although Alloy 600 shows little strain hardening at high temperatures, its flow stress is a function of not only temperature but also strain rate. Intuitively, failure pressure or temperature would be expected to be truly rate-independent if the pressure or temperature ramps were sufficiently rapid so that time is insufficient for creep to influence the deformation or damage of the ligament and the crack tip ligament fails by plastic instability because the ligament stress exceeds the maximum load-carrying capability of the material. At the other extreme, if the pressure or temperature ramps were sufficiently slow (in the limit, a constant-pressure or constant-temperature hold), failure should be controlled by creep processes, and a failure model based on creep rupture would be more appropriate.

To determine which of the two models is more accurate for severe-accident transients, tests were conducted at ANL on constant pressurized tubes (16.2 MPa or 2.35 ksi) subjected to both the INEEL- and EPRI-calculated temperature ramps. The actual ramps for the tests are indicated by the dashed lines in Figs. 4.86 and 4.87. The EPRI-calculated temperature history indicates a dropoff in temperature after ≈223 min, corresponding to a predicted rupture of the SG hot leg nozzle. Because the ANL tests were concerned only with the validation of a failure model, this event was ignored, and the tests were ramped to failure at a rate of 2°C/min (3.6°F/min) after a 2-h hold time at 667°C (1233°F). As shown in Figs. 4.88 and 4.89, the creep rupture model is more accurate than the flow stress model for the temperature ramps considered.

4.5.5.5 Electrosleeved Tubes

Behavior of Electrosleeved tubes during a severe accident is of interest to NRC, because it has the potential of being used as a repair technique for steam generator tubes. Although the nanocrystalline Electrosleeve has superior mechanical properties compared to Alloy 600 at reactor operating temperatures (Fig. 4.90), it loses strength at high temperatures because of grain growth. This behavior raises concern as to its integrity during severe accidents.

Two approaches were developed for predicting failure of Electrosleeved tubes [42]. The first is an approximate analytical procedure based on a linear-damage-rule hypothesis analogous to that often used to analyze creep failures. The second is a more mechanistically based approach that accounts for the loss of flow stress due to grain growth. Initial studies showed that the failure temperatures predicted by the two approaches were comparable, but the mechanistic model was used for most of the analyses. The reference geometry selected for tests and analyses is shown in Fig. 4.91.

After the initial development of the analytical model, Framatome Technologies, Inc. (FTI) provided failure data from six tests on internally pressurized tubes that were subjected to a variety of temperature ramps simulating those expected during the most challenging severe accidents, i.e., "high–dry" sequences that can occur when the core melts, the primary side remains at high pressure, and the secondary side is depressurized. The initial comparison showed that the predicted failure temperatures were within 35–70°C (63-126°F) of those observed in the experiments. FTI also provided 11 Electrosleeved specimens containing 100% TW notches in the parent tubes that were subsequently tested at ANL using the severe accident transient designated as case 6RU in NUREG-1570 (Fig. 4.92) [43]. The results from these tests were used to refine the input parameters in the analytical model. Based on the refined model and more accurate data on the test geometries, the predicted failure

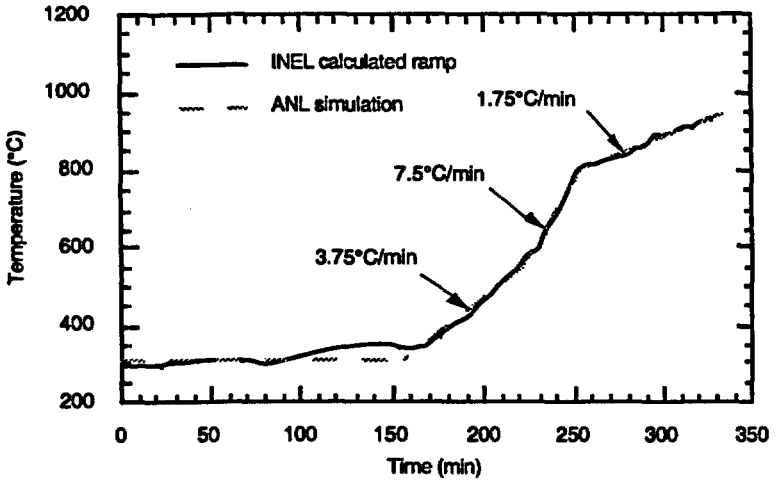

Figure 4.86.
INEEL-calculated severe-accident temperature ramp and simulated ramp used in ANL severe-accident tube-rupture tests.

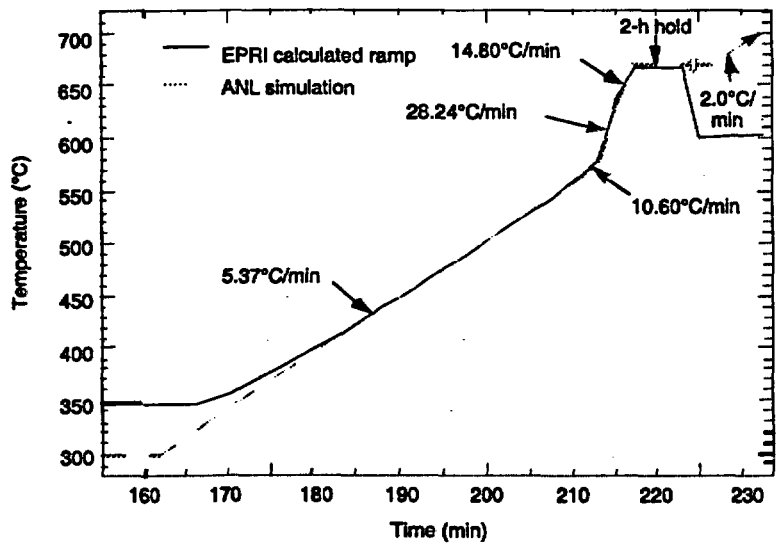

Figure 4.87,
EPRI-calculated severe-accident temperature ramp and simulation used in ANL severe-accident tube-rupture tests. In the ANL simulation, the temperature is held constant at 670°C (1240°F) after ≈217 min rather than following the subsequent drop shown in the calculated curve.

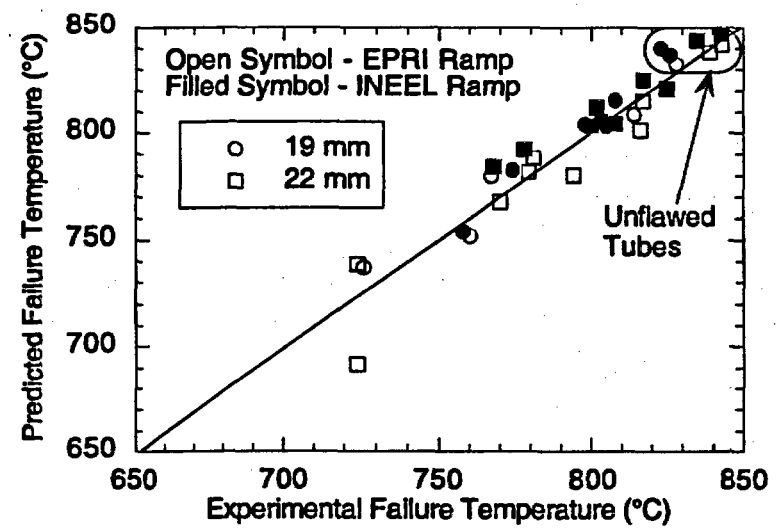

Figure 4.88.
Creep-rupture-model predicted vs. observed failure temperatures for high-temperature failure tests conducted with the INEEL and EPRI temperature ramps.

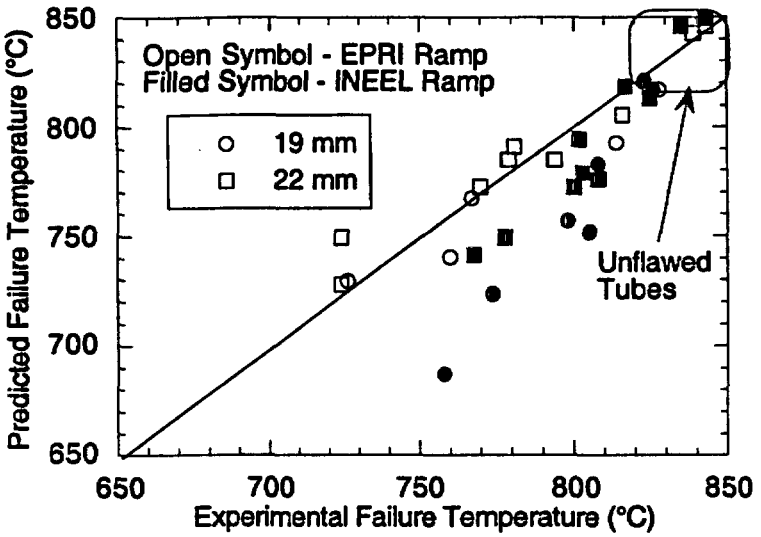

Figure 4.89.
Flow-stress-model predicted vs. observed failure temperatures for high-temperature failure tests conducted with the INEEL and EPRI temperature ramps.

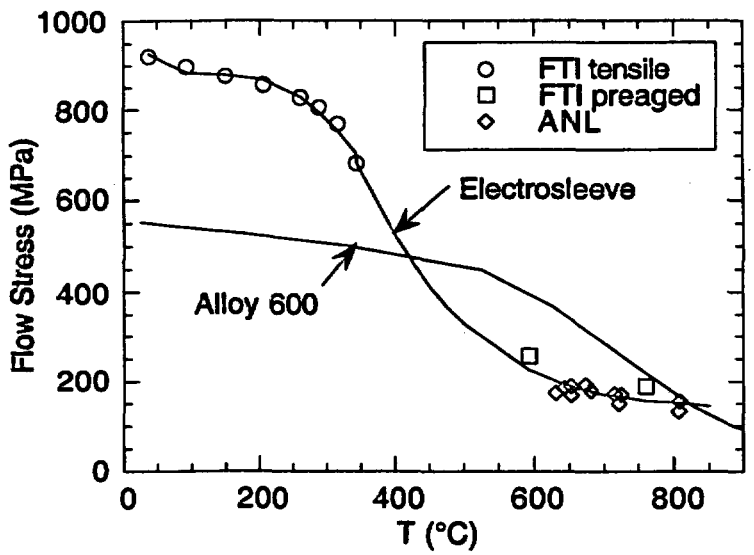

Figure 4.90.
Flow stresses of Alloy 600 and Electrosleeve material as a function of temperature.

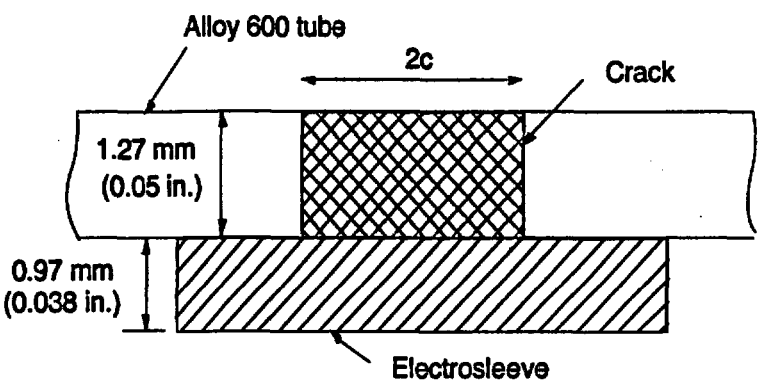

Figure 4.91.
Reference geometry for Electrosleeved steam-generator tube with axial crack.

temperatures in the FTI and ANL tests are within 15°C (27°F) of the observed failure temperatures (Fig. 4.93). [42]. The test results indicate a leveling-off of failure temperature with crack length beyond 51-76 mm (2-3 in.), which is consistent with finite element analysis. Tests were also conducted on Electrosleeved tubes with part-throughwall notches in the parent tubes. An FEA-based model was used to predict failure temperatures of Electrosleeved tubes with part-throughwall cracks in the parent tubes. The results showed that, depending on the crack length, the failure temperatures of 80% deep cracks can be 40-80°C (72-144°F) higher than those of 100% TW cracks. [42].

The model predicts that Electrosleeve repairs on tubes with throughwall axial cracks ≤25 mm (1 in.) and throughwall 360° circumferential cracks will survive all "high-dry" sequences, including the Case 6RU transient based on the temperature histories for such sequences presented in NUREG–1570. Tubes with throughwall axial cracks of any length but with depths ≤80% are also predicted to survive these transients.

4.5.6 High-Temperature Leak Rate and Jet Impingement Erosion

NUREG–1570 presented the results of a study by the NRC to assess the risk implications of steam generator tube ruptures (SGTRs) induced by severe-accident conditions. One of the phenomena considered in NUREG–1570 was the potential for the propagation of tube failures during design basis and severe accidents. In the event of a tube failure, escaping jet of superheated steam could entrain particles from the core debris and impinge on a neighboring tube. The particle-laden jet could then erode through the neighboring tube, leading to another escaping jet and the possibility of a cascading failure event in the steam generator. Some analyses based on high-temperature fossil–plant experience were performed in NUREG–1570 to estimate the time required for a jet from a failed tube to induce failure in an adjacent tube. These analyses were, at best, scoping estimates. Additional analyses and tests were performed to obtain more accurate estimates of the potential for failure propagation by jet impingement. Details may be obtained from Ref. 44.

4.5.6.1 Computational Fluid Dynamics Calculations of High Temperature Jets

Detailed computational fluid dynamics (CFD) calculations were performed at the University of Maryland to obtain a better understanding of the jet velocities and potential for particle entrainment that could be associated with leaks in SG tubes under severe accident conditions.* Calculations were done primarily for a square array of tubes. The distance to the adjacent tube was taken as 8.23 mm (0.32 in.), which corresponds to an L/h value for the jet of ≈16. Comparison with the results shows that this value is less than the predicted L/h ratio for cracks <6.35 mm (0.25 in.) in length for temperatures up to 750°C. The fluid properties were taken as those of air, and ideal gas behavior was assumed. The use of air rather than steam will lead to an underprediction of velocities by about 25%. The baseline calculations were performed for stagnation pressures of 8 and 16 MPa (1160 and 2320 psi), a stagnation temperature of 1175 K (902°C), and a slit opening of 0.5 mm (0.02 in.). Because the pressure in the tube is much higher than on the secondary side of the steam generator, the jet expands rapidly and becomes supersonic. However, as the flow approaches the adjacent tube, it must

* "Steam Generator Jet Impingement Calculations," Memorandum to Nilesh C. Chokshi, USNRC/RES from John H. Flack USNRC/RES, December 26, 2000.

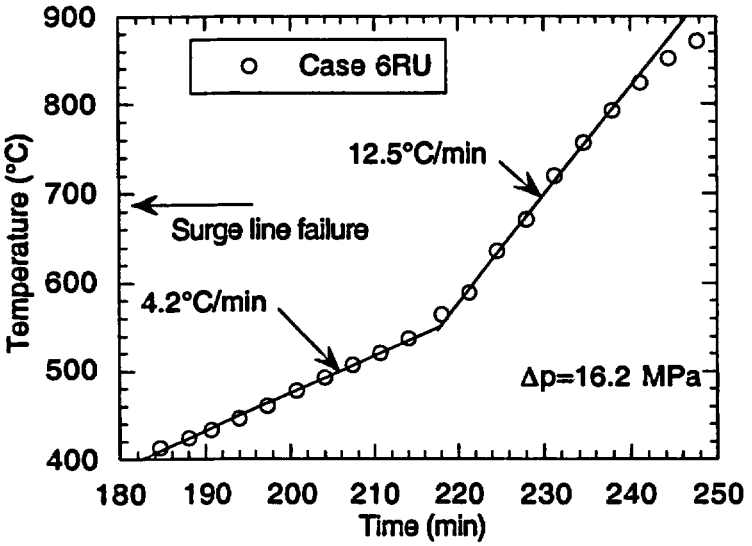

Figure 4.92.
Time-temperature history used for testing Electrosleeved tubes with notches in the parent tubes at ANL.

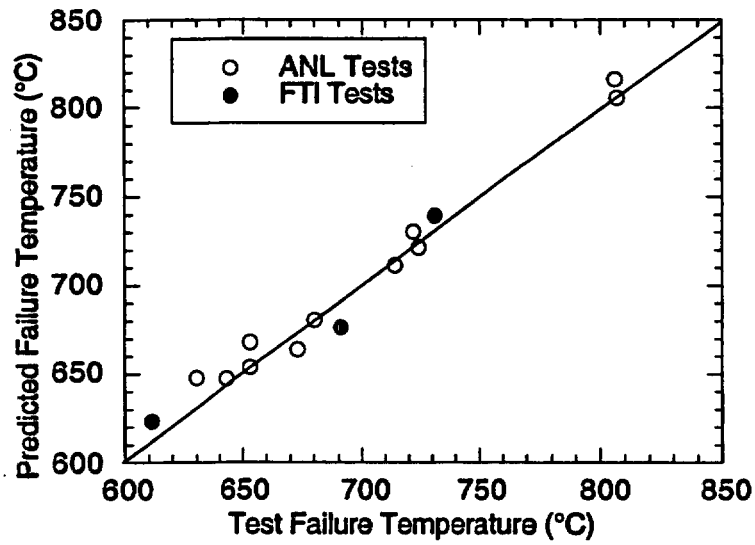

Figure 4.93.
Observed vs. predicted failure temperatures of ANL and FTI tests using actual notch and Electrosleeve geometry and, for the FTI tests, actual test temperature ramp.

decelerate, and a detached shock wave forms in front of the impacted tube. The position and strength of the detached shock wave depends on the stagnation pressure associated with the jet flow. The CFD results showed that just in front of the shock the jet has expanded from ±0.25 mm in width to ≈ ±2.5 mm. The maximum fluid velocity along the centerline is 1400 m/s (4600 ft/s). The velocity across the shock is 300 m/s (985 ft/s), and the fluid velocity decreases rapidly as the jet approaches the impacted tube. For the aerosol particles of interest, which have masses $<10^{-12}$ kg, the particle motions are expected to track the fluid motions very closely, as seen from the CFD results in Fig. 4.94.

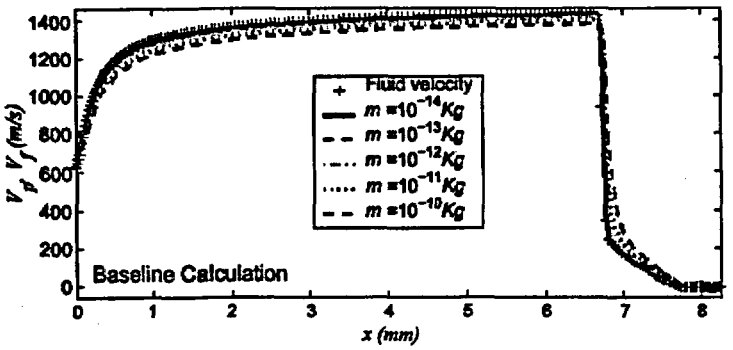

Figure 4.94.
Comparison of velocity of small particles entrained in flow with fluid velocity. Small particles with low mass follow fluid flow very closely.

4.5.6.2 Crack Opening Area

To determine the erosion rate due to jet impingement during severe accidents, the crack-opening area as a function of time must be estimated [44]. A simple model was developed to calculate the crack-opening area as a function of time and temperature during severe accidents. It is derived by analogy to elastic–plastic solutions for a power law hardening material [45] and is applicable to materials that obey a power-law creep rate, i.e.,

$$\dot{\varepsilon} = A\sigma^n, \tag{4.21}$$

where $\dot{\varepsilon}$ is the creep rate, σ is the applied stress, and A and n are constants. The crack opening displacement solution for the elastic–plastic model gives a crack opening rate of:

$$\dot{\delta} = Ach_2(0,n)(m\sigma)^n, \tag{4.22}$$

where h_2 is a function tabulated in Ref. 45, c is the crack half-length, σ is hoop stress due to pressure, and m is the bulging factor (Eq. 4.7b). The model was validated with a number of high-temperature tests on tubes with two symmetrical circumferential notches under axial tensile loading. [44]. An example is shown in Fig. 4.95a. The predicted crack opening area as a function of axial crack length for a tube subjected to the severe-accident transient Case 6RU at final temperatures of 700 and 750°C (1292 and 1382°F) is shown in Fig. 4.95b.

4.5.6.3 Erosion Rate Due to Jet Impingement

During severe accidents, typical conditions involve a maximum temperature of 700-900°C (1292-1652°F), a maximum pressure gradient across the tube wall of 16.2 MPa (2350 psi), and an escaping jet consisting of superheated steam plus 10-20% H_2. The particulates in the gas jet arise from the volatilization of low-melting-temperature core materials. The volatiles agglomerate at the relatively low temperatures found in the reactor coolant piping system. Results from earlier severe accident analyses showed that the particles in the jet were primarily

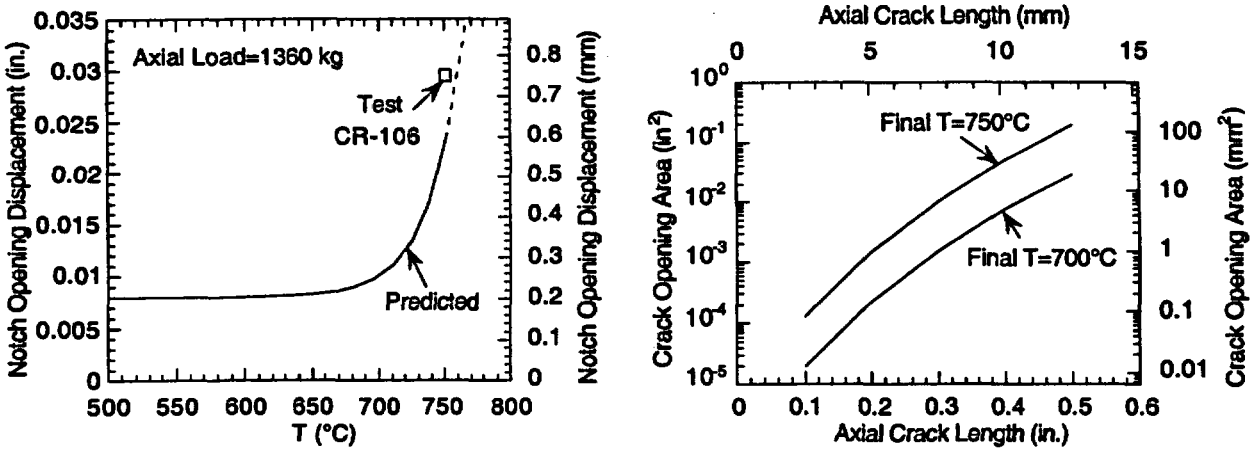

Figure 4.95. Predicted and experimentally measured (symbol) notch opening displacement for two 6.4-mm (0.253-in.) circumferential notches loaded axially and subjected to the Case 6RU (Fig. 4.92) temperature transient and predicted crack-opening area with crack length at final temperatures 700 and 750°C (1292 and 1382°F) for a tube subjected to Case 6RU transient.

Ag (≈100 g/m^3), with significantly lesser amounts of In_2O_3, $CsMoO_4$, SnO_2, CsI, and other species (these results are typical of Westinghouse PWRs).* The median particle diameter is ≈ 1.5 μm, with the bulk of particles having diameters < 3 μm.

A test program was initiated at the University of Cincinnati to determine erosion rates of Alloy 600 at high temperatures by particles with sizes and characteristics, including hardness and density, similar to those expected in a reactor accident. Ni and NiO particles were chosen initially as surrogate particles for the tests. Because the surrogate particles are somewhat larger and a higher hardness at temperature than the real particles, they should give realistic to somewhat conservative estimates of erosion rates. Initial tests showed that erosion was most severe at an angle of 30°, in agreement with previous literature data on the erosion of Alloy 600 (and other metals), and this angle was used in all of the subsequent tests.

Tests were conducted at 700°C (1292°F) and a 30° impact angle using 3-7 μm Ni erodent at velocities of 91-549 m/s (300-1800 ft/s). Four test series (A, B, C, and D) were conducted at different times to determine the reproducibility of the data. The results from test series A and B indicate that the erosion rate increases markedly with increasing particle velocity, and that for a given velocity, the rate is independent of total particle loading (fluence). While test series A and B yield consistent results, the data from the subsequent test series C indicate no erosion at 91 and 183 m/s (300 and 600 ft/s) and a substantially lower erosion rate at 549 m/s (1800 ft/s). The reason for these discrepancies is not clear. Overall, however, the erosion rates are relatively low in all cases. To determine the rate of thinning of the target, it is convenient to convert the rate of mass loss into a rate of volume loss by dividing by the density of the target

* D. R. Diercks, "Minutes of Expert's Meeting on Jet Impingement and Leak Rates from Steam Generator Tubes During Severe Accidents," held at Argonne National Laboratory (ANL), Nov. 19, 1999; minutes published Dec. 6, 1999.

material, which in this case is Alloy 600, and to note that the erosion rate (based on the results from test series A and B) can be expressed in terms of a power-law dependence on velocity:

$$E = 8.0 \times 10^{-12} V^{2.43}, \tag{4.23}$$

where the erosion rate E is in cm^3/g and denotes the rate of loss of material per gram of impinging particles, and V is the velocity of the impinging particles in m/s.

To determine the thinning rate of tubes, erosion data must be coupled with the results of the CFD analyses of the jet behavior discussed above:

$$\frac{dh}{dt} = E \bullet \Phi, \tag{4.24}$$

where dh/dt is the wall thinning rate in cm/s, E is the erosion rate in cm^3/s, and Φ is the mass flux of particles in $g/cm^2/s$. If we make the conservative assumptions that the impact velocity is ≈200 m/s, and the erodent particles are 3-7 μm diameter Ni particles, then the power-law estimate of the erosion rate of Alloy 600 given by Eq. 4.23, together with the estimate of the mass flux (0.52 $g/cm^2/s$), suggests that the maximum wall thinning rate will be less than ($8.0 \times 10^{-12} \times 200^{2.43} \times 0.52 \times 36000$) = 0.06 mm/h (2 mil/h). Because of conservatism in the analyses, the bounding rate of 0.06 mm/h (2 mil/h) should be applied only for that portion of the history for which the temperature is >700°C. Thus, even after a crack has opened by creep at high temperatures, failure of an adjacent tube would take >10 h. Thus, jet impingement is very unlikely to play any significant role in the failures.

5 Integrated Model for Steam Generator Integrity Assessments

The Nuclear Regulatory Commission (NRC) is developing a "performance-based" regulatory framework to assure steam generator tube integrity. Instead of just meeting prescribed rules on allowable flaw sizes for tubes that have been inspected, evaluations and assessments are necessary to show that adequate levels of integrity can be maintained until the next scheduled outage. This will require the use of a comprehensive validated model that integrates all important aspects of integrity evaluations, starting from in-service inspection results and ending with a total leak rate at the end of an operating cycle under various assumed conditions. Furthermore, the probabilities of single and multiple tube ruptures under various reactor coolant conditions must be quantified. The nuclear industry has developed codes and procedures to carry out these assessments. ANL/CANTIA is intended to provide a tool that could be used for an independent assessment of steam generator integrity.

Under contract from the Atomic Energy Control Board of Canada [AECB, now the Canadian Nuclear Safety Commission], Dominion Engineering, Inc. [46] developed a Monte Carlo-based code called CANTIA (CANDU Tube Inspection Assessment) to simulate the effects of tube inspection and maintenance strategies on the safe operation of CANDU design nuclear steam generators. The integrity and leak rate models in CANTIA were specifically intended for the CANDU steam generators in Canada. A decision was made to incorporate into CANTIA the integrity and leak rate models that have been developed at ANL under the Integrated Steam Generator Tube Integrity Program (ISGTIP-2) sponsored by the NRC. The original CANTIA was written in Visual Basic 3.0, and a copy of the program, together with the user's manual, were obtained by ANL from the AECB. The program was updated to Visual BASIC 6.0 to run in a Windows NT environment and was then modified to incorporate the integrity and leak rate models developed at ANL. The basic Monte Carlo simulation portion of the code, together with much of the input format, was retained unchanged in the modified CANTIA code, renamed ANL/CANTIA. For a detailed description of ANL/CANTIA, see Ref. 47.

5.1 Description of Original CANTIA

The CANTIA code uses Monte Carlo techniques to determine probabilities of steam generator tube failures under accident conditions and primary-to-secondary leak rates under normal and accident conditions in the future. An initial flaw size distribution is input, and the program determines future flaw size distributions. The effect of inspections of the steam generator tubes at future points in time, and subsequent removal of defective tubes from the population, on the probabilities of failure and leak rates and the future flaw size distributions is calculated. Thus, the effect of different inspection and maintenance strategies on the probability of tube failure and primary-to-secondary leak rate can be determined.

CANTIA is designed to handle various defect types (including circumferential and axial SCCs, frets, and pits), though only one type of degradation can be modeled at a time. All tubes modeled in a trial are treated as being equally susceptible to the chosen degradation mode, so that the same distributions of growth rates, flaw initiation, etc., are used for all the tubes in the trial. If different distributions are believed to describe the degradation in different parts of the steam generator, then separate simulations should be run with the appropriate distributions for the portion of generator being modeled.

The CANTIA failure model is of the probabilistic fracture mechanics type. It calculates the time-dependent flaw size and number distribution so that the probability of failure or the rate of leakage can be estimated. It uses a Monte Carlo approach; each important parameter is treated as a random variable with known or predictable median behavior and a known or predictable distribution of behavior (i.e., variation) around the median. Both the median and variance of each random variable are specified by the user, or, if desired, a fixed (deterministic) value can be used. For each Monte Carlo trial, the value of each variable is chosen randomly in accordance with the selected distribution function, or the fixed value is used, so that the trials reflect the variability of the actual situation. A large enough number of trials (chosen by the user) are then run for each analysis to provide a stable statistical distribution of the results.

For each Monte Carlo trial, CANTIA determines flaw sizes, growth rates, inspection results, material properties, etc. for each tube, and tracks the progression of the flaws in each tube throughout the model time period. After all trials are run, the conditions from each trial at each time of interest are compiled to determine the distributions of flaw sizes, inspection results, leak rates, and tube failures at the times of interest.

5.2 New Features Added in ANL/CANTIA

5.2.1 Initial Flaw Size Distributions

A major feature added in ANL/CANTIA is the ability to treat the growth of two-dimensional cracks, i.e., cracks are allowed to grow (by stress corrosion) in length and depth. Thus, the input in ANL/CANTIA requires an initial flaw depth distribution as well as an initial flaw length distribution. Currently, the depth is taken as the primary dimension, whereas the initial length distribution is entered in terms of a distribution in the aspect ratio (length/depth). The distribution for the aspect ratio can be any of the five statistical distributions: beta, gamma, Gumbel, lognormal, and Weibull. Alternatively, a fixed deterministic ratio can be chosen.

5.2.2 Flaw Growth Model

The basic flaw considered in the original CANTIA is a one-dimensional flaw, e.g., an infinitely long shallow part-throughwall crack with a stress intensity factor K given by $K = BS\sqrt{size}$, where the user must specify constants B and S. In the ANL/CANTIA, we consider an initially elliptical two-dimensional surface flaw of length 2c and depth a. ANL/CANTIA then computes, by numerical integration (4^{th} order Runge-Kutta), the growth (by stress corrosion) of the crack both through the wall and in length, up to the point where it becomes a throughwall crack. CANTIA then follows the growth (by stress corrosion) of the throughwall crack until unstable rupture.

5.2.3 Growth Rate of Stress Corrosion Crack

In ANL/CANTIA we have provided two models for SCC growth rates: one due to Scott [48] and the other due to Ford and Andresen [49]. It is assumed that the same equation can predict crack growth rates in the thickness and the length directions.

5.2.4 Failure Models

In addition to the failure models provided in the original CANTIA, ANL/CANTIA includes options for the failure of axial cracks the ANL ligament rupture model [4] and the unstable-rupture model due to Erdogan [29]. A circumferential crack failure model, based on a modification of the work of Kurihara et al. [35], was also added.

5.2.5 Leak Rate Models

In addition to the leak rate models available in the original CANTIA, ANL/CANTIA provides a leak rate model based on simple orifice flow through a crack with an opening area A and a coefficient of discharge $C_d = 0.6$:

$$Q = 0.6A\sqrt{\frac{2\Delta p}{\rho}}, \tag{5.1}$$

where A is the crack opening area, Δp is the pressure differential, and ρ is the mass density. This model has been used successfully to predict leak rates in experiments conducted at room temperature and 282°C on specimens with EDM notches and stress corrosion cracks at ANL down to a leak rate of ≈0.44 L/min (≈0.1 gal/min). The correlation will break down at lower levels of leak rate for very tight stress corrosion cracks, particularly at elevated temperatures where flashing may occur inside the cracks; but such a limit has not yet been established. The crack opening area is calculated from a model developed by Zahoor [37] and validated by finite element analyses and tests at ANL.

5.2.6 Residual Stress

In ANL/CANTIA, the peak residual stress value (mean and variance) is entered by the user. Currently, the residual stress is idealized as a membrane stress that is reduced linearly with increasing crack depth until it is zero at 100% crack depth. Unless the initial crack depths are very deep, pressure stresses alone cannot grow the stress corrosion cracks through the tube wall without the assistance of residual stresses. However, the current residual stress model in ANL/CANTIA is highly simplified and should be made more realistic in the future.

5.3 Applications of ANL/CANTIA

5.3.1 Effect of POD

The change in the conditional probability of one or more tube ruptures with time is plotted in Fig. 5.1 for the case when the probability of detection (POD) = 0.9. Variations of distributions of crack depth and crack length with time for the same POD are plotted in Figs. 5.2a and 5.2b, respectively. Similar results are plotted in Fig. 5.3 and Figs. 5.4a and 5.4b for a POD = 0.6 and in Fig. 5.5 and Figs. 5.6a and 5.6b for a POD of 0.01.

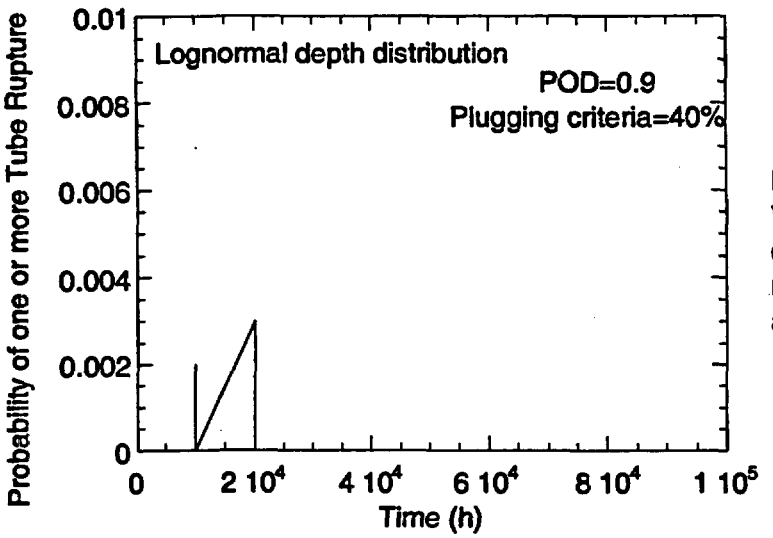

Figure 5.1.
Variation of probability of burst of one or more tubes with time for initial residual stress = 30 ksi, POD = 0.9, and inspection interval of 10,000 h.

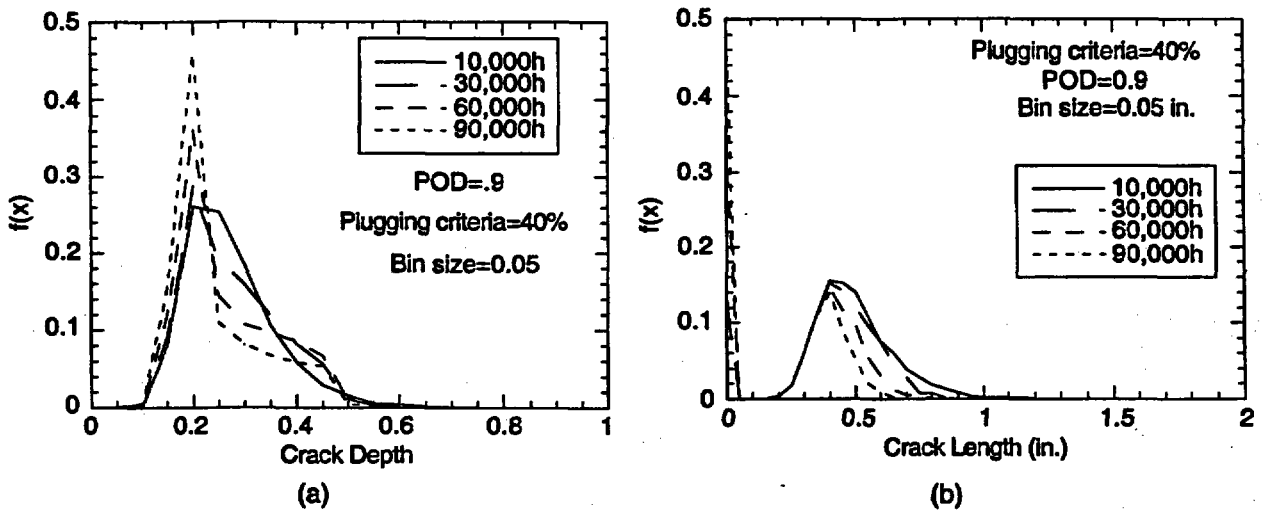

Figure 5.2 Variation of the distribution of (a) nondimensional crack depth and (b) crack length with time for initial residual stress of 30 ksi and POD = 0.9.

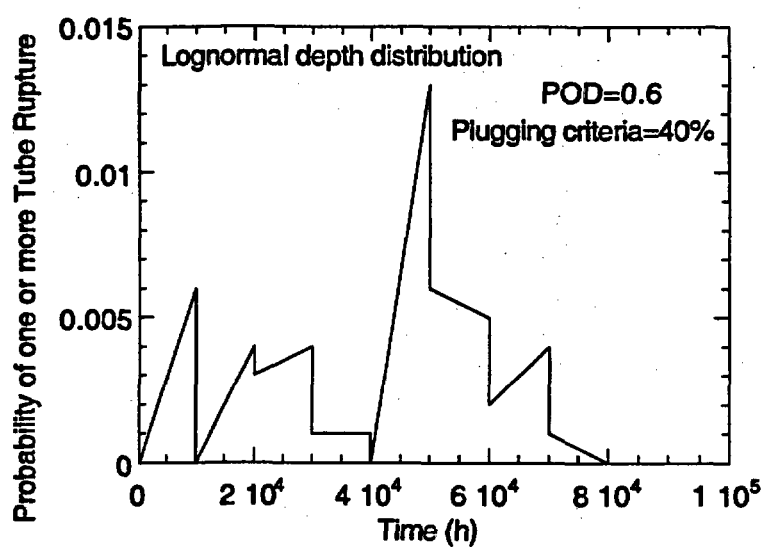

Figure 5.3.
Variation of probability of burst of one or more tubes with time for initial residual stress = 30 ksi, POD = 0.6, and inspection interval of 10,000 h.

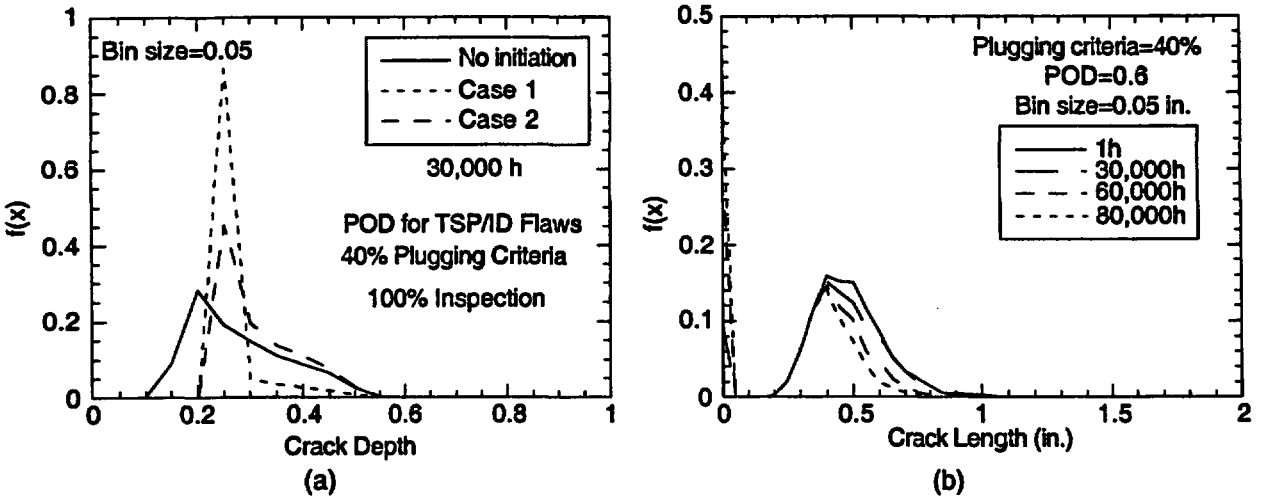

Figure 5.4. Variation of the distribution of (a) crack depth and (b) crack length with time for initial residual stress of 30 ksi and POD = 0.6.

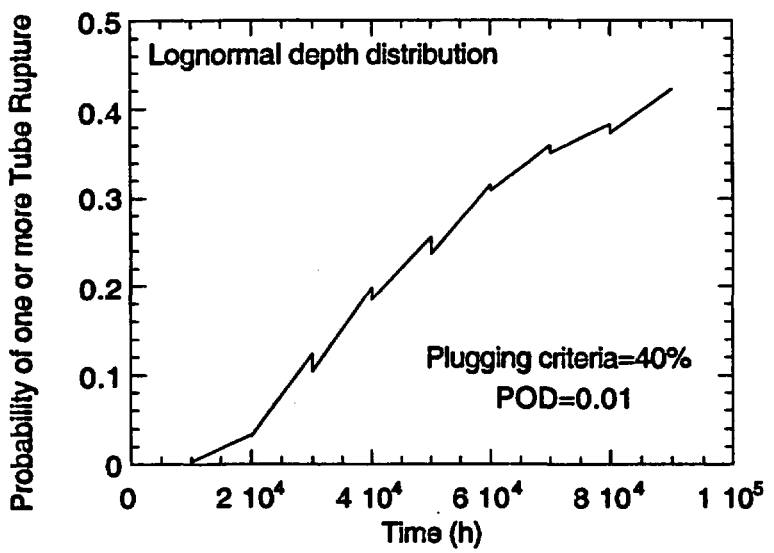

Figure 5.5.
Variation of probability of burst of one or more tubes with time for initial residual stress = 30 ksi, POD = 0.01, and inspection interval of 10,000 h.

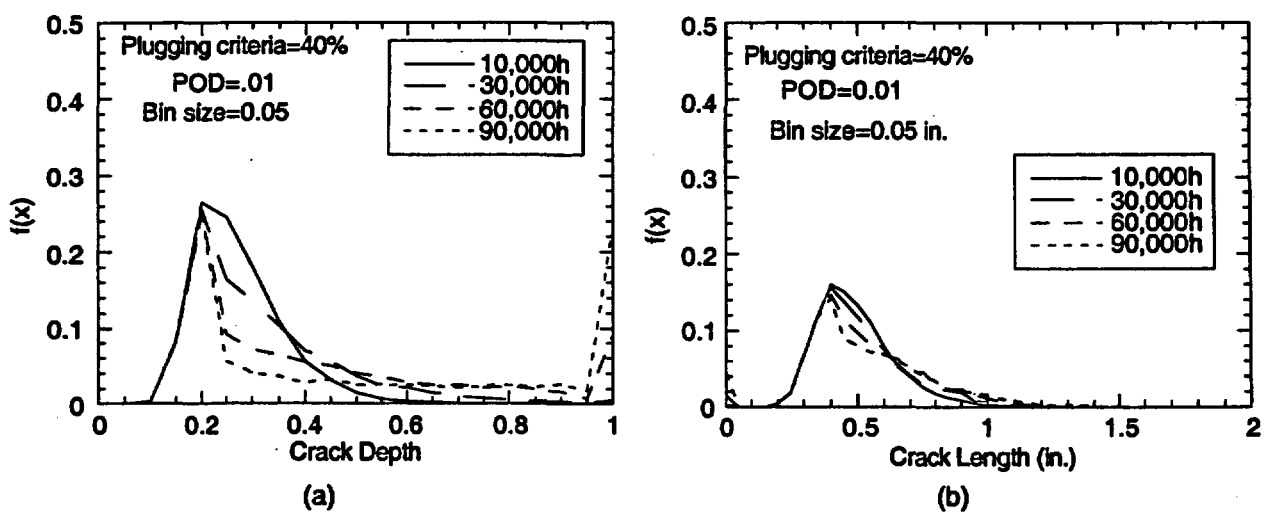

Figure 5.6. Variation of the distribution of (a) crack depth and (b) crack length with time for initial residual stress of 30 ksi and POD = 0.01.

As expected, the probability of one or more tube rupture increases with decreasing POD. Peaks and valleys in Fig. 5.3 represent the effect of plugging on the probability of tube rupture. The probability of tube rupture is very small for POD = 0.9. For POD = 0.6, the probability of one or more tube rupture peaks at an intermediate time. In the case of POD = 0.01, the probability of one or more tube rupture increases monotonically with time. The locations of the peak in the probability of crack depth and crack length change very little with time or POD. The spikes in the probability of crack length at zero crack length represent plugged tubes. Similarly, the spike in the probability at a crack depth of 100% in Fig. 5.6a represent cracks that become throughwall. As expected, the probability for plugging is essentially zero when the POD = 0.01.

Next, we explored the difference between assuming a fixed probability of crack detection (POD = 0.6) and assuming a POD curve determined for TSP/ID flaws in the recent ANL mockup round robin on the probability of one or more tube ruptures. Although the ANL round-robin POD was best-fitted with a linear logistic curve (not available as an option in the current ANL/CANTIA), the POD curve can also be approximated with a lognormal curve, which is one of the options in ANL/CANTIA. This lognormal curve for POD was used in the calculations and 100% tube inspection was assumed. A steam generator with 10 susceptible tubes, each containing a single crack, was considered. A lognormal distribution of initial crack depth was assumed with a fixed initial length to depth aspect ratio of 40. No new cracks were assumed to initiate during the lifetime of the steam generator. The Scott model with a conservative threshold stress intensity factor (K_{th} = 5 ksi-$\sqrt{in}$) was used to determine crack growth rates. For the purpose of this exercise, we assumed ΔP_{norm} = 1.3 ksi, ΔP_{MSLB} = 2.5 ksi, T = 288°C, an in-service-inspection interval of 10,000 h with a 40% plugging criterion, and a total life of 80,000 h. Also, an initial membrane residual stress of 30 ksi was used, and the residual stress was assumed to relax linearly with crack depth, reducing to zero when crack depth = 100%.

One-thousand simulations were used for the Monte Carlo analyses. The variations of distributions of crack depth and crack length with time for the assumed PODs are plotted in Figs. 5.7a and 5.7b, respectively. Because of plugging, the depth and length at peak probability decrease slightly with time. Also, plugging causes a spike in the probability distribution of crack length at zero crack length. Evolution of the probability of one or more tube ruptures with time is plotted in Fig. 5.8 for both POD curves. The discontinuous drops in the probability of rupture curve are caused by plugging of tubes. The probability of tube rupture is basically zero (< 0.001) beyond two equivalent full power years (EFPY) of operation if the full POD curve is used. On the other hand, if a fixed POD = 0.6 is used, the probability of tube rupture does not reduce to zero until 9 EFPY of operation. Of course, these conclusions are valid only for cases where no new cracks are allowed to initiate during the lifetime of the steam generator.

As expected, the probability of one or more tube ruptures is greater when a fixed POD is used than when the full POD curve is used. The crack depth and length distributions are quite similar for both POD curves, although the probability of plugging (spike at zero crack length in Fig. 5.7b) is greater when the full POD curve is used,

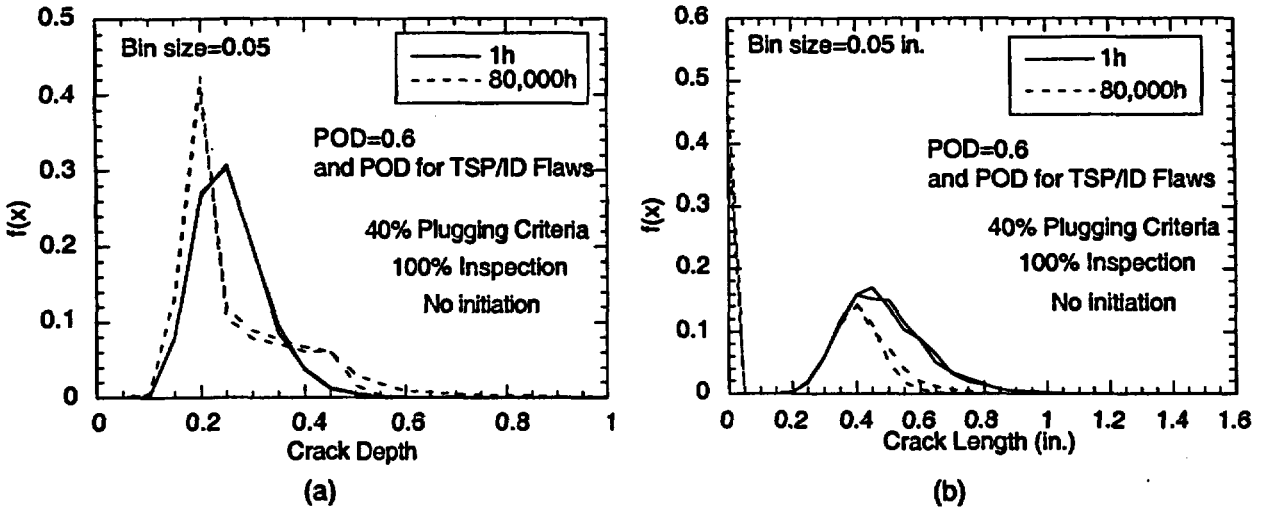

Figure 5.7. Variation of the distribution of (a) crack depth (bin size = 0.05) and (b) crack length (bin size = 0.05 in.) with time using POD curve for TSP ID flaws and a constant POD = 0.6. Initial residual stress is 20.7 MPa (30 ksi).

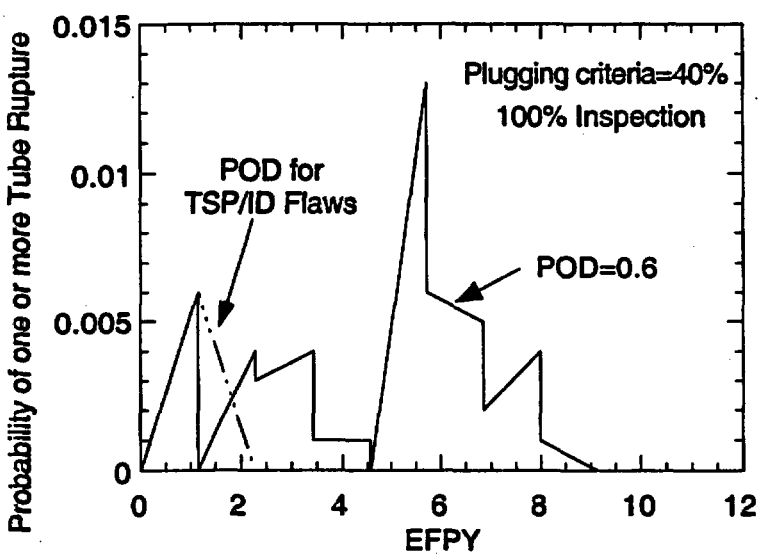

Figure 5.8.
Variation of probability of rupture of one or more tubes with time in effective full power years (EFPY) for a constant POD = 0.6 and a POD curve for TSP/ID flaws. No new flaw initiation was assumed.

5.3.2 Effect of Crack Initiation

Until now no new crack initiation with time has been assumed. To explore the effect of crack initiation on failure probabilities, we assumed two cumulative Weibull distributions for crack initiation times, denoted by Case 1 and Case 2 in Fig. 5.9. Case 1 represents a steam generator that has very low crack initiation resistance, while Case 2 represents an steam generator with greater initiation resistance. Each new crack initiated has a deterministic initial depth of 0.2 of the wall thickness and deterministic initial aspect ratio of 40 (i.e., initial length = 1.0 cm or 0.4 in.). For the purpose of calculation, a steam generator with 50 susceptible tubes was considered, and initially 10 tubes were assumed to contain a crack with a lognormal size distribution. The evolution of the distributions for the number of cracks with time for the two cases is plotted in Figs. 5.10a and 5.10b. The evolution of the distributions of

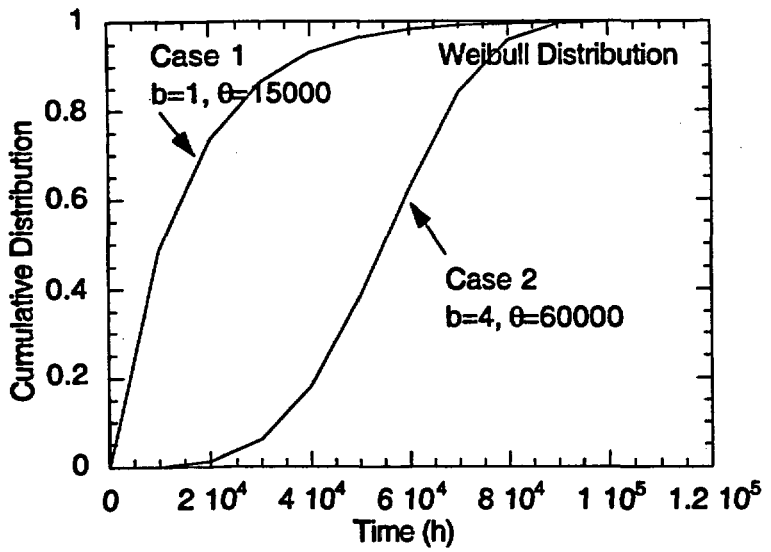

Figure 5.9.
Two cases of cumulative Weibull distributions assumed for crack initiation times.

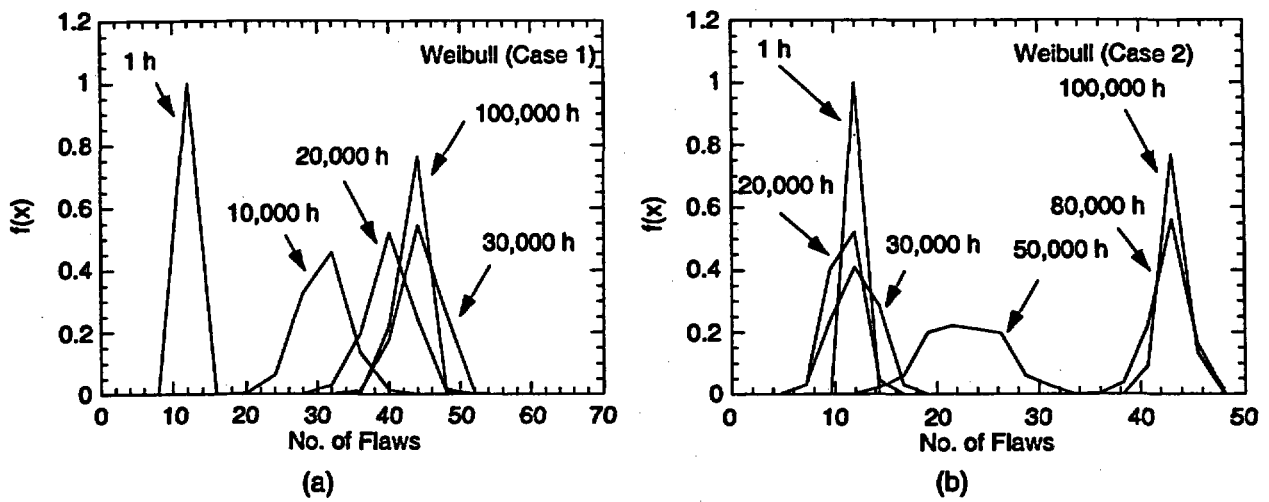

Figure 5.10. Evolution of the distribution for the number of flaws with time for Weibull initiation (a) Case 1 and (b) Case 2.

crack depth for various cases is presented in Figs. 5.11a and 5.11b, and similar presentations for crack length are given in Figs. 5.12a and 5.12b. It is evident that allowing new cracks to initiate changes the distributions slightly compared to a case without new crack initiation. However, for the POD curve (TSP/ID flaws) and plugging criteria (40%) assumed (with 100% inspection), the distributions are not significantly different for the two cases in which new cracks are allowed to initiate. The probability of one or more tube ruptures or for leak rate >4 L/min (>1 gpm) under normal operation for all cases was calculated to be very small (< 0.001).

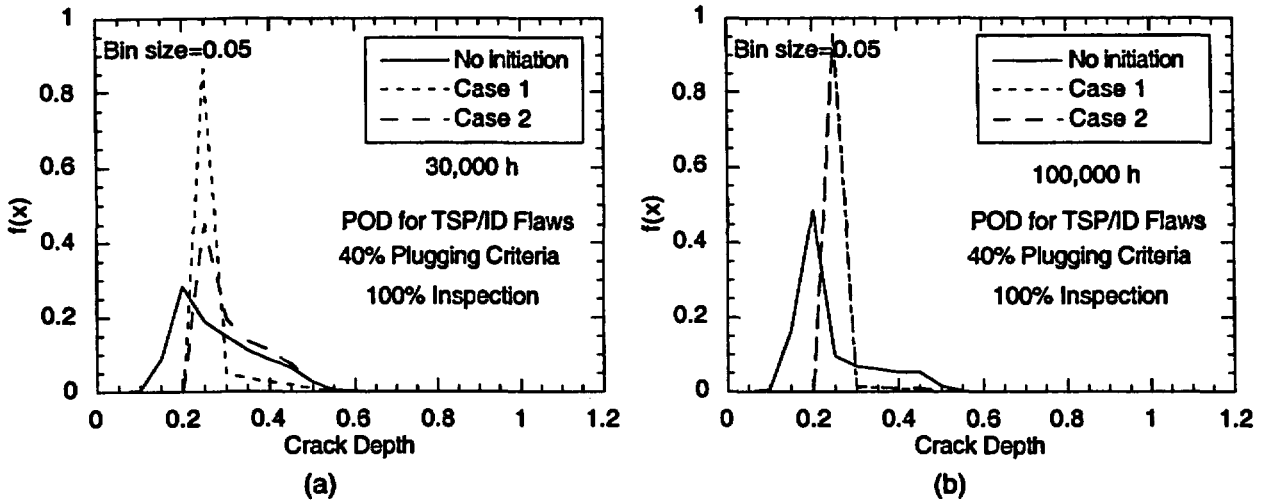

Figure 5.11. Distributions of crack depth calculated without initiation and with Weibull initiation Case 1 and Case 2 at (a) 30,000 and (b) 100,000 h.

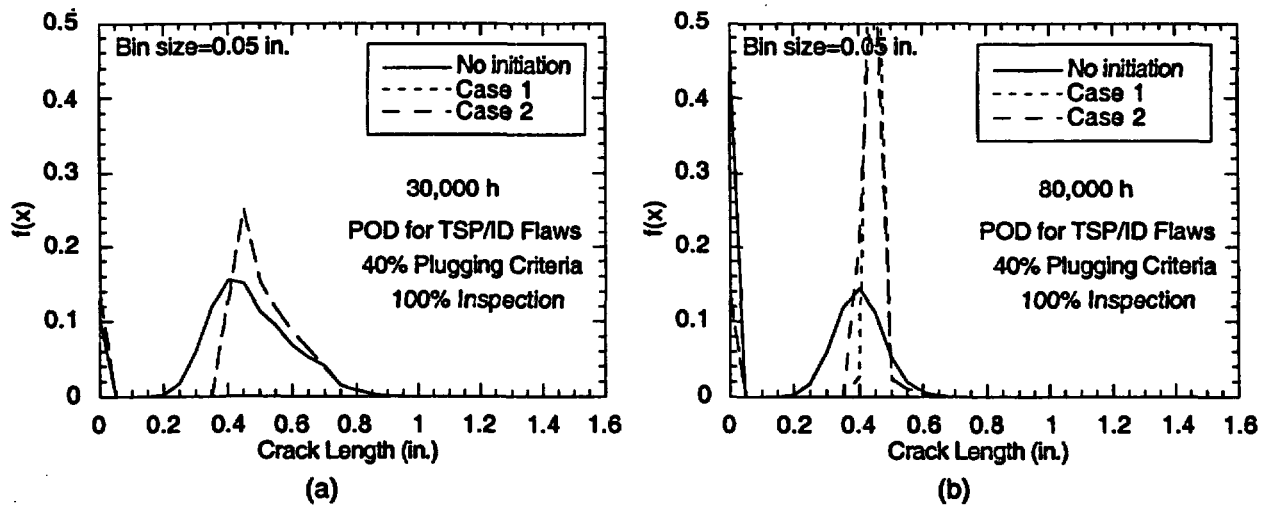

Figure 5.12. Distributions of crack length calculated without initiation and with Weibull initiation Case 1 and Case 2 at (a) 30,000 and (b) 80,000 h.

References

1. D. R. Diercks, S. Bakhtiari, K. E. Kasza, D. S. Kupperman, S. Majumdar, J. Y. Park, and W. J. Shack, *Steam Generator Tube Integrity Program, Annual Report, October 1998-September 1999*, NUREG/CR-6511, Vol. 8, U.S. Nuclear Regulatory Commission, Washington, DC (July 2002).

2. S. Bakhtiari, J. Y. Park, D. S. Kupperman, S. Majumdar, and W. J. Shack, *Advanced NDE for Steam Generator Tubing*, NUREG/CR-6746, U.S. Nuclear Regulatory Commission, Washington, DC (September 2001).

3. D. S. Kupperman, S. Bakhtiari, W. J. Shack, J. Y. Park, and S. Majumdar, *Evaluation of Eddy Current Reliability from Steam Generator Mock-Up Round Robin*, NUREG/CR-6785, U.S. Nuclear Regulatory Commission, Washington, DC (September 2002).

4. S. Majumdar, K. Kasza, and J. Franklin, *Pressure and Leak-Rate Tests and Models for Predicting Failure of Flawed Steam Generator Tubes*, NUREG/CR-6664 (2000).

5. *Steam Generator Program Guidelines*, NEI 97-06, Nuclear Energy Institute, Washington, DC (1997).

6. *PWR Steam Generator Examination Guidelines, Rev. 5*, EPRI TR-107569-V1R5, Electric Power Research Institute, Palo Alto, CA (1997).

7. P. R. Bevington and D. K. Robinson, *Data Reduction and Error Analysis for the Physical Sciences*, 2nd Ed., McGraw Hill, New York (1992).

8. A. H. Bowker and G. J. Lieberman, *Engineering Statistics*, Prentice Hall, Englewood Cliffs, NJ (1972).

9. D. A. Powers and Y. Xie, *Statistical Methods for Categorical Data Analysis*, Academic Press, New York (2000).

10. "Voltage-Based Repair Criteria for Westinghouse Steam Generator Tubes Affected by Outside Diameter Stress Corrosion Cracking," NRC GL 95-05, U.S. Nuclear Regulatory Commission, Washington, DC (August 3, 1995).

11. "Proc. 20th Annual EPRI Steam Generator Tube NDE Workshop," Orlando, FL, July 9–11, 2001, Electric Power Research Institute, Palo Alto, CA (2002).

12. J. L. Rose, K. M. Rajana, and F. T. Carr, "Ultrasonic Guided Wave Inspection Concepts for Steam Generator Tubing," Mater. Eval., Vol. 52, Feb. 1994, pp. 307-311.

13. D. R. Diercks, S. Bakhtiari, K. E. Kasza, D. S. Kupperman, S. Majumdar, J. Y. Park, and W. J. Shack, *Steam Generator Tube Integrity Program, Annual Report, October 1995-September 1996*, NUREG/CR-6511, ANL-97/3, Vol. 2, U.S. Nuclear Regulatory Commission, Washington, DC (December 1997).

14. S. Bakhtiari and D.S. Kupperman, "Modeling of eddy current probe response for steam generator tubes", *Nuc. Eng. and Design*, 194, 1999.

15. S. Bakhtiari, J. Y. Park, D. S. Kupperman, S. Majumdar, and W. J. Shack, *Advanced Nondestructive Evaluation for Steam Generator Tubing*, NUREG/CR-6746, ANL-01/21, U.S. Nuclear Regulatory Commission, Washington, DC (September 2001).

16. R. Bandy, R. Roberge, and R. C. Newman, "Low Temperature Stress Corrosion Cracking of Inconel 600 under Two Different Conditions of Sensitization", *Corrosion Science*, Vol. 23, No. 9, pp. 995–1006, 1983

17 D. R. Diercks, et. al., *Steam Generator Tube Integrity Program, Annual Report, October 1996–September 1997*, NUREG/CR-6511, ANL-98/15 Vol. 4, U.S. Nuclear Regulatory Commission, Washington, DC (January 1999).

18. R. A. Clark and R. L. Burr, "A Method for Controlled Stress Corrosion Cracking in Nonsensitized Inconel 600 Tubing", *Corrosion*, Vol. 36, July 1980, pp. 382–383

19. S. Bakhtiari, J. Y. Park, D. S. Kupperman, S. Majumdar, and W. J. Shack, Advanced Nondestructive Evaluation for Steam Generator Tubing, NUREG/CR-6746, ANL-01/21, U.S. Nuclear Regulatory Commission, Washington, DC (September 2001).

20. D. R. Diercks, et. al., *Steam Generator Tube Integrity Program, Semiannual Report, October 1998–March 1999*, NUREG/CR-6511, ANL-00/4 Vol. 7, U.S. Nuclear Regulatory Commission, Washington, DC (September 2000).

21. M. Da Cunha Belo, N.E. Hakiki, and M.G.S. Ferreira, *Electrochimica Acta* Vol.44 pp. 2473–2481 (1999).

22. R.M. Carranza and M.G. Alvarez, *Corrosion Science*, Vol. 38, No. 6, pp. 909–925 (1966)

23. K. Kasza, S. Majumdar, J. Y. Park, and J. Franklin, *Results From Pressure and Leak Rate Testing of Laboratory Degraded Steam Generator Tubes*, NUREG/CR-6789, Argonne National Laboratory (2002).

24. C. N. Amos and V. E. Schrock, "Two-phase critical flow in slits," *Nuclear Science and Engineering*, 88, 3 pp. 261-74 (1984).

25. S. Majumdar, W.J. Shack, D.R. Diercks, K. Mruk, and J. Franklin, *Failure Behavior of Internally Pressurized Flawed and Unflawed Steam Generator Tubing at High Temperatures—Experiments and Comparison with Model Predictions*, NUREG/CR-6575, Argonne National Laboratory (1997).

26. J. M. Alzheimer, R. A. Clark, C. J. Morris, and M. Vagins, *Steam Generator Tube Integrity Program Phase I Report*, NUREG/CR-0718, PNL-2937, Richland, WA, September (1979).

27. P. G. Ellison, L. W. Ward, C. A. Dobbe, S. A. Chavez, C. L. Atwood, L. N. Haney, W. G. Reece, and H. S. Blackman, *Steam Generator Induced Rupture from Operating Transients, Design-Basis Accidents, and Severe Accidents*, INEL-95/0641, Idaho National Engineering Laboratory, Aug. 1996.

28. G. T. Hahn, M. Sarrate, and A. R. Rosenfield, "Criteria for crack extension in cylindrical pressure vessels," *Int. J. Fracture Mech.*, Vol. 5, No. 3, 1969.

29. F. Erdogan, "Ductile failure theories for pressurized pipes and containers," *Int. J. of Pres. Ves. & Piping*, Vol. 4, 1976.

30. J. F. Kiefner, W. A. Maxey, R. J. Eiber, and A. R. Duffy, "Failure stress levels of flaws in pressurized cylinders," in *Progress in Flaw Growth and Fracture Toughness Testing*, Sixth National Symposium on Fracture Mechanics, Philadelphia, J. G. Kaufman, ed., American Society for Testing and Materials, Committee E-24 on Fracture Testing of Metals, American Society for Testing and Materials, ASTM Special Technical Publication 536, Philadelphia 1973.

31. S. Ranganath and H. S. Mehta, "Engineering Methods for the Assessment of Ductile Fracture Margin in Nuclear Power Plant Piping," Elastic Plastic Fracture Second Symposium, Vol. 2, Fracture Resistance Curves and Engineering Applications, American Society for Testing and Materials, ASTM Special Technical Publication 803, Philadelphia 1973.

32. M. F. Kanninen, A. Zahoor, G. M. Wilkowski, I. Abou-Sayed, C. Marschall, D. Broek, S. Sampath, C. Rhee, J. Ahmad, "*Instability Predictions for Circumferentially Cracked Type 304 Stainless Steel Pipes under Dynamic Loading*," EPRI NP-2347 (Vol. 1: Summary; Vol. 2: Appendices), Electric Power Research Institute, Palo Alto, CA, April 1982.

33. B. Cochet, J. Engstrom, and B. Flesch, "PWR steam generator tube and tube support plate plugging criteria," Paper 4.1, *Steam generator tubes mechanical, LBRB, and probabilistic studies*, EDF, France, 1990.

34. S. Majumdar, "Failure and leakage through circumferential cracks in a steam generator tubing during accident conditions," International Journal of Pressure Vessels and Piping, Vol. 76, pp. 839-847, 1999.

35. R. Kurihara, S. Ueda, and D. Sturm, Estimation of the Ductile Unstable Fracture of Pipe with a Circumferential Surface Crack subjected to Bending, *Nucl. Eng. Design*, Vol. 106, 1988.

36. D. R. Diercks, S. Bakhtiari, O. K. Chopra, K. E. Kasza, D. S. Kupperman, S. Majumdar, J.Y. Park, and W.J. Shack, *Steam Generator Tube Integrity Program, Annual Report, August 1999-September 2000*, NUREG/CR-6511, Vol. 6, U.S. Nuclear Regulatory Commission, Washington, DC (2001).

37. A. Zahoor, *Ductile Fracture Handbook*, Electric Power Research Institute, Palo Alto, 1989.

38. P. C. Paris and H. Tada, *The application of fracture proof design methods using tearing instability theory to nuclear piping postulating circumferential throughwall cracks*, NUREG/CR-3464, USNRC, Washington, DC, 1983.

39. S. Majumdar, S. Bakhtiari, K. Kasza, and J.Y. Park, *Validation of failure and leak rate correlations for stress corrosion cracks*, NUREG/CR-6774, USNRC, Washington, DC, May 2002.

40. P. G. Ellison, L. W. Ward, C. Dobbe. S. A. Chavez, C. L. Atwood, C. L. Smith, L. M. Wolfram, J. L. Jones, L. N. Haney, and W. J. Reece, *The Risk Significance of Induced Steam Generator Tube Rupture, INEL-95/0641, Rev. 1* (Draft), Lockheed Martin Idaho Technologies, Inc., Idaho National Engineering Laboratory, December 15, 1995.

41. E. L. Fuller, M. A. Kenton, M. Epstein, R. E. Henry, and N. G. Cofie, *Risks from Severe Accidents Involving Steam generator Tube Leaks or Ruptures*, EPRI TR-106194 (Draft), Electric Power Research Institute, Palo Alto, CA, January 1996.

42. SGTR Severe Accident Working Group, *Risk Assessment of Severe Accident-Induced Steam Generator Tube Rupture*, NUREG-1570, USNRC, Washington DC, 1998.

43. S. Majumdar, "Structural analysis of Electrosleeved tubes under severe accident transients", *Nuclear Engineering and Design*, Vol, 208, pp. 167-179, 2001.

44. S. Majumdar, D.R. Diercks, and W.J. Shack, *Analysis of Potential for Jet-Impingement Erosion from Leaking Steam Generator Tubes during Severe Accidents*, NUREG/CR-6756, USNRC, Washington, DC, May 2002.

45. V. Kumar, M. D. German, and C. F. Shih, *An Engineering Approach for Elastic-Plastic Fracture Analysis*, EPRI NP-1931, Electric Power Research Institute, 1981.

46. J. E. Harris, J. A. Gorman, and A.P.L. Turner, *Probabilistic Methodology for Assessing Steam Generator Tube Inspection – Phase II*, Report prepared by Dominion Engineering, Inc. for AECB Research Project No. 2.353.2, March 1997.

47. S. Majumdar, *ANL/CANTIA: A Computer Code for Steam Generator Integrity Assessments*, NUREG/CR-6786, USNRC, Washington, DC, September 2002.

48. P. M. Scott, *An Analysis of Primary Water Stress Corrosion Cracking in PWR Steam Generators*, Proc. of the Specialists Meeting on Operating Experience with Steam Generators, Brussels, Belgium (Sept. 1991), pp. 5-6.

49. F. P. Ford and P. L. Andresen, *Development and Use of a Predictive Model of Crack Propagation in 304/316L, A533B/A508, and Inconel 600/182 Alloys in 288°C Water*, Proc. 3rd Int. Symp. on Environmental Degradation of Materials in Nuclear Power Systems—Water Reactors, Traverse City, MI, The Metallurgical Society/AIME, Warrendale, PA (1988), pp. 789-800.

NRC FORM 335 (2-89) NRCM 1102, 3201, 3202

U. S. NUCLEAR REGULATORY COMMISSION

BIBLIOGRAPHIC DATA SHEET

(See instructions on the reverse)

1. REPORT NUMBER *(Assigned by NRC. Add Vol., Supp., Rev., and Addendum Numbers, if any.)*
NUREG/CR-6804
ANL-02/28

2. TITLE AND SUBTITLE
Second U.S. Nuclear Regulatory Commission International Steam Generator Tube Integrity Research Program
Final Project Summary Report

3. DATE REPORT PUBLISHED
MONTH: September
YEAR: 2003

4. FIN OR GRANT NUMBER
W6487

5. AUTHOR(S)
S. Bakhtiari, K. E. Kasza, D. S. Kupperman, S. Majumdar, J. Y. Park, W. J. Shack, and D. R. Diercks

6. TYPE OF REPORT
Technical; Topical

7. PERIOD COVERED *(Inclusive Dates)*

8. PERFORMING ORGANIZATION – NAME AND ADDRESS *(If NRC, provide Division, Office or Region, U.S. Nuclear Regulatory Commission, and mailing address; if contractor, provide name and mailing address.)*
Argonne National Laboratory
9700 South Cass Avenue
Argonne, IL 60439

9. SPONSORING ORGANIZATION – NAME AND ADDRESS *(If NRC, type "Same as above"; if contractor, provide NRC Division, Office or Region, U.S. Nuclear Regulatory Commission, and mailing address.)*
Division of Engineering
Office of Nuclear Regulatory Research
U. S. Nuclear Regulatory Commission
Washington, DC 20555 -0001

10. SUPPLEMENTARY NOTES
J. Muscara, NRC Project Manager

11. ABSTRACT (200 words or less)

This report summarizes work performed under the USNRC Steam Generator Integrity Program at Argonne National Laboratory. The areas addressed by the program include assessment of procedures and equipment used for in-service (ISI) inspection of steam generator (SG) tubes; recommendations for criteria and requirements to improve the reliability and accuracy of ISI; validation and improvement of correlations and models that are used to evaluate integrity and leakage of degraded SG tubes; and validation and improvement of correlations and models that predict the generation and progression of degradation in SG tubes as a function of aging.

12. KEY WORDS/DESCRIPTORS *(List words or phrases that will assist researchers in locating this report.)*
Steam Generator
Tubes
Nondestructive Evaluation
Eddy Current Testing
Inservice Inspection
Stress Corrosion Cracking
Alloy 600, Inconel 600

13. AVAILABILITY STATEMENT
Unlimited

14. SECURITY CLASSIFICATION
(This Page)
Unclassified
(This Report)
Unclassified

15. NUMBER OF PAGES

16. PRICE

NRC FORM 335 (2-89)

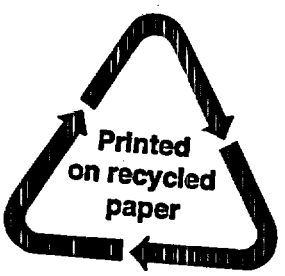

Federal Recycling Program

UNITED STATES
NUCLEAR REGULATORY COMMISSION
WASHINGTON, DC 20555-0001

OFFICIAL BUSINESS